Synthesis, Characterization and Mechanical Behavior of a Novel Sustainable Structural Binder Utilizing the Chemistry of Iron Carbonation

by

Sumanta Das

A Dissertation Presented in Partial Fulfillment
of the Requirements for the Degree
Doctor of Philosophy

Approved May 2015
Graduate Supervisory Committee:

Narayanan Neithalath, Chair
S. D. Rajan
Barzin Mobasher
Nikhilesh Chawla
Robert Marzke
David Stone

ARIZONA STATE UNIVERSITY

August 2015

ABSTRACT

Increased priority on the minimization of environmental impacts of conventional construction materials in recent years has motivated increased use of waste materials or bi-products such as fly ash, blast furnace slag with a view to reduce or eliminate the manufacturing/consumption of ordinary portland cement (OPC) which accounts for approximately 5-7% of global carbon dioxide emission. The current study explores, for the first time, the possibility of carbonating waste metallic iron powder to develop carbon-negative sustainable binder systems for concrete. The fundamental premise of this work is that metallic iron will react with aqueous CO_2 under controlled conditions to form complex iron carbonates which have binding capabilities. The compressive and flexural strengths of the chosen iron-based binder systems increase with carbonation duration and the specimens carbonated for 4 days exhibit mechanical properties that are comparable to those of companion ordinary portland cement systems. The optimal mixture proportion and carbonation regime for this non-conventional sustainable binder is established based on the study of carbonation efficiency of a series of mixtures using thermogravimetric analysis. The pore- and micro-structural features of this novel binding material are also evaluated. The fracture response of this novel binder is evaluated using strain energy release rate and measurement of fracture process zone using digital image correlation (DIC). The iron-based binder system exhibits significantly higher strain energy release rates when compared to those of the OPC systems in both the unreinforced and glass fiber reinforced states. The iron-based binder also exhibits higher amount of area of fracture process zone due to its ability to undergo inelastic deformation facilitated by unreacted metallic iron particle inclusions in the microstructure that helps crack

bridging /deflection. The intrinsic nano-mechanical properties of carbonate reaction product are explored using statistical nanoindentation technique coupled with a stochastic deconvolution algorithm. Effect of exposure to high temperature (up to 800°C) is also studied. Iron-based binder shows significantly higher residual flexural strength after exposure to high temperatures. Results of this comprehensive study establish the viability of this binder type for concrete as an environment-friendly and economical alternative to OPC.

Dedicated to my parents for their support and encouragement

ACKNOWLEDGMENTS

Any attempt to acknowledge my advisor Dr. Neithalath who has constantly conferred love and support on me, would fall short. I would like to express my deepest gratitude to him for guiding me throughout my thesis work and helping me to develop the ability to assess, create, and articulate ideas. I would never have been able to complete my thesis without his timely suggestions and support. I would also like to thank Dr. David Stone for helping me in my research. I would additionally like to thank my committee members: Profs. Rajan, Mobasher, Marzke, and Chawla for dedicating their time and guidance to this work.

Special thanks to my fellow labmates at Arizona State University: Akash, Pu, Ahmet, Swaptik, Kirk, Ben, Vikram, Yiming, Robert, Ussala, Breezy, Matt, Aashay, Nihat for their support.

I have no words to express my gratitude to my parents and my sister. I would never have had the strength and will to reach this stage without their support and encouragement.

TABLE OF CONTENTS

Page

CHAPTER Page

CHAPTER Page

CHAPTER Page

LIST OF FIGURES

Figure Page

Figure Page

Figure Page

Figure Page

LIST OF TABLES

Table Page

Chapter 1 Introduction

1.1 Background

The rapid growth of civilization and the phenomenal industrial and technological developments of human society over the past few decades have placed unprecedented demands on construction materials such as cement. But, production of cement results in generation of a significant amount of CO_2, a major contributor to the global warming (Worrell et al. 2001; Mehta and Monteiro 2006). Manufacturing of cement involves heating of raw materials to a very high temperature which makes it a severely energy-intensive process. Besides, a significant amount of CO_2 is produced chemically from cement production (Worrell et al. 2001). Moreover, cement industry accounts for about 5% of the total global CO_2-emission (Worrell et al. 2001). These issues have potentially devastating consequences to mankind in the long term if left unchecked. Hence, this is an ideal time to focus on increasing sustainability of infrastructural materials through novel alternative strategies with a view to seeking new and innovative ways to manage natural resources in a manner that is ecologically sustainable and yet economically viable. With this quest, the current study explores synthesis and properties of a novel sustainable structural material through carbonation of waste metallic iron dust. The main concept of this study is inspired by the idea of CO_2-corrosion of, and scale formation in carbon-steel pipelines in the oil and gas industry, which is a result of CO_2 injection into the oil wells to reduce the viscosity of the oil and thus increase oil production. The novel binder system provides yet-unheard-of synergistic benefits through: (i) consumption and trapping of CO_2 from a GHG-emitting industrial operation and subsequent carbonate formation, and (ii) providing a means to reduce the overall Ordinary Portland Cement

(OPC) production through its complete elimination. Thus, the novel structural binder provides an environment-friendly, carbon-negative and economically viable alternative to traditional structural materials.

1.2 Objective

The main objectives of the present study are

a) Preliminary investigation on possibility of carbonating metallic iron powder to form a sustainable binder.

b) Determination of optimal mixture proportions and carbonation regime for strength based on the study of carbonation efficiency.

c) Detailed pore- and microstructural characterization of the novel binder.

d) Investigation of fracture-response of this novel binder through evaluation of strain energy release rates and fracture process zone. Also, detailed study on fundamental difference in crack-propagation and strain-localization mechanism between this novel iron-based binder and hardened cement paste.

e) Nano-mechanical characterization of individual phases in iron-based novel binder using statistical nanoindentation technique and quantification of effective homogenized properties using mean-field homogenization theories.

f) Investigation of high-temperature resistance of novel iron-based binder and comparison with traditional OPC.

g) Evaluation of fundamental modification in crack-propagation mechanism imparted by metallic iron powder waste in cement mortars towards enhancement of toughness of the material.

1.3 Dissertation Layout

This dissertation is primarily composed of seven research papers that are published, submitted or will be submitted for publication. Some chapters contain additional data that are not presented in papers. These papers are presented in Chapter 4-10. Chapter 4-9 discuss detailed investigation on synthesis and mechanical behavior under various loading and exposure conditions whereas Chapter 10 shows effect of metallic iron particulate inclusion as OPC-replacement on fracture response of cement mortars. This section shows overall organization of the thesis for clarity.

Chapter 2 consists of extensive literature review on (1) carbonation of metallic particles and is effect on mechanical behavior; (2) effect of metallic particulate inclusion on mechanical behavior of cement mortars.

Chapter 3 provides brief description of experimental methodologies and materials used in this study. Various instruments were used in different experiments in this dissertation. This chapter gives a generalized description on the instruments. Detailed application-specific information on materials and experimental methods are detailed in individual chapters.

Chapter 4 reports preliminary investigation on synthesis and mechanical behavior of novel binder. Effect of source materials on carbonation efficiency and thus strength is elucidated. Optimal mixture proportion and carbonation regime is established.

Chapter 5 carries out a detailed pore- and microstructural characterization of the novel material. The pore-structure is evaluated using mercury intrusion porosimetry and ESEM under backscattered mode on plane polished surfaces is used for microstructural characterization.

Chapter 6 evaluates the fracture-response of the novel binder using compliance-based strain energy release rates. A comparison with traditional hardened cement paste is also evaluated.

Chapter 7 shows fundamental difference in crack-propagation mechanism between iron-based novel binder and hardened cement paste through evaluation of fracture process zone (FPZ) characterized by digital image correlation (DIC). In addition geometric measurements of FPZ, thus measured, are used in a strain energy release rate-based inverse analysis approach applying a crack-face bridging model to predict the tensile behavior of the novel binder.

Chapter 8 evaluates intrinsic nano-mechanical properties of different phases present in novel iron carbonate binder using statistical nanoindentation technique. Effective homogenized Young's modulus of the bulk material is also predicted using mean-field homogenization theories. Further the results are validated through macro-scale experiments.

Chapter 9 provides response of novel iron-based binder subjected to elevated temperatures. A comparison with hardened cement paste and alkali-activated blast furnace slag binder is also evaluated. The thermal damage in pore-structure at different temperatures is evaluated using MIP and BSE SEM images are used along with elemental mapping on plane polished surfaces to assess the comparative microstructural damage at different elevated temperatures.

Chapter 10 investigates fundamental modification in crack-propagation mechanism imparted by metallic iron powder waste in cement mortars towards enhancement of

toughness. This idea is inspired by the study on effect of unreacted iron particles in iron-based binder in facilitating microstructural reinforcement explored in Chapter 6 and 7.

Chapter 2 Literature Review

The proceeding literature review is divided into three sections: the first one is on possibility of using mineral carbonation as a pathway to form a structural binder; the next one is on characterization of fracture behavior of cementitious materials and the last one is on constitutive material modelling of cementitious materials.

2.1 Mineral carbonation as a pathway to form a structural binder

2.1.1 Background and Overview

Concrete is the most widely used construction material and it contains cement, water, coarse and fine aggregates. The environmental impacts associated with concrete production have been studied in detail (Worrell et al. 2001; Mehta and Monteiro 2006) . It has been reported that major contributor of greenhouse gas emissions in concrete is manufacturing of cement (Worrell et al. 2001; Mehta and Monteiro 2006). Manufacturing of portland cement involves heating of raw materials such as limestone and clay in a kiln at 1500°C. Thermal decomposition of limestone produces approximately 0.5 ton of CO_2 for every ton of CaO produced (Worrell et al. 2001; Mehta and Monteiro 2006). Besides, there is significant amount of additional CO_2-emission is associated with high energy consumption of the kiln. Cement is currently one of enormously used materials on this planet. Human civilization has never used any such material in such tremendous quantities except water. Hence, greenhouse gas emissions from cement production can make a significant impact due to its large consumption. Cement industry has been reported to be responsible for 5% of the global anthropogenic CO_2 emissions (Worrell et al. 2001). These issues have potentially devastating consequences to mankind in the long term if left unchecked. Hence, this is ideal time to focus on sustainability of construction

materials. There are three primary ways of enhancing sustainability of construction materials: (1) decrease the energy demand associated with cement production (Popescu, Muntean, and Sharp 2003); (2) partial replacement of cement with inert fillers such as limestone powder or reactive pozzolanic materials such as fly ash and blast furnace slag (Vance et al. 2013; Bonavetti et al. 2003; J. J. Chen, Kwan, and Jiang 2014; Berndt 2009; Atiş 2002) and (3) 100% replacement of cement using reactive pozzolanic materials through alkali-activation (Ravikumar, Peethamparan, and Neithalath 2010; Chithiraputhiran and Neithalath 2013). Strategies have been implemented to decrease the energy demand by increasing the efficiency of the production plant and by implementing a procedure that requires lower temperature to produce cement and use of low-energy cement (Popescu, Muntean, and Sharp 2003). But these procedures are not effective in obtaining significant reduction in CO_2-emission since the CO_2-emission in cement industry is primarily contributed by calcination of limestone. Another strategy for reduction in CO_2-emissions is partial replacement of cement with pozzolanic materials such as fly ash, blast furnace slag or metakaolin. These pozzolanic materials are aluminosilicate materials which chemically react to form additional C-S-H gel. Studies have been done on using fine limestone powder as partial replacement of OPC to increase sustainability (Vance et al. 2013; Bonavetti et al. 2003; J. J. Chen, Kwan, and Jiang 2014). Limestone is interground with OPC clinker in the cement manufacturing process or blended with the cement during concrete batching. Current ASTM standards allow for up to 15% of limestone (by mass) in OPC (Vance et al. 2013). Inter-grinding limestone with clinker -provides improved particle packing (Vance et al. 2015; A. Kumar et al. 2013), while the finer limestone particles in both interground and blended systems act as

nucleation sites which enhance the rate of hydration of the OPC phases (Vance et al. 2013). The incorporation of limestone powder in low water-to-cement ratio (w/c) concretes has been shown to provide similar or better strengths to companion OPC systems in spite of a reduction in the amount of cement used (Vance et al. 2013). While the above-mentioned methods incorporate partial replacement of cement with reactive pozzolanic materials or inert fillers, the need to reduce the CO_2 footprint of portland cement production has motivated studies on several new types of alternative binding materials for concrete such as the family of alkali activated aluminosilicate binders (Ravikumar, Peethamparan, and Neithalath 2010). These binders generally are alkali-activated systems that use an alkaline activator, typically sodium hydroxide or sodium silicate, along with a silica-and-alumina rich precursor material such as fly ash or ground granulated blast furnace slag to synthesize a final product with properties comparable to or better than those of ordinary Portland cement concrete (Ravikumar, Peethamparan, and Neithalath 2010). However, availability of these raw waste ingredients is limited, especially for fly ash, due to enhanced use of natural gas and alternative energy sources that may limit operation of coal-fired power plants and thereby limit the availability of fly ash (Vance 2014). Hence, this is ideal time to focus on new and innovative ways to use existing natural resources to form structural binder in a manner that is ecologically sustainable and yet economically viable. With this quest, this study aims at finding a novel route to form carbon-negative structural binder by trapping CO_2 in metallic minerals. The proceeding sections introduce the concept of CO_2-minimization through mineral carbonation that can be used as an innovative pathway to synthesize a structural binder.

2.1.2 Mineral carbonation for CO_2-minimization

According to U.S. Environmental Protection Agency (EPA) an average coal-fired power plant which produces 4 million MWh of electricity emits about 4 million tons of CO_2 (Oelkers, Gislason, and Matter 2008). Several studies (Flower and Sanjayan 2007; H. Yang et al. 2008; M. Schneider et al. 2011; Rehan and Nehdi 2005) over the past two decades suggest that the most stable, long-term storage mechanism of atmospheric CO_2 is the formation of carbonate minerals. Mineral carbonation is the process which captures CO_2 as stable carbonate minerals, such as calcite ($CaCO_3$), dolomite ($Ca_{0.5}Mg_{0.5}CO_3$), magnesite ($MgCO_3$) and siderite ($FeCO_3$) (Oelkers, Gislason, and Matter 2008; Gislason et al. 2010; Matter and Kelemen 2009). This route of CO_2-capture can be either ex situ, as a part of industrial operation or in situ, by injection of CO_2 into the geological formations where potential minerals are available for carbonation (H. Yang et al. 2008). The energy state of mineral carbonate is 60-180 kJ/mol which is lower than that of CO_2 (400 kJ/mol) (M. M. Maroto-Valer et al. 2005; M. Mercedes Maroto-Valer, Tang, and Zhang 2005). Hence, CO_2-capture in the form of mineral carbonation ensures long-term fixation of CO_2 rather than temporary storage. This process thus eliminates the risk of any accidental release of stored CO_2 which may otherwise leak from underground if mineral carbonation is not used.

Mineral carbonation requires reaction of CO_2 with metals to form carbonate minerals. The required cations include Ca^{2+}, Mg^{2+} and Fe^{2+}. The most abundant natural source of these cations is silicates which are energetically favored to form carbonate minerals (Seifritz 1990; Lackner et al. 1995; Lackner 2002). Mineral carbonation reactions, where rocks such as Forsterite, anorthite, olivine, serpentine etc. react with CO_2 to form

carbonate minerals, are observed in nature and in the laboratory (McGrail et al. 2006; Giammar, Bruant, and Peters 2005). Although formation of mineral carbonates in such process is thermodynamically favorable, it is not straightforward due to mammoth scale and slow rate of reaction that reduces the efficiency of the overall process (Oelkers, Gislason, and Matter 2008). The natural weathering of rocks to form carbonates happens in nature over geological time scales. But, expedition of the process is needed to make this process viable. Artificial mineral carbonation was first proposed in a study (Seifritz 1990) to imitate the natural process. But, in order to accelerate the process, two methods were proposed: (1) enhancement of dissolution of mineral ions using stronger acids; (2) use of higher CO_2-pressure to increase the rate of reaction. Many researchers investigated these possibilities (Oelkers 2001; S. A. Carroll and Knauss 2005; Golubev and Pokrovsky 2006; Oelkers, Gislason, and Matter 2008). With this increment in reaction rates, the capacity of CO_2-fixaion becomes huge, even though use of strong acid may cause problem in reaction facilities and in the environment (Oelkers, Gislason, and Matter 2008). On the other hand, higher pressure requires additional energy (Oelkers, Gislason, and Matter 2008). In order to eliminate the problems regarding use of strong acids, organic acids were proposed later which have been observed to accelerate silicate dissolution rates (Golubev and Pokrovsky 2006). The mineral carbonation of silicate minerals were also studied using mechanical process (Nelson 2004; Oelkers, Gislason, and Matter 2008). Silicate minerals such as forsterite, lizardite, wollastonite and synthetic minerals such as magnesium silicate were grinded in presence of gaseous CO2 and it resulted in a small amount of CO2-fixation. But, this efficiency of this process is limited considering energy needed to grind these silicate minerals (H. Yang et al. 2008).

Acceleration of carbonation reaction is also investigated through surface-activation physically and chemically (M. Mercedes Maroto-Valer, Tang, and Zhang 2005; M. M. Maroto-Valer et al. 2005). Significant improvement in carbonation efficiency with surface-activation was reported. Results of all the above mentioned literatures in this section suggests that fine minerals (bearing Ca2+, Mg2+, Fe2+ etc.) with large surface area can produce carbonates in realistic timescale using organic acids to augment the rate of reaction. Another very interesting fact is that the secondary carbonate rocks formed during mineral trapping perform very well under both compression as well as tension (Hobbs 1964; Hobbs 1967; Herget and Unrug 1976). This opens up the possibility of using fine waste iron powder from industrial shotblasting facility in steel plants as a cationic source to perform mineral carbonation with a view to form a structural binder which is studied in detail in this dissertation. This shot-blasted iron powder waste is generated in significant amount during manufacturing process of steel as bag house dust. This dust is typically extracted by the air pollution control system on Electric Arc Furnace (EAF). The traditional means of disposing of EAF dust is at a waste landfill site as it is not economically feasible to recycle back iron from the dust. The proceeding section sheds light on some comprehensive literatures that deals with carbonation of iron to better-understand its potential to be used for mineral carbonation for binder formation.

2.1.3 CO_2-corrosion of steel in oil and gas industry

CO_2-corrosion and carbonate film formation in steel pipelines were first observed in oil and gas industry. Since then, several researchers have published many articles on evaluation of the mechanism of this scale-formation which served as background knowledge in this dissertation towards synthesis of carbonate from waste iron powder.

This section highlights several aspects of CO_2-corrosion, reported in the literature, which are beneficial in development of the novel binder.

2.1.3.1 Background

With increasing energy-demand, new sources of oil and gas are increasingly explored in harsher environments in deep high temperature/pressure conditions (M. B. Kermani and Morshed 2003). These have created challenges in terms of economy of the project, maintenance exploration facilities. The CO_2-corrosion of carbon steel pipelines and equipment in the oil and gas industry (M. B. Kermani and Morshed 2003), therefore, remains a major obstacle, due to increased tendency to inject CO_2 into the oil wells to reduce the viscosity of the oil to increase the efficiency of the oil production and thereby reduction of project cost. The following sections report on several key aspects of CO_2-corrosion of steel that are necessary to assess the potential of using fine iron powder waste to be beneficially carbonated for binder formation.

2.1.3.2 CO_2-corrosion mechanism

In the CO_2-containing environment there are various species that are present such as H^+, CO_3^{2-}, HCO_3^-, H_2CO_3 etc. Hence, the electrochemical process becomes complicated. The electrochemical process is greatly influenced by pH of the solution. At lower pH (pH<4.0), reduction of H^+ becomes dominant cathodic process (Equation 2-1). However, as the pH increases (pH 4.0-6.0) the dominant cathodic reaction is switched to reduction of HCO_3^- and H_2CO_3 (Equation 2-2 and 2-3) (J. B. Sun et al. 2012).

$$2H^+ + 2e \rightarrow H_2 \uparrow \qquad [2\text{-}1]$$

$$2H_2CO_3 + 2e \rightarrow HCO_3^- + H_2 \uparrow \quad [2\text{-}2]$$

$$2HCO_3^- + 2e \rightarrow 2CO_3^{2-} + H_2 \uparrow \quad [2\text{-}3]$$

The anodic reaction includes dissolution of iron as follows:

$$Fe \rightarrow Fe^{+2} + 2e \quad [2\text{-}4]$$

Here Equation 2-4 consists of three steps (J. B. Sun et al. 2012)

$$Fe + H_2O \rightarrow FeOH + H^+ + e \quad [2\text{-}5]$$

$$FeOH \rightarrow FeOH^+ + e \quad [2\text{-}6]$$

$$FeOH^+ + H^+ \rightarrow Fe^{2+} + H_2O \quad [2\text{-}7]$$

Now, $FeCO_3$ can form when concentrations of Fe^{2+} ions and CO_3^{-2} ions exceed the solubility product of $FeCO_3$ (J. B. Sun et al. 2012):

$$Fe^{+2} + CO_3^{-2} \rightarrow FeCO_3 \quad [2\text{-}8]$$

$$Fe^{+2} + HCO_3^- + e \rightarrow FeCO_3 + H \quad [2\text{-}9]$$

There are several other CO_2-corrosion mechanism reported (M. B. Kermani and Morshed 2003). However, irrespective of the mechanism type the concentrations of dissolved CO_2 in solution and the mass transport of dissolved CO_2 to the steel surface have a great influence on carbonation efficiency (M. B. Kermani and Morshed 2003).

2.1.3.3 Factors influencing CO_2-corrosion of steel

The rate of CO_2-corrosion is influenced by a number of parameters including environmental, physical and metallurgical parameters. The effects of these factors are sufficiently described in detail by a number of authors (M. B. Kermani and Morshed 2003). The key factors influencing the rate of CO_2-corrosion are: (1) pH of solution, (2)

CO_2-concentration, (3) temperature, (4) pressure, (5) morphology of steel surface, (6) fluid dynamics involving transport of CO_2 to the steel surface and (7) steel chemistry. All these parameters are inter-dependent and can influence CO_2-corrosion. Effect of these parameters on corrosion rate is described in detail elsewhere (M. B. Kermani and Morshed 2003). Here, these effects are mentioned briefly. The influential parameters are shown in Figure 2-1.

While there are still debates on which ionic species are involved in corrosion reaction, it is evident that the resulting cathodic reaction is influenced by partial pressure of CO_2 and temperature. For a given temperature, partial pressure of CO_2 determines the pH of solution and concentrations of different species in the solution (M. B. Kermani and Morshed 2003).

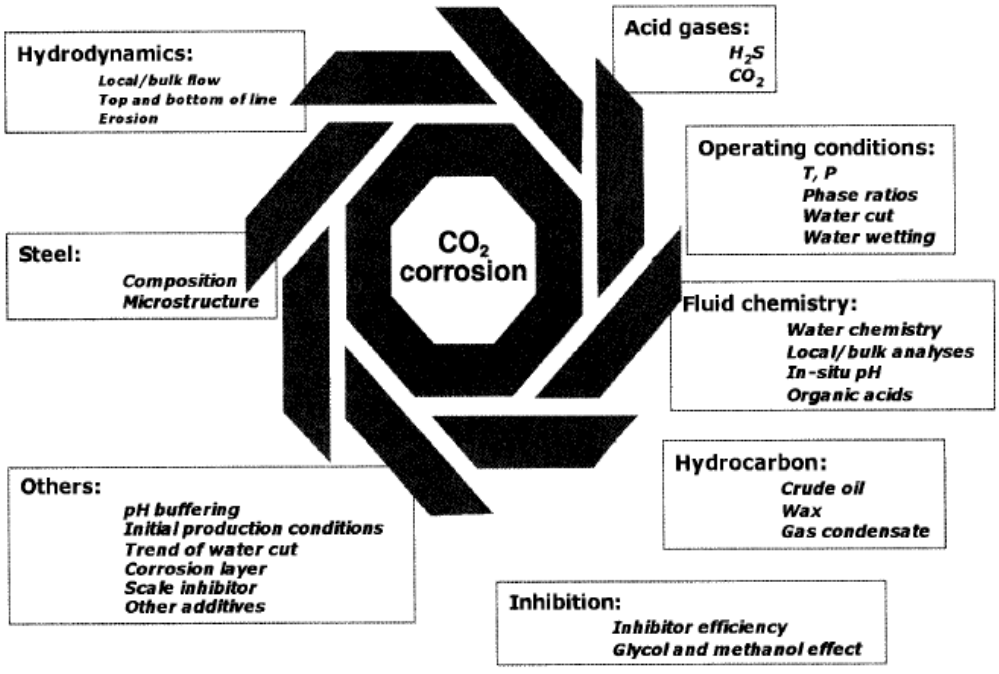

Figure 2-1 Parameters influencing CO_2-corrosion (M. B. Kermani and Morshed 2003)

Supersaturation plays a key role in determining the stability of protective layer. For a ionic dissolution $AB=A^{+}+B^{-}$, the supersaturation is defined as "$\log[A^{+}][B^{-}]/K_{sp}$ where K_{sp} is the solubility product . High concentrations of A^{+} and B^{-} leads to precipitation of corrosion layer through various mechanisms (M. B. Kermani and Morshed 2003) such as: (1) diffusion barrier i.e. diffusion length between the metal substrate and corrosive medium, (2) formation of low-porosity layer, (3) creation of concentration gradients of the main species (Fe^{++} and HCO_3^{-}). The supersaturation is reported to be influenced by rate of iron dissolution (Dugstad 1992; M. B. Kermani and Morshed 2003). Supersaturation is achieved at much lower Fe^{++} concentrations with increasing temperature facilitating precipitation of $FeCO_3$ (Figure 2-2).

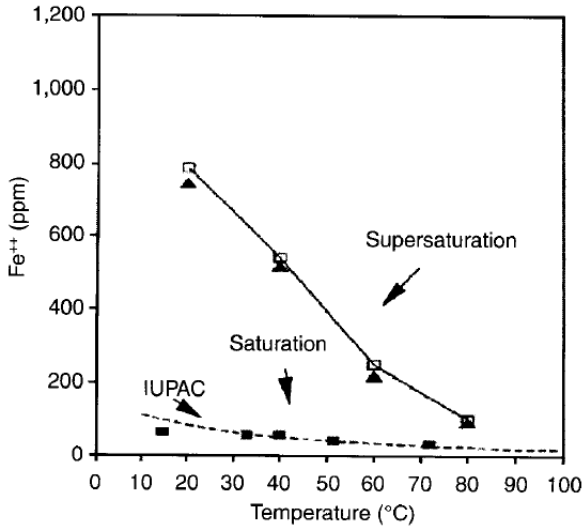

Figure 2-2 Fe^{++} solubility in pure water at 0.1 MPa partial pressure of CO_2 as a function of solution temperature (Dugstad 1992)

The operating temperature strongly affects the corrosion process. The corrosion rate is reported to be increasing with increase in temperature up to 80°C as the possibility of supersaturation is progressively increased at lower iron dissolution as explained earlier. Figure 2-3 shows effect of temperature on corrosion rate.

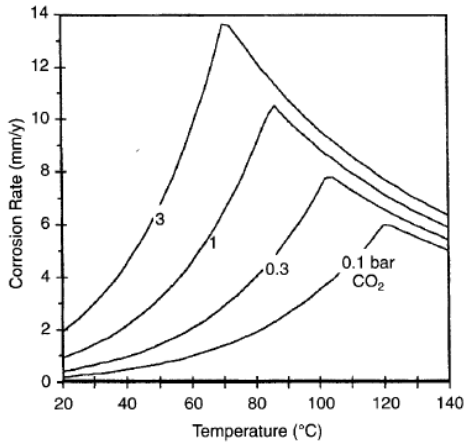

Figure 2-3 Effect of temperature on CO_2-corrosion (de Waard, Lotz, and Milliams 1991; M. B. Kermani and Morshed 2003)

Besides, increasing corrosion rate with increasing temperature in the low-temperature range has been attributed to increased mass-transfer rate as a consequence of flow rate and slow iron carbonate formation (M. B. Kermani and Morshed 2003). Above 80°C solubility of iron carbonate in the solution decreases (M. B. Kermani and Morshed 2003) and iron carbonate is precipitated due to supersaturation. The corrosion rate diminishes due to formation of protective layer as the diffusion process becomes dominant which is slow in nature (M. B. Kermani and Morshed 2003). Besides, localized corrosion occurs at sites where the surface film breaks or a nonprotective layer is formed (M. B. Kermani and Morshed 2003).

The effects of partial pressure of CO_2 are also influential as it controls CO_2-concentration and pH of the solution up to a great extent. The general rule of thumb criteria for corrosion of carbon or low-alloy steel is given as (M. B. Kermani and Morshed 2003): (1) if $P_{CO2} < 0.5$ bar (7 psi), corrosion is unlikely implying corrosion is uniform and rate of corrosion is very low (0.1 mm/y); (2) if 0.5 bar (7psi) $< P_{CO2} < 2$ bar (30 psi), corrosion is possible with a rate in between 0.1-1 mm/year; (3) if $P_{CO2} > 2$ bar (30 psi), corrosion is

likely with corrosion arte exceeding 1mm/year implying severe damage is expected. These effects are described in detail in (M. B. Kermani and Morshed 2003).

Solution pH plays a key role in CO_2-corrosion of steel as it influences both electrochemical process as well as the surface film formation. The surface film formation governs the electrochemical process as well as it deals with transport of CO_2 to the steel surface. It has been reported that solubility of Fe^{++} reduces with increase in pH (M. B. Kermani and Morshed 2003). The solubility of Fe^{++} reduces five times when pH is increased from 4 to 5 and it is reduced 100 times when pH is increased from 5 to 6. If the pH is increased above 5, reduction in solubility of Fe^{++} results in higher supersaturation, which increases the corrosion rate and thus protective layer if formed. The protective layer lowers the corrosion rate as it facilitates dominance of diffusion-controlled process (M. B. Kermani and Morshed 2003).

It has been reported that organic acids significantly influence and complement CO_2-corrosion (M. B. Kermani and Morshed 2003). Organic acids are shown to aid CO_2-corrosion by reducing the protectiveness of the films and thereby increasing the sensitivity to attack (Joosten et al. 2002; M. B. Kermani and Morshed 2003). Significant reduction in the film-stability was observed in many studies (Crolet 1985; Garsany et al. 2002; Hedges, McVeigh, and others 1999; M. B. Kermani and Morshed 2003). It has also been reported that presence of organic acids tend to solubilize the dissolving iron ions and hinder the formation of the film which can otherwise passivate the iron surface reducing the rate of corrosion (Crolet 1985; Garsany et al. 2002; Hedges, McVeigh, and others 1999; M. B. Kermani and Morshed 2003). Another study (Crolet, Thevenot, and Nesic 1998) reports that at a given pH the solubility of iron increased significantly when

bicarbonate of some concentration is replaced by equal quantity of acetate. Overall, the presence of organic acids caused considerable about of increase in corrosion rates (M. B. Kermani and Morshed 2003; Crolet, Thevenot, and Nesic 1998; Crolet 1985; Garsany et al. 2002; Hedges, McVeigh, and others 1999). This information is beneficial towards reducing the timescale of mineral carbonation for binder formation which is detailed later.

CO_2-corrosion is shown to occur when water is present and wets the steel surface and the intensity of CO_2-corrosion attack increases with increase in water-exposure time (Rolf Nyborg and others 2002; de Waard, Lotz, and Milliams 1991; Dugstad and others 1998; B. Kermani and Smith 1997). It is well known that oil/water systems can form emulsions. The rate of corrosion reduces in case of water-in-oil emulsions as it prevents water-wetting of steel (Lotz, Van Bodegom, and Ouwehand 1991). On the other hand, the corrosion rate has been shown to increase in case of formation of oil-in-water emulsions (Lotz, Van Bodegom, and Ouwehand 1991; M. B. Kermani and Smith 1997; M. B. Kermani and Morshed 2003).

Wax layer formed in the pipelines have been shown to be influential in CO_2-corrosion of steel. The effect can be damaging or protective based on nature of wax layer (M. B. Kermani and Smith 1997; M. B. Kermani and Morshed 2003). Crude oil has also been found to be influential in CO_2-corrosion of steel. It has been reported that crude oils modify the morphology, composition and compaction of corrosion products (Choi, Tonsuwannarat, and others 2002; M. B. Kermani and Morshed 2003). It destabilizes the corrosion layer and aids localized corrosion. Metallurgical compositions of steel have also been shown to influence the CO_2-corrosion process (Rolf Nyborg et al. 2000).

Increase in Chromium and Molybdenum in steel have been found to reduce the corrosion-potential (Ikeda 1985; Rolf Nyborg et al. 2000; M. B. Kermani and Morshed 2003). High Sulphur containing steel has been reported to have higher corrosion potential than low Sulphur containing steel (M. B. Kermani and Morshed 2003).

Information provided in this section regarding influence of different factors on CO_2-corrosion potential is employed towards development of novel structural binder through carbonation or waste iron particles which are detailed later.

2.1.3.4 Carbonate surface film formation

CO_2-corrision of steel is strongly dependent on the morphology of the surface film formed during corrosion process. Hence, it is not only the thickness, but also the structure and morphology of the surface film controls the corrosion rate (M. B. Kermani and Morshed 2003). The formation of iron carbonate scale is strongly dependent on the thermodynamics and kinetics of iron carbonate precipitation and supersaturation plays a key role in this respect as explained earlier. A high supersaturation of iron carbonate is required for formation of protective layer at low temperatures (M. B. Kermani and Morshed 2003; Dugstad 1992). The precipitation process is reported to be comprised of two steps: nucleation and growth (M. B. Kermani and Morshed 2003). The dominating step is determined by the morphology of the surface film formed (M. B. Kermani and Morshed 2003; Rolf Nyborg et al. 2000). Iron carbonate reduces the corrosion rate by reducing the film porosity without altering local phase compositions or concentration gradients (M. B. Kermani and Morshed 2003). Figure 2-4 shows the SEM surface morphologies of the corrosion scale formed on the low alloy steel surface after exposure to CO_2-saturated water.

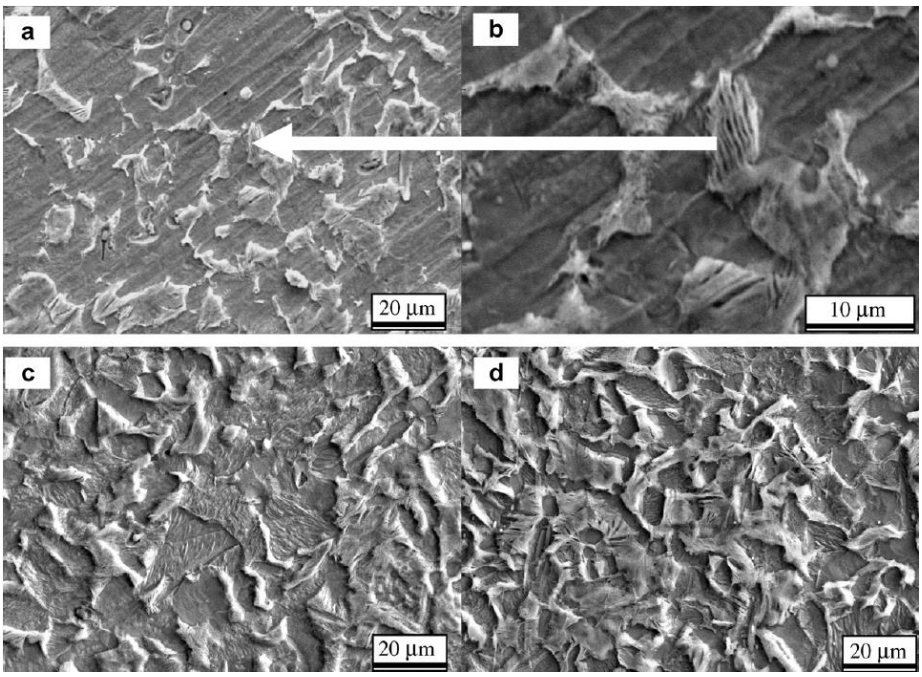

Figure 2-4 Figure : SEM surface morphologies of the surface film formed on low alloy steel after potentiostatic polarization in carbon dioxide-saturated formation water for: (a and b) 0.25 h; (c) 0.5 h; and (d) 1 h. (J. B. Sun et al. 2012)

Growth of iron carbonate scale is a slow temperature-dependent process as explored earlier. Increasing temperature within the threshold limit improves not only the protectiveness of the scale, but also adhesion and hardness of the film (M. B. Kermani and Morshed 2003). Maximum rate of corrosion has been observed from 60°C to 70°C and beyond 70°C the rate drops due to increasing protectiveness of the surface film formed (M. B. Kermani and Morshed 2003). Another study (Videm et al. 1996) found that the lowest temperature, necessary to reduce corrosion rate significantly, was 50°C. Several other studies (Dayalan et al. 1995; R. Nyborg and Dugstad 1997) reported that protectiveness of the surface film drops significantly at lower temperatures (<60°C) and iron carbide film is predominantly formed. Another study (SHANNON 1976) reported some key findings on characteristics of corrosion film/layer such as: (1) at 75°C, 1 bar

CO_2-Pressure and at a pH range of 5.6-6.3, the corrosion film mainly consisted of iron carbonate. ; (2) Perfectly rhombohrdric iron carbonate (siderite) crystals were found; (3) he film was few microns thick and was formed after 24 hours of exposure; (4) periodic exposure to atmosphere (oxygen) provided improved scale adhesion and hardness; (5) similar immersion of 99.5% pure iron into CO_2-saturated water produced a patchy cracked and loosely adherent iron carbonate scale which was attributed to the absence of carbide network in the pure iron; (6) the scale formation is influenced by solution chemistry also. Scale formed in distilled water was very loose whereas water containing Mg^{2+} ion was shown to provide increased adhesion; (7) the nucleation and growth of iron carbonate scale is a slow temperature dependent process and any environmental change has significant influence on the precipitation process and thereby on corrosion rate.

2.1.3.5 Summary of literature review on CO_2-corrosion of steel

This overview of the above literature review on CO_2-corrosion of steel has led to a number of key points which are beneficial towards development of the novel binder formed based on iron carbonation.

(1) Nucleation and growth of iron carbonate is a slow temperature dependent process and any environmental change has significant influence on the precipitation process and thereby on corrosion rate.

(2) Rate of carbonation of steel increases with temperature. But, increased temperature also increases protectiveness of the iron carbonate layer. The protectiveness of the surface film drops significantly at lower temperatures (<60°C) and the lowest temperature, necessary to reduce corrosion rate significantly is about 50°C.

(3) At temperatures less than 60°C, higher concentrations of Fe^{++} is needed in order to obtain supersaturation and thereby precipitation of iron carbonate. Hence, in order to increase Fe^{++}-concentrations some reagents are needed that facilitates dissolution of iron.

(4) The rate of iron carbonation increases with increase in CO_2 partial pressure. At ambient pressure higher concentration of Fe^{++} is needed.

(5) An organic reducing agent is needed to facilitate better dissolution of the metallic iron and enhance its reactivity. Thus the rate of reaction can be significantly increased.

(6) pH in the range 5.8-6.3 is necessary to form iron carbonate precipitations. But, it should be noted that high pH in combination with high temperature provides very protective layer that inhibits further ingress of CO_2 into the steel substrate.

(7) Pure iron exposed to CO_2-saturated water produces a patchy cracked and loosely adherent iron carbonate scale. Hence, filler materials are needed in order to decrease the porosity for development of novel binder.

(8) Presence of water is necessary as it acts as a transport medium for CO_2.

2.1.4 Carbonation of iron for development of a novel carbon-negative binder

The section evaluates the information obtained from the extensive literature review on mineral carbonation and carbonation of steel in the previous sections towards developing a novel pathway for binder formation using carbonation of waste iron powder. The fundamental premise of this study is that metallic iron powder can be carbonated (in anoxic conditions, with oxidation inhibiting additives) to produce a strong, durable, and microstructure-designed multi-phase composite. The attempt of this study is to engineer

the material (from a viewpoint of both the source materials used and the processing conditions) to pave the way for its large-scale production and implementation, especially in special engineering applications. The chemical pathway that is being relied upon in the material design process of iron carbonate matrix are the anodic dissolution of iron, and the cathodic proton reduction and reduction of carbonic acid (Singer and Stumm 1970; M. B. Kermani and Morshed 2003).

$$Fe + 2CO_2 + H_2O \rightarrow Fe^{+2} + 2HCO_3^- + H_2 \uparrow \qquad [2\text{-}10]$$

$$Fe^{+2} + 2HCO_3^- \rightarrow FeCO_3 + CO_2 + H_2O \qquad [2\text{-}11]$$

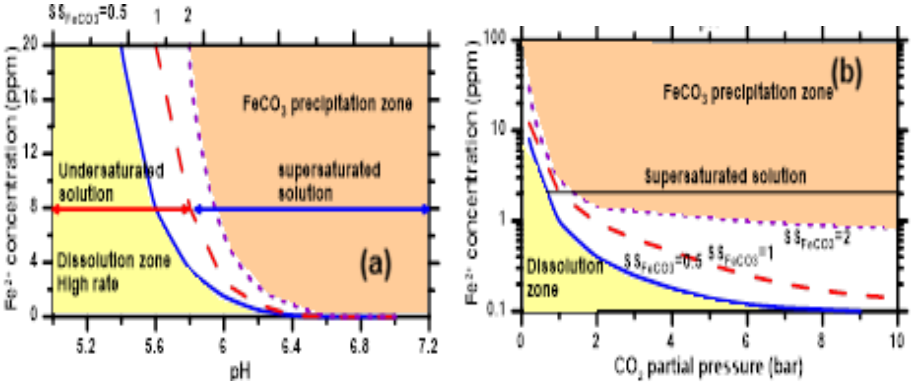

Figure 2-5: Influence of (a) Ph and (b) CO_2 partial pressure on Fe^{+2} concentration in the solution and the precipitation potential

The above reaction mechanism is similar to that of iron carbonate scale formation in steel pipes carrying oil and gas, which is a multi-billion dollar problem for the oil and gas industry (M. B. Kermani and Morshed 2003; Tomson, Johnson, and others 1991; Rolf Nyborg 2005; Koteeswaran 2010; El-Lateef et al. 2012; Allison 2012; Linter and Burstein 1999). In this research, this deleterious mechanism is put into beneficial use as an attractive and sustainable processing route for binding matrices. When CO_2 dissolves in water, it forms carbonic acid (H_2CO_3), which quickly dissociates into H^+ and HCO_3^-

ions. H_2CO_3 is very effective in its attack on iron and is more corrosive than HCl at the same pH (Bruno, Wersin, and Stumm 1992). Iron will bond with the bicarbonate ion and precipitate as iron carbonate (FeCO3) which has low solubility in water (W. Sun 2006; Bénézeth, Dandurand, and Harrichoury 2009; Ohmoto, Watanabe, and Kumazawa 2004). This simple reaction series, which proceeds under ambient conditions, and which can be accelerated using other additives, highlights the application potential of iron carbonates.

The necessary condition for the precipitation of $FeCO_3$ is that the concentrations of Fe^{2+} and CO_3^{2-} ions exceed their solubility limits (Ohmoto, Watanabe, and Kumazawa 2004). Typical iron carbonate precipitation diagrams (Figure 2-5a and b) show the influence of pH and CO_2 partial pressure on Fe^{2+} concentration and hence the precipitation of iron carbonate (Johnson 1991; Kemp 1971; J. J. Carroll and Mather 1992; Lower 1999; Han, Brown, and Nešic 2010). A low pH induces better dissolution of Fe^{2+} but as the carbonate ions in solution are consumed towards the formation of iron carbonate, precipitation of the reaction product ensues. If the CO_2 partial pressure exceeds 2 bars, for any Fe^{2+} concentration greater than 1 ppm, iron carbonate will theoretically precipitate (Han, Brown, and Nešic 2010). Increasing iron solubility (through dissolution agents) results in product precipitation at atmospheric pressure itself. These figures provide general guidelines on the synthesis conditions required for the production of iron carbonate binders. It however needs to be remembered that thermodynamics only dictates if iron carbonate can precipitate out of the solution; it is the kinetics that determines the extent to which it forms. Precipitation happens on the particle surfaces and the reaction rate reduces with time because the reaction product acts as a diffusion barrier for the dissolved CO_2 (Do 1982; Ar and Doğu 2001). Incomplete reaction, that retains a strong

iron core inside the carbonate reaction product, is a desired outcome as will be shown later in this proposal. However, it should be remembered that the iron carbonate binder is very different from the OPC-based binders with respect to the reaction mechanisms, kinetics, and products; the role played by water in the reaction sequence and the reaction rates being important determinants of properties. Water is not bound to the reaction products in iron carbonate, and is electrolyzed to H_2 which is released (Koteeswaran 2010), influencing the microstructure.

2.2 Fracture-behavior of cementitious materials

Fracture mechanics is a branch of solid mechanics that involves evaluation of the behavior of the materials in the vicinity of a crack and at the crack tip. Linear elastic fracture mechanics (LEFM) has been applied by researchers since the earlier works of Griffith, Orowan and Irwin (Griffith 1921; Orowan 1948; Irwin 1958). LEFM has been successfully employed by researchers and engineers for safe design of engineering materials and for development of new materials based on fracture energy- microstructure relationship. Many brittle ceramics and high strength metals are adequately characterized by LEFM using single parameter like stress intensity factor. However, its application in cementitious materials such as cement paste, mortars and concrete has not been successful due to development of a tension-softening area or damage zone at the tip of the notch. Hence, cementitious composites are termed as ‘quasi-brittle’. The success of application of LEFM in these materials depends on appropriate consideration of damage zone. The crack-tolerance of such quasi-brittle materials is greatly influenced by the nature of stress transfer in the fracture process zone (FPZ). This complex nature of strain localization in the main crack as well as various branches of secondary cracks and micro-

cracks is a major contributor to the non-linearity in quasi-brittle material fracture. The FPZ dissipates substantial energy through various mechanisms such as micro-cracking, crack-deflection, crack bridging, crack-tip blunting, and crack-branching, thereby facilitating steady-state crack propagation in the pre-peak load region and prevention of catastrophic failure of structures after the peak load capacity is exceeded (Shah 1995a). Hence this study addresses the crack propagation mechanisms in novel iron carbonate binder and particulate reinforced OPC systems through monitoring the strain softening and strain localization behavior using the concept of FPZ. The dimensions of the FPZ and its evolution with load (and crack mouth opening displacement (CMOD), in a CMOD-controlled regime) are complex functions of the matrix microstructure and provide valuable information on matrix contributions to crack propagation and energy dissipation. While several experimental techniques such as high speed photography (Bhargava and Rehnström 1975), acoustic emission (Haidar et al. 2005; Carpinteri and Lacidogna 2003; Maji, Ouyang, and Shah 1990), scanning electron microscopy (SEM) (Mindess and Diamond 1980; Hadjab.S, Chabaat, and Thimus 2007; Nemati 1997; X. Hu and Wittmann 1990), and laser-speckle interferometry (Jia and Shah 1994; Horii and Ichinomiya 1991) have been used to investigate FPZ in concretes, this study employs a non-contact digital image correlation (DIC)-based speckle-tracking method (Yates, Zanganeh, and Tai 2010; Nunes and Reis 2012a; Roux, Réthoré, and Hild 2009; Skarżyński, Kozicki, and Tejchman 2013; Skarżyński, Syroka, and Tejchman 2011; Das, Aguayo, et al. 2014; Das, Hendrix, et al. 2014c; Skarżyński and Tejchman 2013) to assess the surface displacements and strains, and thus the width of the FPZ. More

application-specific information on fracture behavior are provided later in subsequent chapters in detail.

2.3 Micro/Nano-mechanical characterization towards development of constitutive material model for cementitious materials

This section first discusses information obtained from literature on determination of nano-mechanical properties using nanoindentation. Application of nanoindentation on heterogeneous materials is elucidated. In addition, information on constitutive material modelling techniques for heterogeneous materials such as concrete is provided with a view to develop a constitutive material model for novel iron carbonate binder which is highly heterogeneous in nature as explored later.

2.3.1 Nanoindentation:

Indentation has been most commonly used technique for determination of mechanical properties of materials. During the early 1970s the potential of measurement of elastic modulus from indentation load-displacement curve was established (Bulychev et al. 1975; Li and Bhushan 2002) which promoted development of instrumented indentation testing technologies (Li and Bhushan 2002). During the past three decades, the scope of indentation testing has been extended to nanometer range motivated partly by development of nano-composites, nanometer thick films and due to newly available techniques of probing mechanical properties in small volumes (Bhushan 2010; Oliver and Pharr 1992; Pharr 1998; Li and Bhushan 2002). Among all the available materials, diamond is the most frequently used material because of its high hardness and elastic modulus to minimize the contribution of indentation itself on the indentation load-displacement data (Li and Bhushan 2002). There are several shape of indenter available

such as four-sided Vickers, Knoop indenter, Berkovich triangular pyramidal indenter etc. Among these, Berkovich triangular pyramidal indenter is preferred over others as three sided pyramid is easily grounded to a sharp point (Tabor 1951; Bhushan 2010; Oliver and Pharr 1992). There are primarily two methods available for determination of Young's modulus from nanoindentation: (1) traditional Oliver-Pharr method (Oliver and Pharr 1992) and (2) Continuous stiffness measurement (CSM) (Li and Bhushan 2002).

2.3.1.1 Oliver-Pharr method:

This method uses slope of initial portion of unloading curve to obtain the Young's modulus. Figure 2-6 shows a typical load-displacement curve during indentation followed by withdrawal. Here h_{max} represents displacement at peak load, h_c is the contact depth, h_f is the final displacement after full unloading and S is the initial unloading stiffness i.e $S = dP/dH$.

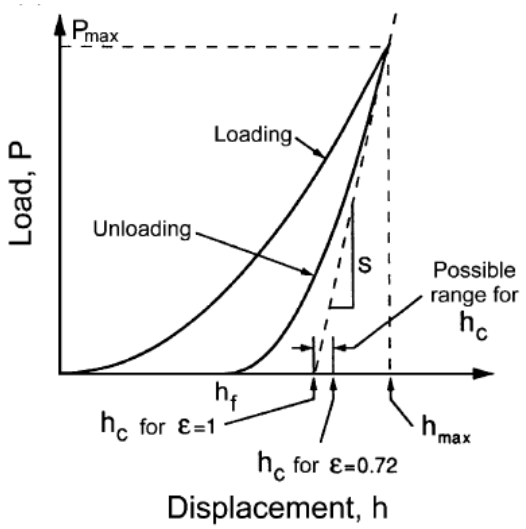

Figure 2-6: Typical load-displacement curve during and after nanoindentation (Oliver and Pharr 1992; Li and Bhushan 2002)

A geometry-independent relationship between contact stiffness, contact area and elastic modulus is given as (Sneddon 1965):

$$S = 2\beta\sqrt{\frac{A}{\pi}}E_r \qquad [2\text{-}12]$$

Where β is a constant which depends on geometry of indenter (β =1.034 for Berkovich indenter) (Oliver and Pharr 1992) and E_r is the reduced elastic modulus given as:

$$E_T = \frac{1-\upsilon^2}{E} + \frac{1-\upsilon_i^2}{E_i} \qquad [2\text{-}13]$$

Where, υ and E are Poisson's ratio and Young's modulus of the sample; υ_i and E_i are Poisson's ratio and Young's modulus of indenter (for diamond, υ_i =0.07 and E_i = 1141 GPa). The elastic modulus of the sample can be calculated using Equation 2-12 and 2-13 with available stiffness data and projected area which is given as (for Berkovich indenter):

$$A_c = 24.56h_c^2 + C_1h_c^1 + C_2h_c^{1/2} + C_3h_c^{1/4} + ... + C_8h_c^{1/128} \qquad [2\text{-}14]$$

Where C_1-C_8 are constants. The lead term in the above equation corresponds to perfect Berkovich indenter and others take into account the blunting of the tip (Oliver and Pharr 1992).

The Oliver-Pharr methodology works well for hard ceramics (Li and Bhushan 2002). However it underestimates the area as much as 50% for softer materials. Again this methodology requires multiple loading-unloading process at different depths separately in order to obtain depth-dependent properties and thus there was need for a continuous measurement technique. That's why, the continuous stiffness measurement (CSM) method was introduced.

2.3.1.2 Continuous stiffness measurement (CSM):

While the traditional Oliver-Pharr methodology (Oliver and Pharr 1992) measures the contact stiffness only at the point of unloading, the CSM technique allows measurement of contact stiffness at any point of the loading curve corresponding to any depth of penetration. In the CSM technique a small sinusoidal signal is imposed over the DC signal. For a given excitation frequency, the displacement response (Figure 2-7(a)) and the phase angle are measured continuously as a function of depth.

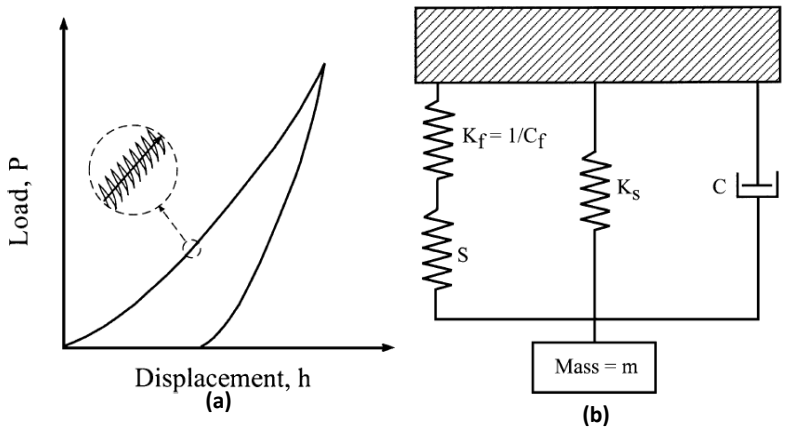

Figure 2-7: Schematic of (a) CSM loading cycle, (b) dynamic indentation model (Li and Bhushan 2002)

For quantification of contact stiffness the dynamic response of the indentation system is needed to be determined. Figure 2-7(b) shows a schematic of dynamic indentation model used for evaluation of dynamic response. The model involves mass, m of the indenter, spring constant K_S, leaf springs that support the indenter K_f , contact stiffness S, and damping coefficient C for air in the gaps of capacitor displacement sensing system. For an imposed driving force $P = P_{OS} e^{i\omega t}$ and displacement response $h(\omega) = h_0 e^{(i\omega t + \phi)}$, the contact stiffness can be obtained from displacement signal (Li and Bhushan 2002).

$$\left|\frac{P_{OS}}{h(\omega)}\right| = \sqrt{\left\{(S^{-1}+K_f^{-1})^{-1}+K_S-m\omega^2\right\}^2+\omega^2C^2} \quad [2\text{-}15]$$

$$\tan(\phi) = \frac{\omega C}{(S^{-1}+K_f^{-1})^{-1}+K_S-m\omega^2} \quad [2\text{-}16]$$

Where P_{OS} is the magnitude of the force, $h(\omega)$ is the magnitude of the displacement, ω is the frequency of oscillation and ϕ is the phase angle between the force and the displacement. Equation 2-15 and 2-16 can be solved for contact stiffness and damping. Obtained contact stiffness is given as:

$$S = \left[\frac{1}{\frac{P_{OS}}{h(\omega)}Cos\phi-(K_S-m\omega^2)}-K_f^{-1}\right]^{-1} \quad [2\text{-}17]$$

The obtained contact stiffness, thus obtained, corresponding to any displacement at any depth can be used in Equations 2-12 and 2-13 to obtain the Young's modulus of the material.

2.3.1.3 Application of nanoindentation on heterogeneous cementitious materials:

Nanoindentation is a powerful tool to measure local mechanical properties of materials. This technique was developed for investigation of local mechanical properties of homogeneous materials. But, many engineering materials especially structural materials such as concrete exhibits heterogeneity spread in different length scales (nanometer to meters). Hence, determination of intrinsic mechanical properties of different phases at different length scales becomes important in order to assess its bulk mechanical properties. Nanoindentation has been a widely used technique to measure local mechanical properties of cement paste at micron level. Several authors have reported

indentation results on cement (G. Constantinides, Ulm, and Van Vliet 2003; Sorelli et al. 2008; Mondal, Shah, and Marks 2007; Zhu et al. 2007; Pelisser et al. 2013; C. Hu and Li 2014; Hughes and Trtik 2004; Davydov, Jirásek, and Kopeckỳ 2011). Stiffness of calcium hydroxide (CH) and two different types of CSH (low density and high density) is reported (G. Constantinides, Ulm, and Van Vliet 2003). Figure 2-8 displays nanoindentation results on CSH. Low density CSH has a mean stiffness of 21.7 GPa whereas high density CSH exhibits a stiffness of 29.4 GPa (Georgios Constantinides and Ulm 2004; G. Constantinides, Ulm, and Van Vliet 2003). These properties are reported to be material properties that are independent of mixture proportions (G. Constantinides, Ulm, and Van Vliet 2003).

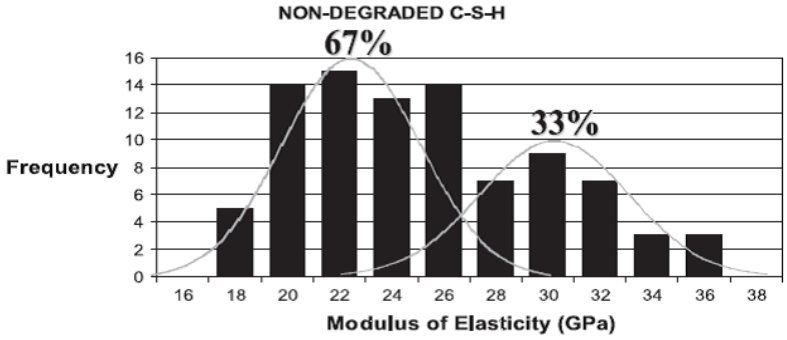

Figure 2-8: Histogram of Young's modulus for CSH in hydrated cement paste (Georgios Constantinides and Ulm 2004; G. Constantinides, Ulm, and Van Vliet 2003)

Several other studies also evaluated nano-mechanical properties of cement paste at different w/c ratios and at different curing age (Georgios Constantinides and Ulm 2004; Hughes and Trtik 2004; Zhu et al. 2007; Georgios Constantinides and Ulm 2007; Howind et al. 2011). Most of these studies used statistical nanoindentation technique to deconvolute the mechanical properties of individual phases from a large number of indentation tests on polished surface of hardened cement paste. Effect of penetration

depth on nano-mechanical properties has also been evaluated (Davydov, Jirásek, and Kopeckỳ 2011). It has been reported that general shift of NI results are observed with increase in penetration depth due to surface roughness. It has also been reported that the depth of penetration should be at least equal to the size of RVE in order to capture representative properties (Davydov, Jirásek, and Kopeckỳ 2011). Similar methodology, based on depth sensing nanoindentation and statistical deconvolution of individual phase-properties, has been adopted in this study to evaluate intrinsic nano-mechanical properties of individual phases in heterogeneous iron-based novel binder as reported in detail in this dissertation.

2.3.2 Development of constitutive material model for cementitious materials

Evaluation of the constitutive relation of concrete is a challenging and complicated task since concrete has a variety of microstructures and no single distinctive one. Usually the macroscopic behavior of concrete is modeled by plastic constitutive relations (Drucker and Prager 2013; Riedel et al. 1999) and the material is assumed to be homogeneous. Several empirical constitutive models based on experimental data are reported (Bencardino et al. 2008; Graybeal 2007; Thomas and Ramaswamy 2007). However the microstructural inhomogeneity is completely neglected in these models. A closer look reveals that concrete has heterogeneous microstructure and the nonlinear behavior of concrete is attributed to the initiation, propagation, accumulation and coalescence of micro-cracks. Thus coupling of microstructure and macroscopic properties are needed to appropriately model the concrete behavior and multiscale modelling becomes vital.

With the advent of parallel computing power, simulation-based design and analysis were emerged, and multiscale modelling became a key tool for characterization of structure-

property relation down to atomic level (Horstemeyer 2010; Byun and Schere 2006; Andersson, Yuan, and Sundén 2010; Macklin et al. 2009; Formaggia et al. 1999; Kanouté et al. 2009). This method produces simulation-based precise and accurate property predictions eliminating the need for large scale expensive tests.

Essentially, the idea of simulation-based design/analysis as a substitute to large scale tests became more popular after comprehensive test ban treaty of 1996, in which many countries promised to discontinue large scale system level tests. With this perspective, the experiments shifted from large scale tests to multiscale tests to provide validation of material models at different length scales and the simulations were being performed based on physical characteristics rather than being empirical. The rapid growth in the capabilities of parallel computing helped the development of multiscale modeling research since more number of degrees of freedoms can be solved under parallel computing environment and it leads to more precise and accurate property prediction.

Multiscale modelling has been used in the field of solid mechanics effectively (Atluri 2004; Zienkiewicz and Taylor 2005; Qian et al. 2002; Bazant and Jirásek 2002; Van Houtte et al. 2006). While the modern continuum theories are driven by conservation of mass, momentum and energy, there are too many unknowns than the number of equations available. Hence, constitutive relations are required to solve differential equations using finite element analysis. There are many postulates that guide the development of multiscale constitutive theory: objectivity, physical admissibility, equipresence and locality. Among all these, the multiscale modeling has historically driven by physical admissibility which essentially means identification of discrete microstructural feature

that is the main source of phenomenological behavior at the macro scale (Horstemeyer 2010).

Two different methodologies are there in the solid mechanics continuum theory: hierarchical and concurrent. In the hierarchical method the numerical techniques are independently run at different length scales and a bridging mechanism such as homogenization technique is used to relate a property in a small scale to that at larger scales. There are multiple ways of multiscale-bridging in hierarchical technique although the use of thermodynamically constrained internal state variables (ISVs) is most popular (Clerk-Maxwell 1875; Onsager 1931a; Onsager 1931b; Eckart 1948). This is a top-down approach i.e. ISVs exist in the macro scale and they can reach down to subscales to obtain property. ISV formulation captures the effects of a representative volume element and hence ISVs provide macroscopically average of microscopic arrangement. The hierarchical method can also be coupled or uncoupled. The uncoupled hierarchical method is characterized by bottom up staggered strategy which is information transfer only from fine scale to the coarse scale whereas the coupled hierarchical method involves data exchange in both directions i.e. fine and coarse scale for each time/load step. In the uncouple hierarchical method the effective material properties are obtained by averaging the structural response of the heterogeneous material in the fine scale representative volume element (RVE) (Lloyd 1994; Elssner, Korn, and Ruehle 1994; Griffith 1921; Robertsausten 1887; McClintock 1968). Historically, analytical models such as isostress, isostrain or Hashin-Shtrikman models (Horstemeyer and Ramaswamy 2000; Horstemeyer et al. 2000; Potirniche et al. 2006) are used to obtain effective material properties although these models do not include important features such as phase

geometry and spatial distribution of phases . Besides, assuming a uniform strain does not ensure equilibrium in the tractions in the phase boundaries and on the other hand, uniform stress model implies that the matrix and the inclusions are not bonded together. Although some analytical models have been developed (Nemat-Nasser and Hori 1999; Mura 1987; Aboudi 1991) to take particle shape and spatial distribution into account, most of them are restricted to spherical particle shape. Numerical homogenization schemes (Varvara Kouznetsova, Geers, and Brekelmans 2002; Toro et al. 2014; T. Zohdi et al. 1998) are required for more complex shapes. Uncoupled homogenization techniques are also applied to nonlinear material behavior. Several models such as homogenized plasticity model (Sanchez-Palencia and Zaoui 1987), anisotropic continuum damage model (Unger and Eckardt 2011) etc. are available.

Although two-scale multiscale model is well known in the area of composite materials, its application to cement and concrete is not old. Several researches were carried out in the last decade on the application of multiscale analysis to evaluate the constitutive relation of the concrete (Markovic and Ibrahimbegovic 2004; Ibrahimbegović and Markovič 2003; Varvara Kouznetsova, Geers, and Brekelmans 2002; V. Kouznetsova, Brekelmans, and Baaijens 2001; Ghosh, Lee, and Raghavan 2001; J. Lee et al. 2009; Pichler, Hellmich, and A Mang 2007; Wriggers and Moftah 2006; Sanahuja, Dormieux, and Chanvillard 2007). Most of these papers involve application of theory of homogenization to predict the material properties and the method is applied on statistically representative volume elements. It has also been established that Finite Element Method (FEM) is one of the most effective numerical methods to predict macroscopic homogenized material property by volumetrically averaging the numerical

solutions of a unit cell (T. I. Zohdi and Wriggers 2001; Tarek I. Zohdi and Wriggers 2008; Gal and Kryvoruk 2011). Generation of RVE and distribution of aggregates also play a key role in these simulations. The aggregate distribution in the RVE is generally done by means of grading curves (Wriggers and Moftah 2006; Z. M. Wang, Kwan, and Chan 1999; Gal and Kryvoruk 2011; Gal et al. 2008). Recently, the homogenized constitutive relation of fiber reinforced composite is modeled (Gal and Kryvoruk 2011; Gal and Kryvoruk 2011b; J. L. Zhang et al. 2014) and the effect of interfacial transition zone (ITZ) on homogenized modulus of elasticity has also been explored (J. L. Zhang et al. 2014; M. Zhang, Ye, and Breugel 2013). The constitutive relation of concrete has also been approximated by neural networks when the shape of stress-strain curve is a priori (Ghaboussi, Garrett Jr, and Wu 1990; Ghaboussi, Garrett Jr, and Wu 1991). The main advantage of the uncoupled hierarchical method is its numerical efficiency which comes at the cost of a disadvantage of lack of mutual interaction between scales and the material behavior is captured in only a homogenized way. Coupled hierarchical method has also been employed for constitutive relations of heterogeneous composites. In the coupled hierarchical method, the constitutive relation at a point in macro-scale is not defined by effective equations, but it is described by the constitutive behavior of the point in the finer scale (Smit, Brekelmans, and Meijer 1998; V. Kouznetsova, Brekelmans, and Baaijens 2001; Miehe and Koch 2002). In this method, a heterogeneous RVE is assigned to each integration point of the finite element discretization and the boundary value problem is solved. It has also been reported in the literature (Unger and Eckardt 2011; Gitman 2006) that the classical homogenization techniques described above are not really suitable a heterogeneous material such as concrete due to localized behaviors resulting in

softening which violates the assumption of scale-separation. This problem is taken care of by means of gradient-enhanced homogenization scheme (Varvara Kouznetsova, Geers, and Brekelmans 2002), which is extension of classical homogenization scheme. The details of this method can be found in (Gitman 2006).

Chapter 3 Materials and Experimental Methods

3.1 Materials

This study uses metallic Iron powder with median particle size 19.03 μm as main starting material. The iron powder is obtained from a shotblasting facility as a waste material. The other materials used include Class F fly ash and metakaolin conforming to ASTM C 618, and limestone powder with a median particle size 0.7 μm conforming to ASTM C 568. Commercially available Type I/II ordinary Portland cement (OPC) conforming to ASTM C 150 was also used mainly for comparison purpose except in the case of metallic particulate reinforced mortars. The chemical compositions of these materials and their reason of selection are detailed later in subsequent chapters in detail in this dissertation.

3.2 Experimental Methods

Experimental methods varied significantly depending upon different objectives of the study. This section gives a generalized broad overview of the experimental methods used in this dissertation. More in depth application-specific aspects of different experimental methods are provided individually in the experimental methods sections in each chapter.

3.2.1 Simultaneous Thermal Analysis (STA/TGA)

The Thermogravimetric Analysis (TGA) is a very common material-characterization technique that provides information about the change in weight of materials in air or under inert conditions as a function of the temperature. Measurements are used primarily to determine the composition of materials and to predict their thermal stability at temperatures up to 1000°C. The technique can characterize materials that exhibit weight loss or gain due to decomposition, oxidation, or dehydration. Here in this project TGA is

used to assess the influence of CO2 penetration on the degree of reaction. A Perkin Elmer STA 6000 simultaneous thermal analyzer was used for thermo-gravimetric analysis (TGA). The analyzer was programmed to increase the temperature from 30°C to 995°C at a rate of 15°C/minute in a N_2 environment. The STA 6000 used in this research project is shown in Figure 3-1.

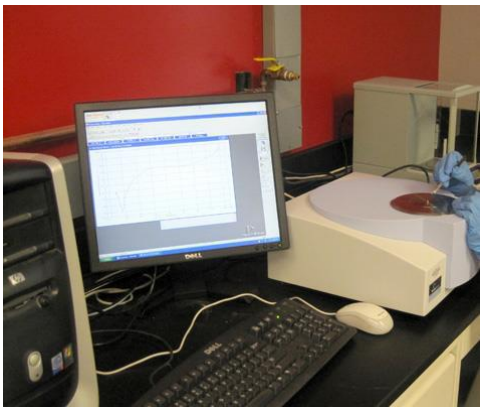

Figure 3-1: Perkin Elmer STA 6000 instrument setup

3.2.2 Mercury Intrusion Porosimetry (MIP)

Mercury intrusion porosimetry (MIP) is a well-established technique to investigate the pore structure of porous materials. MIP was performed in this research projet in two steps: (i) evacuation of gases, filling the sample holder with mercury and increasing the pressure to 345 kPa, and (ii) intrusion of the mercury into the sample at high pressures (up to 414 MPa). The contact angle and surface tension used for the analysis were 130° and 0.485 N/m respectively. Accurate determination of the contact angle was not carried out in this study, which could have introduced errors in the pore size determination. In addition, mercury intrusion porosimetry has several possible sources of error: (i) error due to the ink-bottle effect, where a pore with a smaller entrance to a larger pore is recorded as a large volume of the smaller pore, (ii) unconnected isolated fraction of pores

are not detected by MIP and (iii) high pressures exerted on the sample during mercury intrusion may damage the underlying pore structure. However, since the emphasis is on comparative evaluation of pore sizes, this inaccuracy is not deemed to be critical. The pore diameters can be evaluated using standard Washburn equation, based on the assumption that the pores in the porous media are cylindrical in shape. A minimum pore diameter of 0.003 µm can be evaluated using MIP. Total volume of mercury intruded (which is the total porosity) and critical pore diameter (which is the peak in the differential volume intruded curve) can be obtained from MIP. The instrument used in the experiments is shown in Figure 3-2.

Figure 3-2: Quantachrome PoreMaster mercury intrusion porosimeter

3.2.3 Three-point bending test in MTS load frame

Three-point-bending tests were performed using MTS loading frame on notched beams as shown in Figure 3-3. The beams were tested in a crack mouth opening displacement (CMOD)-controlled mode (CMOD acting as the feedback signal) during the loading cycles and in a load-controlled mode during the unloading cycles. Thus, several loading-

unloading cycles were implemented in the load-CMOD plot. These multiple loading=unloading cycles were implemented in order to obtain compliance-based strain energy release rates for evaluation of fracture response.

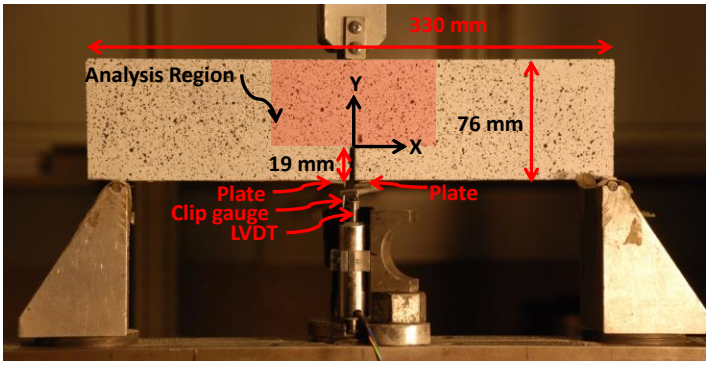

Figure 3-3: Experimental setup for closed loop CMOD-controlled three-point bending test

3.2.4 Digital image correlation (DIC)

DIC is used to obtain full-field surface displacements through successive post-processing of digital images taken at specific intervals of time during the test. In order to obtain a good correlation, the specimen surface should be flat. The specimen surface (region of interest) is painted white using spray paint. After the painted surface dries, black speckles are made on the surface randomly using black spray paint. The black speckle area should be approximately 50% of the overall area of region of interest. There should be good contrast between the black speckles and painted white surface. While application of spray-paints is most common speckling technique for specimen size in the range of 25mm-1.25m, other techniques are available for smaller samples. For samples of size less than 12 mm, toner powder can be applied to create very fine pattern. Lithography or vapor–deposition technique is applied for extremely small specimens (approximately 500 microns). Stencils can be used to spray a perfect speckle pattern if the specimen size is too large (greater than 2m). Precautions should be taken while making speckles and the

following information must be kept in mind: (i) the speckle patterns should not have repetitiveness, (ii) the speckle size should not be too big. If the speckle size is too large, there will be certain subsets where entire region would be in black or in white. This would result in a bad match since we have an extra match everywhere in the field. Increase in subset size further to solve this problem would result in loss of spatial resolution, (iii) on the other hand, too small speckle patterns (relative to size of region of interest) would have problems such as aliasing.

The cameras should be positioned somewhat symmetrically about the specimen; this will keep the magnification level consistent. The exact angle between the cameras is not critical; a broad range of angles between 15º and 45º generally gives excellent results. As the image is made sharp through the focus adjustment, it will also be necessary to adjust the brightness of the image. There are two controls available for this: the aperture/iris setting on the lens, and the exposure time setting of the camera. Opening the aperture allows more light to fall on the sensor. Exposure time is the amount of time the camera sensor gathers light before reading out a new image. Longer exposure times make the image brighter but can also create blur if significant motion happens during the exposure times. For many tests, blur is not a concern for the specimen itself, but can be an issue when acquiring images of a hand-held calibration grid. When exposure and aperture settings are complete, the image should be as bright as possible without showing any overdriven (red) pixels in the speckled area. In many cases, ambient light will not be enough to achieve this without using unacceptably large exposure times or aperture settings; for these cases, supplemental light will be required. For calibration purpose, a suitable grid is selected that approximately fills the field of view. Occasionally, lighting

configuration can affect grid selection. Some grids may be slightly reflective; under intense or directional light sources, these reflections can wash out the grid image. For these cases, especially matte grids should be used, or care taken to avoid reflections.) After calibration process is completed, images were taken every 5 seconds (12 images per minute) during the three point bending test. After collection of all the images, the imaged area was analyzed using the commercial VIC-2D software™.to obtain the displacement fields. Figure 3-4 shows experimental setup of DIC during three point bending test.

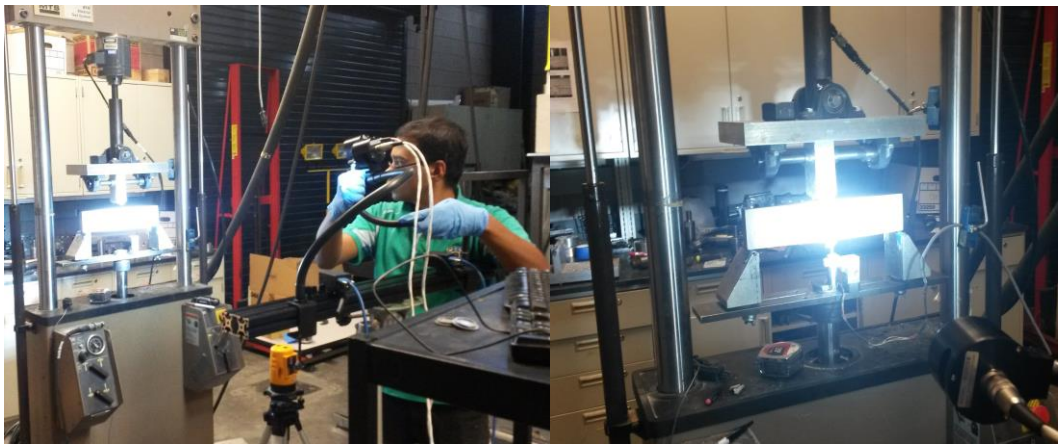

Figure 3-4: Digital image correlation setup for three-point bending test

3.2.5 Scanning electron microscopy (SEM)

Morphological analysis was done using a Philips XL30 Field Emission Environmental scanning electron microscope (FESEM) coupled with energy dispersive X-ray analysis (EDX), as shown in Figure 3-5, in order to get an understanding on morphology as well as chemical composition of reaction product.

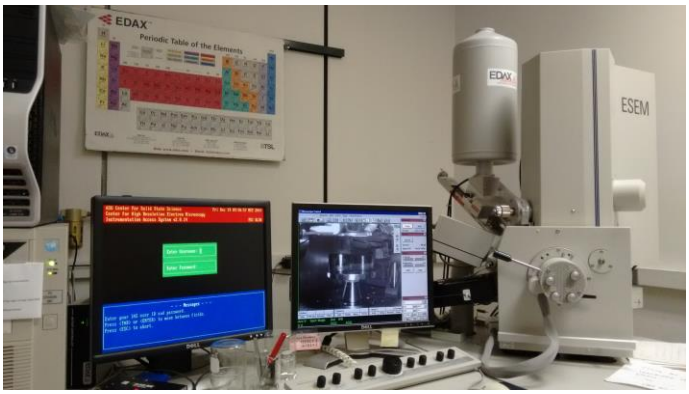

Figure 3-5: SEM-XL30 Environmental FEG (FEI)

While secondary imaging techniques are useful to examine the morphology of the fracture surfaces, the roughness of these surfaces introduces errors in the quantification of the microstructural or compositional features. Hence a suitable combination of grinding and polishing was carried out to achieve a level of flatness appropriate for microstructural and compositional analysis by the Electron Micro-Probe Analyzer (EMPA). JEOL JXA-8530F Hyperprobe, as shown in Figure 3-6, was used in this study primarily to detect elemental compositions of novel reaction product. The grinding/polishing procedure is explained later in detail. The polished sample was placed under electron gun of JEOL JXA-8530F Hyperprobe (EMPA). The hyperprobe features a field emission electron gun surrounded by five Wavelength Dispersive Spectrometers (WDS). The combination of WDS and EDS makes it a very powerful analytical tool.

Figure 3-6: JEOL JXA-8530F Hyperprobe featuring Field Emission Scanning Electron Microscope (FESEM) surrounded by five Wavelength Dispersive Spectrometers (WDS)

3.2.6 Nanoindentation

The nanoindentation measurements were carried out on the polished sample in a commercial Nanoindenter (MTS Nanoindenter XP) using a Berkovich tip as shown in Figure 3-7. Polished vacuum saturated epoxy-impregnated sample was mounted on aluminum stubs for nanoindentation testing using superglue. All the indentation locations were carefully selected prior to testing to ensure that the pores or cavities are not encountered in the process. Thus, the indentation experiments were carried out mostly on the solid phases, which resulted in very few spurious peaks in the modulus frequency distribution curves. The depth of penetration was chosen to be 500 nm which is smaller than the characteristic size of unreacted fly ash inclusions in order to avoid phase-interactions during penetration. Continuous stiffness measurement (CSM) technique was employed here to measure the contact stiffness. More in depth application-specific aspects of statistical nanoindentation method is provided in the chapter involving Nano-mechanical properties of novel iron-based binder.

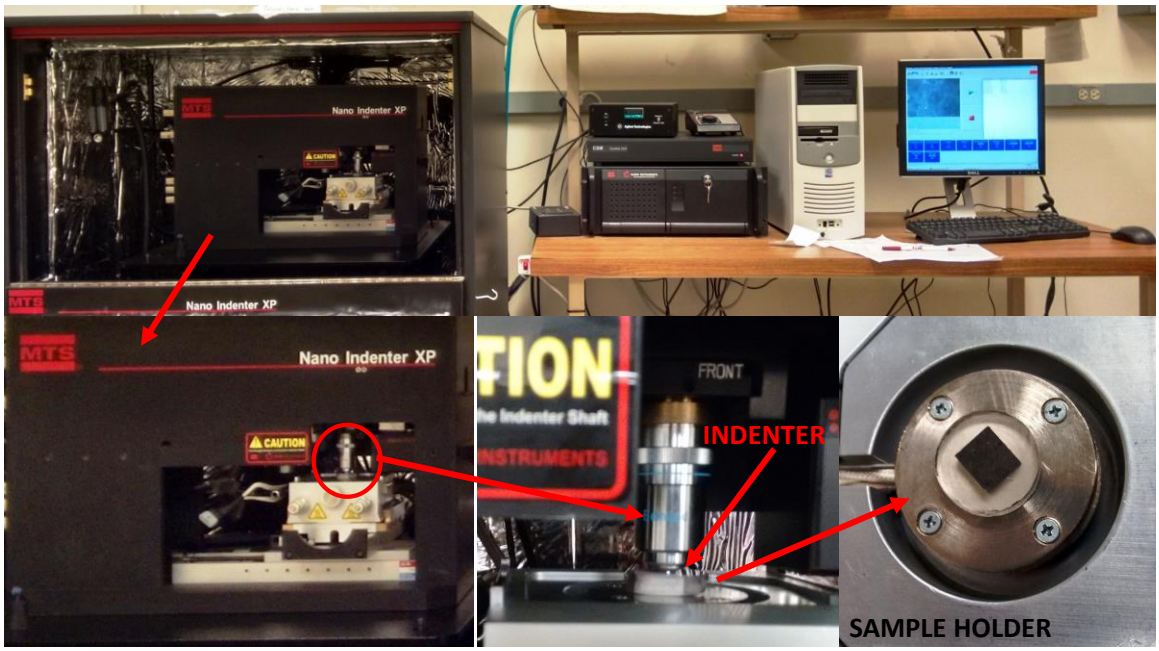

Figure 3-7: MTS Nanoindenter XP instrument setup

Chapter 4 Preliminary Investigation on the Synthesis of Novel Cementitious Binders Utilizing the Chemistry of Iron Carbonation

4.1 Introduction

Reduction in the amount of greenhouse gases (GHG) such as CO_2 in the atmosphere has been the spotlight in numerous research papers (Bachu, Gunter, and Perkins 1994; Holloway 1997; T. Xu, Apps, and Pruess 2004; Flaathen et al. 2009; Gislason et al. 2010; Qafoku et al. 2012). Mineral route of carbonation, where mined mineral rocks are used as the feedstock through which CO_2 is passed is one of the promising routes to reduce the concentration of CO_2 in the atmosphere (Klein et al. 2013; T. Xu et al. 2007; Naganuma et al. 2011). One of the major benefits of mineral carbonation is that CO_2 is chemically sequestered (as opposed to physical sequestration in almost all other methods, which is not always leakage-proof), thus making the sequestration virtually permanent. It has also been noticed that the secondary carbonate rocks formed during mineral trapping demonstrate mechanical strength (Hobbs 1964; Hobbs 1967; Herget and Unrug 1976) which reflects the possibility of usage of mineral trapping in conjunction with sustainable binder formation for construction. Magnesium oxide bearing rocks such as olivine and serpentine has been used as candidates for mineral carbonation; however possibilities exist for the use of several other metal or alkali metal species to be beneficially carbonated (Matter and Kelemen 2009; T. Xu, Apps, and Pruess 2005).

In this study, the results of a preliminary study that investigates the potential of formation of a novel binder from metallic waste iron powder is reported. Metallic iron powder is generated in significant amounts as bag house dust waste during the Electric Arc Furnace (EAF) manufacturing process of steel and from the shot blasting operations of structural

steel sections. The traditional means of disposing EAF and shotblasting dust is landfilling as it is not economically feasible to recycle back iron from the dust. Several million tons of such waste material is being landfilled at great costs all over the world. In the present work, an approach to form a sustainable binder system for concretes from carbonation of iron dust is proposed, which is inspired by the idea of CO_2-corrosion of, and scale formation in carbon steel pipelines in the oil and gas industry, which is a result of CO_2 injection into the oil wells to reduce the viscosity of the oil and thus increase oil production (Rivera-Grau et al. 2012; M. B. Kermani and Morshed 2003). The novel binder system, relying on the beneficial effects of "corrosion" of iron particles to form a binding matrix provides yet-unheard-of synergistic benefits through: (i) consumption and trapping of CO_2 from a GHG emitting industrial operation and subsequent carbonate formation, and (ii) providing a means to reduce the overall Portland cement production (which is a significant emitter of GHG) through the use of carbonated metallic iron powder as the binder material for concrete.

Several studies on iron carbonate formation by CO_2 corrosion of steel have been reported (Wu et al. 2004; Nordsveen et al. 2003; Nesic, Postlethwaite, and Olsen 1996). The most common reaction of iron involves the formation of oxides. However dissolved CO_2 is also capable of reacting with iron where a dense layer of iron carbonate forms and adheres strongly to the substrate. The accepted reaction steps for this process are (J. B. Sun et al. 2012):

$$Fe + 2CO_2 + H_2O \rightarrow Fe^{+2} + 2HCO_3^- + H_2 \uparrow \quad [4\text{-}1]$$

$$Fe^{+2} + 2HCO_3^- \rightarrow FeCO_3 + CO_2 + H_2O \quad [4\text{-}2]$$

The net reaction then is:

$$Fe + CO_2 + H_2O \rightarrow FeCO_3 + H_2 \uparrow \quad [4\text{-}3]$$

Though the basic reaction scheme seems straightforward and simplistic, the kinetics of the reaction and the rate of product formation are often very slow so as to be of any use for beneficial industrial applications. Hence dissolution agents (organic) that have the potential to enhance the corrosion rate of iron due to their high reducing power and complexing capacity (S. O. Lee et al. 2007; Taxiarchou et al. 1997; Ambikadevi and Lalithambika 2000; M. B. Kermani and Morshed 2003) need to be employed to control the reaction rates. In addition, several other factors are important when an alternate material is being considered for applications that commonly use Portland cement. These relate to early age properties including the rheological behavior (flowability and castability) and early strength development. Hence additives common to Portland cement concretes such as class F fly ash, powdered limestone, and metakaolin have been used in this study as minor ingredients along with metallic iron powder to form pastes with adequate binding capabilities. This chapter reports the optimal proportions of iron powder and other additives, and investigates the influence of curing regime (CO_2 and air exposure) for desired mechanical properties of these binder systems. Characterization of the reaction products in these binder systems is carried out using thermo-gravimetric analysis in this study. A proper understanding of the influence of source materials and processing on the mechanical properties of this unique binding system is expected to contribute to other related studies on this sustainable material as well as lead to entrepreneurial ventures to make beneficial products out of this technology, which is the ultimate objective of this research task.

4.2 Experimental Program

4.2.1 Starting materials: Composition and particle size

Metallic Iron powder with median particle size of 19 μm is used as the main starting material in this study. The iron powder is obtained from a shotblasting facility in Phoenix, AZ. The iron powder has mostly elongated and angular particles as can be seen from Figure 4-1, thereby influencing the rheological properties of the mixture. However the larger surface area-to-volume ratio of this shape provides benefits related to reactivity.

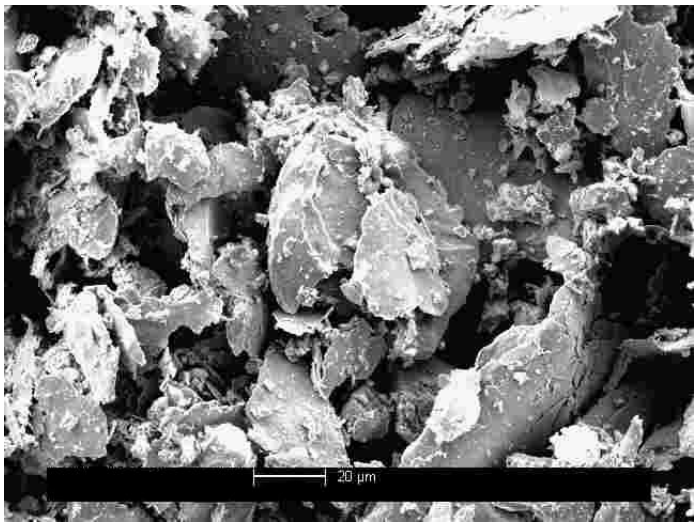

Figure 4-1: SEM image of angular iron particles

The chemical composition of the iron powder as obtained using Particle Induced X-ray Emission (PIXE) is shown in Table 4-1.

Table 4-1. Chemical composition of Iron powder (from PIXE)

Fe(%)	Cu(%)	Mn(%)	Cr(%)	Ca(%)	K(%)	O(%)
88	0.2	0.8	0.3	0.1	0.04	10

The other materials used include Class F fly ash and metakaolin conforming to ASTM C 618, and limestone powder with a median particle size 0.7 μm conforming to ASTM C 568. Fly ash was used to provide a silica source for the reactions[1] (to potentially facility iron silicate complexation (R. Kumar et al. 1990; Fairén et al. 2004)), fine limestone powder to provide nucleation sites, and metakaolin to provide cohesiveness in the fresh state to the iron-based mixtures. It needs to be remembered that the water is reduced in the chemical reactions but does not form part of the binder. Hence, in order to minimize the water demand, yet keeping the consistency and cohesiveness of the mixture, metakaolin was used. An organic reducing agent/chelating agent for metal cations was also used. Commercially available Type I/II ordinary Portland cement (OPC) conforming to ASTM C 150 was used to prepare conventional cement pastes and compare the compressive strengths of the novel iron-based binder systems with those of the traditional OPC-based systems. OPC was also partially replaced by class F fly ash and blast furnace slag up to 40% and 50% respectively by mass for comparison purpose. The oxide compositions of OPC, fly ash and metakaolin and slag are tabulated in Table 4-2.

Table 4-2. Chemical composition (%) of minor ingredients used in iron carbonation

[1] Other more reactive silica sources such as silica fume can also be used, but fly ash has been chosen partly to make beneficial use of its spherical shape that enhances the workability characteristics of the material.

Components	Cement	Fly ash	Metakaolin	Slag
SiO_2	21.0	59.52	51.7	39.42
Al_2O_3	3.61	23.03	43.2	8.5
Fe_2O_3	3.47	4.62	0.5	0.37
CaO	63.0	4.87	-	35.53
MgO	3.26	-	-	12.63
SO_3	3.04	0.48	-	2.89
Na_2O	0.16	2.32	-	1.7
K_2O	0.36	-	-	0.39
LOI	2.13	0.37	0.16	-

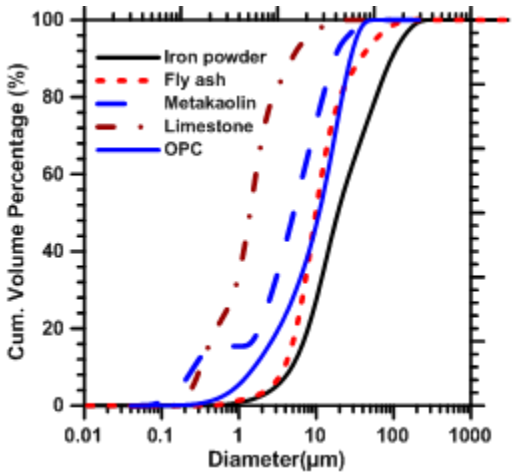

Figure 4-2: Particle size distribution of Metallic Iron powder, OPC, Fly ash, metakaolin and limestone powder

The particle size distributions of the iron powder, fly ash, metakaolin, limestone powder and OPC, obtained from a laser diffraction-based particle size analyzer are shown in Figure 4-2. All the ingredients are finer than the iron powder used. Please note that the

quantified data presented in this study could vary based on iron powder fineness[2], but the general mechanisms and trends are expected to remain the same.

4.2.2 Mixing procedure and sample preparation

The mixing procedure involves initial dry mixing of all materials (iron powder, fly ash, limestone powder, metakaolin, and the organic reducing agent). Water was then added and mixed in order to obtain a uniform cohesive mixture. The mass-based water-to-solids ratio (w/s) was varied between 0.22 and 0.25 depending upon the proportions of the constituents in the mixtures to attain a cohesive mix. The mixture was then tamped into cylindrical molds (32.5 mm diameter x 65 mm long) of the Harvard miniature compaction apparatus (Figure 4-3a) in five layers to fill the mold completely. The specimens were demolded immediately using the Harvard miniature specimen ejector (Figure 4-3b) and placed inside clear plastic bags filled with 100% CO_2 in room temperature inside a fume hood for 1 to 4 days. The bags were refilled with CO_2 every 12 hours so as to maintain saturation inside the chamber. After the respective durations of CO_2 exposure, the samples were placed in air at room temperature to allow the moisture to evaporate for 1 to 30 days. The samples that are ready for compressive strength testing are shown in Figure 4-3c. Compressive strengths of the OPC-based systems were performed in accordance with ASTM C 109 on 50 mm cubes. The water-to-cementitious materials ratio adopted for the OPC-based mixtures was 0.40.

[2] Note that reducing the fineness does not always result in strength enhancement as in the case of OPC mixtures. Larger size iron particles with a smaller carbonation ring to just facilitate binding of adjacent particles could result in better properties (flexural and fracture response in particular) because of the better properties of iron.

Figure 4-3: (a) Harvard miniature compaction apparatus, (b) specimen ejector, (c) Cylindrical samples for compression test

4.2.3 Determination of optimal mixture-proportions and curing procedure

A total of eight different mixtures with varying iron powder, fly ash, limestone, and metakaolin contents were proportioned in this preliminary study to select a few best performing mixtures, first in terms of compressive strength. The iron powder content ranged from 58 to 69% by mass whereas fly ash, limestone and metakaolin varied in the range of 15-20%, 8-10% and 6-10% by mass respectively. The w/s ratios varied between 0.22 and 0.25. These preliminary proportions were arrived at based on several trial proportions that used iron powder from 50-100% of the total binder content along with the other ingredients, and several w/s ratios in the range of 0.15 to 0.30. The proportions of the eight short-listed mixtures are shown in Table 4-3. In all cases, the organic reducing agent, which is a weak acid, was added in a powder form at 2% of total mass of the constituents.

Table 4-3. Mixture proportions for the preliminary study

	Mix 1	Mix 2	Mix 3	Mix 4	Mix 5	Mix 6	Mix 7	Mix 8
Iron	64	60	62	58	69	65	67	63
flyash	20	20	20	20	15	15	15	15
limestone	8	8	10	10	8	8	10	10
metakaolin	6	10	6	10	6	10	6	10

For the preliminary study, the specimens were kept in a 100% CO_2 atmosphere for 3 days immediately after casting and demolding and cured in air for 2 days before they were tested in uniaxial compression. The best performing mixture contained 60% iron powder, 20% fly ash, 8% limestone and 10% metakaolin (Mix 2 in Table 4-3) whereas another mixture containing 64% iron powder, 20% fly ash, 8% limestone, 6% metakaolin (Mix 1 in Table 4-3) also performed quite similarly in terms of average compressive strength (>25 MPa). Once the two best performing mixtures were determined, the CO_2 curing duration was varied from 1 to 4 days and the air curing duration varied from 1 to 3 days in order to determine the optimal combination of CO_2 and air-curing durations.

4.2.4 Flexural strength test

The flexural strength tests were carried out on Mixes 1 and 2 (best performing mixtures under compression). Paste beams, 250 mm x 25 mm x 25 mm in size were prepared and cured in a 100% CO_2 environment for 2-6 days. The air-exposure time was maintained constant at 3 days. The 3-point bending tests were conducted as shown in Figure 4-4 and the load and displacement data were recorded using NI LabVIEW data acquisition software. A displacement rate of 0.375 mm/min was maintained for all the flexural tests.

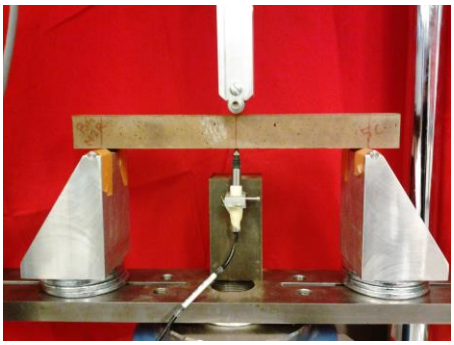

Figure 4-4: 3-point bending test of beams

4.2.5 Thermo-gravimetric analysis (TGA)

A Perkin Elmer STA 6000 simultaneous thermal analyzer was used for thermo-gravimetric analysis (TGA). The analyzer was programmed to increase the temperature from 30^{o}C to 995°C at a rate of 15°C/minute in a N_2 environment. The samples for TGA were taken from the cylindrical samples. Samples from both surface as well as core of the cylindrical specimens were analyzed in order to assess the influence of CO_2 penetration on the degree of reaction.

4.3 Results and Discussions

4.3.1 Influence of source materials and curing conditions on compressive strength

4.3.1.1 Influence of source materials and determination of optimal mixtures for compressive strength

As mentioned earlier, eight different mixtures (Table 4-3) were proportioned to understand the effects of various constituents on compressive strength of iron carbonate binders and to determine the optimal mixtures in terms of compressive strength for a specific curing duration and procedure. The samples were kept in a CO_2 environment for 3 days and then cured in air for 2 days at 23±2^{o}C to get a comparative view of

compressive strengths of the eight mixtures. The compressive strengths of different mixtures are reported in Figure 4-5 (a), from which it can be observed that Mixes 1 and 2 are the best performing ones. The variability of strength between a number of identical samples tested is also low as can be observed from this figure. Figure 4-5 (b) shows the 7-day compressive strengths of moist-cured OPC-based pastes with and without several cement replacement materials for comparison, which demonstrates the similarity in strengths at the chosen ages of treatment. While it is well known that OPC-based systems gain strength over a period of time and will likely end up with much higher compressive strengths, the values reported here for iron carbonate based binder systems are in the range of strengths that are used for a large number of construction applications.

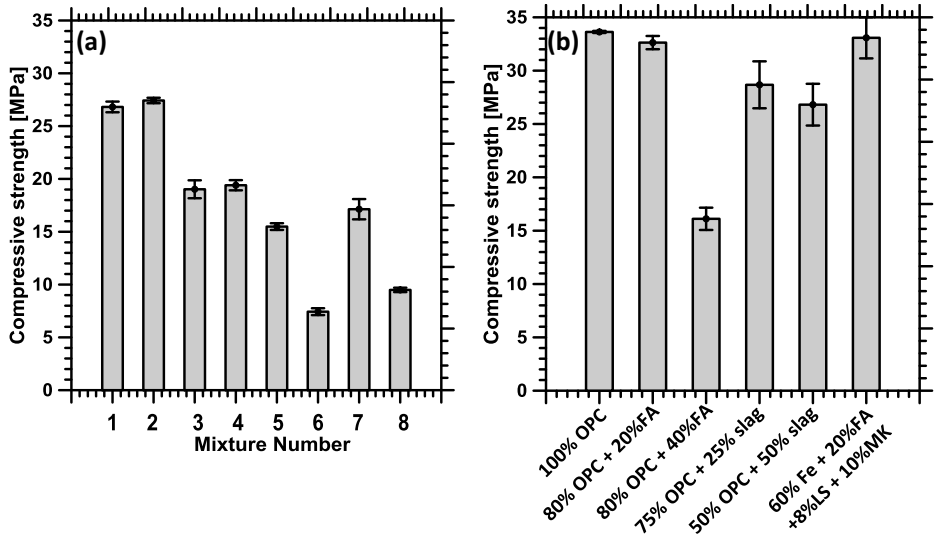

Figure 4-5: (a) Compressive strength vales of the mixtures (3 days in CO_2 and 2 days in air), and (b) comparison of strength with conventional OPC mixtures

The influence of various constituents on compressive strength is elaborated in Figure 4-6. Figure 4-6 (a) implies that the samples with 20% fly ash were significantly stronger than the ones with 15% fly ash, irrespective of the contents of limestone and metakaolin. Both the best performing mixes (Mix 1 and 2) contained 20% fly ash by mass. A pore-structure

study, detailed in the forthcoming chapter, has shown that these mixtures have the lowest porosity, as determined from mercury intrusion porosimetry, plausibly a combined effect of particle packing and increased reaction product formation (as will be confirmed from TGA results in a later section). From Figure 4-6 (b), it can be seen that the limestone content exerts negligible influence on compressive strength at lower fly ash contents, but at higher fly ash contents, a lower amount of limestone powder is preferable. Compressive strength is relatively insensitive to variations in metakaolin content for the samples containing 20% fly ash as the synergistic effect of silicates and cohesive nature of metakaolin likely ensures a denser matrix. At a lower fly ash content, an increase in the metakaolin content is associated with significant decrease in the compressive strength values.

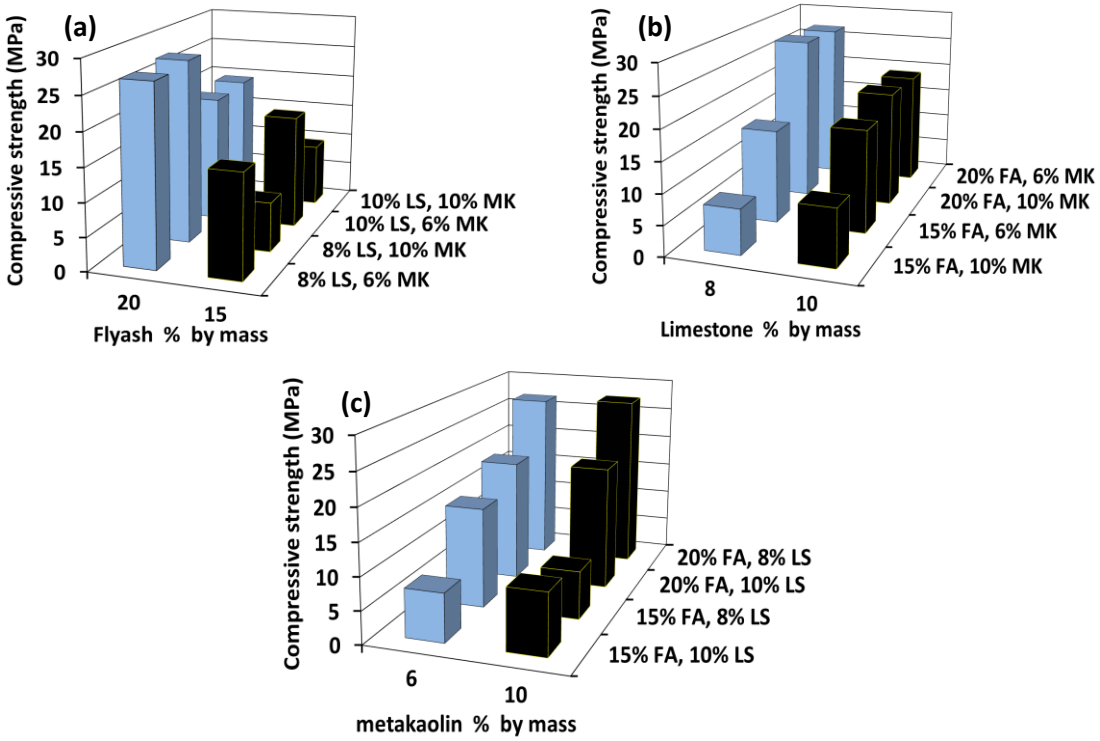

Figure 4-6: Effect of: (a) flyash, (b) limestone, and (c) metakaolin content on compressive strength of iron carbonate binders

In order to discern the statistical influence of the amounts of fly ash, metakaolin and limestone on the compressive strength and the relative sensitivity of strength to these factors, a 2^3 factorial analysis was carried out. The response surfaces of compressive strength are shown in Figure 4-7. It is confirmed that fly ash is the dominant factor among the three as far as compressive strength is concerned. The sensitivity of compressive strength with variations in the amount of limestone and metakaolin is relatively low. Metakaolin is basically used as a rheology modifier in these systems whereas the fine limestone is expected to be a nucleation site for the reaction products. The range of amount of limestone used in this study (8-10%) does not significantly impact the strength. More studies are required to understand how fine limestone powder participates in the reactions; however TGA studies in the forthcoming section do indicate some consumption of limestone in the reaction.

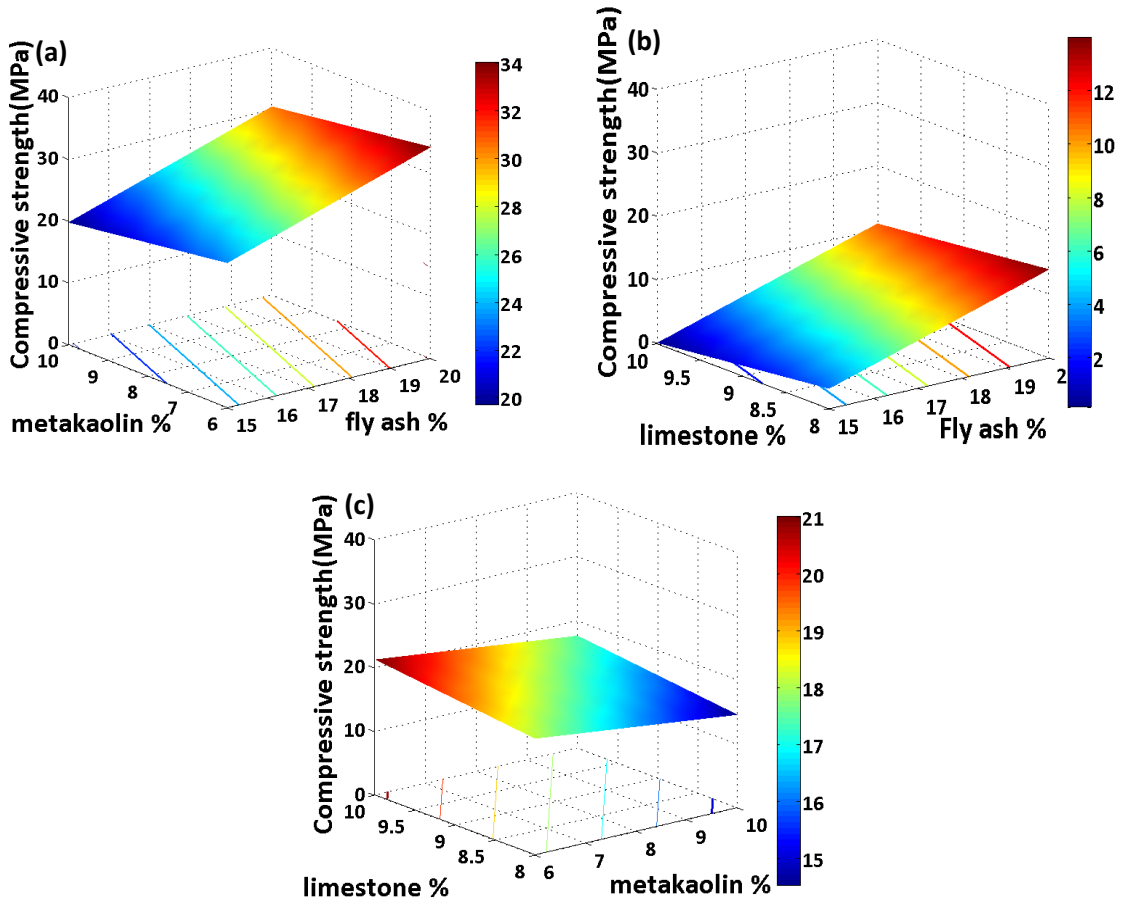

Figure 4-7: Response surfaces showing the statistical influence of amount of (a) fly ash and metakaolin, (b) fly ash and limestone, (c) metakaolin and limestone on compressive strength

As discussed earlier, Figure 4-5 (a) does not provide any realistic differences in strengths between Mixes 1 and 2 under the chosen curing condition. To observe whether changes in curing conditions would elicit varied response from these mixes, the cylindrical specimens were carbonated for 3 or 4 days and air cured for 1 or 3 days. Figure 4-8 demonstrates the strengths of these mixes after being cured under such conditions. Here the number before 'C' represents the days of carbonation whereas the number before 'A' represents the air-exposure time in days. Mix 2 was chosen for all further studies reported here because it performed similar to or better than Mix 1 for all the curing procedures in terms of compressive strength.

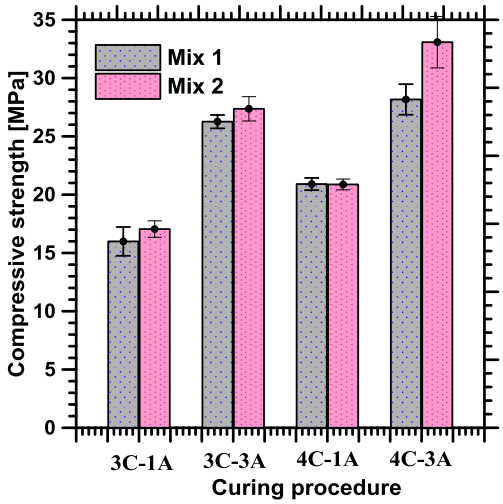

Figure 4-8: Comparison of compressive strength of Mixes 1 and 2 under different curing condition

4.3.1.2 Effect of curing conditions on compressive and flexural strength

The effects of curing procedure and duration on compressive as well as flexural strengths are shown in Figure 4-9. The samples were cured in CO_2 for 1 to 4 days and in air for 1 to 3 days thereafter. The strength values are shown in a response surface plot as function of CO_2 and air-curing durations in Figure 4-9a. The influence of CO_2 curing duration is obvious from this figure. The compressive strength values were very low for the samples cured in CO_2 for 1 day only due to the very low degree of carbonation. Since it is the carbonation that provides the mechanical strength, there is no discernible strength increase when the moisture leaves the system through air exposure. This can be seen from this figure where for 1 day of carbonation, increasing the air exposure duration from 1 to 3 days does not impact the compressive strength positively. However the effect of air-curing is evident when the carbonation duration is increased. A significant increase in strength is observed for specimens carbonated for a longer duration when the air curing time was increased. This is attributed to the fact that the pore sizes decrease with

increased carbonation duration as shown in Figure 4-10. More details on the pore structure are reported in the forthcoming chapter. The characteristic pore size of 1–day carbonated samples are larger, which consequently exerts less internal moisture pressure under a compression test and therefore loss of moisture through air exposure does not have a larger effect on internal pressure and thus the compressive strength. The pore sizes of samples carbonated for a longer duration are lower due to increased reaction product formation, resulting in an increased sensitivity of compressive strength to the loss of moisture. In order to clearly bring in the effect of air exposure, Figure 4-9b plots the compressive strengths as a function of air exposure duration after the samples were carbonated for 4 days. First three days of exposure to air results in an enhancement in the compressive strength but as the moisture dries out completely there is no significant change in compressive strength which signifies that the reaction product is passive and stable in nature in air and it does not cause any deterioration when exposed to air for longer time. Thus the air exposure duration (depending on the pore structure of the material that lets moisture escape from the bulk of the specimen) influences the compressive strength at longer carbonation durations.

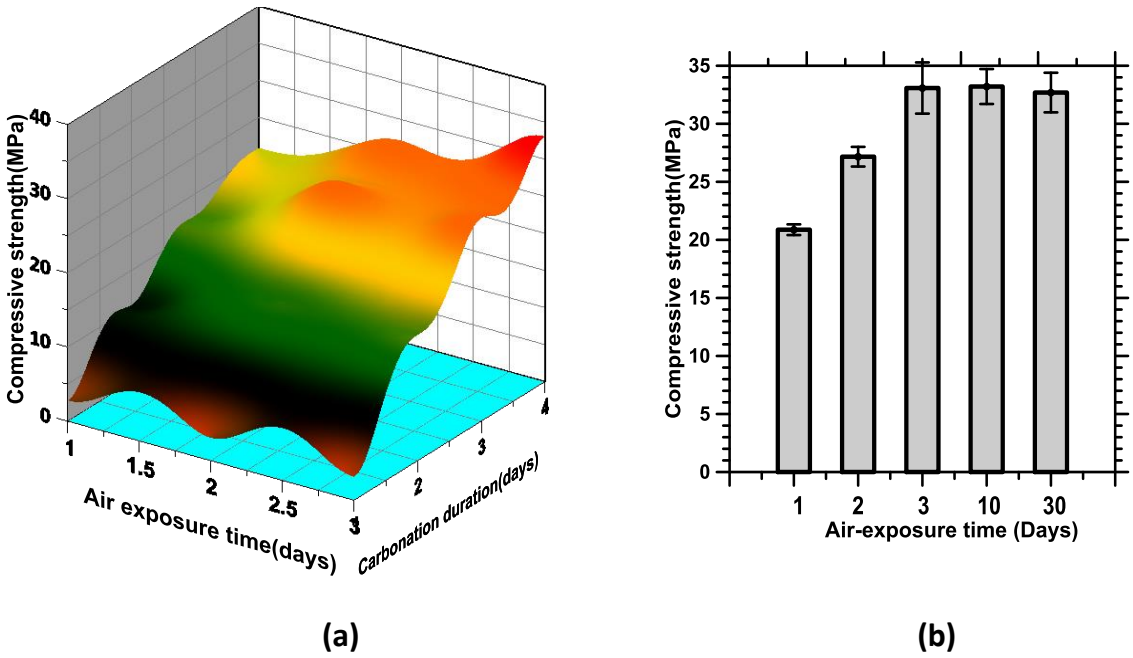

Figure 4-9: Effect of (a) curing procedure and curing duration, (b) air-curing duration on compressive strength of Mix 2. The samples were carbonated for 4 days for the data in Figure 4-9b.

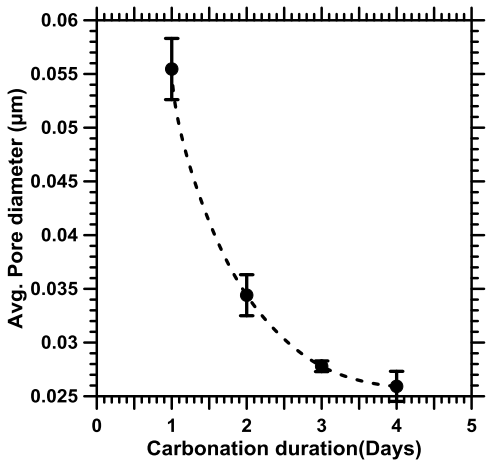

Figure 4-10: Variations in average pore diameter with varying carbonation duration

Figure 4-11 (a) shows the variation in flexural strength of iron carbonate binders (both Mix 1 and Mix 2) with an increase in carbonation duration. The flexural strengths are very similar for both the mixes, which is in line with the trends for compressive strength. It can be noticed that a carbonation duration of 6 days result in a relatively high flexural

strength of about 8 MPa. Figure 4-11 (b) shows the relationship between flexural strength and density for these mixes. Higher carbonation durations results in more reaction product formation and increased density as the reaction product fills the pores more efficiently.

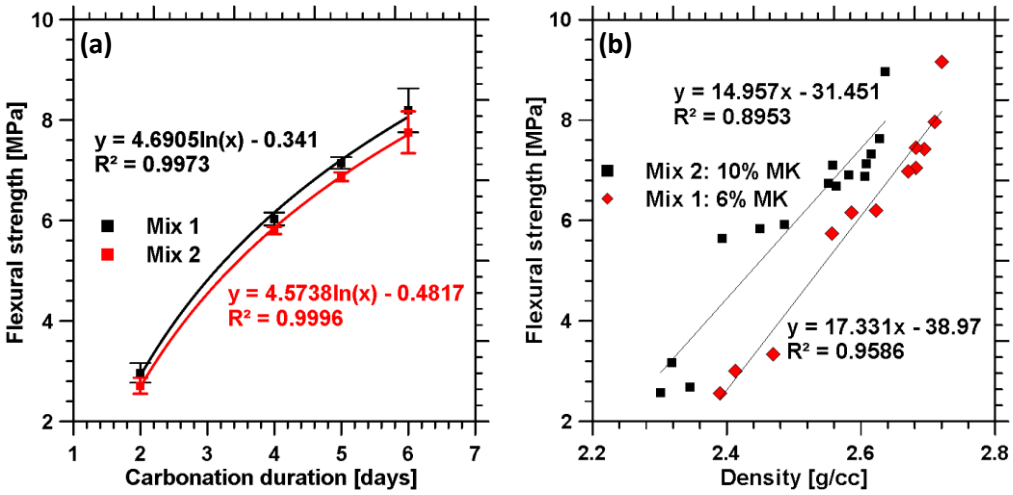

Figure 4-11: (a) Logarithmic increase of flexural strength with increase in carbonation duration, (b) interaction between bulk density and flexural strength

4.3.2 Reaction products and extent of carbonation

Thermo-gravimetric analysis was carried out on powdered samples extracted from the surface as well as the core of the cylindrical specimens in order to investigate the degree of reaction that is responsible for differences in mechanical properties. First, thermal analysis results of Mixes 2 and 6 have been compared in order to understand the differences in product constitution between the best and worst performing mixtures as far as compressive strength is concerned. The major differences between these mixtures are in the iron powder and fly ash contents. Figure 4-12 (a) and (b) depict the TG curves and their derivatives for the samples from the surface and core of cylindrical specimens corresponding to Mixes 2 and 6 respectively. Both the specimens were carbonated for 3

days. A comparison of Figure 4-12 (a) and (b) suggests that the total weight loss for Mix 2 is significantly higher than that for Mix 6, indicating that the overall degree of reaction and product formation is lower under the chosen carbonating conditions for the starting material combination of Mix 6. The total weight loss of the sample from the surface of Mix 6 cylinder is slightly lower than the weight loss from the core sample of Mix 2 cylinder. This shows that the constitution of Mix 6 is not amenable to desirable levels of carbonation and product formation, which reflects in the compressive strength of the binder. This observation also points to the fact that the carbonation efficiency and mechanical properties of iron carbonate binders are very sensitive to the overall starting material composition – from a compositional viewpoint, the difference between Mixes 2 and 6 are not very large. It should also be considered that the range of iron powder contents that provided reasonable strengths were rather narrow - between 60 and 69%, as shown in Table 4-3.

The DTG curves demonstrate three distinct peaks for the binder samples as can be observed in Figure 4-12. The peak at around 110^{o}C is attributed to evaporable water, the one at around 300^{o}C to products belonging to the carbonate-oxalate-cancrinite group (Olysycha et al., 2011), and the one at around 740^{o}C to calcium carbonate. The DTG for Mix 2 provides a distinct peak at about 300°C (for samples from both the core and the surface) whereas the intensity of the peak reduces for samples from Mix 6. The peak is almost non-existent for the sample from the core of Mix 6, indicating that the carbonation efficiency for that mixture constitution is low.

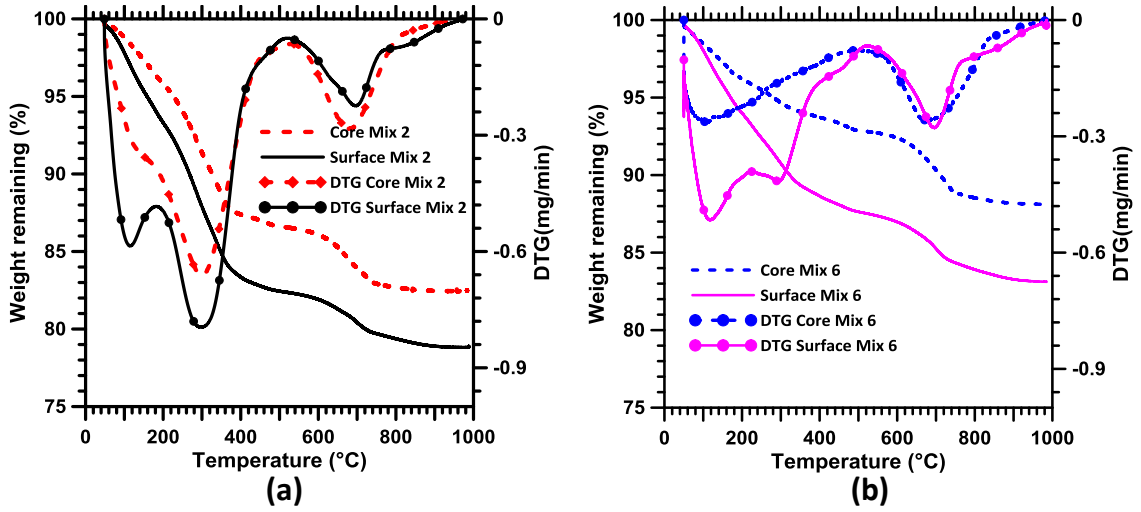

Figure 4-12: TG and DTG curves corresponding to the core and surface of: (a) Mix 2, and (b) Mix 6, carbonated for 3 days

Further, the effect of carbonation duration on reaction product formation is investigated and explained using Figure 4-13. Figure 4-13 shows the TG and DTG curves for samples of Mix 2 corresponding to the surface and core of the carbonated cylindrical specimen after 1 to 4 days of carbonation and 3 days of air-exposure. The peak at 110°C in the DTG plot (due to evaporation of water) reduces in magnitude with increase in carbonation duration especially after 2 days of carbonation whereas the peak at 300°C increases in magnitude significantly when the carbonation period is increased. This peak at 300°C is very common for carbonate-oxalate cancrinite group materials (Olysych et al. 2011). Another important phenomenon observed in Figure 4-13 is that the difference in final weight loss between surface and core reduces as the carbonation duration is increased. This indicates that CO_2 diffusion extends to the core with an increase in exposure duration as expected. By 4 days, there is virtually no difference in the TG and DTG signatures between the core and the surface indicating that complete carbonation can be achieved in these samples. However it must be remembered that this is a function of specimen size, constitution, and the carbonating environment.

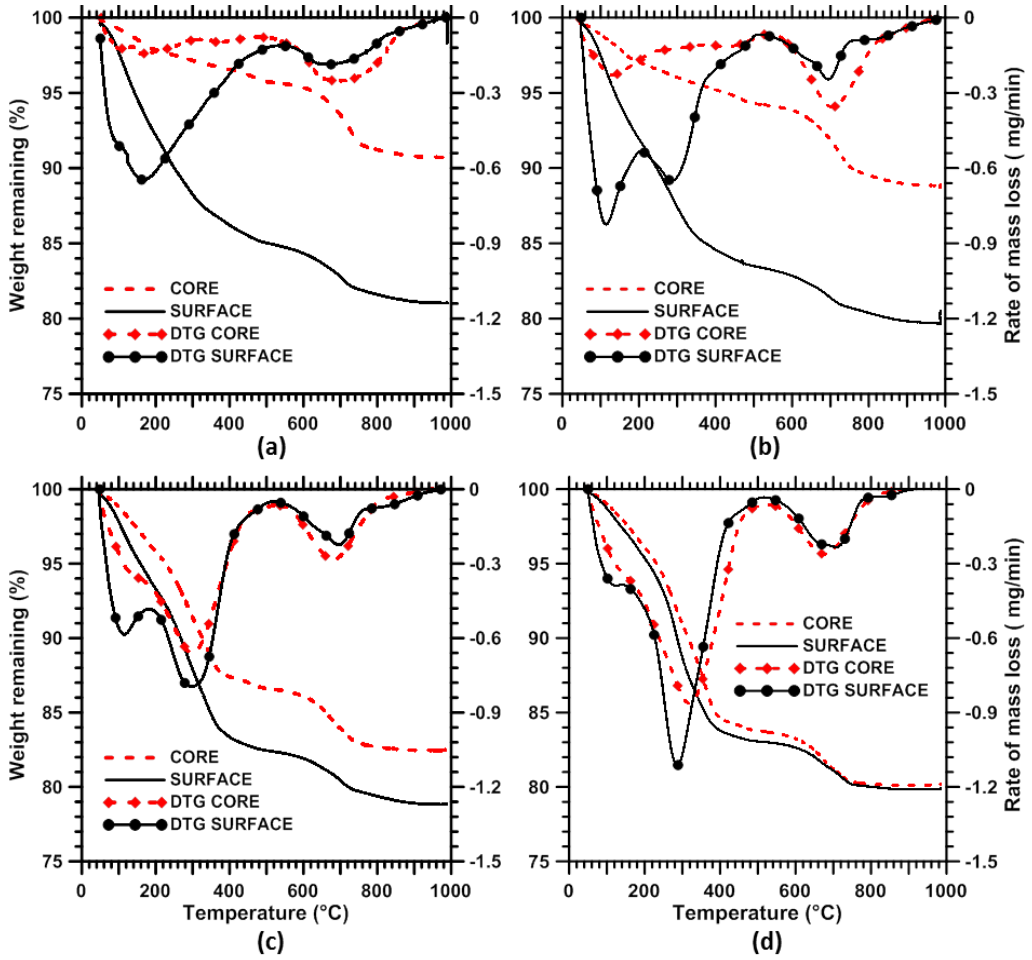

Figure 4-13: Thermal analysis results of samples from Mix 2 carbonated for (a) 1 day, (b) 2 days, (c) 3 days and (d) 4 days. All samples were exposed to air for 3 days after carbonation

A further analysis of the carbonation duration-dependent mass loss patterns is attempted in Figure 4-14. Figure 4-14a shows the percent mass loss in the 250-400^{o}C range and tracks the relative degree of carbonation in the surface and core of the samples. The mass loss observed in the 650-800°C range in the DTG plots correspond to thermal decomposition of calcium carbonate into calcium oxide. The amount of calcium carbonate remaining in the system was calculated based on the stoichiometry of the thermal decomposition reaction of calcium carbonate. The percentage of unreacted calcium carbonate present in the system for various carbonation durations is shown in

Figure 4-14 (b) which shows a significant difference in the amount of unreacted $CaCO_3$ between the core and the surface in the first two days of carbonation. However this difference is reduced as the carbonation period is increased to 3 to 4 days. The amount of unreacted $CaCO_3$ is generally the same at the specimen surface at all carbonation durations as can be observed from Figure 4-14 (b). As carbonation proceeds, the amount of $CaCO_3$ remaining in the core drops because of the consumption of some limestone in the reaction product formation. Thus it can be inferred that some portion of calcium carbonate is utilized to form the carbonate-oxalate complex and the remaining unreacted limestone is decomposed in that temperature range. Since, the thermal analysis study confirms similar degree of carbonation of core and surface after 4 days of carbonation, the upper limit of carbonation duration has been restricted to 4 days in the studies reported here.

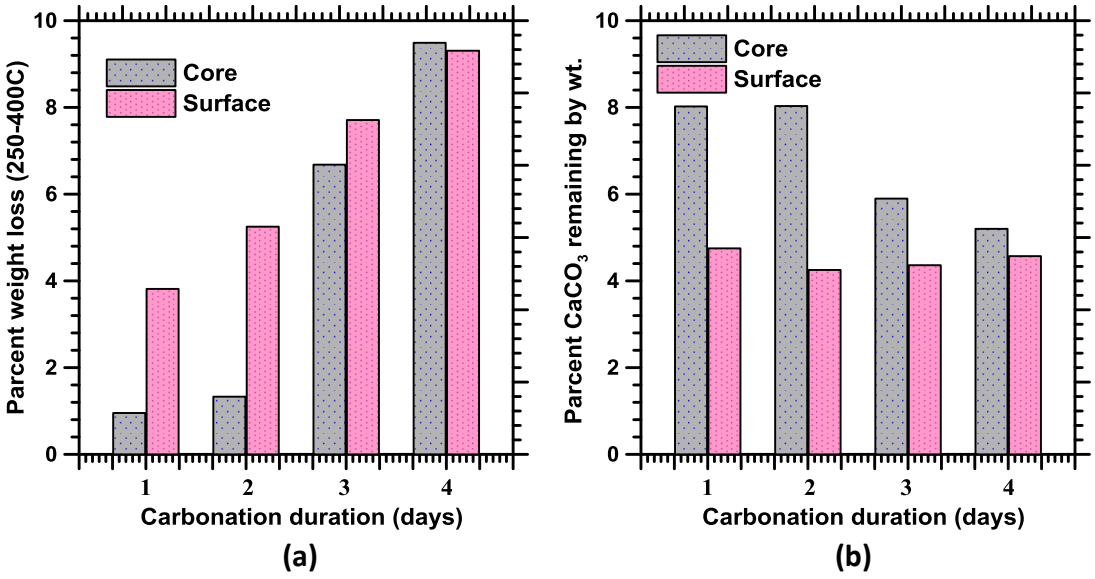

Figure 4-14: Effect of carbonation duration on: (a) mass loss in the 250-400^{o}C in TGA, and (b) amount of $CaCO_3$ remaining

4.4 Conclusions

This study has reported experimental results and analysis on the effect of source materials and curing conditions on mechanical properties of a unique binder system that utilizes the carbonation of metallic iron powder for cementation properties. The experiments carried out here showed that waste iron powder in combination with commonly used concrete ingredients such as fly ash, limestone powder, and metakaolin as minor components can be carbonated to produce a binding material with acceptable properties for a wide range of construction applications. In addition, this route of binder formation is a method of CO_2 minimization both in terms of CO_2 trapping in the form of carbonate formation as well as provision of an alternate structural binder that helps reduce portland cement consumption. Compressive strengths in the 30-35 MPa range were obtained after four days of carbonation.

The compressive strength of the binder systems were significantly influenced by the fly ash content. While limestone in the chosen range did not influence the strength at lower fly ash contents, the synergistic effects were evident at higher fly ash contents. Metakaolin primarily influenced the processing of the binder by providing cohesion to the mixtures. CO_2 exposure duration and air curing duration were also found to be influential on the mechanical properties of the binder. The effect of air-exposure time on compressive strength was found to be negligible at lower levels of carbonation (1-2 days) although the sensitivity increased significantly at higher carbonation durations (3-4 days). Thermo-gravimetric analysis showed that the carbonation efficiency of iron carbonate binders is very sensitive to the overall starting material composition. The difference in mass loss between surface and core reduced significantly as the CO_2 diffusion is

extended to the core with an increase in carbonation duration. The distinct DTG peak at 300 °C which is very common for carbonate-oxalate cancrinite group materials was evident in the signals of these binders. The mass loss in the temperature range of 250-400 °C increased as the carbonation duration increased, indicating the formation of more carbonate-bearing binding products. $CaCO_3$ content in the specimen core decreased when the carbonation was increased, which served as an indication of the consumption of limestone in reaction product formation. These results point to the fact that the reaction product formation increases as the carbonation progresses resulting in a denser structure and therefore better mechanical performance.

Chapter 5 Pore- and Micro-structural Characterization of the Novel Structural Binder based on Iron Carbonation

5.1 Introduction

While the effect of source materials (including minor ingredients) on the compressive strength and extent of reaction product formation were investigated in detail in the previous chapter, the current chapter investigates the pore structure and microstructure of the iron-based binder. The pore structure of the iron-based binder is characterized in detail using mercury intrusion porosimetry (MIP). The pore structure features extracted using MIP are used in established theoretical models to predict the gas diffusivity and moisture permeability of these novel binders. Electron microscopy coupled with energy-dispersive X-ray spectroscopy (EDS) is used to evaluate the morphology of the reaction products and the chemical constituents of the microstructure. Thus this study sheds light on the pore- and micro-structure of iron-based binder systems and provides valuable information that is critical towards positioning this material as a potential alternative to OPC systems, especially in regions where the requisite source materials and CO_2-emitting processes are present.

5.2 Experimental program

5.2.1 Starting materials: Composition and particle size

Metallic Iron powder with median particle size 19.03 μm has been used as main starting material in this study. The other materials used include Class F fly ash and metakaolin conforming to ASTM C 618, and limestone powder with a median particle size 0.7 μm conforming to ASTM C 568. Commercially available Type I/II ordinary Portland cement

(OPC) conforming to ASTM C 150 was used to prepare conventional cement pastes and compare the compressive strengths of the novel iron-based binder systems with those of the traditional OPC-based systems. More information on chemical compositions and particle size distributions are detained in the previous chapter.

5.2.2 Mixing and curing procedure

The mixing procedure involves initial dry mixing of all materials (iron powder, fly ash, limestone powder, metakaolin, and the organic reducing agent). Water was then added and mixed in order to obtain a uniform cohesive mixture. The mass-based water-to-solids ratio (w/s) was varied between 0.22 and 0.25 depending upon the proportions of the constituents of the mixtures to attain a cohesive mix. Cylindrical samples of 32.5 mm diameter and 65 mm length were prepared using Harvard miniature compaction apparatus and Harvard miniature specimen ejector. The samples were placed immediately inside clear plastic bags filled with 100% CO_2 in room temperature inside a fume hood for 1 to 4 days. The water-to-Cement ratio adopted for OPC was 0.40.

A total of eight different mixtures with varying iron powder, fly ash, limestone, and metakaolin contents were proportioned as explained in the previous chapter (Table 4-3). The iron powder content ranged from 58 to 69% by mass whereas flyash, limestone and metakaolin varied in the range of 15-20, 8-10 and 6-10% by mass respectively. The proportions of the eight mixtures are shown in Table 4-3.

For comparison purpose, the specimens were kept in the CO_2 atmosphere immediately after casting and demolding, for 3 days and cured in air for 2 days before they were tested in uniaxial compression as explained in the previous chapter on preliminary investigations. The best performing mixture contained 60% iron powder, 20% flyash, 8%

limestone, 10% limestone (Mix 2 in Table 4-3). Four days in carbon dioxide curing followed by 3 days of air drying was found to result in the maximum compressive strength. Hence, Mix 2 is mainly used here in the pore- and microstructural characterization of iron-based novel binder.

5.2.3 Pore Structure Determination using MIP

Mercury intrusion porosimetry (MIP) which is a well-established technique to investigate the pore structure of porous materials, was adopted here to study the pore structure of iron carbonate systems. The samples for MIP were taken from the same core of the cylindrical sample prepared for compressive strength testing. Thermal analysis results had shown that the selected CO_2 exposure duration resulted in similar carbonation levels in the core of the 32.5 mm diameter sample as that of the surface (Das, Souliman, et al. 2014). MIP was performed in two steps: (i) evacuation of gases, filling the sample holder with mercury and increasing the pressure to 345 kPa, and (ii) intrusion of the mercury into the sample at high pressures (up to 414 MPa). The contact angle and surface tension used for the analysis were 130° and 0.485 N/m respectively. Accurate determination of the contact angle was not carried out in this study, which could have introduced errors in the pore size determination. However, since the emphasis is on comparative evaluation of pore sizes, this inaccuracy is not deemed to be critical. The pore diameters can be evaluated using Washburn equation, based on the assumption that the pores in the porous media are cylindrical in shape (Moon, Kim, and Choi 2006; Ghafari et al. 2014; Sánchez-Fajardo, Torres, and Moreno 2014). A minimum pore diameter of 0.003 μm can be evaluated using MIP. Total volume of mercury intruded (which is the total porosity) and critical pore diameter (which is the peak in the differential volume intruded curve) can be

obtained from MIP. The average pore diameter (d_a) is calculated from the total pore volume and the pore surface areas as: (Moon, Kim, and Choi 2006)

$$d_a = \frac{4V}{A} \tag{5-1}$$

where V is the volume of mercury intruded per gram of sample (cc/g) and A is the total pore area (m^2/g) obtained from MIP. The pore tortuosity (τ) was empirically determined from the pore volume (ϕ) as (Carniglia 1986):

$$\tau = 2.23 - 1.13\phi \qquad \text{for } 0.05 \le \phi \le 0.95 \tag{5-2}$$

5.2.4 Microstructural Evaluation

Morphological analysis was done using a Philips XL30 Field Emission Environmental scanning electron microscope (FESEM) coupled with energy dispersive X-ray analysis (EDX) in order to get an understanding on morphology as well as chemical composition of reaction product. The pastes were crushed and small pieces from core were mounted to the stub with epoxy resin for FESEM.

Secondary imaging techniques essentially show the morphological nature of the surface of the specimen. The minimum effort to prepare a sample and the ease of interpreting the topographical feature makes secondary imaging techniques very attractive. However, the roughness of the fractures surface which is not representative of the material affects the scattered electron imaging especially the quantitative analysis. A flat surface is required for more accurate compositional analysis. A suitable combination of grinding and polishing has been done on the sample in order to achieve flatness of the surface. Prior to mounting, the sample was ultrasonically cleaned in GP cleaning solution, rinsed with ethyl alcohol and dried with compressed air spray to remove debris from

sectioning/handling. The cleaning process improves the adhesion of the mounting material to the sample. After drying, the sample was placed into a 32 mm two-part mounting cup. EpoxySet was used for encapsulation which does not require any external heating to cure. The cup was placed into a VacuPrep^{TM} epoxy impregnation system and subjected to 28 inHg of vacuum for 5 to remove entrapped air from epoxy. After hardening the epoxy gains enough strength to withstand the stresses during grinding and polishing. The sample was then prepared using MetPrep 3^{TM} grinder/polisher with power head as listed in Table 5-1. 600 and 800 Grit Silicon Carbide (SiC) abrasive discs were used to remove deformations caused by sectioning. Removal of deformations caused by grinding was done by 3 µm and 1 µm diamond suspensions. Final polishing was done with 0.04 µm colloidal silica suspension. After each grinding and polishing step the sample as well as the sample holder were cleaned using organic soap and dried using compressed air spray and images were taken under optical microscope to see the progress of the polishing (Figure 5-1). The polished sample was placed under electron gun of JEOL JXA-8530F Hyperprobe (Electron Microprobe). The hyperprobe features a field emission electron gun surrounded by five Wavelength Dispersive Spectrometers (WDS). The combination of WDS and EDS makes it a very powerful analytical tool.

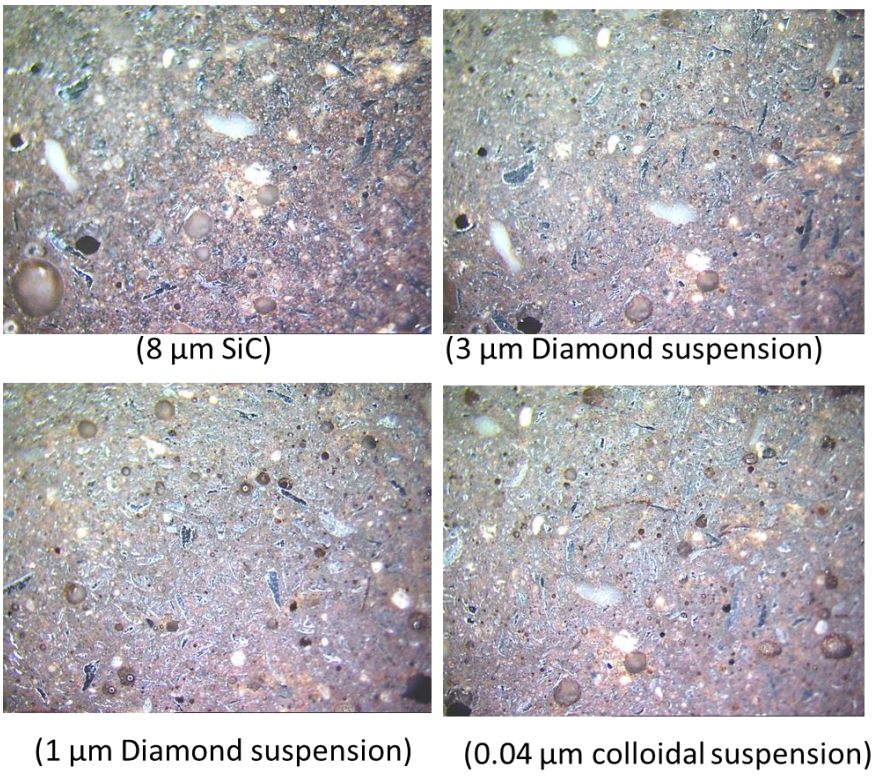

Figure 5-1: Surface of the sample as the polishing progresses (images taken using optical microscope at 100X)

Table 5-1: Grinding and Polishing procedure

	step	1	2	3	4	5
Consumables	Abrasive	600 Grit	800 Grit	3 µm	1 µm	0.04 µm
	Type	SiC	SiC	Diamond	Diamond	Colloidal silica
	Carrier	Abrasive Disc	Abrasive Disc	Glycol Suspension	Glycol Suspension	Suspension
	coolant	Water	Water	GreenLube	GreenLube	Water
Settings	Platen Speed(RPM)	300/Comp	300/Comp	150/Comp	150/Comp	150/Comp
	Sample speed (RPM)	150	150	150	150	150
	Force(N)	25	25	25	30	30
	Time (min)	Until flat	2	2	5	2

5.3 Results and discussions

5.3.1 Pore-Structural Analysis of Iron-Based Binders

This section examines the pore structure of the iron carbonate binders. It is well known that the pore structural features exert a significant influence on the mechanical and transport properties (Scheidegger 1963; Plessis and Masliyah 1988), of any porous material. The influences of source material composition and treatment conditions (carbonation and air-exposure durations) on the resultant pore structure are discussed.

5.3.1.1 Effect of Starting Material Composition

Mixture 2 (Table 4-3) was the best-performing mixture from a compressive strength standpoint, while Mixture 6 performed the worst as shown in Figure 4-5. A comparison of the pore structure of these two mixtures as determined using MIP is shown in Figure 5-2. There is a significant difference in the total volume of mercury intruded, with Mixture 2, showing a pore volume of about half as that of Mixture 6, implying a denser microstructure in the former mixture. The critical pore size, which is indicated by the peak location in the derivative of the pore size-volume intruded curve, remains generally invariant between the two mixtures. A companion study has confirmed through thermo-gravimetric analysis that the carbonation efficiency and the amounts of reaction products formed in Mixture 6 was much lower as compared to Mixture 2 and, that the carbonation efficiency and mechanical properties of iron carbonate binders are very sensitive to the overall starting material composition (Das, Souliman, et al. 2014).

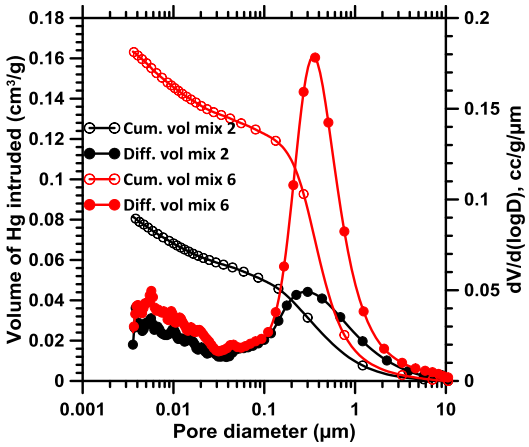

Figure 5-2: Comparison of pore structure of Mixtures 2 (60% iron powder, 20% fly ash, 8% limestone, 10% metakaolin) and 6 (65% iron powder, 15% fly ash, 8% limestone, 10% metakaolin) after 4 days of carbonation and 3 days of air-exposure.

5.3.1.2 Effect of Carbonation and Air-Exposure Duration

The volume of mercury intruded as a function of the pore sizes and the derivative of this relationship are shown in Figure 5-3 for various carbonation regimes applied to Mixture 2. For all the carbonation durations, an air-exposure duration of 3 days following carbonation was chosen as there is no appreciable increase in compressive strength beyond this air-exposure duration as shown in Figure 4-9. The total volume of mercury intruded reduces significantly with an increase in carbonation duration due to the increased formation of reaction products (Das, Souliman, et al. 2014). The consequent increase in specimen density results in improved mechanical properties. The derivative plots show no significant differences in the peak locations as a function of the carbonation duration. However, the reduction in porosity with increasing carbonation duration can be expected to reduce the number of pores of the critical size (the size corresponding to the major peak in the derivative curve). Therefore, while the critical pore sizes remain rather unchanged, the average pore size is reduced considerably with an

increase in the carbonation duration. The reduction in the total pore volume is known to primarily influence the mechanical properties, whereas, the reduction in pore size is more influential in transport properties.

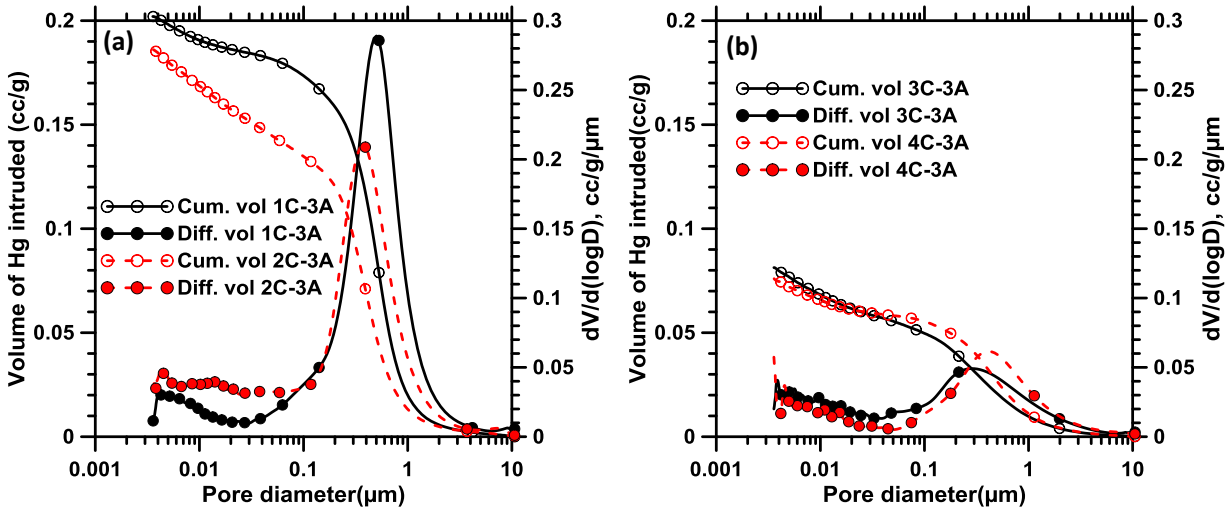

Figure 5-3: Effect of carbonation duration on pore structure for Mixture 2. Carbonation duration of: (a) 1 day and 2 days; (b) 3 days and 4 days. Air exposure of 3 days after all carbonation regimes. The number before 'C' represents the days of carbonation whereas the number before 'A' represents the air-exposure time in days.

Figure 5-4 depicts the carbonation efficiency as a function of CO_2 exposure time in relation to pore size and the representative range of sizes as determined using MIP. The percentage of pores of three different size ranges determined using the Washburn equation is shown here. Even though the size range determination using MIP is somewhat flawed, it is useful to compare between materials of similar chemical composition and processed in a similar fashion (Winslow 1984; Giesche 2006; Feldman 1984; Lawrence 1978). The fraction of pores greater than 0.2 µm (the larger pores, which are unfilled owing to insufficient reaction product formation) decreases with increasing carbonation period whereas the fraction of pores in the range 0.0036 – 0.05 µm increases correspondingly. For example, after 1 day of carbonation, the pores > 0.2 µm constitute

more than 70% of the overall pore volume. After 4 days of carbonation, this fraction drops to approximately 45%. The smaller pores are likely to be the ones which are part of the reaction product structure. Their relative increase represents an increase in product formation with carbonation as the thermal analysis (Das, Souliman, et al. 2014) and mechanical property results suggest. Also, the trends in the pore sizes depicted in Figure 5-4 follow the trends in compressive strength, thereby lending credibility to the use of this method.

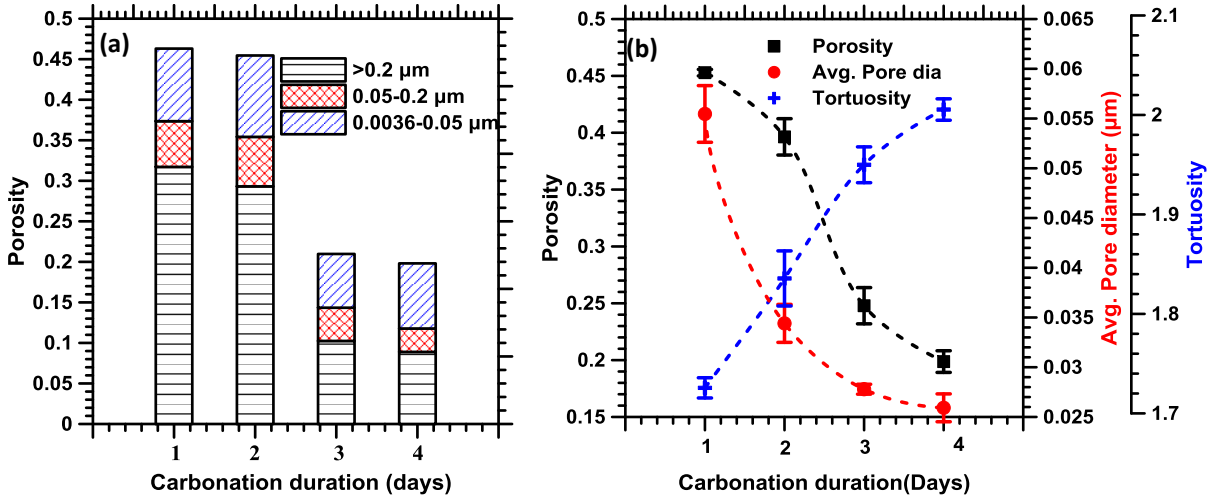

Figure 5-4: (a) Pore size ranges in iron carbonate binder (Mixture 2) as a function of carbonation duration; and (b) variation of porosity, pore sizes, and tortuosity as a function of carbonation duration. Air exposure duration of 3 days after respective carbonation durations

Figure 5-4(b) depicts the variation of porosity, average pore diameter (calculated using Equation 5-1 and tortuosity (calculated using Equation 5-2 with varying carbonation durations. As seen in this figure, both porosity and average pore diameter decrease significantly when the carbonation duration is increased from 1 to 4 days. These observations are in agreement with the compressive strength results in Figure 4-5 and the thermogravimetric analysis results described in the previous chapter on preliminary investigations. With an increase in the carbonation duration, the pore structure becomes more tortuous due to increased amounts of reaction product formation. The porosity and

tortuosity values presented here are used to calculate the theoretical transport parameters of iron carbonate systems which are presented later in this study.

5.3.1.3 Comparison of the Pore Structures of Iron Carbonate and OPC-based Systems

In this section, a comparison of the overall pore volumes and the critical pore size of iron carbonate and OPC binder systems is described. Figure 5-5(a) shows that the porosity of the hardened OPC paste (cured in moisture for 28 days) is higher as compared to the iron-based binder (carbonated for 4 days, followed by air-exposure for 3 days). However, one should be aware of the fact that the porosity of OPC systems can be controlled through several means such as reduction in water-to-cementing materials ratio (w/cm) facilitated by the use of chemical admixtures, incorporation of other reactive ingredients and improved curing practices. The pore structure of OPC pastes provided here is only used as a point of comparison and not intended to derive quantitative conclusions regarding the pore structure of OPC systems, which can be found in several other publications (Chindaprasirt, Jaturapitakkul, and Sinsiri 2005; Cook and Hover 1999; Goto and Roy 1981; Tanaka and Kurumisawa 2002). Also, for the iron-based binder systems, the composition and curing conditions used are designed to provide the optimal microstructure and strength. From the derivative plots shown in Figure 5-5(a), it is clear that the iron-based binder has a larger critical pore diameter than the OPC system which will impact the transport of moisture, ions, and gases through the pore structure. The increased pore size is likely a result of the H_2 gas which is a by-product of iron carbonation. The pore volume of the OPC paste corresponding to a pore diameter range of 0.0036-0.05 µm (smallest pores) is higher than that for the iron-based binder as shown in Figure 5-5(b). Since the pores of this range are generally observed as part of the

reaction product, this implies a larger amount of reaction products in the OPC paste, which is unsurprising. The volume of pores corresponding to the size range of 0.05-0.2 µm is higher for the iron-based binder, whereas the amount of larger pores remains relatively the same in both these systems. The larger amount of pores in the transport-controlling pore size range (> 0.05 µm) in the iron carbonate binder indicates the need for studies on refining the pore structure in these novel materials.

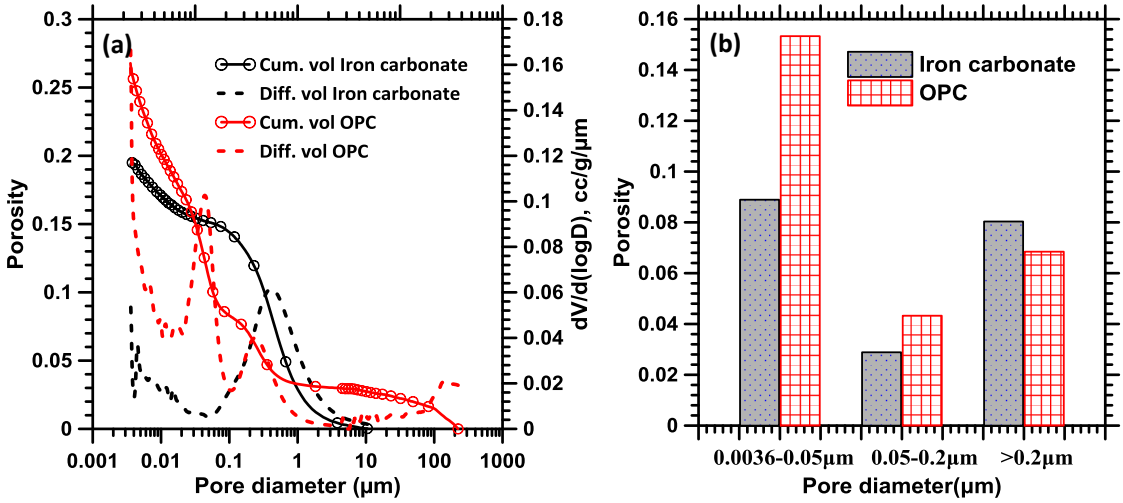

Figure 5-5: Comparison between the pore structures of iron carbonate and OPC paste systems: (a) porosity and the derivative volume intruded as functions of the pore diameter, and (b) pore volume fraction for different pore size ranges. For the iron carbonate binder, the data corresponds to Mixture 2 after 4 days of carbonation and 3 days of air-exposure while the OPC pastes were cured for 28 days in a moist environment.

5.3.1.4 Extracting the Transport Characteristics of Iron-Based Binders from Pore Structure Information

The pore structure features of the iron-based binder systems described in the previous sections are used here to obtain relative indicators of the transport performance of iron-based binders. Transport of moisture and ions (e.g., Cl^-) through mechanisms such as permeability and diffusivity are important in dictating the durability of binders which have the potential to be used in infrastructural construction. The major transport

descriptors extracted from the measured pore structure features in this study are water vapor diffusivity and moisture permeability.

Diffusion of a gaseous phase into a porous media under steady state conditions can be expressed using Fick's first law as shown in Equation 5-3.

$$F_g = -D_e \frac{\partial c}{\partial x} \tag{5-3}$$

Here, F_g is the diffusion flux, D_e is the effective diffusion coefficient of gas in the porous media, c is the concentration and x is the distance. The normalized diffusivity (D') is the ratio of D_e to the gas diffusion coefficient D_a in air. The relationship between the diffusivity and porosity is often expressed using Archie's law (Archie 1942) as shown in Equation 5-4. The exponent m is called the cementation factor determined experimentally by fitting the data for diffusivity and porosity. Different m values ranging from 1.65 to 4.89 are reported in the literature for porous media including rocks of varying morphology and pore structure (Peng, Hu, and Hamamoto 2012).

$$D' = \frac{D_e}{D_a} = \phi^m \tag{5-4}$$

Diffusion of gases in a porous media can be considered to take place primarily through one of the three mechanisms: (i) through the interconnected pore volume, (ii) through the pore surface, or (iii) through the solid matrix material (Iii, Watson, and Mason 1961). In many porous media, diffusion through the pore volume is likely to be the dominant path unless the porosity and permeability are extremely low. There are two limiting cases of such a diffusion process: Knudsen diffusion and normal diffusion. In Knudsen diffusion, collision of gas molecules with the solid pore wall is the dominant mechanism whereas in

normal diffusion the collision between gas molecules is limiting and the gas-wall collision is negligible (Iii, Watson, and Mason 1961). Mean free transport paths determine the type of dominant diffusion mechanism. For Knudsen diffusion to be the limiting case, the mean free path needs to be greater than the average pore diameter in the media, and for normal diffusion to become dominant, the mean free path has to be smaller than the average pore diameter (Iii, Watson, and Mason 1961). The diffusion coefficient of water vapor in air, D_a, is 25 x 10^{-6} m^2/s (Gelderblom et al. 2011; LaManna and Kandlikar 2011). The mean free path of water vapor (λ) at standard temperature and pressure (25° C, 1 bar) is calculated as 0.12 μm using the following equation (Liu 2008; Lide 2003):

$$\lambda = \frac{RT}{\sqrt{2} N_A \pi d^2 p} \tag{5-5}$$

Here, R is the universal gas constant, T is the temperature in K, N_A is the Avogadro constant, d is the diameter of water vapor molecule (0.275 nm) and p is the pressure. The pore structure details of iron carbonate binders from MIP suggests that the average pore diameter for the matrices investigated here are smaller than the mean free path of water vapor. Hence, the Knudsen diffusion can be considered to be the dominant mechanism. The gas diffusion coefficient (D) can be obtained from the Knudsen diffusion coefficient (D_{KA}) and diffusion coefficient in air as (Iii, Watson, and Mason 1961):

$$\frac{1}{D} = \frac{1}{D_a} + \frac{1}{D_{KA}} \tag{5-6}$$

The Knudsen diffusion coefficient (m^2/s) can be expresses as follows (Kast and Hohenthanner 2000):

$$D_{KA} = 48.5 d_a \sqrt{\frac{T}{M}} \tag{5-7}$$

where T is the absolute temperature (K); M is the molecular weight of water (g/mole) and d_a is the average pore diameter (μm). The effective diffusion coefficient (D_e) can then be calculated as (Iii, Watson, and Mason 1961; Ataka, Kato, and Zhu 2005; Carniglia 1986):

$$D_e = \frac{\phi}{\tau} D \tag{5-8}$$

where ϕ is the total volumetric porosity and τ is the tortuosity of the pore structure.

The intrinsic permeability is a measure of relative ease with which a fluid can be transported through a porous media under a potential gradient. Many studies derive permeability of a porous material from MIP data (Swanson 1981; Stanley 1980; Katz and Thompson 1986; Katz and Thompson 1987). Among them, the Katz-Thompson model is widely used and is employed here to evaluate the intrinsic permeability of iron-based binder. For a medium with a characteristic length scale L_c, intrinsic permeability (k) can be expressed as,

$$k = \frac{1}{226} \left(\frac{\sigma_{eff}}{\sigma_0}\right) (L_c)^2 \tag{5-9}$$

Here the term $(\sigma_{eff} / \sigma_0)$ is the normalized electrical conductivity of the medium. (1/226) is a constant developed by Katz and Thompson for rock specimens. The Katz-Thompson theory is based on the assumption the pores are cylindrical. Previous studies have used the pore structure data (extracted from MIP or image analysis techniques) to derive the permeability of porous media (Swanson 1981; Stanley 1980; Katz and Thompson 1987; Neithalath, Sumanasooriya, and Deo 2010; Sumanasooriya and Neithalath 2011). Katz and Thompson simplified Equation 10 to include only

characteristic length terms extractable from MIP to predict the permeability, which is given as (Katz and Thompson 1987):

$$k = \frac{1}{89}(L_{\max})^2 (\frac{L_{\max}}{L_c}) \phi S(L_{\max}) \quad (5\text{-}10)$$

Here, L_C is characteristic length or the pore diameter corresponding to threshold pressure (the pressure corresponding to point of inflection in the rapidly rising range of the cumulative mercury intrusion curve) (Katz and Thompson 1987; Webb 2001), L_{max} is the pore diameter at which the hydraulic conductance is maximum; ϕ is the porosity and $S(L_{\max})$ is the fraction of volume of connected pore space composed of pores of size L_{max} or larger.

The normalized water vapor diffusivity and moisture permeability as a function of carbonation duration is shown in Figure 5-6(a). With a reduction in porosity and pore sizes and a consequent increase in tortuosity as a result of increased carbonation, both the normalized diffusivity and permeability decrease as expected. The reduction in diffusivity and permeability follows the same trend as the reduction of porosity with increase in carbonation duration for the binder as shown in Figure 5-4. Figure 5-6(b) shows the normalized diffusivity-porosity relationship for the iron-based binder. The diffusivity values are calculated from the porosity data by incorporating the effective diffusion coefficient values (D_e) (Equation 5-8) in Equation 5-4. The value of the exponent m in Equation 5-4 is obtained as 3.18 through a non-linear regression fit to Archie's law with 95% confidence bounds. The value of m is in the realistic range of 1.6 (red brick) to 4.89 (mudstone) as reported elsewhere (Peng, Hu, and Hamamoto 2012). It has also been reported that a smaller m value correlates to larger

pores indicating higher diffusivity due to the lower tortuosity and increased pore connectivity. The relationship between porosity and moisture permeability is shown in Figure 5-6(c). As expected, permeability increases as the porosity increases—note the conventional power-law permeability-porosity relationship that is seen to be valid for the iron-based binder. It should be noted that the value of permeability of the iron-based binder after 4 days of carbonation ($k = 2.5 \times 10^{-16}$ m^2) is significantly higher than that of a 28-day moist-cured hardened cement paste ($k = 6.17 \times 10^{-20}$ m^2) (Goto and Roy 1981). This is primarily due to larger pore sizes in iron carbonate binders even though the total pore volumes in the iron-based binder system are lower. However, it should also be considered that the transport characteristics of concretes (containing aggregates in large volume fractions along with the binder) are more important in application scenarios. The lower volume of the paste (or the binding fraction) in concretes result in the paste properties being less dominant as compared to those where pure paste is used.

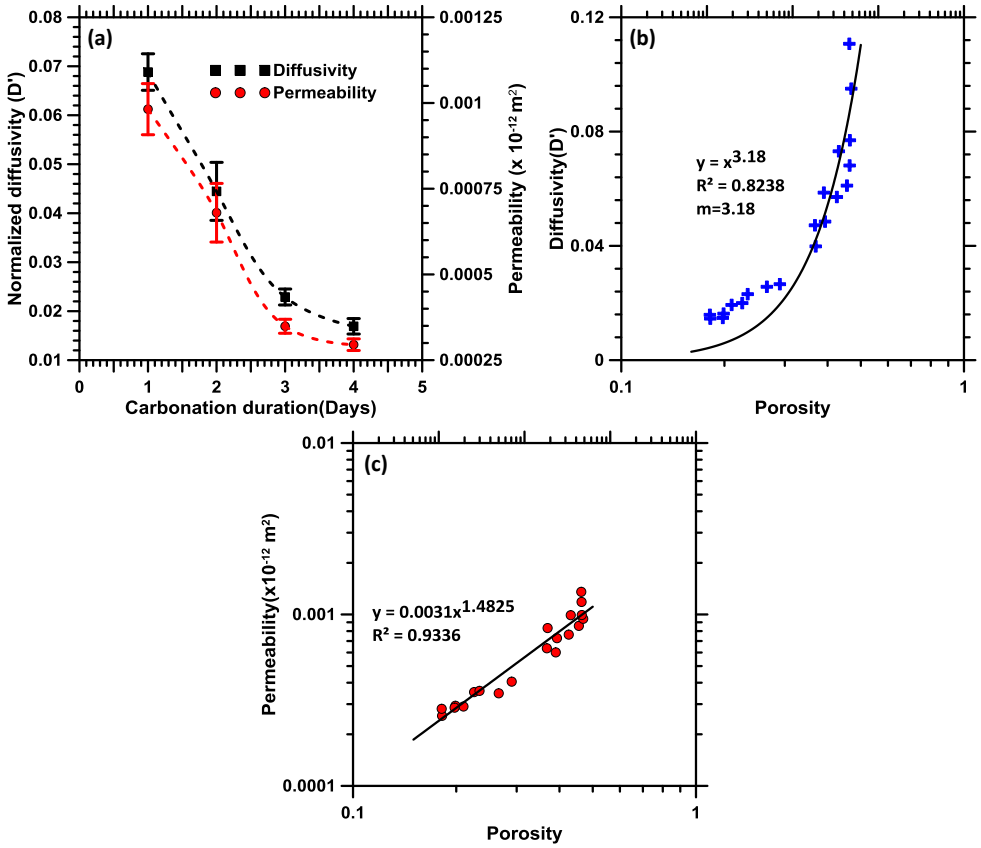

Figure 5-6 (a): Effect of carbonation duration on diffusivity and permeability; (b) diffusivity-porosity relationship (Archie's law); (c) permeability-porosity relationship for the iron-based binder. All the data points correspond to those of Mixture 2.

5.3.2 Microstructural Evaluation

5.3.2.1 Reaction product morphology and composition

The reaction products formed from iron carbonation and the influence of source materials have been described in detail (Das, Souliman, et al. 2014). In this study, the morphological and compositional features of these binders are outlined. Compositional analysis using both secondary electron (SE) imaging and backscattered electron (BE) imaging is described here. There are several publications that report microstructural quantification of cementitious systems using SEM/EDS (Thaulow, Jakobsen, and Clark 1996; S. Wang, Baxter, and Fonseca 2008; H. Xu and Van Deventer 2002; Mijno et al.

2004; Scrivener 2004). But, it should be noted that the main objective here is to identify the elements present in the reaction product since SEM/EDS is effort-intensive for the quantification of reaction product composition, especially for heterogeneous microstructures such as the ones discussed here (Scrivener 2004). Hence, in this study the microstructural analysis is restricted to identification and distribution of different phases in the binder system.

Figure 5-7 (a) and (b) show the morphology of the reaction products observed on a fracture surface of the iron carbonate binder. The microstructure is heterogeneous, containing angular iron particles, spherical fly ash particles and porous reaction products. Reaction product film formation is observed on the surface of iron particles. Some reaction product formation is noted on the surface of the fly ash particles as well. A few small cracks are also detected. Figure 5-8(b) shows the EDS spectrum of the reaction product formed on the surface of the iron particle shown in Figure 5-8(a). The results indicate that the final reaction product contains iron, calcium, aluminum, and silicon representing an iron-oxalate-carbonate complex incorporating silica. This confirms what has been shown in the previous chapter. EDS spectrum is also reported for the non-carbonated sample (Figure 5-8 (c)) and is shown in Figure 5-8(d). The microstructure along with the composition is significantly different from that of the carbonated system. Large, unreacted iron particles are observed with no detectable reaction product formation on the surface. Only Fe, C and Si are present in EDS spectra. This confirms that no binding product formation occurs in the absence of dissolved CO_2.

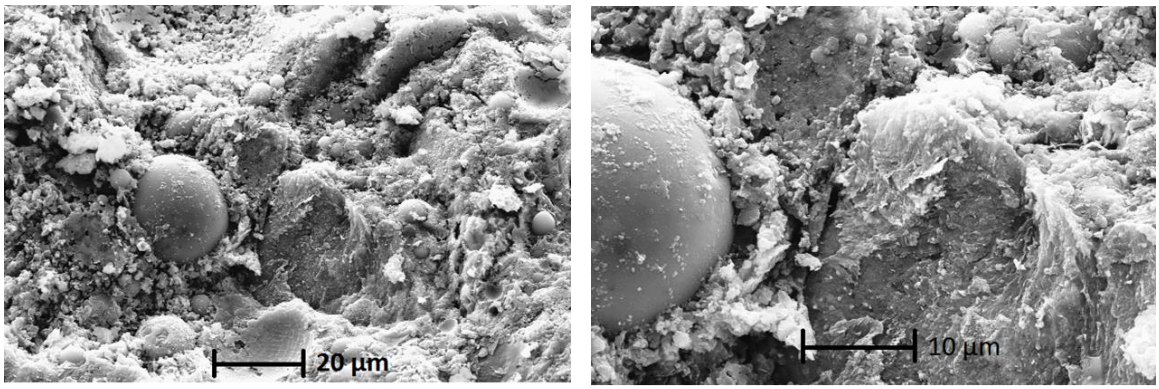

Figure 5-7: SE images of iron carbonate binder (Mixture 2) after 4 days of carbonation for and air-exposure for 3 days.

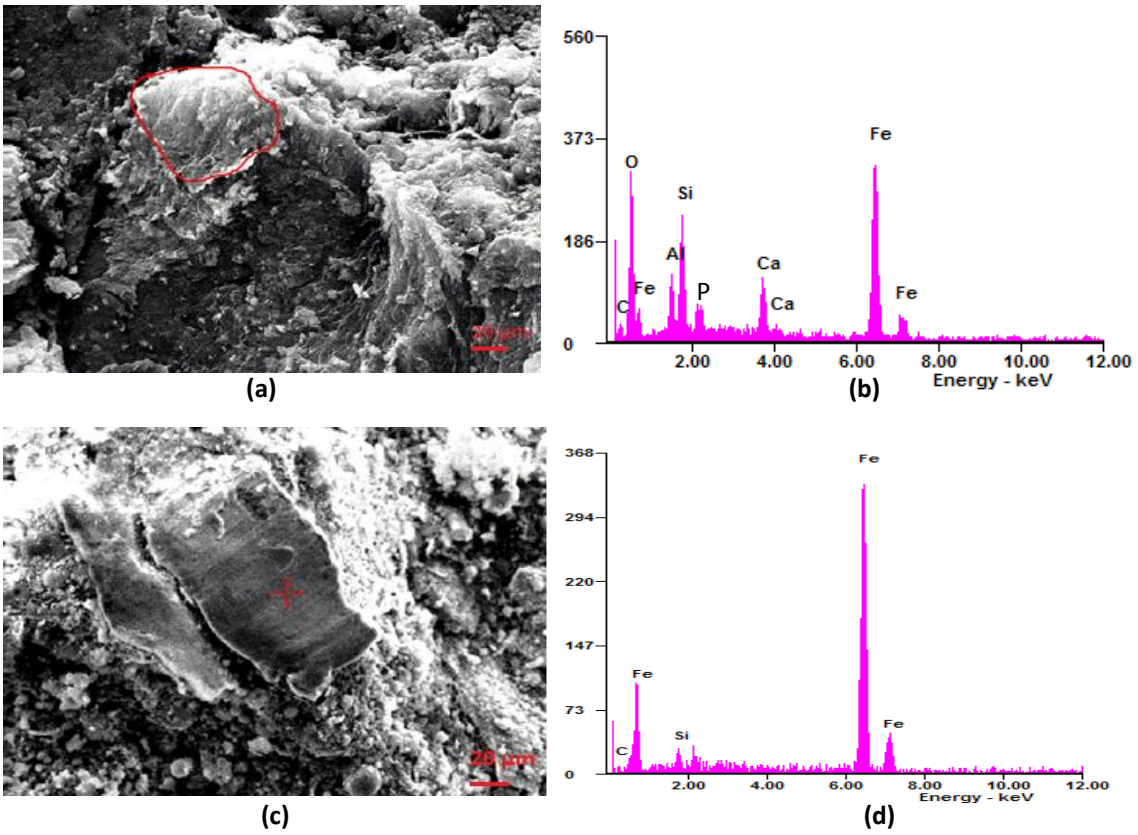

Figure 5-8: (a) SE image of Mixture 2 after 4 days of carbonation and 3 days of air-exposure, (b) EDS spectrum of area shown in (a); (c) SE image of Mixture 2 after only 3 days of air curing (no carbonation), (d) EDS spectrum at location shown in (c)

Secondary imaging techniques essentially only provide the surface morphology of the region investigated. The minimum effort to prepare a sample and the ease of interpreting the topographical feature makes secondary imaging techniques very attractive. However, the roughness of the fracture surface renders quantitative analysis virtually impossible. A flat surface is required for more accurate compositional analysis. A suitable combination of grinding and polishing has been carried out in order to achieve desired surface flatness. Figure 5-9(a) and (b) show the backscatter electron (BE) images of polished surfaces of the iron carbonate binder along with representative EDS spectra of the points indicated in the images. The elemental composition corresponding to the EDS map of Figure 5-9(a) indicates that the bright particles are the iron particles. These particles are highly angular as can be seen from the micrograph. The location chosen for EDS analysis shown in Figure 5-9(b) is on the relatively dense reaction product formed around the iron particle. EDS confirms the presence of iron as the major component, followed by silica, aluminum, and calcium rich components.

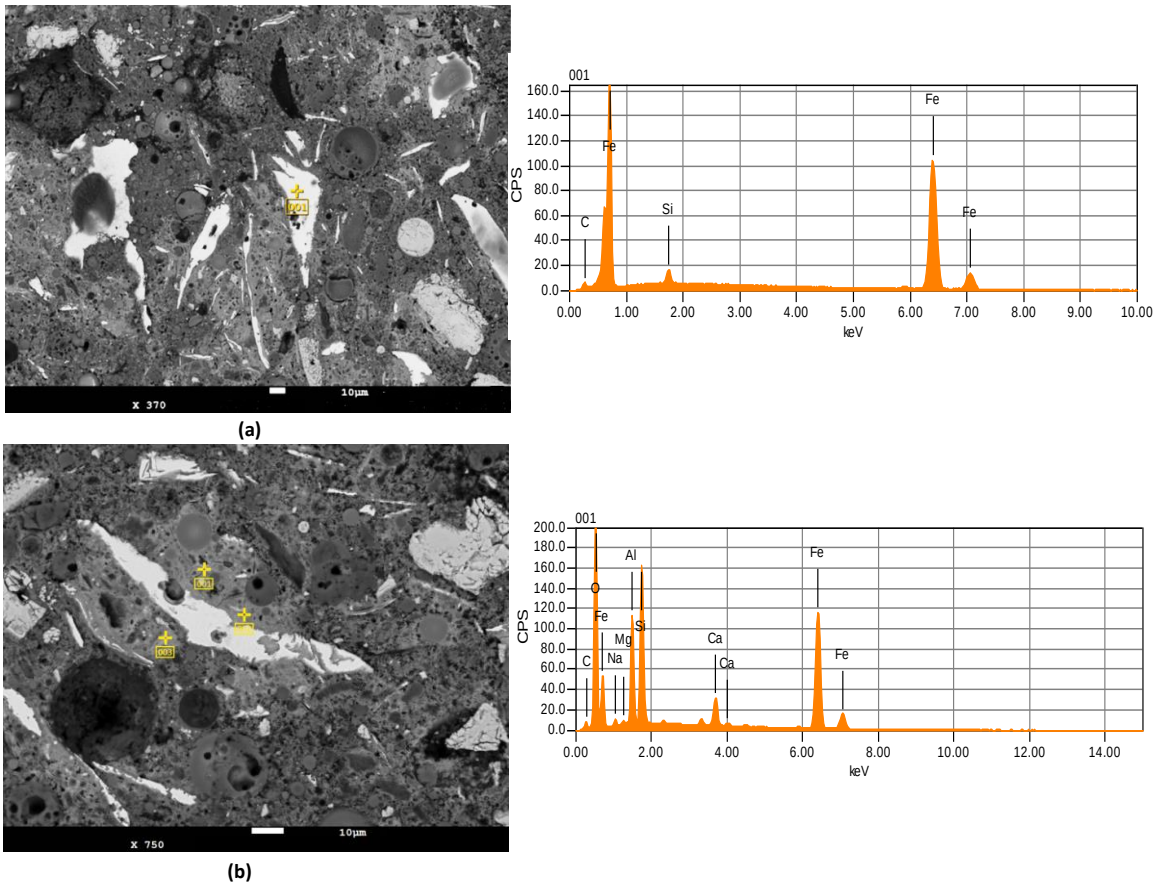

Figure 5-9: (a) and (b): BE images of Mixture 2 at two different locations after carbonation for 4 days and air curing for 3 days. The representative EDS spectra of the points marked in the micrographs are shown on the right.

5.3.2.2 Elemental maps

Elemental maps were acquired using the EPMA to better understand the spatial distribution of the reaction products. Maps were acquired of iron, silicon, aluminum, calcium, and carbon. The results are shown in Figure 5-10. The brighter the color, the higher the concentration of the element shown for each map. Iron is observed at locations away from the particles also, aided by the organic dissolution agent. The distribution of carbon is fairly uniform, except in regions occupied by the unreacted iron particles and the fly ash particles where it shows a higher concentration. This indicates that the

reaction products which are formed away from the iron particles are also complex iron carbonates, although the stoichiometry could be locally different (this is not discounting the presence of carbon from the calcium carbonates added in the matrix also). The circular black regions in the iron elemental map indicate unreacted, rounded fly ash particles which is confirmed by the presence of high concentrations of Si and Al. The distribution of Calcium is also shown to be mostly uniform. This is likely due to the small size (0.7 μm) of the calcium carbonate (limestone) particles used in the matrix. The utilization of limestone in reaction product formation has also been confirmed through thermo-gravimetric analysis in the previous chapter.

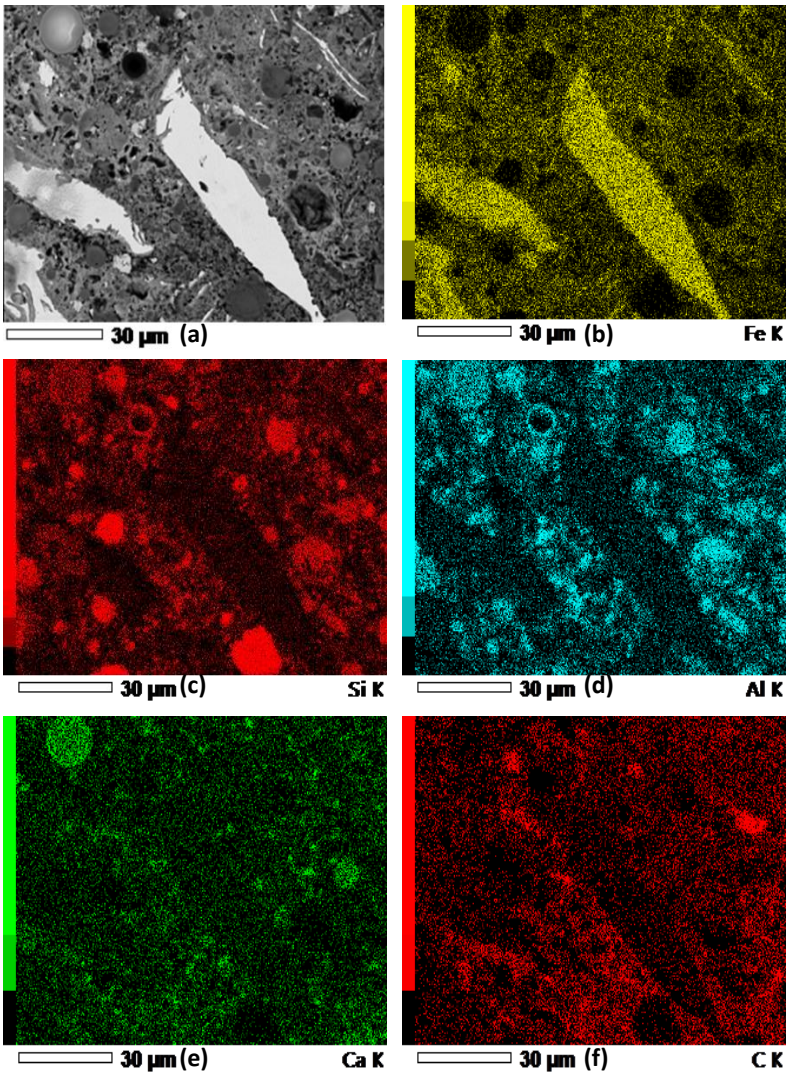

Figure 5-10: (a) A backscattered electron micrograph of the iron carbonate binder (shown in the upper left) along with EDS elemental maps of: (b) Fe, (c) Si, (d) Al, (e) Ca, and (f) C.

5.3.2.3 Using BSE images to determine porosity

Image analysis was carried out on backscattered electron micrographs to obtain the area fraction of porosity. The images with significant edge effects were discarded and 5 images are thus obtained at different resolutions. The chosen images are processed and analyzed using ImageJ©, a freely available image analysis software, using procedures already established in (Neithalath, Sumanasooriya, and Deo 2010; "Influence of Aggregate Size and Gradation on Acoustic Absorption of Enhanced Porosity Concrete"

2004). The grey-scale images were converted to binary image by thresholding to separate the solid and the pore phases. The threshold limits were chosen based on grey level histogram. Figure 5-11(a) shows a representative original grey scale BSE image and Figure 5-11(b) shows the thresholded binary image where darker phase represents the pore phase. Five such images for the mixture carbonated for 4 days and subsequently air cured for 3 days were used to determine the total pore area. The average area fraction of porosity obtained was 9.48%, with a standard deviation of 2.5%, which is lower than that obtained from mercury intrusion porosimetry (MIP) (about 19%). This is expected because much lower pore sizes can be interrogated using MIP (ranging between 10 microns and 0.003 microns). It has also been recognized that a large number of images need to be analyzed to obtain statistically significant figures for the pore structure features (Scrivener 2004).

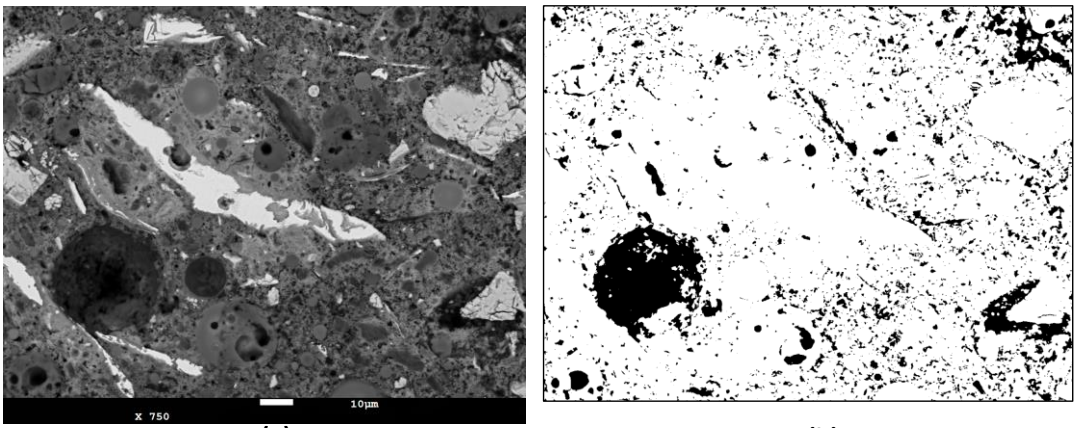

Figure 5-11: (a) A representative BSE image of an iron carbonate matrix (carbonated for 4 days, and cured in air for 3 days), and (b) thresholded greyscale image showing the solid phase (bright) and pore phase (dark).

5.4 Conclusions

Fundamental characterization of pore- and micro-structure of a novel complex binder system based on the carbonation of metallic iron powder has been discussed in this study.

With metallic iron powder (sourced as a waste/by-product material) used as the major component, minor components such as fly ash, metakaolin, limestone and an organic acid were used in different proportions to impact the reaction product formation as well as rheological characteristics of this binder. The pore- and micro-structural properties of the best-performing (based on compressive strength) binder system were reported in this study.

Increasing the carbonation duration from 1 to 4 days significantly reduced the total pore volume in the iron carbonate binder as determined by MIP. This was in turn reflected in the compressive strength of the binders, while the critical pore size remained relatively unchanged. However, it was observed that the fraction of the larger pores and the average pore size significantly reduced with increasing carbonation duration. A comparison with the pore structure of 28-day cured OPC pastes showed that the overall pore volume was lower in iron carbonated binders, however, the critical pore sizes were larger. The pore structure features (porosity, average pore size, and tortuosity) were used to theoretically determine the water vapor diffusivity through a consideration of Knudsen diffusion, and moisture permeability using a modified version of the Katz-Thompson equation. The implementation of Archie's law to the normalized diffusivity-porosity relationship yielded a cementation factor of around 3 for the iron carbonate binders, which is close to those of many porous engineering materials. The porosities and moisture permeabilities of iron carbonate binders were found to be well correlated by a power-law expression.

Secondary and backscattered imaging revealed many of the important features of the microstructure of this novel binder material. The influence of carbonation on the reaction product formation on iron particle surfaces was established. A dense, heterogeneous

microstructure was obtained after carbonation. The reaction product analysis using EDS showed the presence of iron, carbon, silicon, aluminum and calcium, indicating that the reaction product is a complex carbonate which was quantified in an earlier study using thermogravimetric analysis.

Chapter 6 Fracture Response of Iron-based Novel Binder

6.1 Introduction

This chapter reports on fracture response of the novel Iron Carbonate binder and draws a comparison with hardened cement paste. One of the major drawbacks of ceramic matrices in general and cementitious matrices in particular relate to their low toughness. In addition, these low-toughness ceramics lose a significant portion of their strength because of service-related damage such as crack growth under static load or cyclic fatigue. Thus, enhancing the toughness of these materials contributes to minimization and control of strength loss. In the synthesis of the iron-based binder, metallic iron powder is carbonated only to a small fraction (necessitated by limitations in reaction kinetics (Das, Souliman, et al. 2014)), which results in the presence of large amounts of residual metallic powder in the microstructure. The presence of this phase, a significant fraction of which is elongated, will likely render notable increase in the toughness of this binder because of the energy dissipation by plastic deformation (Trusty and Yeomans 1997) imparted by the metallic particulate phase. In addition, the matrix contains other processing additives including harder fly ash particles, softer limestone particles, and ductile clayey phases which influence the overall fracture performance of the novel binder significantly. The performance of glass fiber reinforcement in iron-based and OPC binder systems are also explored so as to investigate the synergistic influence of unreacted metallic iron particles in the matrix and the fiber reinforcement on the properties of interest. Center-point cyclic flexural tests on single-notched beams are carried out to determine the critical stress intensity factor (K_{IC}^{S}) and the critical crack tip opening displacement ($CTOD_C$) using the well-accepted two parameter fracture model

(TPFM). The differences in fracture behavior between the iron-based binder and the traditional OPC binder are also quantified using R-curves. Additionally, the use of digital image correlation (DIC) is explored as a non-contact means of extracting the fracture parameters of iron-based binders.

6.2 Experimental program

6.2.1 Materials, Mixtures and Specimen Preparation

The major starting material used in this study is a waste metallic iron powder with a median particle size of 19.03 μm, obtained from an industrial shot-blasting operation. The iron particles are elongated and angular in shape; while influencing the rheological properties of the fresh mixture, angular shape also provides benefits related to increased reactivity owing to the higher surface-to-volume ratio of the particles. Some minor ingredients such as Class F fly ash and metakaolin conforming to ASTM C 618, and limestone powder (median particle size of 0.7 μm) conforming to ASTM C 568 were also used in the binder synthesis (Das, Souliman, et al. 2014). Fly ash provides a silica source for the reactions (to potentially facilitate iron silicate complexation (R. Kumar et al. 1990)), while the fine limestone powder provides nucleation sites. Metakaolin imparts cohesiveness to the paste mixtures because of its clayey origins. In the process of iron carbonation, water only serves as an agent of mass-transfer and does not as such chemically participate in the reactions. Minimization of water demand, yet keeping the consistency and cohesiveness of the mixture was achieved through the use of metakaolin. An organic reducing agent/chelating agent for metal cations (oxalic acid, in this case) was also used. Commercially available Type I/II OPC conforming to ASTM C 150 was used to prepare conventional cement pastes that were used as the baseline system to compare

the properties of the novel iron-based binder systems. The chemical compositions of OPC, fly ash and metakaolin can be found in our previous publications (Vance et al. 2013; Das, Aguayo, et al. 2014). The iron powder is coarser than all other ingredients used here. While the quantified data presented in this study could vary depending on the fineness of the iron powder, the general trends and mechanisms remain the same.

The powder fraction of the iron-based binder mixture used in this study consists of 60% iron powder, 20% fly ash, 8% limestone, 10% metakaolin, and 2% organic acid by mass. This combination demonstrated the highest compressive strength and lowest porosity among a series of trial mixtures prepared as part of material design studies (Das, Souliman, et al. 2014). The mixing procedure involves initial dry mixing of all the starting materials and then adding water to obtain a uniform cohesive mixture. A mass-based water-to-solids ratio $(w/s)_m$ of 0.24 was used to attain a cohesive mix, which also was arrived at based on several preliminary studies (Das, Souliman, et al. 2014). Since the carbonation process of iron does not incorporate water in the reaction products and it is merely an agent of mass-transfer, the $(w/s)_m$ used is primarily based on the criteria of obtaining desired workability.

Prismatic specimens of size 127 mm (length) x 25.4 mm (depth) x 25.4 mm (width) were prepared in polypropylene molds and immediately placed inside clear plastic bags filled with 100% CO_2 in room temperature inside a fume hood. The samples were demolded after 1 day of carbonation in order to attain enough strength so as to strip the molds without specimen breakage. After demolding, the beams were placed again in a 100% CO_2 environment for another 5 days. The bags were refilled with CO_2 every 12 hours or so to maintain saturation. After the respective durations of CO_2 exposure, the samples

were placed in air at room temperature to allow the moisture to evaporate for 4 days. These CO_2 and moisture exposure durations are considered in this study because the mechanical properties demonstrated insignificant changes beyond these curing times. It can be safely assumed that, for the specimen sizes evaluated here, these durations result in kinetic carbonation limits, and further carbonation cannot be achieved without changes in process conditions (e.g., temperature or pressure). Companion OPC mixtures of the same size as mentioned above were prepared with a water-to-cement ratio (w/cm) of 0.40, which is common for moderate-strength concretes in many buildings and infrastructural applications. The OPC beams were demolded after 1 day and were kept in a moist chamber (>98% RH and 23±2 ^{o}C) for a total of 28 days. The fiber-reinforced binders were prepared by adding 0.5% and 1.0% glass fibers (25 μm diameter and 10 mm long) by volume to the blends while mixing. The fiber reinforced iron-based and the OPC binders were cured in the same way as their non-reinforced counterparts.

6.2.2 Determination of Flexural Strength and Fracture Parameters

The flexural strengths of both iron-based and OPC binders were determined using standard center-point loading as per ASTM C293/293M-10, on beams having a span of 101.6 mm. The fracture properties, viz., the critical stress intensity factor (K_{IC}^{S}) and the critical crack tip opening displacement ($CTOD_C$), were determined from three-point bend tests on notched beams using the two-parameter fracture model (TPFM) (Y. Jenq and Shah 1985; Shah 1995a) as shown in Figure 6-1. For each mixture four replicate beams were tested. The notch depth was 3.8 mm (corresponding to a notch depth-to-beam depth ratio of 0.15). The beams were tested in a crack mouth opening displacement (CMOD)-

controlled mode (CMOD acting as the feedback signal) during the loading cycles and in a load-controlled mode during the unloading cycles.

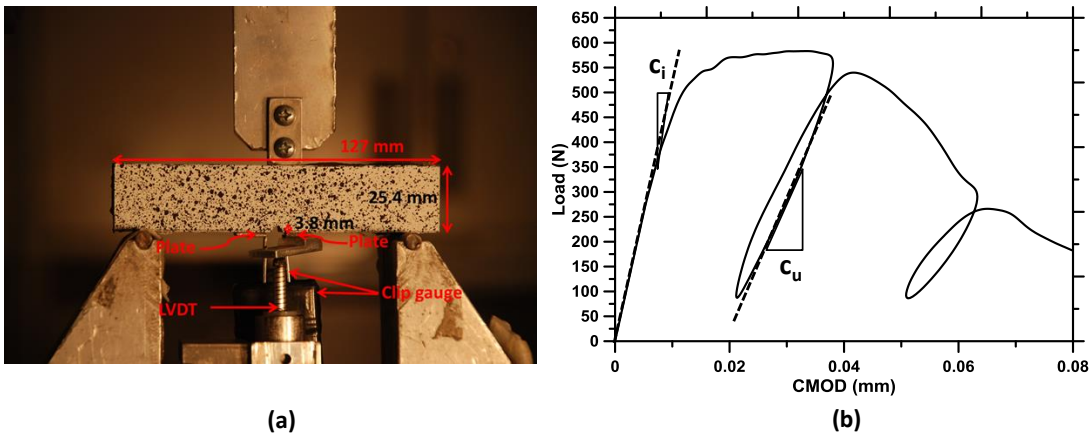

Figure 6-1: (a) Experimental setup for the TPFM test, and (b) a typical load-CMOD plot showing the loading and unloading compliances

The TPFM involves the use of the loading and unloading compliances, peak load, specimen and notch geometries, and a geometry correction factor, to determine the values of K_{IC}^{S} and $CTOD_C$. A typical load-CMOD plot is shown in Figure 6-1(b) with the loading and unloading compliances. The steps used in TPFM to determine the fracture parameters and the relevant mathematical operations are adequately described in many publications (Y. Jenq and Shah 1985; Shah 1995a; Rehder, Banh, and Neithalath 2014; Y. S. Jenq and Shah 1985; Mobasher 2011).

6.2.3 Scanning Electron Microscopy (SEM)

Microstructural analysis was carried out using a JEOL JXA-8530F Hyperprobe (Electron Microprobe). Small rectangular pieces (10 x 10 mm in size) were used for microscopic observations. The samples were from the interior portions of the beams, and it was shown in a companion study that the CO_2 curing regimen adopted in this study resulted in carbonation across the entire depth for samples of comparable or larger sizes (Das,

Souliman, et al. 2014). Prior to mounting, the sample was ultrasonically cleaned and rinsed with ethyl alcohol and dried with compressed air spray to remove debris from sectioning/handling. After drying, the sample was placed into a 32 mm two-part mounting cup, filled with a room-temperature setting epoxy, and subjected to 95 kPa of vacuum for 5 minutes to remove entrapped air. After hardening, the sample was polished using 600 and 800 grit Silicon Carbide (SiC) abrasive discs, and further ground using 3 μm and 1 μm diamond paste. Final polishing was done with a 0.04 μm colloidal silica suspension before they were placed under the electron gun of JEOL JXA-8530F Hyperprobe.

6.2.4 Digital Image Correlation (DIC) for the Determination of Fracture Properties

DIC is a non-contact optical method to analyze digital images to extract the full displacement field on a specimen surface (Das, Aguayo, et al. 2014; Krottenthaler et al. 2013; Rossol et al. 2013; Yuan et al. 2014; Ghorbani, Matta, and Sutton 2014; Tominaga et al. 2014; Yates, Zanganeh, and Tai 2010; Nunes and Reis 2012a; Roux, Réthoré, and Hild 2009; Lin and Labuz 2013; Sutton, Orteu, and Schreier 2009). Here, the beam surface was painted with random black and white speckles to improve image correlation. A charge coupled device (CCD) camera was used to record images every 5 seconds. After the collection of images during the entire loading-unloading sequence as described in the previous section, a suitable analysis region was chosen as shown in Figure 6-2(a) and image correlation performed to obtain the displacement fields on the specimen surface.

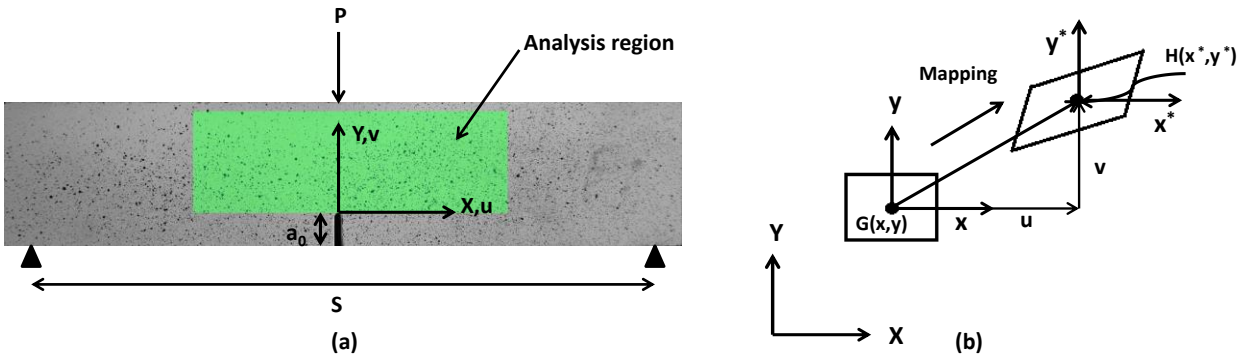

Figure 6-2: (a) Three-point bend specimen showing the analysis region for displacement field mapping, and (b) schematic of mapping of points in DIC

In the DIC method, the correlation between the subsets of images from the deformed and undeformed state is determined in order to calculate the displacement fields. A point (x,y) in the undeformed state is mapped with a point (x^*,y^*) in the deformed state as shown in Equation 6-1 and Figure 6-2(b).

$$x^* = x + u(x,y)$$
$$y^* = y + v(x,y) \qquad [6\text{-}1]$$

The horizontal (u) and vertical (v) displacement fields in the surface analysis region are then computed by minimization of the correlation coefficient (C) which can be defined as (Yates, Zanganeh, and Tai 2010):

$$C = \frac{\sum [G(x,y) - H(x^*,y^*)]^2}{\sum G^2(x,y)} \qquad (6\text{-}2)$$

Here, G and H are grey scale light intensities corresponding to the point in the subset. From the results of u-displacement fields, the crack tip opening displacement (CTOD) and the crack extension (corresponding to the load and CMOD pertaining to that time step) can be obtained as described later in the study.

6.3 Results and discussions

6.3.1 Microstructure of Iron Carbonate Binders

As discussed earlier, microstructural analysis was carried out on polished iron carbonate binder samples to understand the material morphology and the impact of the material microstructure on its properties. The images shown here are for specimens cured for 6 days in a CO_2 environment. Figure 6-3(a) shows the general appearance of the material microstructure with bright (high density) iron particles along with the reaction products and pores. The unreacted iron particles are, in general, elongated. The implications of these unreacted particles are discussed in the forthcoming section on fracture properties. The dense reaction products (the grey phases in the microstructure) are formed from the carbonation of smaller iron particles and their complexation with the other minor ingredients in the mixture, which was confirmed from a thermal analysis study to be belonging to the carbonate-oxalate-cancrinite group (Das, Souliman, et al. 2014). A higher magnification image is shown in Figure 6-3(b) where an elongated iron particle and the surrounding microstructure containing spherical fly ash particles are shown. The dark regions in this microstructure are the pores, the volume fraction of which was found to be comparable to those of OPC-based systems as detailed in an extensive quantification work (Das, Souliman, et al. 2014). Dissolution of iron into the matrix from the particle and the formation of reaction products is shown in Figure 6-3(c).

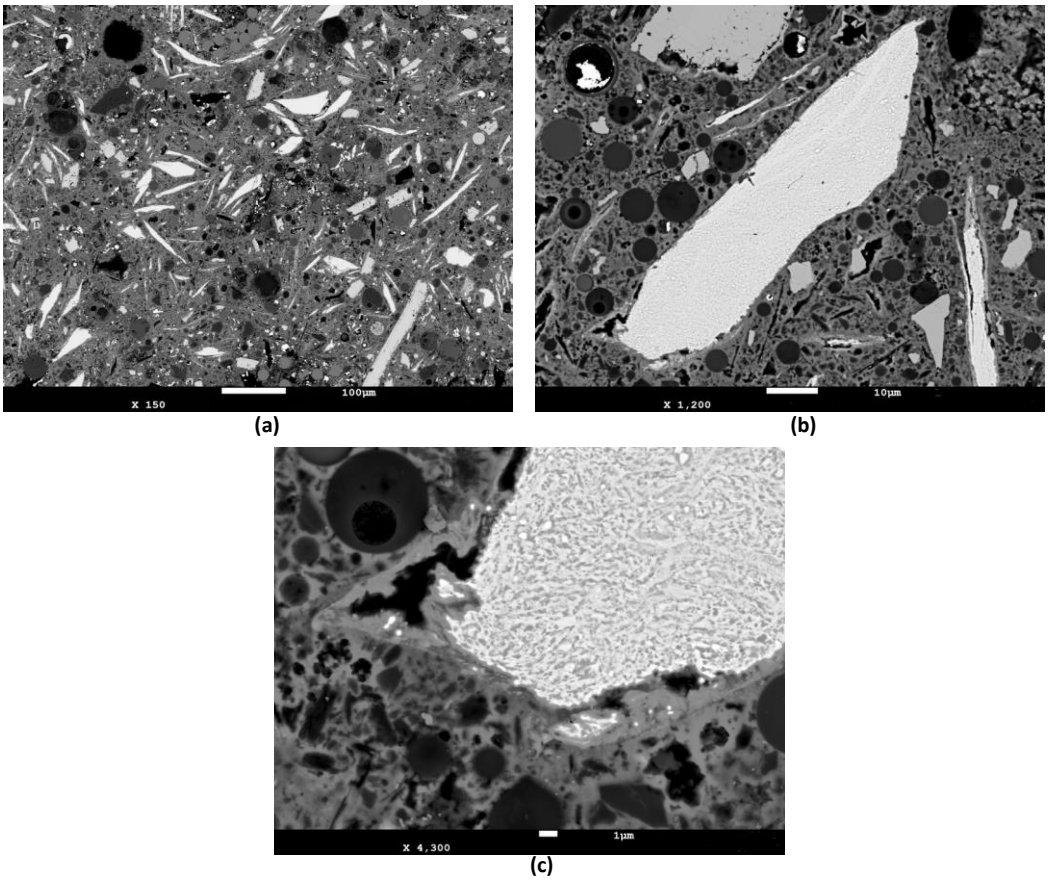

Figure 6-3: Microstructure of iron-based binder: (a) lower magnification (150X) image (scale bar corresponds to 100 µm); (b) higher magnification (1200X) image showing an elongated iron particle and the surrounding regions (scale bar corresponds to 10 µm); and (c) showing dissolution of Fe^{+2} from iron particle into the surrounding matrix (4300X) (Scale bar corresponds to 1 µm)

6.3.2 Flexural Strength

The compressive strengths and the reaction product quantification in iron carbonate binder systems have already been reported in detail (Das, Souliman, et al. 2014; Das, Stone, et al. 2014). Here, the flexural strengths of plain and fiber-reinforced iron-based binder systems are reported along with their comparison to OPC systems. Figure 6-4 shows the flexural strengths of plain and fiber-reinforced iron carbonate binders after 6 days of carbonation and the corresponding OPC pastes after 28-days of hydration for comparison. The results presented here suggest that the iron carbonate binder is about

four-to-six times stronger than the traditional OPC paste in flexure. This can be attributed to a combination of the stronger carbonate matrix along with the presence of unreacted iron particles in the microstructure as shown in Figure 6-3. Both the binders are observed to exhibit increases in flexural strength with inclusion of fibers, with the iron-based system showing a much pronounced increase. While it has been proved that addition of glass fiber in OPC system results in increase in toughness with only minor increase in flexural strength (Sivakumar and Santhanam 2007; Altun, Haktanir, and Ari 2007; Kwan, Ramli, and Cheah 2014), the iron-based binder shows a different trend where the flexural strength is increased significantly with the incorporation of glass fibers into the matrix. An enhancement in flexural strength of about 50% is observed for the iron-based binder when 0.5% glass fibers by volume is incorporated, but further fiber addition does not appear to correspondingly enhance the material behavior. Such an observation is noticed for the Mode I fracture toughness of these binder systems also, and the explanation is provided in a later section.

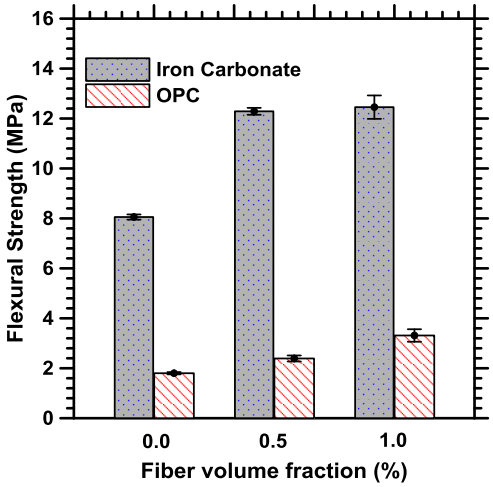

Figure 6-4: Comparison of flexural strength of 6-day carbonated iron Carbonate sample and OPC paste after 28 days for different fiber dosage

6.3.3 Fracture of Notched Beams and Fracture Parameters

In this study, the fracture parameters of the iron-based and OPC binder systems are studied using the TPFM. TPFM idealizes the pre-peak non-linear behavior in a notched specimen through an effective elastic crack approach. The beam sizes and the notch depth are same for both the systems, thereby rendering the comparisons of the fracture parameters free of size effects. The effect of fiber volume fractions on the fracture parameters are also evaluated in conjunction with the response of the matrix phase.

6.3.3.1 Cyclic Load-CMOD response of notched beams

The representative load-CMOD responses are shown in Figure 6-5 for the iron-based binder and the companion OPC-based binder with and without fiber reinforcement. Figure 6-5(a) plots the load-CMOD response for the control OPC and iron-based binder (without fiber reinforcement), which clearly depicts the fundamental differences in the flexural response of these matrices. The significantly higher peak load and improved post peak response of the iron-based binder as compared to control OPC binder can be attributed to the presence of unreacted metallic iron particles (Figure 6-3) which are inherently strong and ductile. It needs to be noted that the iron-based binder contains higher amounts of larger pores (average size > 0.2 μm) even though the total pore volumes are comparable (Das, Stone, et al. 2014), and consequently, demonstrates compressive strength that is slightly lower than that of the OPC binder (Das, Souliman, et al. 2014). However, the presence of strong and ductile phases in the microstructure dominates the flexural response, as shown earlier. The incorporation of fibers in an OPC matrix makes it ductile as observed from the post-peak response and the larger CMODs for the fiber reinforced systems as opposed to the unreinforced materials shown in Figure

6-5 (b) and (c); a response that is well documented. Both the peak load and the residual load are significantly higher for the iron carbonate binder, with and without fiber reinforcement, depicted in Figure 6-6(a) and (b). The incorporation of glass fibers enhances the peak load of the iron-based binder much more than it does to the OPC binder, signifying the synergistic impact of the iron carbonate matrix (including the unreacted iron particles) and fiber on the flexural response. The residual load for the control binders were measured at a CMOD value of 0.12 mm whereas a CMOD value of 0.25 mm was chosen for the binders with fiber reinforcement. The residual loads provide an indication of the crack-tolerance and the post-peak response of these systems.

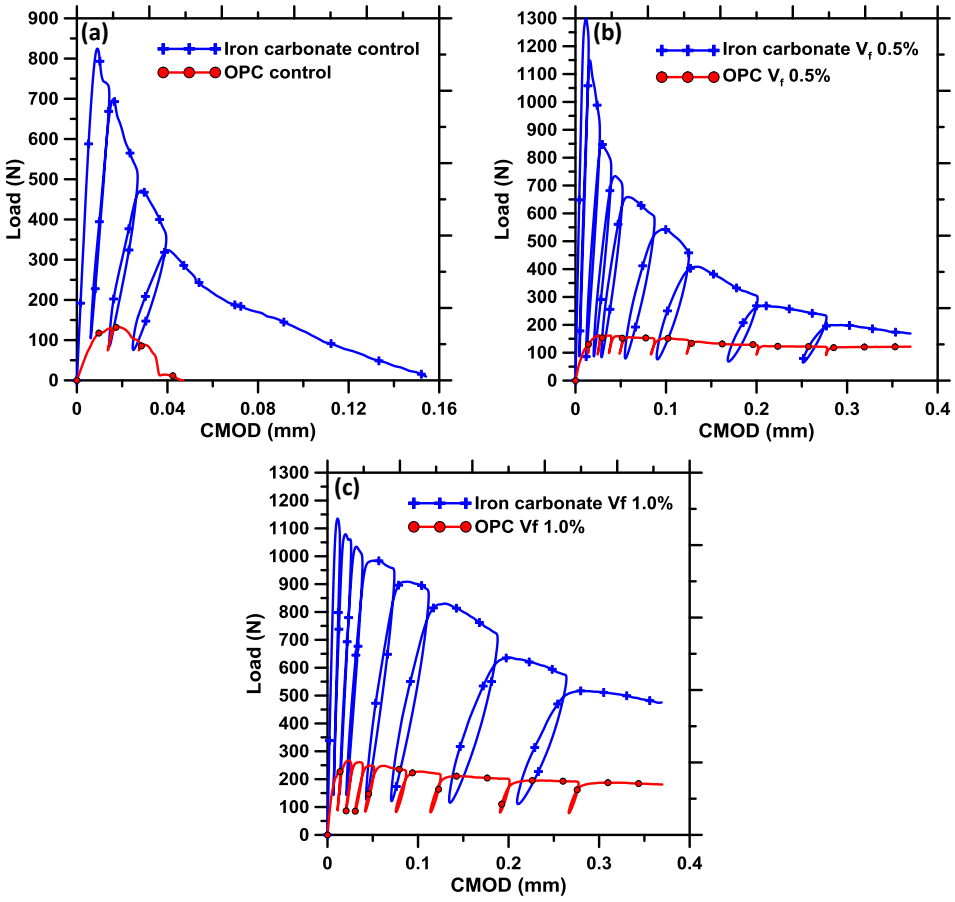

Figure 6-5: Representative Load-CMOD responses for iron carbonate binder and comparison with OPC paste for (a) Control; (b) 0.5% and (c) 1.0% fiber volume fraction

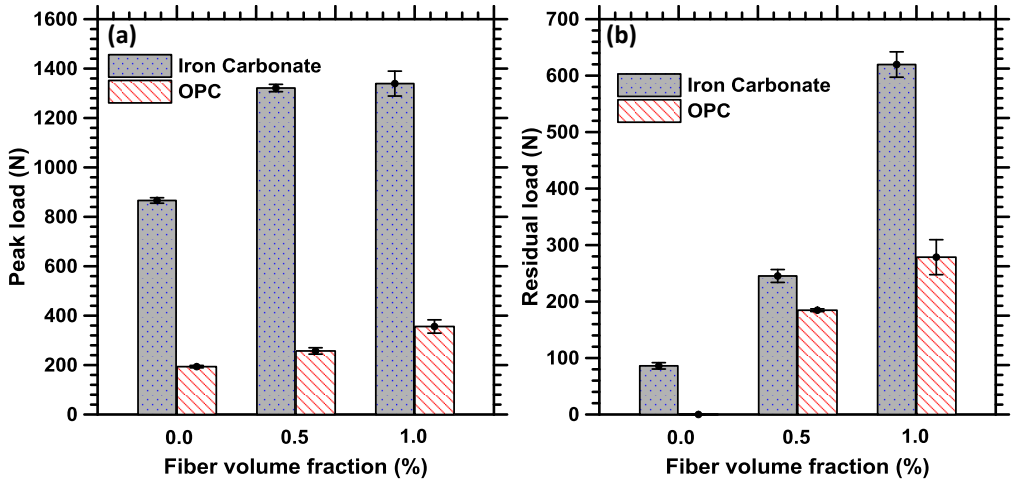

Figure 6-6: (a) Peak load, and (b) residual load of OPC and iron carbonate binders as a function of fiber volume fraction

6.3.3.2 K_{IC}^{S} and $CTOD_c$ of iron carbonate composite systems and their comparison to OPC-based systems

Figure 6-7 reports the two major fracture parameters-fracture toughness (K_{IC}^{S}) and critical crack tip opening displacement ($CTOD_C$) derived using TPFM for both the binders, as a function of the fiber volume fraction. Figure 6-7(a) shows that the fracture toughness values of the iron-based binders are much higher than those of the control OPC binders (~ 5-7 times) irrespective of the fiber volume fraction. An increase in fiber volume fraction is found to enhance the toughness of both the binder systems, as expected, attributed to the crack-bridging effects of the fiber and the resultant increase in energy dissipation under load. The K_{IC}^{S} values of the iron carbonate binder range from 30 $MPa.mm^{0.5}$ to 50 $MPa.mm^{0.5}$, which is approximately half of those of glass ceramics (HAN 2009), polycrystalline cubic zirconia, SiN, Alumina (Becher 1991) and high-performance structural ceramics such as SiC (Mukhopadhyay, Datta, and Chakraborty 1999), and five times larger than the companion OPC binder. It is noteworthy to state that the above-mentioned ceramics are prepared via high-temperature processing whereas the

iron-based binder in this study is processed at ambient temperature and pressure in a CO_2 environment. In the unreinforced OPC matrix, the only mechanism of strain energy dissipation is crack extension. The significantly higher K_{IC}^{S} of the iron-based binder, even for the unreinforced case, as compared to the OPC binder could be attributed to the crack bridging and/or deflection effects of the ductile, unreacted metallic iron particles in the matrix, many of them which are elongated as can be observed from the micrographs in Figure 6-3. The strong reinforcing phase (the unreacted metallic particles) imposes a closing pressure on the crack thereby bridging the cracks and the elastic incompatibility and debonding between the metallic particle-carbonate matrix interfaces contributes to crack deflection. The influence of the unreacted iron particles in improving the crack resistance and toughness is augmented by the toughening mechanisms due to the incorporation of fibers, as can be noticed from Figure 6-7. Beyond a certain volume fraction of fibers, further toughness enhancement is negligible for the iron-based binders because the distribution of the unreacted iron particles and the fibers in the matrix is expected to be sufficient for crack bridging/deflection. However, as expected, an increase in fiber volume fraction, in the ranges reported in this study, enhances the toughness of the OPC-based binder system, the reasons for which are well documented (Tassew and Lubell 2014; Banthia and Sheng 1996; Gopalaratnam and Gettu 1995; Reis 2006; Bakhshi, Barsby, and Mobasher 2014; Banthia et al. 2014).

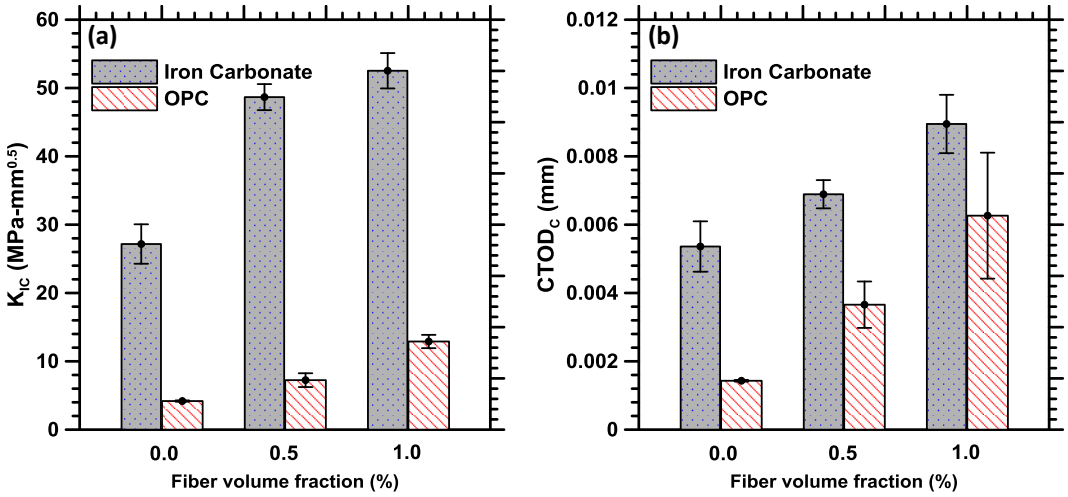

Figure 6-7: (a) Fracture toughness, and (b) critical crack tip opening displacements of iron carbonate and OPC-based binders

The critical crack tip opening displacements ($CTOD_C$), which indicates the limit beyond which unstable crack propagation begins is shown in Figure 6-7(b) as a function of the fiber volume fraction for both the binders. A rather uniform increase in $CTOD_c$ with fiber volume fraction is observed for both the binders. The unstable crack propagation threshold limit ($CTOD_C$) for the unreinforced iron-based control binder is found to be about three times higher as compared to that of the corresponding OPC paste, also attributable to the reasons described earlier. The difference in $CTOD_C$ between the two binder types reduce to a certain extent as fibers are incorporated. The K_{IC} and $CTOD_C$ values of the two binders indicate that the iron-based binder yields significantly improved crack resistance and ductility than the conventional OPC systems due to the presence of unreacted metallic iron powder surrounded by a carbonate matrix (Das, Stone, et al. 2014; Das, Souliman, et al. 2014).

The K_{IC}-$CTOD_C$ relationships of the two binders are compared in Figure 6-8(a), where an increase in the fracture toughness is observed with an increase in the critical opening size of the crack. While the increase in K_{IC}^S is proportional to an increase in $CTOD_c$ for the

OPC binders, for the iron-based binder, the increase in K_{IC}^{S} is not prominent beyond a certain $CTOD_c$ value (or fiber volume fraction, since $CTOD_c$-fiber volume fraction relationships are linear for both the binder systems as shown in Figure 6-7(b)). The reason for this observation was provided earlier. The critical crack length (a_c) values obtained from TPFM are shown in Figure 6-8(b), as a function of the fiber volume fraction. The critical crack length increases with increase in fiber volume for both the binders as expected. In unreinforced binders, the iron-based system has a higher critical crack length owing to the contribution from elongated, elastic iron particles. However, at a higher fiber volume fraction, the critical crack lengths for both the binders are comparable even though K_{IC}^{S} and $CTOD_c$ are higher for the iron-based binder. This shows that, in the iron-based systems, beyond a certain fiber volume fraction, enhancement in fracture properties are negligible for reasons explained earlier (even though the performance is much better than the corresponding OPC systems). This aspect is investigated in further detail through the use of resistance curves in the following section.

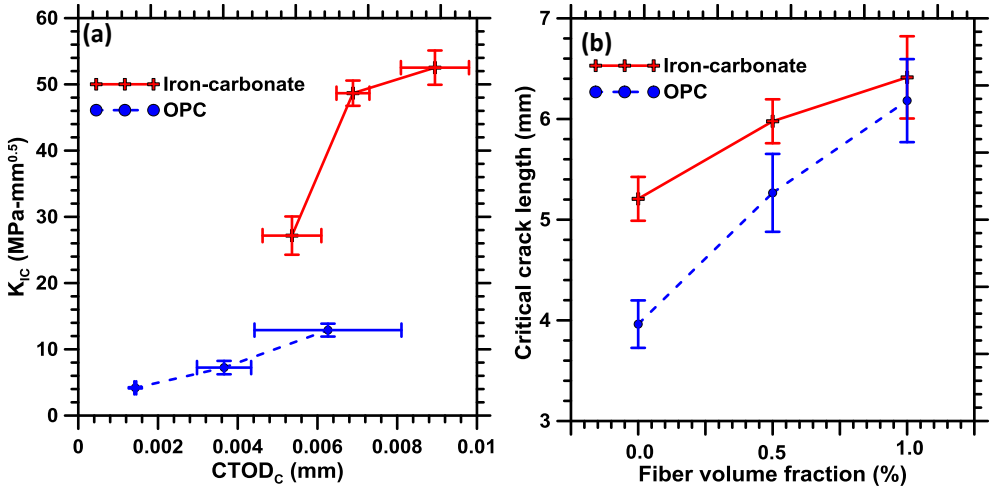

Figure 6-8: (a) Fracture toughness-critical crack tip opening displacement relationship; (b) Variation in critical crack length with change in fiber dosage for iron carbonate binder and OPC

6.3.3.3 Matrix and fiber effects on the strain energy release rates

In order to explore the influence of matrix (including the unreacted, elongated iron particles) and the fibers on the fracture response, this section utilizes the resistance curves (R-curves) (Das, Aguayo, et al. 2014; Mobasher 2011; Wecharatana and Shah 1983; Chengsheng, Barzin, and Surendra P. 1990; Mai and Hakeem 1984; Sakai and Bradt 1986; Arino and Mobasher 1999). R-curves are developed here by making use of the multiple loading-unloading cycles in the load-CMOD plots as shown in Figure 6-5. R is defined as the strain energy rate required for crack propagation and it is an increasing and convex function for quasi-brittle materials. The contribution from both the elastic and inelastic strain energies are considered in the development of the R-curve, which makes it beneficial in obtaining a better understanding of the matrix and fiber effects. The elastic component is calculated from the unloading compliances whereas the inelastic CMOD is used to calculate the inelastic strain energy release rate. The total strain energy release rate (G_R) is given as (Mobasher 2011; Wecharatana and Shah 1983; Mai and Hakeem 1984; Sakai and Bradt 1986; Arino and Mobasher 1999; Das, Aguayo, et al. 2014):

$$G_R = G_{elastic} + G_{inelastic} = \frac{P^2}{2t}\frac{\partial C}{\partial a} + \frac{P}{2t}\frac{\partial (CMOD_{inelastic})}{\partial a} \quad (6\text{-}3)$$

Here C is the unloading compliance, t is the thickness of the specimen, P is the applied load, and a is the crack length.

A compliance-based approach (Mobasher 2011; Das, Aguayo, et al. 2014; Wecharatana and Shah 1983) is used in this study to develop the resistance curves. This approach is based on the assumption that stable crack propagation leads to an increase in compliance. Three parameters were obtained for each loading-unloading cycle (Figure 6-5): the

compliance, the load at the initiation of the unloading, and inelastic CMOD, which is the residual displacement when the sample is unloaded. The unloading compliance is used to solve for the effective crack length (a_0+ Δa, where Δa is the crack extension) using a non-linear equation described in (Mobasher 2011; Das, Aguayo, et al. 2014). The compliance and the inelastic CMOD are then plotted as functions of the crack length and the relationships differentiated to obtain the rate terms in Equation 6-3.

Figure 6-9 shows the R-curves for both the binder systems at all levels of fiber reinforcements. The R-curves comprise of a region where the resistance increases with crack length denoting the formation of a process zone and an energy plateau denoting steady-state crack extension. The location of the transition point between the two regions depends on the matrix type and fiber volume as can be observed from Figure 6-9. The unreinforced OPC system shows almost negligible resistance whereas the corresponding iron-based system demonstrates some resistance to crack formation and growth, attributable to the reasons described elsewhere in this study. The use of fiber reinforcement improves the crack growth resistance of OPC systems, but the overall resistances are significantly lower than those of the iron-based binder systems.

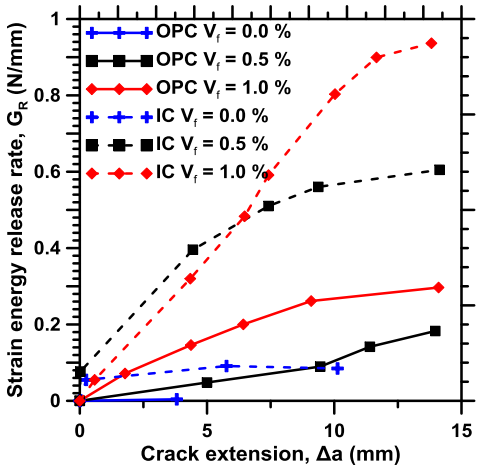

Figure 6-9: Resistance curves for the unreinforced and fiber reinforced iron-based and OPC binder systems

It is instructive to separate the elastic and inelastic components of the strain energy release rate to obtain further insights on the relative influence of matrix (and the discrete phases in it) and the fiber reinforcement on the fracture response of these widely different material systems. The results are presented in Figure 6-10(a) and (b) for the iron- and OPC-based binder systems respectively. The elastic component of the strain energy release rate corresponds to the energy release rate due to incremental crack growth whereas the inelastic component corresponds to effects such as permanent deformation caused due to crack-opening. An important observation from these figures is that the contribution of the elastic component to the overall strain energy release rate is found to be higher than the inelastic component for the iron-based binder systems (both unreinforced and reinforced) whereas for the OPC systems, the contribution of inelastic component is higher. It is also found that both the elastic and the inelastic components increase with increase in crack extension for the fiber-reinforced iron-based system whereas for the fiber-reinforced OPC systems, the elastic component remains relatively constant with crack extension and the increase in total strain energy is mainly due to increase in the inelastic component. The higher contribution of the elastic component in the iron-based systems is attributed to the presence of a stronger matrix along with the presence of elastic metallic iron particles that provide crack growth resistance through the mechanisms described earlier. On the contrary, the brittle OPC matrix cracks easily, and consequently the load is carried almost completely by the fibers. The fibers bridge the crack and energy dissipation is obtained through crack opening, which is reflected in the form of increased inelastic strain energy with increasing crack extension. The R-curve

response is consistent with the values of fracture parameters (K_{IC}^{S} and $CTOD_C$) of these binders. The fracture toughness of the iron-based systems was found to be much higher than the OPC systems whereas the $CTOD_C$ values demonstrated less of a difference. The same trends are reflected in the R-curves: about an order of magnitude higher crack growth resistance (elastic contribution) observed for the iron-based systems than the OPC systems and comparatively lesser improvement (about 60% higher) in the crack-opening resistance (inelastic contribution).

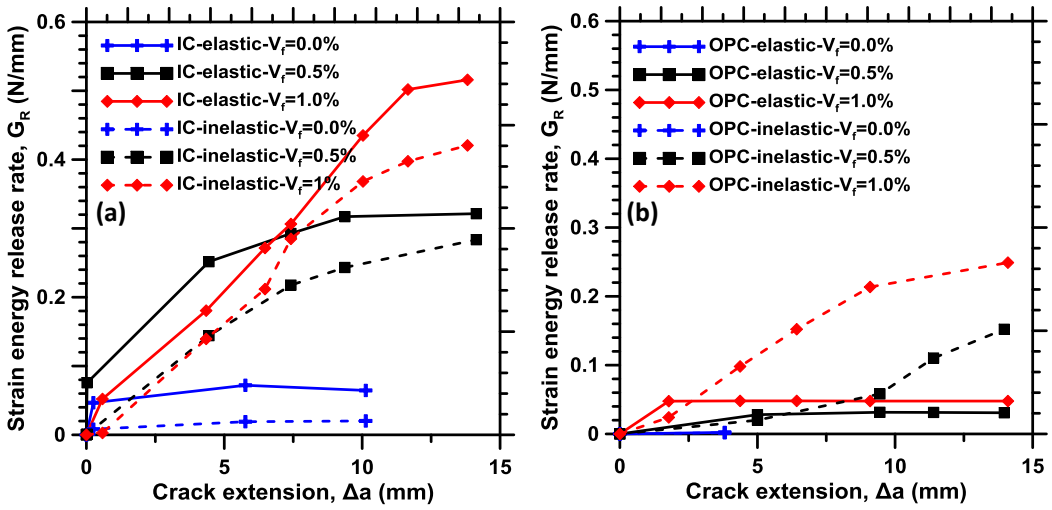

Figure 6-10: Elastic and inelastic components of crack growth resistance with varying crack extension for (a) iron Carbonate binder and (b) OPC paste for different fiber dosage

6.3.4 Use of Digital Image Correlation (DIC) to Determine K_{IC} and $CTOD_c$

DIC is a very useful non-contact optical method to measure displacement fields (Krottenthaler et al. 2013; Rossol et al. 2013; Yuan et al. 2014; Ghorbani, Matta, and Sutton 2014; Tominaga et al. 2014). DIC has been employed in several studies, including those of the authors, to evaluate fracture responses of several materials (J. Chen et al. 2010; Yates, Zanganeh, and Tai 2010; Nunes and Reis 2012a; Roux, Réthoré, and Hild

2009; Das, Aguayo, et al. 2014). To demonstrate the effectiveness of this method for the novel iron-based binder systems, two representative iron carbonate binders (0% and 1% fiber volume fraction) are used here for the extraction of fracture parameters through DIC. Figure 6-11(a) shows the load-CMOD response for the fiber-reinforced iron-based binder, where the points P1-to-P3 correspond to three different stages of crack extension, i.e., in the pre-peak, near-peak, and post-peak stages. The compliance value obtained by unloading at approximately 95% of the peak load in the post-peak region is used for the determination of K_{IC}^{S} and $CTOD_C$ using TPFM, which is required in order to compare with the corresponding values obtained using the DIC technique. The horizontal u-displacement fields (along the crack opening direction) are obtained from image correlation by employing VIC-2D software™ (commercially available, developed by Correlated Solutions). Figure 6-11(b) shows the plot of the crack opening, denoted by the horizontal displacement, and the crack extension, denoted by the jump in the displacement above the notch, which can be extracted from the DIC data (Das, Aguayo, et al. 2014). As can be observed here, the CTOD and Δa values can be determined directly using the DIC method without instrumenting the crack for precise measurements. A threshold value of 0.005 mm is set to qualify the displacement-jump as contributing to crack extension. The crack extension corresponding to 95% of the peak load in the post-peak region is used to determine the DIC-based fracture toughness parameters using a set of simplified expressions as shown later.

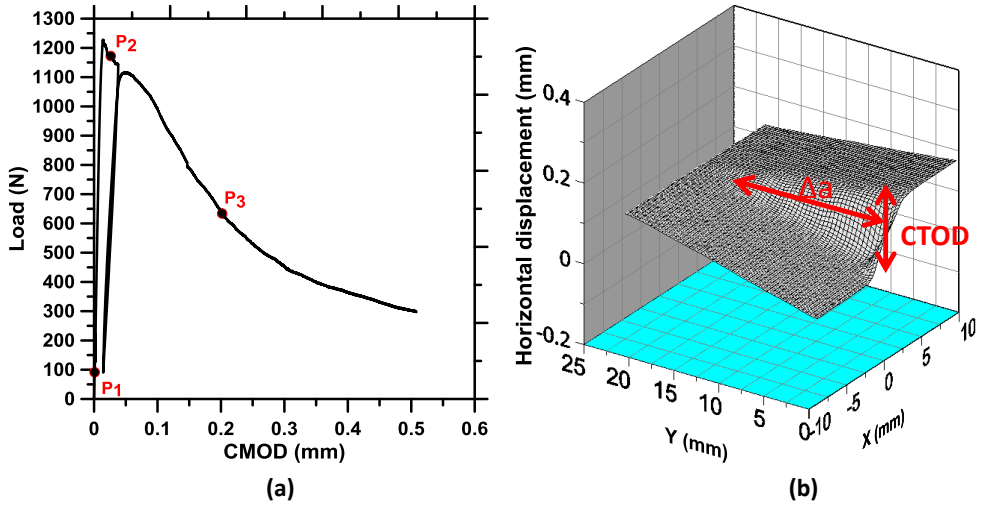

Figure 6-11: (a) Load-CMOD response for iron carbonate binder with 1% fiber volume fraction, and (b) horizontal (u) displacement field represented as a 3D surface plot

The 2D displacement fields for the iron-based binder are shown in Figure 6-12 for three different CTOD values which were selected as shown in Figure 6-11(a). Figure 6-12(a), (c) and (e) show the 2D crack opening displacements, corresponding to the points P1 , P2 and P3 of Figure 6-11(a) whereas Figure 6-12(b), (d) and (f) shows the corresponding horizontal displacements as 3D surface plots. Figure 6-12(a) corresponds to the case where only a very small load is applied to the specimen (Point P1 in Figure 6-11(a)), and the values of both CTOD and crack extension are zero, as shown by the uniform horizontal displacement fields above the notch as well as a flat surface plot (Figure 6-12(b)). Figure 6-12(c) corresponds to 95% of the peak load in the post-peak zone (Point P2 in Figure 6-11(a)). A displacement jump is clearly visible above the notch in both the 2D displacement field (Figure 6-12(c)) and the 3D surface plots (Figure 6-12(d)). Beyond this point, the crack extension is found to be unstable (a large increase in CTOD and crack extension). Figure 6-12(e) shows the displacement field corresponding to Point P3 in Figure 6-11(a). The CTOD and Δa values are very high in the post-peak zone.

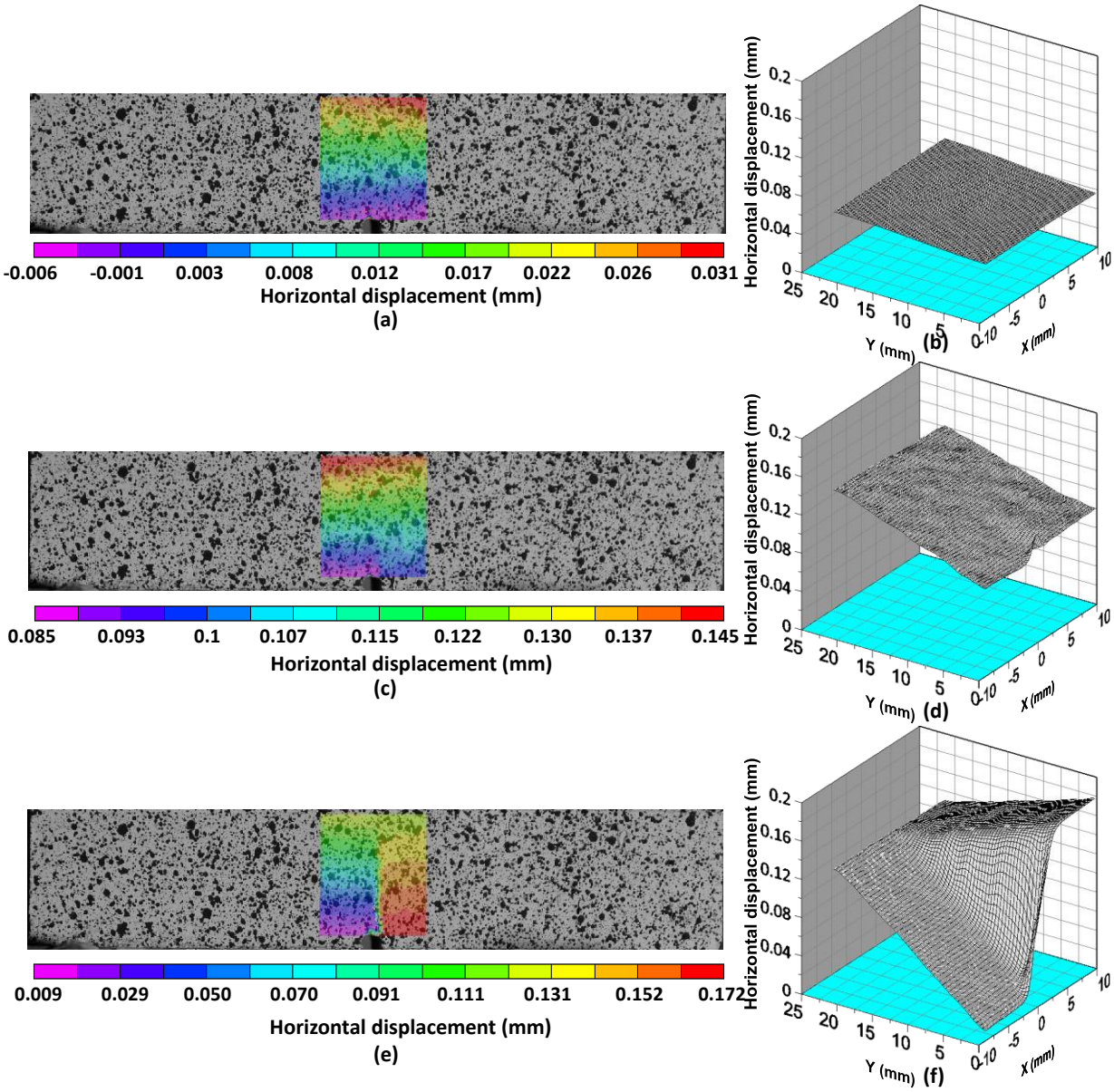

Figure 6-12: Horizontal displacement fields and the 3D surface plots for unreinforced and reinforced (1% fiber volume fraction) iron-based binders corresponding to: (a) and (b) pre-crack stage: P1 (CMOD: 0.0009 mm, Load: 91.4 N, Δa=0 mm, CTOD=0 mm); (c) and (d) stable crack growth stage: P2 (CMOD: 0.0263 mm, Load: 1172 N, Δa=3.95 mm, CTOD=0.0096 mm); (e) and (f) unstable crack-propagation stage: P3 (CMOD: 0.2019 mm; Load: 633.8 N; Δa=18.58 mm; CTOD=0.156 mm).

To determine K_{IC} and $CTOD_C$ from the DIC data, values at 95% of the peak load in the post-peak zone are considered. K_{IC} for a notched beam in three-point bending can be determined as (Nunes and Reis 2012a; Gdoutos 2006; P. Zhang et al. 2013) as:

$$K_{IC} = \frac{PL}{bd^{3/2}} F[\frac{a_{eff}}{d}] \quad (6\text{-}4)$$

The geometry function $F(a_{eff}/d)$ is given as:

$$F[\frac{a_{eff}}{d}] = [2.9(\frac{a_{eff}}{d})^{1/2} - 4.6(\frac{a_{eff}}{d})^{3/2} + 21.8(\frac{a_{eff}}{d})^{5/2} - 37.6(\frac{a_{eff}}{d})^{7/2} + 38.7(\frac{a_{eff}}{d})^{9/2}] \quad (6\text{-}5)$$

where the effective crack length, $a_{eff} = a_0 + \Delta a$.

The $CTOD_C$ and K_{IC} values are also calculated using the TPFM for comparison and are reported in Table 6-1. For the iron-based binders, there is a good correlation between the K_{IC} and $CTOD_c$ values obtained from the contact and non-contact methods, establishing the use of DIC-based techniques as a viable means for non-contact sensing of structural damage parameters.

Table 6-1: Comparison of the K_{IC} and $CTOD_c$ values determined using TPFM and DIC

Specimen composition	K_{IC} (MPa.mm$^{0.5}$)		$CTOD_c$ (mm)	
	TPFM	DIC	TPFM	DIC
Iron carbonate (Control)	31.40	33.56	0.0062	0.0040
Iron carbonate (V_f=1.0%)	52.53	54.14	0.0089	0.0096

6.4 Conclusions

This study has evaluated the flexural fracture response of a novel iron-based binder and compared it with the performance of OPC-based matrices which are the most common and cheapest of the available ceramic matrices. The iron-based binder was prepared by

the aqueous carbonation of metallic iron powder (which contained particles of large aspect ratios also) along with other chosen minor ingredients. Microstructural studies showed a dense reaction product intermixed with pores and unreacted, elongated iron particles. The flexural strength, fracture toughness (K_{IC}^{S}), and the critical crack tip opening displacement ($CTOD_c$) of the iron-based binders were significantly higher than those of the OPC matrices, for both the unreinforced and glass-fiber reinforced systems. The improved performance of the iron-based binder systems were attributed to the presence of the elastic, unreacted metallic particles that facilitate crack bridging and deflection. The use of glass fibers was found to enhance the toughness of OPC-based systems as is well known. For the iron-based binders, up to a certain fiber volume fraction, toughness enhancement was observed. The benefits were negligible beyond that because a further increase in fiber volume was not required to ensure crack bridging/deflection in the presence of elongated iron particles. The K_{IC}^{S} and $CTOD_c$ values for the iron-based binders were also obtained through a non-contact digital image correlation method, which provided comparable fracture parameters as those determined from the TPFM.

R-curves, developed using a compliance-based approach, were used to explore the relative influence of the matrix and the fibers on the fracture response of the novel binder systems. The iron-based binder systems showed significantly higher strain energy release rates than the OPC-based binder at all fiber loadings. The elastic (corresponding to the energy release rate due to incremental crack growth) and inelastic (permanent deformation caused due to crack-opening) components of the strain energy release rate were separated. It was found that the elastic component of the strain energy release rate

was higher than the inelastic component for iron-based binders, attributable to the superior effects of the unreacted metallic particulate phase that provide crack growth resistance. For the fiber reinforced OPC system, the energy dissipation is obtained through crack opening only, which resulted in an increased contribution of the inelastic component towards the total strain energy release. The results from this study has established the improved flexural and fracture performance of a novel and sustainable composite material.

Chapter 7 Crack-propagation and Strain-localization in Novel iron Carbonate binder using Digital Image Correlation

7.1 Introduction

While previous chapters described the material development, characterization, compressive, flexural strength and fracture behavior, the study presented in this chapter investigates the fundamental reasons for the beneficial fracture performance of these binder systems through the evaluation of the fracture process zone (FPZ), defined as a complex localized zone of energy dissipation containing the main crack as well as various branches of secondary and micro-cracks. The development of the FPZ in the iron-based binder systems will be significantly different from those of OPC-based systems due to the differences in the material microstructure, especially the presence of iron particles. The influence of fiber reinforcement in these systems is also explored with respect to its synergistic action with the matrix response, which also is very different from those of OPC-based systems.

By extending the evaluation of the fracture responses, the tensile constitutive behavior of the novel iron-based composite binder is extracted from resistance curves. The maximum fracture energy is compared with the cohesive toughness of a unit tensile stress-crack width model (Suzuki and Sakai 1994; Mobasher, Bonakdar, and Bakhshi 2015) to predict the tensile response. The differences in tensile response between OPC and iron-based binder systems are elucidated. Results are further investigated for the strain localization and crack propagation behavior of the novel binder using the Digital Image Correlation technique,. Adoption of suitable analytical models for tensile response, and comparison

with OPC systems are expected to provide useful insights that aid in the development of guidelines for widespread use of this material.

7.2 Experimental program

7.2.1 Materials, Mixtures and Specimen Preparation

Metallic iron powder with a median particle size of 19 μm was used as the major starting material in this study. The iron powder was obtained from an industrial shot-blasting facility in Phoenix, AZ. The elongated and angular iron particles provide beneficial increased reactivity due to higher surface-to-volume ratio of the particles. The other additives used in the binder formation included Class F fly ash and metakaolin conforming to ASTM C 618, and limestone powder (median particle size of 0.7 μm) conforming to ASTM C568. Here fly ash was added as a silica source to potentially facilitate iron silicate formation and limestone, to provide nucleation sites for reaction. Further details on mixture proportioning of this novel binder material can be found in previous chapters. Unlike, traditional OPC based binders, water serves only as an agent of mass transfer in the iron-based binder systems and the reaction product is not a hydrate. In order to reduce the water demand and to maintain the cohesiveness of fresh mixture, a clay phase (metakaolin) was added. An organic reducing agent/chelating agent (Oxalic acid in this case) was also added to facilitate better dissolution of the metallic iron and enhance its reactivity. For comparison purposes, commercially available Type I/II OPC conforming to ASTM C150 was used to prepare conventional cement paste.

The binder component used in this study includes 60% iron powder, 20% fly ash, 8% limestone, 10% metakaolin and 2% oxalic acid by mass. These proportions were arrived at based on strength and porosity of several trial mixtures as described in detail in an

earlier chapters. The mixing procedure involves initial dry mixing of all the constituents and then addition of water to form a uniform cohesive mixture. A mass-based water-to-powder ratio of 0.24 was used to provide a cohesive and uniform mixture. Since water is not chemically combined in the reaction products, this value was chosen from a rheological perspective.

Prismatic beams of size 127 mm (length) x 25.4 mm (depth) x 25.4 mm (width) were prepared in polypropylene molds and the samples were placed inside clear plastic bags in a 100% CO_2 environment under normal temperature and pressure for 24 hours. The beams were then demolded and kept in a 100% CO_2 environment for 5 more days. The bags were refilled with CO_2 every 12 hours in order to maintain CO_2-saturation. After carbonation, the samples were placed in air for 4 days for evaporation of moisture from the samples. These carbonation and air-curing durations are also arrived at based on a previous study shown in previous chapters. For comparison purpose, companion OPC beams of same size were prepared using a water-to-cement ratio of 0.40 which is common for moderate-strength concrete for infrastructural applications. The beams were demolded after 24 hours and placed in a moist chamber (>98% RH and 23±2^{o}C) for a total of 28 days. The fiber-reinforced binders were prepared by adding 0.5% and 1.0% alkali-resistant glass fibers (25 μm diameter and 10 mm long) by volume to the blends while mixing. The fiber reinforced iron-based and the OPC binders were cured in the same way as their non-reinforced counterparts.

7.2.2 Cyclic Three-point Bending Test for Evaluation of Fracture Properties

Three point bending test was performed on notched beams (notch depth-to-beam depth ratio of 0.15). The beams were tested in a closed-loop flexural testing setup. Several

loading-unloading cycles were employed, and the compliances were used to determine the fracture resistance. Crack mouth opening displacement (CMOD), measured using a clip gauge, was used as the controlling signal during loading cycles whereas load-controlled mode was employed during unloading cycles. The tests were run monotonically under CMOD-controlled mode for evaluation of the zone of strain localization through non-contact measurement using digital image correlation (DIC).

7.2.3 Digital Image Correlation (DIC) for Evaluation of Fracture Process Zone

DIC is an optical speckle-tracking non-contact measurement method to obtain full-field surface displacements through successive post-processing of digital images taken at specific intervals of time. The principle and applications of DIC are well documented (Krottenthaler et al. 2013; Rossol et al. 2013; Yuan et al. 2014; Ghorbani, Matta, and Sutton 2014; J. Chen et al. 2010; Yates, Zanganeh, and Tai 2010b; Nunes and Reis 2012; Das, Aguayo, et al. 2014; Das, Hendrix, et al. 2015; Das, Aguayo, et al. 2015b). The surfaces of the beams were speckled to create random patterns. A CCD (Charged-Couple Device) camera was used to record images every 5 seconds. After collection of all the images, a suitable region of interest (ROI) was chosen for analysis, as shown in Figure 7-1(a). The 2D displacement fields are obtained from correlation between the subsets of images from the deformed and undeformed state as shown in Figure 7-1(b). The horizontal (u) and vertical (v) displacement fields in the surface analysis region are then computed by minimization of the correlation coefficient (C) (Yates, Zanganeh, and Tai 2010b; Das, Aguayo, et al. 2014). The image processing and analysis operations were carried out using a commercial software (VIC-2D ^{TM}).

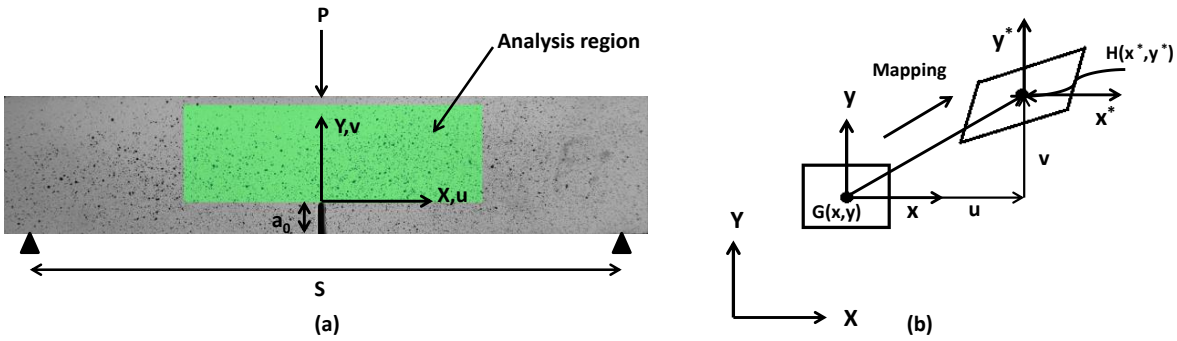

Figure 7-1: (a) Three-point bend specimen showing the analysis region for displacement field mapping, and (b) schematic of mapping of points in DIC

The Lagrangian strain fields are then obtained from the displacement fields as given in Equation 7-1 to 7-3 (Hjelmstad 2007; Sutton, Orteu, and Schreier 2009a; Das, Aguayo, et al. 2015b):

$$e_{xx} = \frac{\partial u}{\partial x} + \frac{1}{2}\left[\left(\frac{\partial u}{\partial x}\right)^2 + \left(\frac{\partial v}{\partial x}\right)^2\right] \tag{7-1}$$

$$e_{yy} = \frac{\partial v}{\partial y} + \frac{1}{2}\left[\left(\frac{\partial u}{\partial y}\right)^2 + \left(\frac{\partial v}{\partial y}\right)^2\right] \tag{7-2}$$

$$e_{xy} = \frac{1}{2}\left[\frac{\partial u}{\partial y} + \frac{\partial v}{\partial x}\right] + \frac{1}{2}\left[\left(\frac{\partial u}{\partial x}\frac{\partial u}{\partial y}\right) + \left(\frac{\partial v}{\partial x}\frac{\partial v}{\partial y}\right)\right] \tag{7-3}$$

While the crack tip opening displacement (CTOD) and the crack extension (corresponding to the load and CMOD pertaining to that time step) can be quantified from the results of u-displacement fields (Nunes and Reis 2012; Das, Aguayo, et al. 2014; Das, Aguayo, et al. 2015b; Das, Hendrix, et al. 2015), the in-plane Lagrangian strain field calculated from the displacement fields, particularly its component e_{xx} that corresponds to the crack opening direction, provides important information on strain localization at the tip of the crack.

7.3 Results and discussions

7.3.1 Cyclic load-CMOD response of notched beams

The representative load-CMOD responses of control and fiber reinforced iron-based binder are shown in Figure 7-2(a). Multiple loading-unloading cycles are employed in order to determine compliance based resistance (R) curves which are used in the present study to determine the tensile stress-strain responses which are discussed in detail later. A significant improvement in the flexural strength and post-peak response is clearly visible in Figure 7-2(a) for the iron carbonate binder when 1% glass fiber by volume is added. Figure 7-2(b) shows the peak flexural loads for OPC and iron-based binder at different fiber loadings. The control iron-based binder shows significantly higher peak flexural load than the OPC paste, which can be attributed to presence of unreacted metallic iron particle inclusions surrounded by strong carbonate matrix in the iron-based binder as is explored in previous chapters. The peak flexural load increases with incorporation of fiber in both the systems but the iron-based binder shows more pronounced increase in flexural peak load due to the synergistic effect of the iron carbonate matrix (including the unreacted iron particles) and the fibers on the flexural response. Figure 7-2(c) shows the total fracture energy, calculated using Hillerborg's work-of-fracture method as shown in Equation 7-4 (Roesler et al. 2007; Das, Aguayo, et al. 2015b), for the OPC and iron-based novel binder.

$$G_F = \frac{W_0 + P_W \delta_0}{(D - a_0)t} \tag{7-4}$$

In Equation 7-4, W_0 is the area under the load-CMOD curve, δ_0 is the CMOD at failure, D is depth of the beam, a_0 is the notch depth, t is the beam thickness, and P_W is the self-weight of the beam. Total fracture energy, a reflection of post-peak performance and

crack-tolerance of materials, is found to be significantly higher in iron-based binder than OPC in both control and fiber-reinforced states for the reasons explained earlier. For instance, at 1% fiber volume fraction, the fracture energy is about 4 times higher for the iron-based binder. The peak loads and fracture energies shown here provide an indication of the performance improvement attainable by the novel iron carbonate binder system as compared to the conventional OPC-based systems.

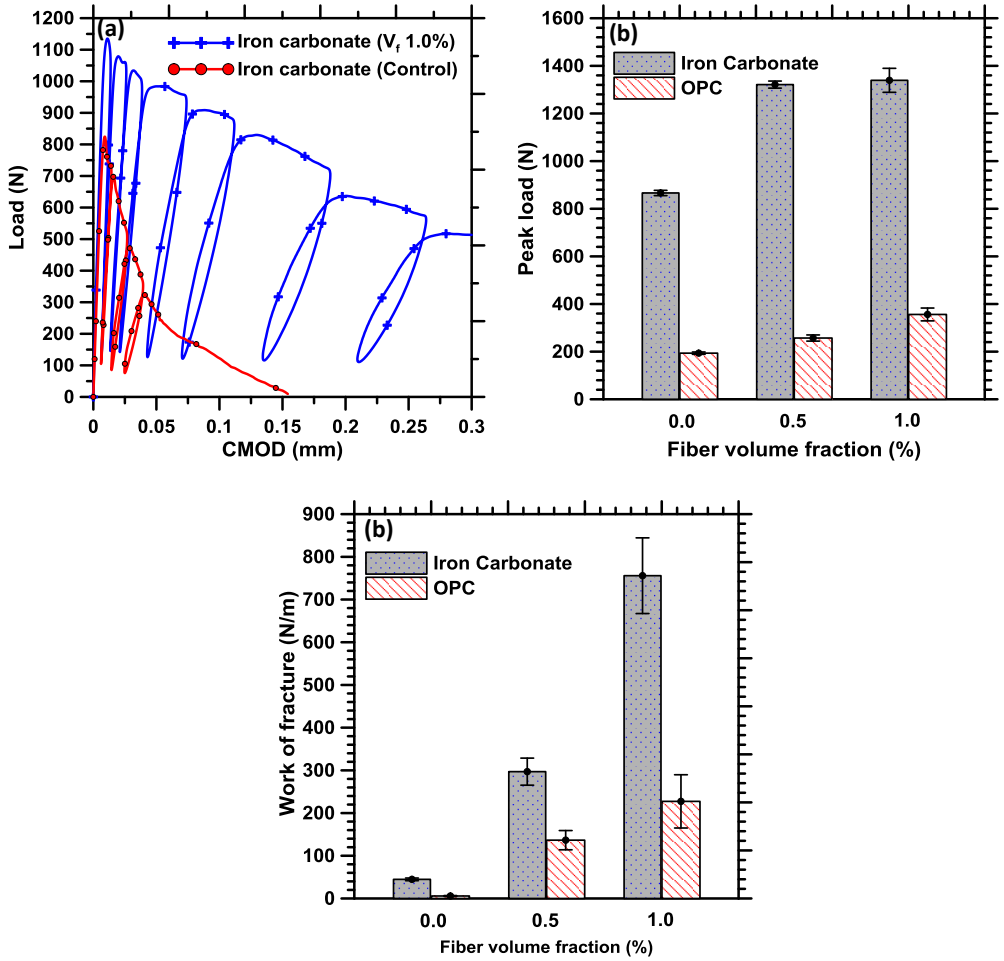

Figure 7-2: (a) Representative Load-CMOD responses for iron carbonate binder with and without fiber reinforcement, (b) peak flexural loads for the OPC and iron carbonate binders, and (c) total fracture energy of OPC and iron carbonate binders used in this study. The error bars represent one standard deviation of peak load or fracture energy obtained from four replicate specimens.

7.3.2 Strain energy release rates (R-curves)

While the superior performance of iron-based binder as compared to OPC is established as shown in previous chapter using a two-parameter fracture model, this section shows the strain energy release rates for ease of reference in the context of determination of tensile stress-strain response using strain energy-based inverse analysis.

Compliance-based determination of (Mobasher 2011b; Das, Aguayo, et al. 2014; Das, Hendrix, et al. 2015; Wecharatana and Shah 1983) strain energy release rate is based on the assumption that stable crack propagation leads to an increase in compliance. The elastic component is calculated from the unloading compliances whereas the inelastic CMOD is used to calculate the inelastic strain energy release rate. The total strain energy release rate (G_R) is given as:

$$G_R = G_{elastic} + G_{inelastic} = \frac{P^2}{2t}\frac{\partial C}{\partial a} + \frac{P}{2t}\frac{\partial (CMOD_{inelastic})}{\partial a} \quad (7\text{-}5)$$

Here ‘C’ is the unloading compliance, ‘t’ is the thickness of the specimen, ‘P’ is the applied load, and ‘a’ is the effective crack length calculated by substituting values of unloading compliance in a nonlinear equation. The unloading compliance and inelastic CMOD is expressed as a function of effective crack length using polynomial fit and the functions are differentiated with respect to ‘a’ to obtain the different terms in Equation 7-5.

R-curves for the OPC and iron-based binders are shown in Figure 7-3(a). In the unreinforced states, the OPC system shows very little crack growth resistance, consistent with the extremely brittle nature of a hydrated OPC paste, whereas the iron-based binder exhibits significantly higher resistance. Incorporation of fibers improves the resistance

for the OPC matrix although the resistance values are still lower as compared to the fiber-reinforced iron-based binder for the reasons explored earlier. Figure 7-3(b) and (c) show the separated contributions of elastic and inelastic components to the total strain energy release rates for the different binders. The elastic component of the strain energy release rate can be attributed to incremental crack growth whereas the inelastic component arises from effects such as permanent deformation caused due to crack-opening (Das, Aguayo, et al. 2014; Das, Aguayo, et al. 2015b). The elastic component is found to be dominant in the iron-based binder systems, whether reinforced or not, whereas the inelastic strain energy release rate, i.e., the result of energy dissipation by crack opening is dominant for the OPC systems. The higher elastic strain energy release rate in iron-based binder is attributed to the presence of unreacted elastic elongated iron particles in the carbonate matrix. On the other hand, the OPC paste, because of its brittleness, shows almost negligible contribution from the matrix and almost all the resistance is provided by the fibers (inelastic resistance). The maximum values of strain energy release rates are used in an inverse analysis procedure (Section 3.4) to calculate the tensile constitutive response of OPC and iron-based binding systems. In the case of iron-based binder, the presence of a stronger matrix phase (unreacted elastic iron particles surrounded by the carbonate reaction products) will likely enhance the tensile strength, as will be elaborated in detail later.

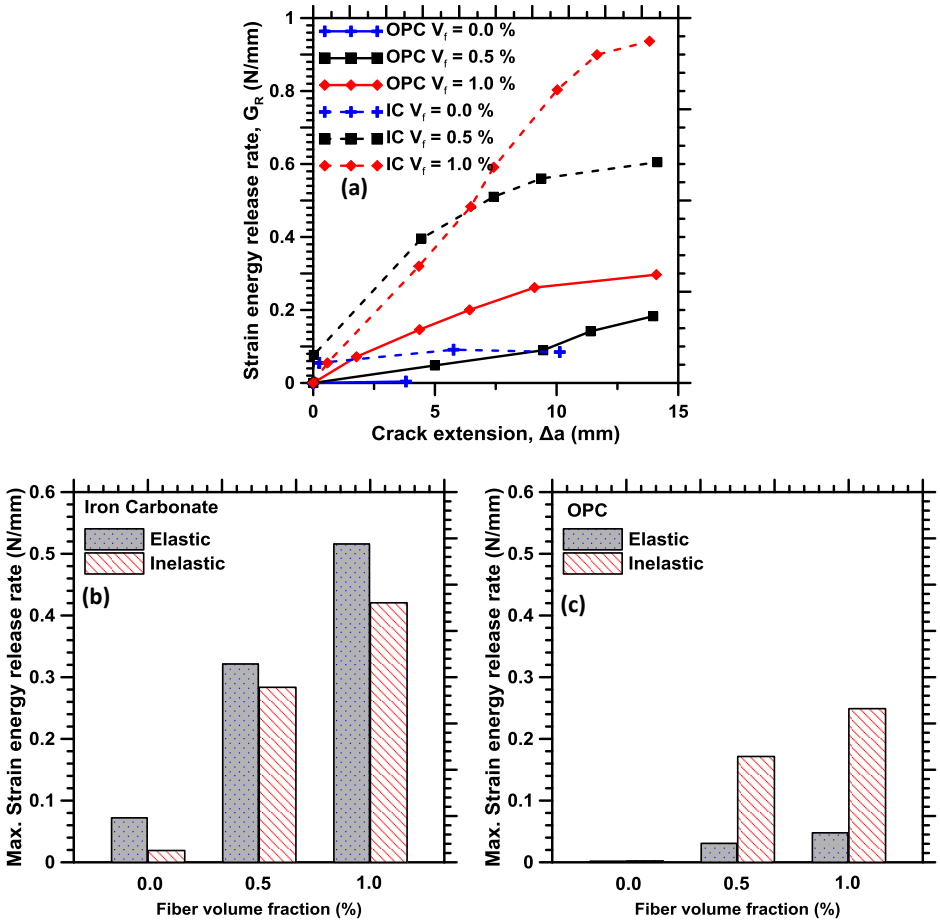

Figure 7-3: (a) Total strain energy release rates for the unreinforced and fiber reinforced iron-based and OPC binder systems; (b) and (c) elastic and inelastic components of maximum strain energy release rates for iron-based binder and OPC paste respectively.

7.3.3 Characterization of Fracture Process zone (FPZ) in the novel binder systems

This section examines the fracture process zone, the zone of micro-cracking ahead of the crack tip, in the selected binder systems to elucidate the differences in the crack propagation mechanism influenced by the matrix type (OPC or iron-based) and the presence of fiber reinforcement. The fundamentally different fracture response demonstrated by the iron carbonate binder is explained through a detailed characterization of FPZ.

7.3.3.1 Determination of width and length of FPZ

The width of the localized region can be expected to provide useful information on the fracture mechanism of the material. In the present study, the width of the localized region is used to compare the fracture characteristics of OPC and iron-based binder in both control and fiber-reinforced states. In addition, the width of localized zone is used as a "gage-length" for the determination of post-peak tensile strain, as explained in a forthcoming section. The process of determination of width of localized region using the Lagrangian strain profiles from DIC is explained below.

Figure 7-4(a) shows a monotonic load-CMOD response of unreinforced iron-based binder. Figure 7-4(b) shows a typical surface strain field (e_{xx}), calculated from the surface displacement field at 95% of the peak load in the post-peak regime from which the localized strain concentration above the notch can be identified easily. Figure 7-4(c) shows the strain profile at a height of 2.5 mm above the notch as a function of its position in the X-direction. In order to determine the width of the localized zone, the surface strain profile is fitted as a normal distribution function using σ as the fitting parameter as shown in Equation 7-6:

$$f(x,\sigma) = \frac{1}{\sigma\sqrt{2\pi}} e^{-\frac{1}{2}\left(\frac{x}{\sigma}\right)^2} \tag{7-6}$$

This fitting parameter σ is a measure of the spread of the strain-localized zone. The FPZ width can be considered to be equal to 4σ since 95% of the values of the normal distribution function are within ±2σ of the mean value. A similar approach has been used elsewhere (Das, Aguayo, et al. 2015b; Skarżyński, Kozicki, and Tejchman 2013; Skarżyński and Tejchman 2013). The FPZ widths reported here are used only for

comparison since it is highly influenced by the image resolution; a higher image resolution resulting in a smaller FPZ width (Skarżyński, Kozicki, and Tejchman 2013). The length of FPZ is measured as the extent of strain localization in the crack extension direction. The localized zone is considered to be terminated when the strain along the crack extension direction is lower than 20% of the strain at the tip of the notch.

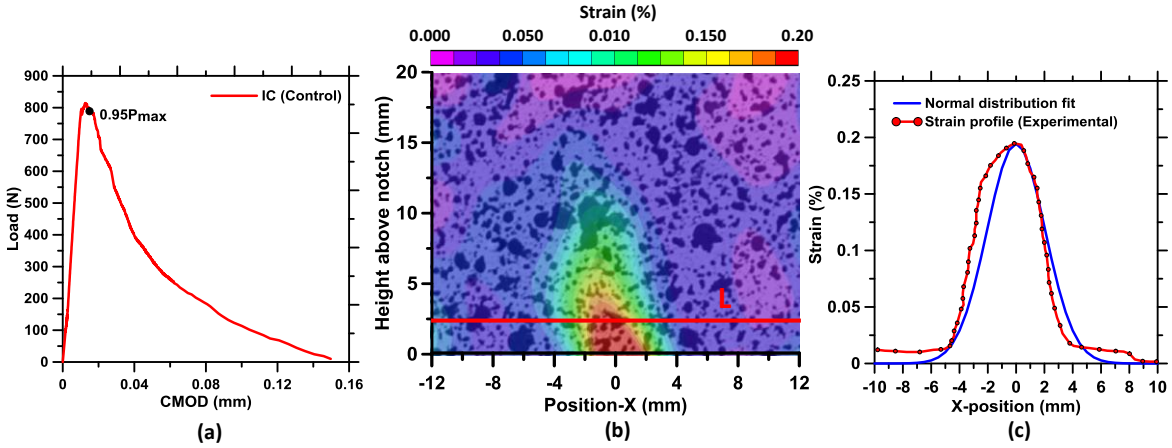

Figure 7-4: (a) Monotonic load-CMOD response of unreinforced iron carbonate binder; (b) Localized zone above the notch obtained from DIC; and (c) horizontal normal strain (ε_{xx}) profile across the localized zone for the iron-based binder at the location denoted by L in (b).

7.3.3.2 FPZ features and the influence of matrix type and the presence of fiber reinforcement

Figure 7-5(a) and (b) show the FPZ for the unreinforced OPC and iron carbonate binders. A qualitative indication of FPZ widths is also obtained from these figures, with the iron-based binder showing a wider FPZ. The results are extracted at 95% of the peak load in the post-peak region. The width of FPZ decreases with increase in distance from the crack (notch) tip for both the binders. Figure 7-5(c) shows that rate of reduction of FPZ width is also very similar for both the unreinforced binders. Figure 7-6(a) and (b) show

the FPZ for the fiber-reinforced (1% by volume) OPC and iron carbonate binders. An observation of the local strain levels show that the strains are higher in the fiber-reinforced systems as compared to those in the unreinforced pastes shown in Figure 7-5. This can be attributed to the increased strain capacity of the fiber-reinforced systems. In addition, the strain in the iron-based binder is slightly lower than that of the corresponding OPC system due to the increased spread of FPZ in the former case as can be noticed from Figure 7-5 and Figure 7-6. Another distinctive feature in the fiber-reinforced binders is the rather uniform localized strain distribution as a function of distance above the notch tip as seen in Figure 7-6(c), attributable to the fiber bridging effect.

The quantified average values of FPZ length, width and area in both the OPC and iron-based (unreinforced and fiber-reinforced) systems are shown in Figure 7-7(a), (b) and (c) respectively. The FPZ width profiles are numerically integrated with respect to the height above the notch to quantify the area of FPZ. The width and area of FPZ for both the unreinforced and reinforced iron-based binders are found to be higher than that of the corresponding OPC binder whereas the length of FPZ is the same for both the binder systems. The higher width of FPZ in the iron-based system can also be related to the higher inelastic strain energy release rates in such systems as was shown earlier. On the other hand, the FPZ lengths in iron-based and OPC binders corresponding to 95% of the peak load in the post-peak regime are almost similar although the iron-based binder showed a higher elastic strain energy release rate, which is a measure of resistance against incremental crack-growth. This behavior can be attributed to the increased load

carrying capacity of iron-based binder (four-to-six times stronger than the OPC binder) being the dominant contributor to strain energy release rates.

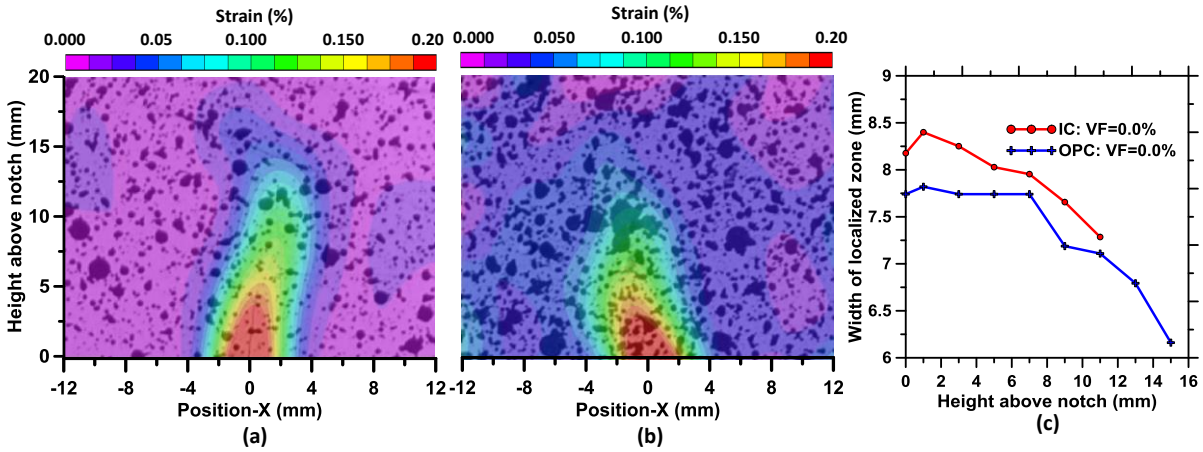

Figure 7-5: (a) and (b) Strain localization above the tip of the notch in unreinforced OPC and iron-based binders respectively, and (c) width of FPZ as a function of distance from the notch tip for both the binders. The data is for 95% of the peak load in the post-peak region.

A comparison between the FPZ characteristics of the unreinforced and fiber-reinforced binders reveals that the length, width and area of FPZ are lower in fiber-reinforced binders. Incorporation of fibers reduces strain localization as the fibers resist the spread of the zone of micro-cracking in the crack-opening and extension directions. The fiber-reinforced systems are shown to exhibit higher inelastic strain energy release rates as compared to the unreinforced systems even when the spread of localized region is reduced. This can be attributed to the fact that higher strain energy release rate in the fiber-reinforced systems is facilitated not just through the spread of the zone of micro-cracking in the matrix, but also through the increased strain capacity in the systems. The ultimate tensile strains extracted from an inverse analysis is shown in a later section to prove this point. While the spread of the localized zone is found to be the dominant mechanism in overall inelastic energy dissipation in unreinforced systems, the increase in strain capacity due to the crack-bridging effect of fibers becomes the dominant

contributor to the inelastic energy release rates in the fiber-reinforced systems, thereby facilitating relatively uniform spread of FPZ above the notch. Similarly, the elastic component of strain energy release rate (Figure 7-3(b)) is found to be the dominant contributor to the overall increase in strain energy release rate of iron-based binders containing fiber reinforcement in spite of reduction in the FPZ length. This is attributed to the elastic component of strain energy release rate being proportional to square of load term (Equation 7-5), and thus the higher load carrying capacity of the fiber-reinforced iron-based binders dominates the FPZ length on their relative influences on the elastic strain energy release rates.

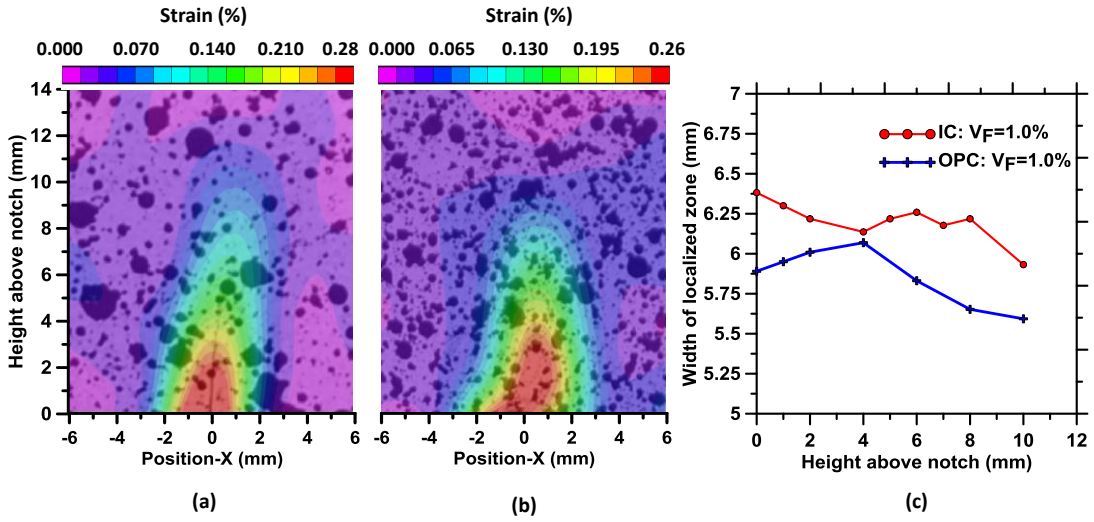

Figure 7-6: (a) and (b) Strain localization above the tip of the notch in fiber-reinforced reinforced OPC and iron-based binders respectively, and (c) width of FPZ as a function of distance from the notch tip for both the binders. The data is for 95% of the peak load in the post-peak region.

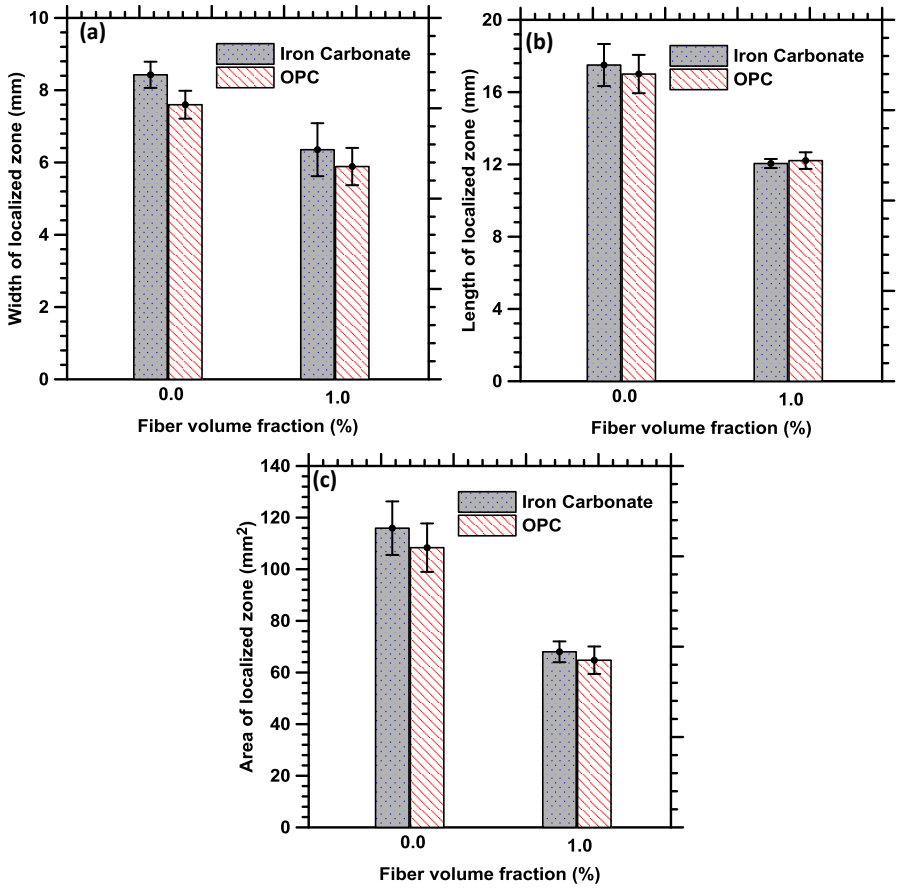

Figure 7-7: Comparison of: (a) width of FPZ, 7 mm above notch; (b) length of FPZ, and (c) area of FPZ. For both the binder types, the FPZ characteristics are determined at 95% of the peak load in the post-peak regime.

Figure 7-8(a) and (b) depict the variation in the width of FPZ with increase in CMOD and crack extension respectively. Both the binders exhibit initiation of localized zone at similar values of CMOD. Full width of FPZ develops at a lower value of CMOD for the unreinforced OPC binder as compared to the iron-based binder, signifying its brittleness which is also reflected in the rapid extension of crack (Figure 7-8(b)) after the formation of FPZ. The increased resistance to cracking of the iron-based binder as compared to the OPC binder can also be noticed from the fact that, at a given FPZ width, the crack extension is always lower for these binders. The higher crack growth resistance of iron-

based binders can be attributed to the presence of unreacted iron particulate inclusions in the strong carbonate matrix of the iron-based novel binders, as was shown earlier in previous chapters. Figure 7-8(c) shows the variation in FPZ width with applied load. The general trends suggest that the FPZ width increases initially as the load increases and the full width of process zone is developed at or close to the peak load, beyond which the width remains almost constant. Here also, superior performance of iron-based binders is reflected in the form of significantly lower rates of increase in FPZ width with increase in load.

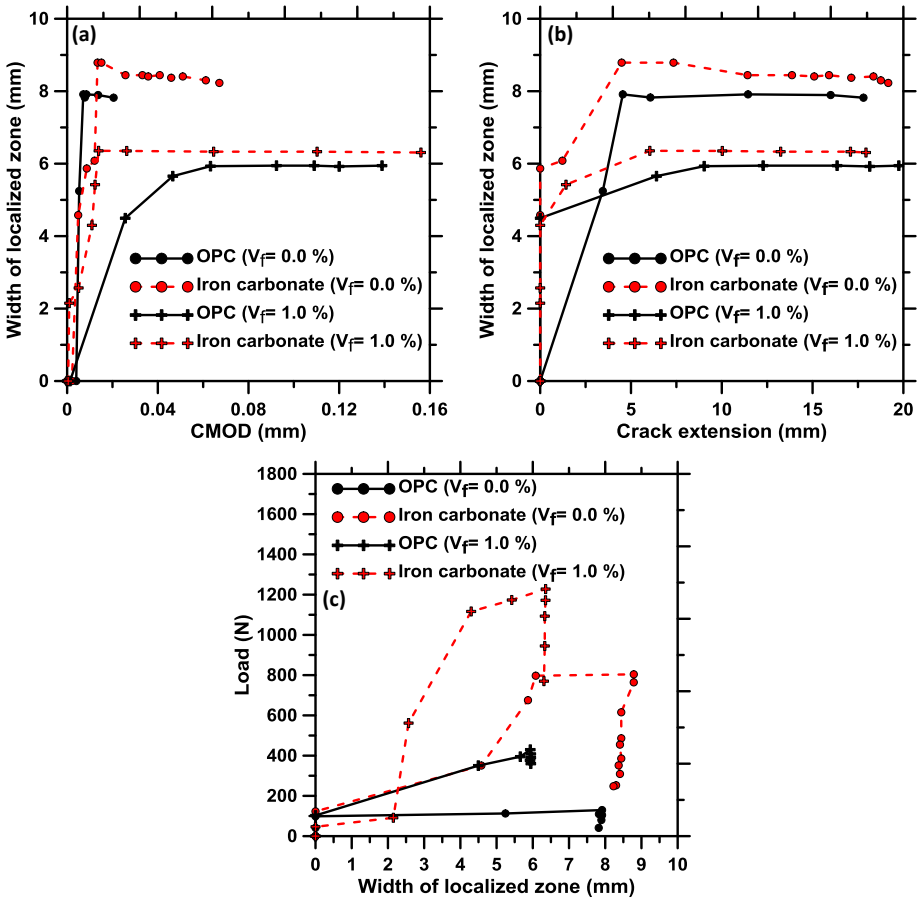

Figure 7-8: Variation of width of FPZ with changes in: (a) CMOD, (b) crack extension, and (c) load.

7.3.4 Extracting the tensile constitutive response from strain energy release rates

The previous sections on strain energy release rates and quantification of FPZ have indicated the fracture performance of unreinforced and fiber-reinforced novel iron-based binders vis-à-vis OPC binders. In this section, the tensile constitutive relationships for these binders are developed since they better represent the material behavior than the flexural response which fails to account for the presence and growth of cracks in the pre-peak regime. The tensile constitutive response is back-calculated from maximum strain energy release rates through a potential energy approach using a crack-face bridging model (Suzuki and Sakai 1994; Mobasher, Bonakdar, and Bakhshi 2015).

7.3.4.1 Crack-face bridging model and contribution to toughening due to closing pressure

Several micro-fracture mechanisms, responsible for toughening in quasi brittle materials, take place at the FPZ ahead of the crack-tip and at crack-face contact regions in the crack-opening direction. Among them, crack-face bridging is a dominant mechanism that contribute to rising crack growth resistance (R) curves (Shah 1995; Mobasher 2011b). In this study, a model for crack-face bridging (Suzuki and Sakai 1994) is employed to determine the tensile stress-strain response from the R-curves through an inverse analysis (Suzuki and Sakai 1994; Mobasher, Bonakdar, and Bakhshi 2015).

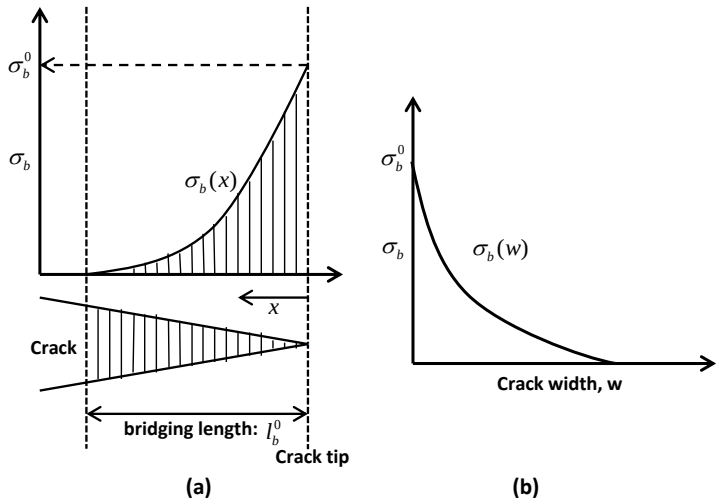

Figure 7-9: (a) Cohesive stress distribution for a unit bridging stress at a=a_c when the FPZ length is fully developed, and (b) stress-crack width relationship (Suzuki and Sakai 1994)

The present study uses a phenomenological power function expression (Suzuki and Sakai 1994) of stress-crack width relationship as shown in Figure 7-9, represented as:

$$\sigma_b(w_b) = \sigma_b^0(1-\frac{w_b}{w_b^0})^n \tag{7-7}$$

$$w_b(x) = w_b^0(\frac{x}{l_b^0})^q \tag{7-8}$$

Where σ_b is the crack-face bridging stress, w_b is the crack-opening displacement, σ_b^0 is the critical bridging stress, w_b^0 is the maximum crack opening displacement, l_b^0 is the bridging zone length calculated as: $l_b^0 = \Delta a_c = (a_c - a_0)$ and 'q' and 'n' are the two constants reflecting the shape and distribution of the crack-face bridging tractions. The values of 'q' and 'n' are taken as 0.6 and 3.0 respectively based on the work of Suzuki and Sakai (Suzuki and Sakai 1994). For a unit value of σ_b^0 or tensile strength, the cohesive toughness can be computed using potential energy approach by integrating the

toughening through crack-face bridging over the entire bridging length given as (Schapery 1975; Mobasher, Bonakdar, and Bakhshi 2015):

$$\Delta G = 2\int_0^{l_b} \sigma_b(w).\left(\frac{\partial w}{\partial x}\right)dx \qquad [7\text{-}9]$$

The toughening energy due to crack closure (ΔG_R), attributed to crack-face bridging, is given as:

$$\Delta G_R = (G_{R_{\max}} - G_{IC}) \qquad [7\text{-}10]$$

Where $G_{R_{\max}}$ is the maximum value of strain energy release rate, and G_{IC} is the critical strain energy given as:

$$G_{IC} = \frac{K_{IC}^2}{E} \qquad [7\text{-}11]$$

Here, E is the initial plane stress-based stiffness and K_{IC} is the critical stress intensity factor calculated using the two-parameter fracture model. The tensile strength can be quantified as the ratio of the toughening energy due to crack closure from the resistance curve, ΔG_R (Equation 7-10) to the toughening energy due to unit tensile strength (Equation 7-9):

$$\sigma_t = \frac{\Delta G_R}{\Delta G} \qquad (7\text{-}12)$$

The tensile stress-strain response can be thus calculated assuming elastic response in the pre-peak region and using the concept of a characteristic length in the post-peak region. The post-peak tensile strains beyond the elastic regime are obtained by implementing an

average value of crack opening displacement (w_b) distributed over a gage-length. The gage-length is quantified using digital image correlation as the average width of strain localization along the height of the beam, at 95% of the peak load in the post-peak regime, since the width remains almost constant beyond that loading state.

$$\varepsilon_t = \frac{\sigma_t}{E} \qquad \text{(Elastic region: pre-peak)} \quad (7\text{-}13)$$

$$\varepsilon_t = \frac{w_b}{L_g} \qquad \text{(Post-peak region)} \quad (7\text{-}14)$$

7.3.4.2 Comparison of tensile behavior of control and glass fiber-reinforced OPC and iron-based novel binder

Figure 7-10 shows the back-calculated tensile stress-strain relationships for the OPC and iron-based binders. Figure 7-10(a) shows the tensile stress-strain relationship of the two binders in the unreinforced state. It is observed that the iron carbonate binder has a substantially higher tensile strength, tensile modulus, and ultimate tensile strain as compared to to the OPC binder because of the stronger matrix with unreacted ductile metallic iron particulate inclusions facilitating crack bridging and/or deflection through imposition of closing pressure on the crack. The elastic incompatibility and debonding between metallic particle-carbonate matrix interface contributes to crack. The effect of glass fibers on the extracted tensile stress-strain response of these systems are shown in Figure 7-10(b). Incorporation of fibers increases the tensile strength and ultimate tensile strain in both the systems although the elastic modulus remain relatively unchanged, which is along expected lines. The ultimate tensile strains are improved by an order of magntiude or more with the incorporation of fibers. The fiber-reinforced iron-based binder shows significantly higher tensile strength and ultimate tensile strain as compared

to fiber-reinforced OPC binder. In the fiber-reinforced iron-based binder, the presence of stronger particulate-reinforced matrix (due to unreacted iron particles) improves the performance of the matrix which is further augmented by the crack-bridging effect of fibers, wheareas in OPC binder, the brittle matrix fails very quickly and the load is completely carried by the fibers resulting in significantly lower tensile strength and ductility.

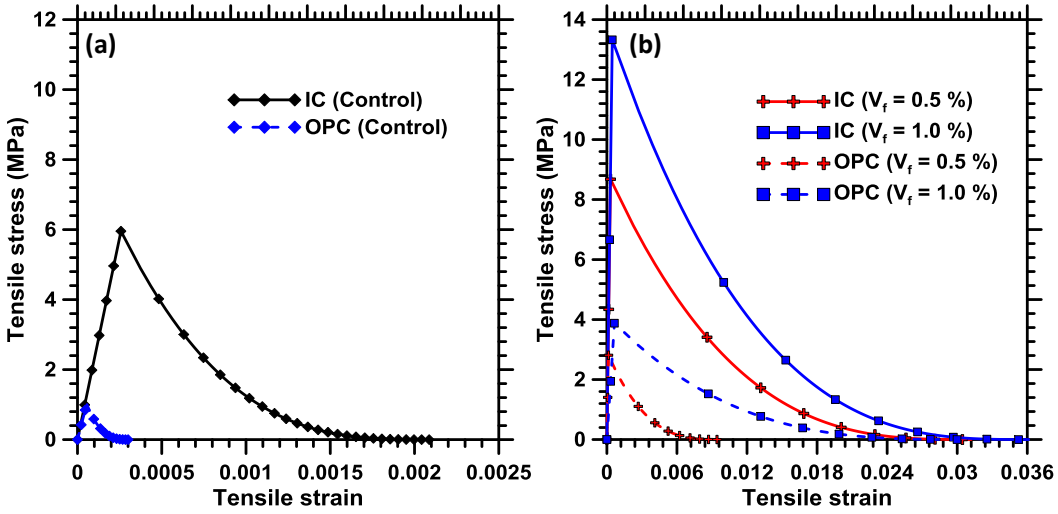

Figure 7-10: Tensile stress-strain response for OPC and iron carbonate binder: (a) unreinforced binder, (b) fiber-reinforced composites. Note that the strain axes scales are different.

Figure 7-11(a) shows the extracted tensile strength of these binders at different fiber loading levels. Tensile strength increases with increase in fiber volume fractions for both the systems with the trend being more pronounced in the iron-based binder. The unreinforced iron-based binder is 5-6 times stronger than the OPC binder, attributable to the reasons described earlier. The trend remains the same for the fiber-reinforced systems also. The ultimate tensile strains (Figure 7-11(b)) for the iron-based binder are also found to be significantly higher as compared to OPC signifying better post-peak performance of iron-based systems. It should be noted here that higher tensile toughness of iron-based binder, shown in Figure 7-11(c) is the reason for the higher FPZ area as compared to the

OPC binder in the unreinforced state (Figure 7-7(c)) whereas the significantly higher tensile toughness of the fiber-reinforced iron-based binder resulted in a decrease in the FPZ area. The latter signifies the dominant effect of crack-bridging mechanism in the fiber-reinforced system. Fiber volume fraction does not seem to impact the elastic modulus of both the binder systems as the fibers are expected mainly to contribute to the post-peak response of the materials and hence the initial stiffness remains relatively unchanged. Iron-based binders exhibit higher value of elastic modulus as compared to that of OPC-based binders which can be attributed to the presence metallic iron particulate inclusions.

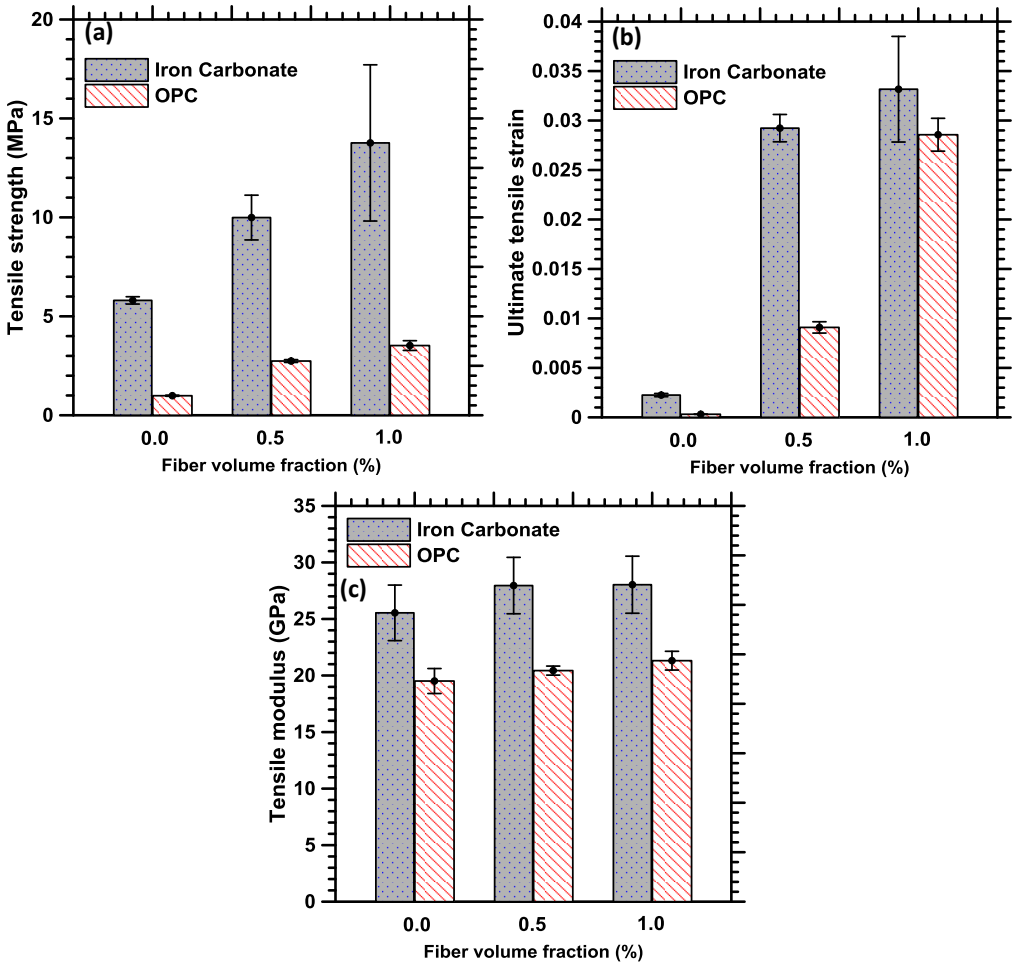

Figure 7-11: Comparison between OPC and iron carbonate binder (control and fiber reinforced): (a) tensile strength, (b) ultimate tensile strain and (c) tensile modulus

Figure 7-12 depicts the stress-crack width relationships in these binder systems. The general trend suggests that the crack becomes wider beyond the peak load with a concomitant reduction in the load capacity. Figure 7-12(a) depicts the stress-crack width relationship for the two binders in the unreinforced state. For any specific crack-width value, the iron-based binder, which has a strong matrix with unreacted metallic iron particle inclusions, can withstand significantly higher stress than OPC, which is brittle in nature. Figure 7-12(b) shows the stress-crack width responses for the glass fiber-reinforced binders. Incorporation of fibers improves the stress tolerance level of both the binders as expected although the iron-based fiber-reinforced systems still exhibit significantly higher stress tolerance corresponding to a given c crack width due to strong matrix-glass fiber synergy which has been elaborated in the previous chapter.

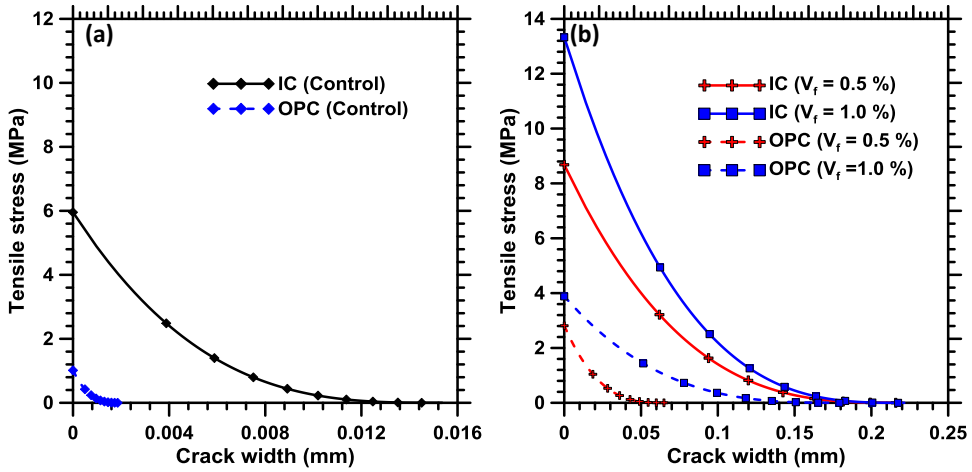

Figure 7-12: Stress-crack width relationships for OPC and iron carbonate binder: (a) unreinforced, and (b) fiber-reinforced composites. Note that the crack width axes scales are different.

7.3.5 Correlation of back-calculated tensile parameters with strain energy release rates and width of FPZ

This section presents the relationship between the back-calculated tensile parameters and the strain energy release rates and FPZ width. Figure 7-13(a) and (b) show that the maximum strain energy release rates increase linearly with both the tension-softening area and the tensile strength. Figure 7-13 (c) and (d) shows the relationship between the FPZ width and ultimate tensile strain and inelastic strain energy release rates for the unreinforced and fiber-reinforced systems respectively. For both unreinforced and fiber reinforced binders, an increase in the ultimate tensile strain is also demonstrated as an increase in the width of FPZ since a significant amount of energy is dissipated through the spread of FPZ. From the perspective of strain energy release rates, this is reflected as an increase in the inelastic strain energy release rate. But a comparison between the unreinforced and fiber-reinforced binder systems reveals that the use of fibers reduces the width of FPZ although the inelastic strain energy release rate and the ultimate tensile strains are noted to increase. This behavior is attributed to the dominant crack-bridging mechanism of fibers which increases the strain capacity of the composite as compared to unreinforced binders and resists spread of microcracking. Although the iron particulates provide microstructural reinforcement to the matrix through angular and elongated shape resulting in significantly improved fracture response as compared to OPC, its crack-bridging capability is not as efficient as fibers with significantly higher aspect ratio.

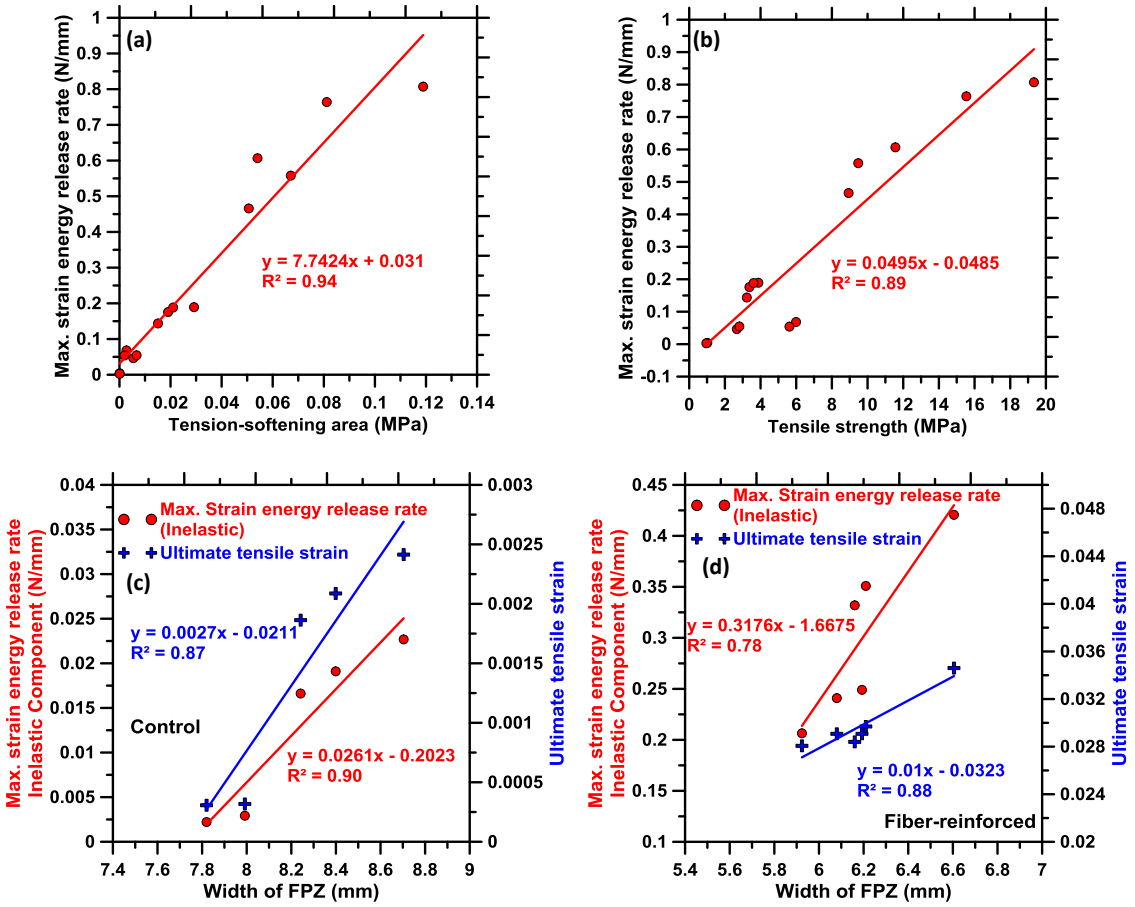

Figure 7-13: The maximum strain energy release rate in unreinforced and fiber reinforced binders as a function of: (a) area under softening portion of tensile stress-strain curve, and (b) tensile strength; Inelastic strain energy release rat and ultimate tensile strain as a function of FPZ width for: (c) unreinforced, and (d) fiber-reinforced OPC and iron carbonate binders. .

7.4 Conclusions

This chapter presents the fundamental difference in crack-propagation mechanism and the effects of fiber-reinforcements in the novel iron-based binder and OPC hardened paste through characterization and evaluation of the fracture process zone and its correlation with strain energy release rates. The characterization of the localized region is done in terms of length, width and area of the fracture process zone, measured through digital image correlation. The width of localized region above notch for iron-based binder

is found to be consistently higher as compared to OPC binder in both control and fiber-reinforced states which can be attributed to the presence of unreacted metallic iron particle inclusions in the microstructure of iron-based binder that enables the material to undergo higher amount of inelastic deformation through crack-bridging and deflection resulting in higher fracture-resistance as compared to OPC which is established in our previous study. The width of localized region reduced with incorporation of fibers in the iron-based binder systems, similar to the phenomenon observed in the fiber reinforced OPC systems, due to the fiber-bridging effect that increases the strain capacity of the material. The distribution of the width of localized region along height above the notch was more uniform as compared to control binders as fibers help uniform distribution of localized strain along height reducing the amount of crack extension. For any given width of localized zone, the iron-based binders exhibited lower amount of crack extension and higher flexural load capacity signifying superior mechanical properties of iron-based binder as compared to traditional OPC. Results of this comprehensive study establish the effectiveness of using glass fibers in the novel iron-based systems.

Tensile stress-strain response for iron-based novel binders was back-calculated from strain energy release rates, measured using unloading compliances, using a crack-face bridging model. The tensile strength of control and fiber-reinforced iron-based binders was significantly higher than that of control and fiber-reinforced OPC counterparts respectively due to metallic particle inclusions in the iron-based binder. Ultimate tensile strains and the Young's modulus values were also higher in iron-based binder for the same reason. The stress-crack width relationships of the binders suggest that for any value of crack width in the deformation process during the test, the iron-based binders

show significantly higher stress capacity as compared to OPC reinforcing overall findings of this chapter. Area under softening portion of the tensile stress-strain curve and the tensile strengths correlate well with the total strain energy release rates. The inelastic strain energy release rate and ultimate tensile strain capacity increased with increase in the width of strain-localization for both the binder systems in unreinforced and fiber-reinforced states separately since increased spread of the zone of micro-cracking facilitates improved energy dissipation. Incorporation of fibers results in reduction in the spread of FPZ in both the fiber reinforced systems as compared to unreinforced binders which can be attributed to the dominant effect of crack-bridging mechanism of fibers that arrests spread of the micro-cracking zone in fiber-reinforced binder systems.

Chapter 8 Nano-mechanical Properties of Carbonate Reaction Product in Iron-Carbonate Binder

8.1 Introduction

In order to develop a deep understanding of the relative contribution of different distinct phases to the overall bulk mechanical behavior of iron-based binder systems, application of micromechanics becomes crucial with a view to provide valuable information towards the material design of heterogeneous materials. While the pore structure of the material is important in dictating the transport behavior and thus the durability characteristics, the mechanical properties of a heterogeneous material are also influenced significantly by the individual phase amounts (both solids and pore) and their properties. The individual phase elastic properties can be obtained through the use of nanoindentation experiments, as has been well documented for cement-based materials (G. Constantinides, Ulm, and Van Vliet 2003; Sorelli et al. 2008; Mondal, Shah, and Marks 2007; Zhu et al. 2007; Pelisser et al. 2013; C. Hu and Li 2014; Hughes and Trtik 2004; Davydov, Jirásek, and Kopeckỳ 2011). Micromechanical homogenization models are in turn necessary to estimate the composite properties at the macro-scale. The response of the heterogeneous material at the micro-scale is averaged through analytical models, generally based on Eshelby's method (Eshelby 1957; Mori and Tanaka 1973; Hori and Nemat-Nasser 1993), that replace the microscopically inhomogeneous strains and stresses by homogeneous values. The successful implementation of this approach demands accurate quantification of the phase volume fractions. The development of empirical models to determine the reaction product and pore volume fractions based on simple stoichiometric equations in highly heterogeneous systems containing complex multiple phases such as such as Iron-

based binder is unlikely to yield satisfactory results. In light of the above, this study multiple schemes for identification and quantification of multiple solid phases. The pore volume fraction is quantified using MIP and image analysis is employed on a series of BSE micrographs on plane-polished samples to quantify the volume fraction of unreacted iron particles. The volume fractions of other phases (fly ash and clayey matrix phase) are assumed to be equal to their initial volume fractions and the remaining volume fraction is assigned to Iron carbonate reaction product. The microscale properties are upscaled using mean field homogenization schemes such as Mori-Tanaka method (Mori and Tanaka 1973; Miled, Sab, and Le Roy 2011; G. K. Hu and Weng 2000; C. C. Yang and Huang 1996; C. C. Yang 1997; da Silva, Němeček, and Štemberk 2013) to extract the homogenized Young's modulus, which is validated through macro-scale experiments. Linking the microstructure and micromechanical properties of a heterogeneous material, and using this information to predict the macroscopic mechanical performance, provides efficient means of optimizing the material design and mechanical behavior of the novel iron-based binder.

8.2 Experimental Program

8.2.1 Materials, Mixtures and Specimen Preparation

Metallic Iron powder with median particle size of 19 μm is used as the main starting material in this study. The binder component used in this study includes 60% iron powder, 20% fly ash, 8% limestone, 10% metakaolin and 2% oxalic acid by mass. These proportions were arrived at based on strength and porosity of several trial mixtures as described in detail in previous chapters. The mixing procedure involves initial dry mixing of all the constituents and then addition of water to form a uniform cohesive mixture. A

mass-based water-to-powder ratio of 0.24 was used to provide a cohesive and uniform mixture. Since water is not chemically combined in the reaction products, this value was chosen from a rheological perspective.

Cylindrical specimens of size 32.5 mm diameter x 65 mm long were prepared in Harvard miniature compaction apparatus molds and the samples were demolded immediately and placed inside clear plastic bags in a 100% CO_2 environment under normal temperature and pressure for 4 days. The bags were refilled with CO_2 every 12 hours in order to maintain CO_2-saturation. After carbonation, the samples were placed in air for 4 days for evaporation of moisture from the samples. These carbonation and air-curing durations are also arrived at based on a previous study detailed previously.

A cubical piece of 4 mm side length was cut from in between the core and the surface of the cylindrical sample using a diamond saw. The sample was ultrasonically cleaned, rinsed with isopropyl alcohol and dried to remove debris from sectioning/handling. The sample was then encapsulated using a two-part epoxy and vacuum impregnated at 95 KPa followed by an overnight cure at room temperature. Coarse grinding steps were accomplished using silicon carbide (SiC) abrasive discs to planarize and remove deformations caused by sectioning. Successive polishing steps were carried out using smaller sized abrasives, and completed using 0.04 μm colloidal silica suspension to ensure a very smooth surface. Thus, the sample was prepared for nanoindentation.

8.2.2 Nanoindentation

The nanoindentation measurements were carried out on the polished sample in a commercial nanoindenter (Nanoindenter XP-II, Agilent) using a Berkovich tip. Indentations were carried out at initially at 10 μm spacing in a grid on an area

approximately 250 μm x 250 μm in. All the indentation locations were carefully selected prior to testing to ensure that the pores or cavities are not encountered in the process. Thus the indentation experiments were carried out mostly only on the solid phases, which resulted in no spurious peaks in the modulus frequency distribution curves. The depth of penetration was chosen to be 500 nm which is smaller than characteristic size of unreacted inclusions in order to avoid phase-interactions during penetration. The contact stiffness for the Berkovich indenter is given as:

$$S = 2\beta\sqrt{\frac{A}{\pi}}E_T h_c \qquad [8\text{-}1]$$

In Equation 8-1, β is a constant (1.034 for Berkovich indenter), h_c is the penetration depth and E_T is the reduced elastic modulus, given as:

$$E_T = \frac{1-\upsilon^2}{E} + \frac{1-\upsilon_i^2}{E_i} \qquad [8\text{-}2]$$

υ and E are the Poisson's ratio and Young's modulus of the sample, and υ_i and E_i are the Poisson's ratio and Young's modulus of the indenter (for diamond, υ_i =0.07 and E_i = 1141 GPa) respectively.

Continuous stiffness measurement (CSM) technique (Oliver and Pharr 2004; Li and Bhushan 2002; Moody et al. 1998) was employed here to measure the contact stiffness, S. While the traditional Oliver-Pharr methodology (Oliver and Pharr 1992) measures the contact stiffness only at the point of unloading, the CSM technique allows measurement of contact stiffness at any point of the loading curve corresponding to any depth of penetration. CSM is accomplished by imposing a harmonic excitation of constant amplitude and frequency to the normally increasing load on the indenter. For any excitation frequency, the displacement response of the indenter and the phase angle are

measured continuously as a function of the penetration depth. The contact stiffness, as a function of penetration depth, is obtained by solving for the in-phase and out-of phase portions of the response which are described in detail in (Li and Bhushan 2002). For any contact stiffness S corresponding to penetration depth h_c , the reduced elastic modulus, E_T can be calculated from Equation 8-1 which can then be used in Equation 8-2 to obtain the Young's modulus of the sample as a function of penetration depth. A constant Poisson's ratio of 0.20 is used since the effect of variation of Poisson's ratio in the range 0.18-0.22 has been reported to be insignificant on the value of calculated Young's modulus for similar systems (Sorelli et al. 2008; da Silva, Němeček, and Štemberk 2013).

8.2.3 Mercury Intrusion Porosimetry (MIP)

The pore structure of the iron-based binder was evaluated using mercury intrusion porosimetry (MIP) to examine the pores in the smaller size ranges that is not accessible using XRT. A porosimeter that can detect minimum pore diameter of 0.0036 μm was employed for this study. This test was performed in two steps: (i) evacuation of gasses and filling the sample holder with mercury in the low-pressure run that increases the pressure from ambient to 345 kPa, and (ii) intrusion of mercury into the sample at high pressure (maximum pressure of 414 MPa). A solid–liquid (pore wall-mercury) contact angle of 130° and a mercury surface tension of 485 mN/m were used to interpret the results using Washburn equation (Moon, Kim, and Choi 2006; Rakesh Kumar and Bhattacharjee 2003; Das, Stone, et al. 2014e)

8.3 Results and discussions

8.3.1 Intrinsic nano-mechanical properties of component phases using Nanoindentation

For the classification of different phases present in novel iron-based binder and quantification of Young's modulus of different phases, a statistically significant number of indentations were performed on carefully chosen solid regions in the paste (based on a 250 μm x 250 μm grid) through microscopic observation of the indentation locations. This ensures that the material microstructure within each interaction volume can be estimated with a high degree of confidence, and the validity of isotropicity and homogeneity within the interaction volume can be ensured, which is absolutely important in interpreting indentation results of heterogeneous materials (Trtik, Münch, and Lura 2009). Penetration depths of up to 500 nm were employed to ensure that the measured elastic properties are not influenced by the sample preparation process that could introduce surface effects. Representative load-penetration depth plots to identify the phases of differing stiffness (the methodology to assign phases is explained below) are presented in Figure 8-1(a). The elastic modulus values as a function of penetration depth were calculated using the CSM technique described in the experimental program section and representative curves are shown in Figure 8-1(b). For all the measurements, average elastic modulus in a penetration depth range of 200-to-300 nm is computed and used for further analysis. The mean Young's modulus, along with a phase quantification procedure described later, is used in a homogenization scheme for quantification of bulk Young's modulus of the iron-based binder.

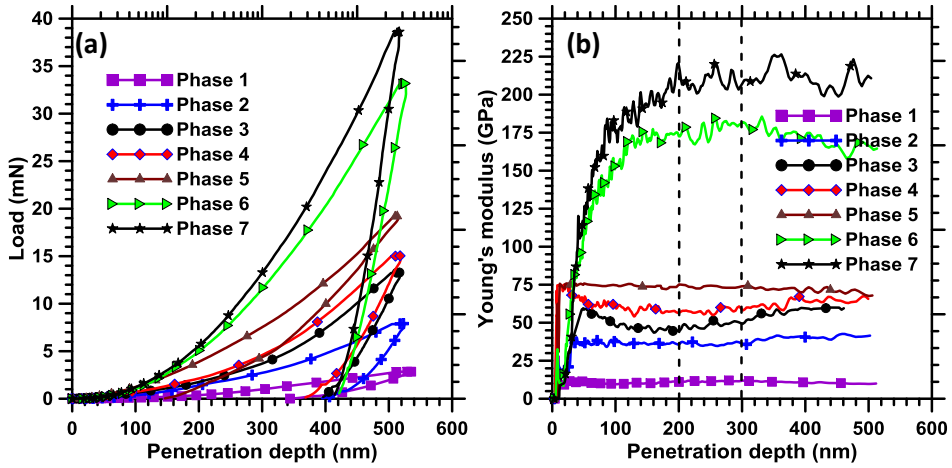

Figure 8-1: (a) Load-penetration depth curves for different phases in the novel iron-based binder, and (b) Elastic modulus as a function of the penetration depth for the distinct solid phases

The experimental probability density functions (PDFs) are obtained from experimental measurements by employing a bin size (b) of 5 GPa which is presented in Figure 8-2 (symbols). Seven characteristic peaks are observed in the histogram. Statistical deconvolution (G. Constantinides et al. 2006; Jiří Němeček, Šmilauer, and Kopecký 2011; da Silva, Němeček, and Štemberk 2013) is applied to the elastic modulus histogram to obtain individual phase elastic properties. Assuming Gaussian distribution for all the seven phases (which is a reasonable assumption based on the data points in Figure 8-2, the theoretical probability distribution function (pdf) is given as:

$$C(x) = \sum_{r=1}^{4} f_r \frac{1}{\sqrt{2\pi s_r^2}} \exp \frac{-(x-\mu_r)^2}{2s_r^2} \qquad [8\text{-}3]$$

Here, x represents the elastic modulus, f_r is the volume fraction of the r^{th} phase, and μ_r and s_r are the mean and standard deviation of the r^{th} phase The deconvolution algorithm involves random seeding using a Monte Carlo simulation and minimization of quadratic deviations between the experimental and theoretical PDFs to find the relevant parameters

for the Gaussian distribution functions. More details on the deconvolution algorithms can be found in (G. Constantinides et al. 2006; Jiří Němeček, Šmilauer, and Kopecký 2011; da Silva, Němeček, and Štemberk 2013).

Figure 8-2 also shows the deconvoluted PDFs for the seven different phases. Visual observation of the microstructure at the indented locations, along with an understanding of the phases present in iron-based novel binder based on past studies, was used for the assignment of the deconvoluted peaks to the individual peaks. The phase with the highest elastic modulus can be attributed to the unreacted pure iron particles, while the phase with the lowest elastic modulus can be attributed to the clayey matrix phase incorporating metakaolin and fine limestone powder. Peaks in the range 25-60 MPa corresponds to iron carbonate phase that is formed through dissolution of iron from the particles into the matrix and reaction with externally supplied carbon dioxide. The density of iron carbonate phase reduces as the distance from iron particles increases. Thus, three characteristic iron carbonate peaks (low density, medium density and high density) are obtained. The component microstructural phases to the two remaining deconvoluted peaks of the elastic modulus distribution are assigned to fly ash and impure/oxidized iron particles. The peak corresponding to the lower among the two peaks corresponds to the unreacted fly ash particles. Similar values for this phase have been reported in (J. Němeček, Šmilauer, and Kopeckỳ 2009; Jiří Němeček, Šmilauer, and Kopecký 2011). The other peak at approximately 180 GPa corresponds to partially reacted/oxidized iron particles. A detailed comprehensive evaluation of the microstructure was carried out towards attributing all these component phases. The deconvolution results are presented in Table 8-1.

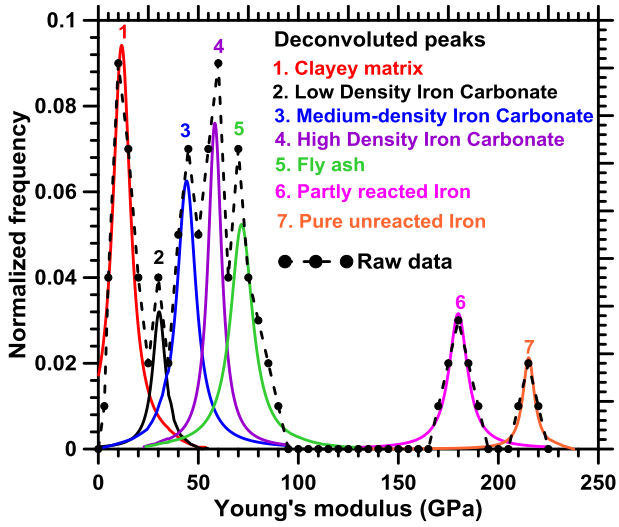

Figure 8-2: Deconvoluted component peaks for the seven distinctly identifiable microstructural phases in the solid component of the paste. The area under each deconvoluted peak is the fraction of that respective solid phase in all solids in the paste.

Table 8-1: Elastic properties of individual solid phases obtained through deconvolution

PEAK NO	E (GPa)	Phases
1	11.67 ± 4.93	Clayey matrix phase
2	30.3 ± 7.8	Low density Carbonate
3	44.11 ± 11.5	Medium density Carbonate
4	58.28 ± 8.26	High Density Carbonate
5	71.65 ± 13.45	Fly ash
6	179.9 ± 11.43	Impure/partially reacted Iron
7	215.2 ± 7.013	Pure Iron

8.3.2 Homogenization methods for elastic property prediction

Homogenization procedures are applied to heterogeneous materials such as cementitious systems to determine the homogenized elastic properties using individual phase properties (e.g., determined from nanoindentation) and phase amounts to be used in material design. Mean field homogenization techniques are based on Eshelby's tensors (Eshelby 1957)to determine the average stresses and strains in inclusions embedded in an elastic matrix. The homogenization method employed in this study is Mori-Tanaka

method (Mori and Tanaka 1973). The analytical schemes of this model has been well documented (Mori and Tanaka 1973; Miled, Sab, and Le Roy 2011; G. K. Hu and Weng 2000; C. C. Yang and Huang 1996; C. C. Yang 1997; da Silva, Němeček, and Štemberk 2013).

8.3.2.1 Determination of volume fractions to be used in the homogenization schemes

The mean-field homogenization schemes that are used for the estimation of macro-level properties requires precise input in terms of phase volume fractions. Here the pore volume fraction after 4 days of carbonation is quantified using MIP as detailed in previous chapter on pore and microstructural characterization of iron carbonate binder. The total unreacted iron volume fraction is calculated through image analysis on a series of SEM images under backscattered mode on plane polished surfaces. The chosen images are processed and analyzed using ImageJ©, a freely available image analysis software. The grey-scale images were converted to binary image by thresholding to separate the iron from the remaining phases. The threshold limits were chosen based on grey level histogram.

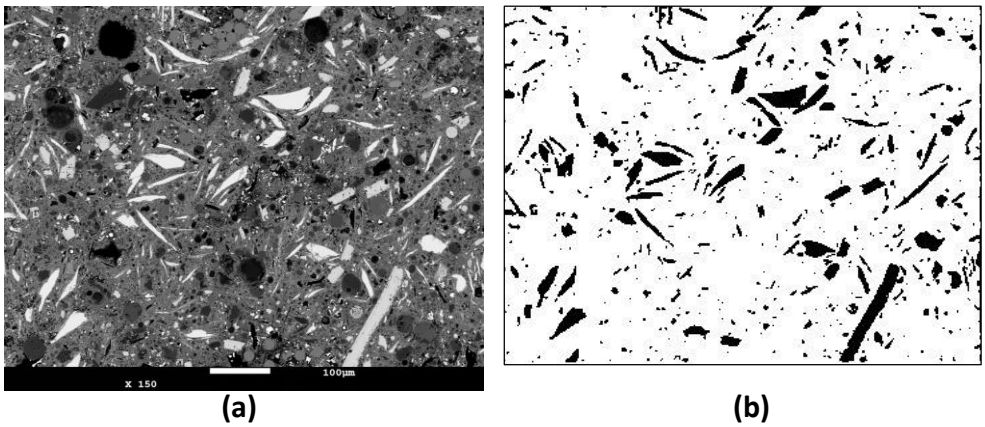

Figure 8-3: (a) original grey-scale image ; (b) binary thresholded image (Iron particles are shown in black)

Figure 8-3(a) shows one such grey-scale BSE image and Figure 8-3(b) shows binary thresholded image of image in Figure 8-3(a). The black phase in the thresholded image corresponds to the iron particles which are easily identifiable in the grey scale image as the bright particles in the microstructure. It should be noted that, BSE SEM images show good contrast between unreacted/partially reacted iron, pore and the other solid phases (at the resolution considered), which makes it suitable for determination of iron volume fraction. Thus, the volume fraction of iron particles in the iron-based binder is directly used in the homogenization schemes for elastic property prediction. However, identification and quantification of other different solid phases in the iron-based binder is challenging due to the low absorption contrast of these different solid phases in the available x-ray energy range. Hence, the volume fraction of fly ash is assumed here as the volume fraction originally added while combined volume fraction of metakaolin and limestone is attributed to the clayey matrix phase. The remaining volume fraction is assigned to iron carbonate reaction product. The volume fractions of different phases and their measurement procedures are detailed in Table 8-2. Again, low-density, medium-density and high-density iron carbonate is not easily distinguishable in the BSE SEM images for the reasons explained earlier. Hence, various combinations of volume fractions (shown later in Table 8-3) of low, medium and high density iron carbonate are used to predict the bulk elastic property.

Table 8-2: Volume fractions of phases

Phases	vol. fractions	measurement method
Porosity	0.1986±0.0041	MIP
Total iron content	0.113±0.014	Image analysis (BSE)
FA	0.276	Originally added
Clayey matrix	0.22	MK and LS originally added
total Iron Carbonate	0.1924	Remaining volume fraction

8.3.2.2 Mean-field homogenization method

Mori-Tanaka method has been used for determination of effective properties in cement-based materials (da Silva, Němeček, and Štemberk 2013; Sorelli et al. 2008; C. C. Yang 1997). It considers a discrete spherical inclusion embedded in an infinitely extended homogeneous reference medium (matrix). In this method, the homogenized bulk and shear moduli for two-phase materials can be quantified from the individual phase properties as given in Equation 8-4 and Equation 8-5. The individual phase shear and bulk moduli are obtained from their elastic modulus and Poisson's ratio.

$$k_{\text{hom}} = \frac{f_i k_i (1 + \alpha_{ref} . (\frac{k_i}{k_{ref}} - 1))^{-1}}{f_i (1 + \alpha_{ref} . (\frac{k_i}{k_{ref}} - 1))^{-1}} \quad [8\text{-}4]$$

$$\mu_{\text{hom}} = \frac{f_i \mu_i (1 + \beta_{ref} . (\frac{\mu_i}{\mu_{ref}} - 1))^{-1}}{f_i (1 + \beta_{ref} . (\frac{\mu_i}{\mu_{ref}} - 1))^{-1}} \quad [8\text{-}5]$$

Here i is the number of inclusions; f_i is the volume fraction of i^{th} inclusion; k_i and k_{ref} are the bulk moduli for the i^{th} inclusion and reference material respectively; μ_i and μ_{ref} are shear moduli for the i^{th} inclusion and reference material respectively and α_{ref} and β_{ref} are given in Equation 8-6 and Equation 8-7 (da Silva, Němeček, and Štemberk 2013; G. Constantinides et al. 2006).

$$\alpha_{ref} = \frac{3k_{ref}}{3k_{ref} + 4\mu_{ref}} \quad [8\text{-}6]$$

$$\beta_{ref} = \frac{6k_{ref} + 12\mu_{ref}}{15k_{ref} + 20\mu_{ref}} \quad [8\text{-}7]$$

From homogenized bulk and shear modulus, the homogenized Young's modulus can be calculated as (da Silva, Němeček, and Štemberk 2013; G. Constantinides et al. 2006):

$$E_{\text{hom}} = \frac{9k_{\text{hom}}.\mu_{\text{hom}}}{3k_{\text{hom}} + \mu_{\text{hom}}} \qquad [8\text{-}8]$$

A seven-step homogenization is performed as shown in Figure 8-4. In Step I, unreacted pure iron is the inclusion in high density iron carbonate matrix, and these two phases are homogenized. In Step II, partly reacted iron is incorporated into the homogenized (step-I) medium. In Step III, homogenized medium from step-II is added as inclusion to the medium-density iron carbonate. In Step IV, homogenized medium from step III is incorporated into the low-density iron carbonate matrix. Step V includes, inclusion of homogenized medium from step-IV into the clayey matrix phase. Step VI involves inclusion of fly ash in the homogenized medium from step-V. In step VII pores are added as inclusions in homogenized medium from step VI to obtain final homogenized Young's modulus.

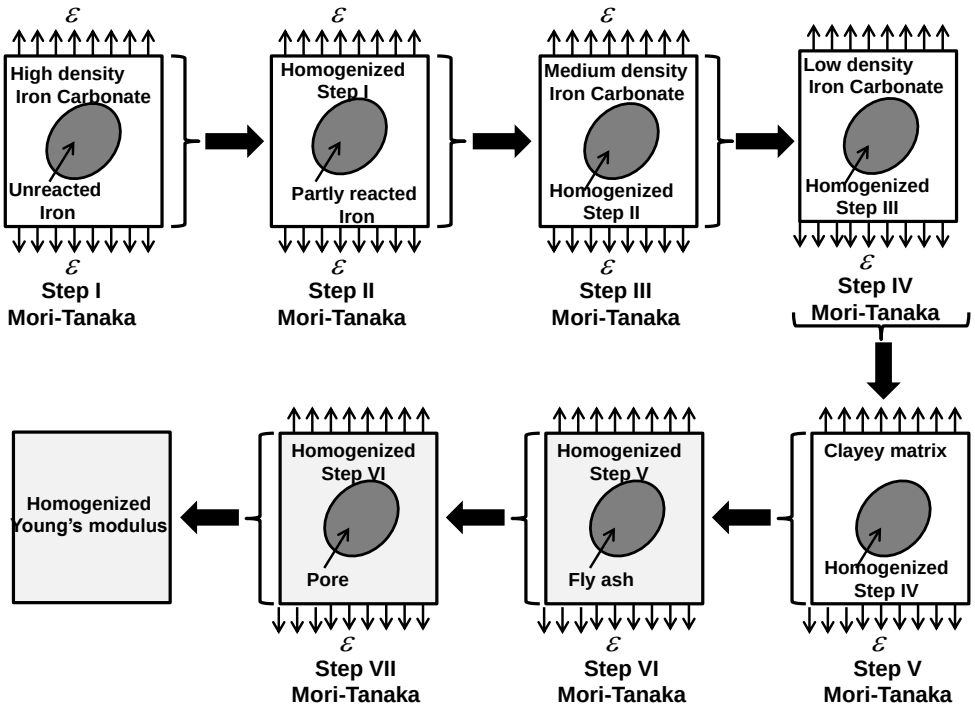

Figure 8-4: Schematic illustration of the multi-step homogenization process using Mori-Tanaka method

8.3.2.3 Homogenization results

Table 8-3 reports the homogenized Young's modulus for novel iron-based binder computed using the Mori-Tanaka approach. Table 8-3 also shows various combinations of volume fractions of low, medium and high density iron carbonate to evaluate the effect of relative volume fractions of these three types of carbonates on the overall homogenized Young's modulus. Group-1 in Table 8-3 assigns all the iron carbonate phase as low-density iron carbonate and all the iron particles as partially reacted/ oxidized iron particles, thus serving as a lower limit for the homogenized Young's modulus. On the other hand, group-21 assigns all the iron carbonate phase as high-density iron carbonate and all the iron particles as pure unreacted iron particles implying

the upper limit for the homogenized Young's modulus. The Mori-Tanaka approach predicts Young's modulus in the range 32.46 (Lower limit) – 38.15 GPa (Upper limit).

Table 8-3: Mean field homogenization Results

Group	Volume % of total carbonate product			Volume % of total Iron remaining		Predicted homogenized Young's modulus (GPa)
	Low density Iron Carbonate	Medium density Iron Carbonate	High density Iron Carbonate	Partly Reacted Iron particles	Pure Iron particles	
1	100	0	0	100	0	32.46
2	100	0	0	50	50	32.58
3	100	0	0	0	100	32.98
4	50	30	20	100	0	33.9
5	50	30	20	50	50	34.23
6	50	30	20	0	100	34.46
7	40	40	20	100	0	34.26
8	40	40	20	50	50	34.54
9	40	40	20	0	100	34.77
10	33.33	33.33	33.33	100	0	34.75
11	33.33	33.33	33.33	50	50	35.16
12	33.33	33.33	33.33	0	100	35.27
13	20	40	40	100	0	35.33
14	20	40	40	50	50	35.61
15	20	40	40	0	100	35.88
16	20	30	50	100	0	35.55
17	20	30	50	50	50	35.76
18	20	30	50	0	100	36.16
19	0	0	100	100	0	37.46
20	0	0	100	50	50	38.04
21	0	0	100	0	100	38.15

8.3.3 Experimental elastic property

Three point bending tests were done on prismatic beams of size 25.4 mm x 25.4 mm x 102.6 mm under center-point displacement controlled mode. The tensile elastic modulus

was extracted from the flexural load-deflection data using a moment-curvature-based inverse analysis methodology (C. Soranakom and Mobasher 2007; Chote Soranakom and Mobasher 2008; Mobasher, Bakhshi, and Barsby 2014; Mobasher et al. 2014) described in detail in this section.

8.3.3.1 Determination of tensile behavior of blends through back calculation using analytical tension model

Simplified tri-linear tension model and elastic-perfectly-plastic compression model are used generally for fiber reinforced and textile reinforced cementitious composites (C. Soranakom and Mobasher 2007; Chote Soranakom and Mobasher 2008; Mobasher, Bakhshi, and Barsby 2014; Mobasher et al. 2014) as shown in Figure 8-5 (a) and (b) respectively. The constant tensile strength (σ_{cst}) at the end of generalized tri-linear tension model, adopted for fiber-reinforced composites only (C. Soranakom and Mobasher 2007; Chote Soranakom and Mobasher 2008; Mobasher, Bakhshi, and Barsby 2014; Mobasher et al. 2014). Hence, this tensile model is essentially a bilinear one for unreinforced control mortars ($\sigma_{cst} = 0$). The material parameters, shown in Figure 8-5, are: tensile stiffness E, first crack tensile strain ε_{cr}, cracking tensile strength $\sigma_{cr} = \varepsilon_{cr} E$, post-cracking modulus E_{cr}, which is negative for strain-softening behavior and ultimate tensile strain ε_{tu} which is equal to transition strain ε_{tr} as the material is unreinforced. The compression model describes an initial linear response before the yield point ($\varepsilon_{cy}, \sigma_{cy}$) is reached. Beyond the yield point the material maintains constant yield stress ($\sigma_{cy} = \omega \varepsilon_{cr} \gamma E$) up to the ultimate compressive strain (ε_{cu}).

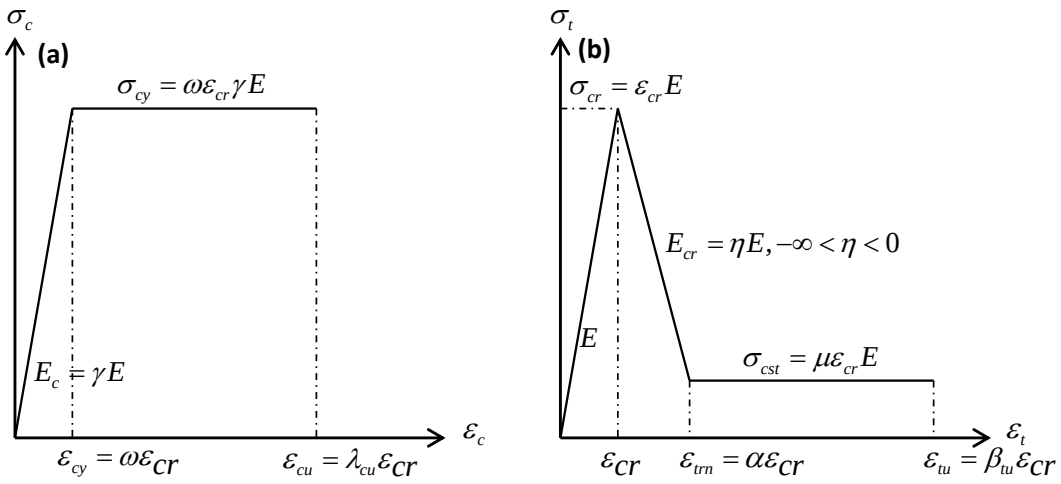

Figure 8-5: Simplified (a) compression and (b) tension model for strain-softening cementitious materials

All the parameters are normalized with respect to two main material parameters Young's modulus (E) and first crack tensile strain (ε_{cr}) as shown in Table 8-4.

Table 8-4: Back calculation model parameters (C. Soranakom and Mobasher 2007; Chote Soranakom and Mobasher 2008; Mobasher, Bakhshi, and Barsby 2014; Mobasher et al. 2014)

Normalized tensile strain:	$\alpha = \frac{\varepsilon_{trn}}{\varepsilon_{cr}}$
Constant post peak stress level:	$\mu = \frac{\sigma_{cst}}{E\varepsilon_{cr}} \approx 0$
Post-crack modulus:	$\eta = \frac{E_{cr}}{E}$
Compressive yield strain:	$\omega = \frac{\varepsilon_{cy}}{\varepsilon_{cr}}$
Tensile strain at bottom fiber:	$\beta = \frac{\varepsilon_t}{\varepsilon_{cr}}$
Compressive strain at top fiber:	$\lambda = \frac{\varepsilon_c}{\varepsilon_{cr}}$

The normalized maximum tensile strain parameter β is linearly related to the normalized compressive strain at top fiber λ as follows:

$$\beta = \frac{\varepsilon_{t\_bottom}}{\varepsilon_{cr}};\ \lambda = \frac{\varepsilon_{c\_top}}{\varepsilon_{cr}};\ \frac{\lambda\varepsilon_{cr}}{kd} = \frac{\beta\varepsilon_{cr}}{d-kd} \text{ or } \lambda = \frac{k}{1-k}\beta \quad [8\text{-}9]$$

The normalized stress-strain responses can be defined using the above normalized parameters as follows (C. Soranakom and Mobasher 2007; Chote Soranakom and Mobasher 2008; Mobasher, Bakhshi, and Barsby 2014; Mobasher et al. 2014):

$$\frac{\sigma_c(\lambda)}{E\varepsilon_{cr}} = \begin{Bmatrix} \gamma\lambda & for & 0 \le \lambda \le \omega \\ \gamma\omega & for & \omega < \lambda \le \lambda_{cu} \\ 0 & for & \lambda_{cu} < \lambda \end{Bmatrix};\quad \frac{\sigma_t(\beta)}{E\varepsilon_{cr}} = \begin{Bmatrix} \beta & for & 0 \le \beta \le 1 \\ 1+\eta(\beta-1) & for & 1 < \beta \le \alpha \\ \mu & for & \alpha < \beta \le \beta_{tu} \\ 0 & for & \beta_{tu} \le \beta \end{Bmatrix} \quad [8\text{-}10]$$

Kirchhoff hypothesis of plane section remaining plane is applied here. The strain distribution is assumed to be linear and the shear deformations are ignored. The stress distributions across the cross section of the beam in three stages of tensile strain (

$$\frac{\sigma_c(\lambda)}{E\varepsilon_{cr}} = \begin{Bmatrix} \gamma\lambda & for & 0 \le \lambda \le \omega \\ \gamma\omega & for & \omega < \lambda \le \lambda_{cu} \\ 0 & for & \lambda_{cu} < \lambda \end{Bmatrix};\qquad \frac{\sigma_t(\beta)}{E\varepsilon_{cr}} = \begin{Bmatrix} \beta & for & 0 \le \beta \le 1 \\ 1+\eta(\beta-1) & for & 1 < \beta \le \alpha \\ \mu & for & \alpha < \beta \le \beta_{tu} \\ 0 & for & \beta_{tu} \le \beta \end{Bmatrix} \quad [8\text{-}10)$$

are obtained in closed form (C. Soranakom and Mobasher 2007; Chote Soranakom and Mobasher 2008; Mobasher, Bakhshi, and Barsby 2014; Mobasher et al. 2014). The moment capacity of the beam for the imposed tensile strain is obtained based on the forces and centroidal distances in the stress profile (C. Soranakom and Mobasher 2007; Chote Soranakom and Mobasher 2008; Mobasher, Bakhshi, and Barsby 2014; Mobasher et al. 2014). The moment M_i and curvature ϕ_i at any stage i corresponding to tensile

strain level β are normalized with respect to cracking moment and curvature respectively in order to obtain normalized moment and curvature.

$$M' = \frac{M_i}{M_{cr}} \; ; \quad M_{cr} = \frac{1}{6} b d^2 E \varepsilon_{cr} \qquad [8\text{-}11]$$

$$\phi' = \frac{\phi_i}{\phi_{cr}} \; ; \quad \phi_{cr} = \frac{2\varepsilon_{cr}}{d} \qquad [8\text{-}12]$$

The location of neutral axis, k, moment capacity, M', and the curvature, ϕ' are obtained in closed form and shown in appendix section for the three stages of tensile strain level, β (Stage I: $0 < \beta \leq 1$; stage II: $1 < \beta \leq \alpha$ and stage III: $\alpha < \beta \leq \beta_{tu}$). The first stage represents linear elastic behavior and it is terminated by initiation of tensile cracking which shifts the neutral axis towards the compression zone. In the second and third stage there are two possibilities: (i) elastic compression zone or (ii) plastic compression zone. All these possibilities are incorporated in the model in order to develop the moment-curvature relationship. The load-deflection response can be quantified from moment distribution and moment-curvature relationship employing crack-localization rules (C. Soranakom and Mobasher 2007; Chote Soranakom and Mobasher 2008; Mobasher, Bakhshi, and Barsby 2014; Mobasher et al. 2014). The deflection at mid-span can be calculated using double integration of curvature distribution or by closed form expressions obtained through moment-area method (C. Soranakom and Mobasher 2007; Chote Soranakom and Mobasher 2008; Mobasher, Bakhshi, and Barsby 2014; Mobasher et al. 2014) which are shown as follows:

$$\delta_{cr} = \frac{1}{12} L^2 \phi_{cr} \quad \text{(elastic)} \qquad [8\text{-}13]$$

$$\delta_u = \frac{\phi_u L_p}{8}\left(2L - 2L_P\right) + \frac{M_u \phi_{cr} L}{12 M_{cr}}\left(L - 2L_P\right) \quad \text{(Deflection-softening)} \qquad [8\text{-}14]$$

Where L is the length of the beam and L_P represents length of the plastic zone under three-point bending. The model parameters (Table 4) are selected in order to obtain simulated load-deflection response that fits to the experimental flexural load-deflection behavior. The fitting parameters, thus obtained, quantify the tensile modulus, tensile strength and ultimate tensile strain corresponding to experimental load-deflection data. The bilinear version of the tension model (considering $\sigma_{cst} = 0$) is used to quantify tensile behavior in a later chapter. The current study uses only linear elastic part of the tension model to calculate tensile stiffness of iron-based binder from flexural load-deflection data.

8.3.3.2 Quantification of tensile Young's modulus using inverse analysis and comparison with predicted homogenized Young's modulus

Four replicate beams were tested to obtain flexural load-deflection data. The tests were terminated at about 90% of the peak load, calculated previously as reported in previous chapters. The linear load-deflection data is fitted with simulated load-deflection in order to obtain optimal fitting parameter E. The tensile Young's modulus is found to be 33.4 ± 2.27 GPa which falls well within the upper and lower limits of the macro-scale estimates of homogenized elastic modulus using two approaches. Hence the experimental Young's modulus is in good agreement with those predicted using mean field microstructural homogenization. Results of this comprehensive study establish the material property-

microstructure link for novel iron-based binder using a combination of MIP, Image analysis, statistical nanoindentation and mean-field homogenization models.

8.4 Conclusions

This study reports the individual intrinsic phase elastic properties determined using statistical nanoindentation technique. Seven distinct phases are identified. The iron carbonate reaction product is further classified as low-density, medium-density and high-density iron carbonate. The individual elastic properties are also quantified. Since the BSE SEM images did not have absorption-contrast to reliably identify the solid phases other than bright iron particles in the iron-based binder, the volume fractions of relatively inert phases such as fly ash and clayey matrix phase are assumed to be same as initial volume fractions of such materials added. The porosity is experimentally determined using MIP and image analysis is used on a series of BSE SEM images to calculate volume fraction or total iron particles. In addition, different combinations of volume fractions of low-density, medium-density, high-density iron carbonate product, unreacted/partly reacted iron particles are employed to quantify lower/upper limits of homogenized Young's modulus and to evaluate the effect of such variations in volume fractions on the overall homogenized property. The individual phase elastic properties determined using nanoindentation along with the pore volume fraction from MIP and solid phase volume fractions from different methods were used in multi-step micromechanical mean-field homogenization model (Mori-Tanaka method) to determine a homogenized Young's modulus of the composite material. The homogenized Young's modulus was found to be in good agreement with the experimental macro-scale Young's modulus. The study described here, linking the microstructure and properties of a highly

heterogeneous material (at the microscale), and the use of upscaling models to predict the bulk elastic response, is expected to lead to better material design of iron-based binder, which currently relies greatly on experimentally obtained bulk mechanical response.

Chapter 9 High-temperature Resistance of Iron Carbonate Binder

9.1 Introduction

Resistance to fire related hazards is one of the important factors for the wide spread acceptance of a material for structural applications. Concrete containing ordinary Portland cement (OPC) is one of most commonly used construction materials. Thus, it has attracted a lot of investigation in the recent past on its resistance to high temperature incidents such as fire (U. Schneider 1988; Naus 2006; Phan et al. 1997). These studies have mainly focused on the residual compressive strength and showed that Portland cement concrete performs very poorly at high temperature. It starts to lose its compressive strength after the critical exposure temperature of approximately 600°C. This loss has been attributed to the decomposition of calcium hydroxide (CH) to calcium oxide and water and consequent volume expansion after cooling due to the rehydration of calcium oxide (Georgali and Tsakiridis 2005). Also explosive spalling occur between the temperature 480 and 510°C which reduces the load bearing capacity of the concrete structure substantially (Chan, Peng, and Anson 1999). Also, due to evaporation of water at around 100-110 °C, porosity increases and thus it lowers the residual strength (Demirel and Keleştemur 2010).

Supplementary cementitious materials such as blast furnace slag, flyash and silica fume, which are considered as alternative to OPC, have been shown to exhibit superior performance in terms mechanical strength in many cases. They are either used as activated binder or in blended form with OPC. Resistance of alkali-activated Fly ash towards fire has also been investigated (Dias, Khoury, and Sullivan 1990). It has been found that fly ash-based binder has superior resistance to high temperature relative to

OPC. Fly ash showed remarkably higher compressive strength (40% of reference samples) up to temperature of 600° C. In a similar study (Sarshar and Khoury 1993), it was found that mixes where OPC is partially replaced by fly ash showed more stability at 600°C as compared to OPC paste. OPC paste lost about 52% of its initial strength whereas OPC blended with FA paste just lost 30 % of its strength. It has also been observed that OPC samples started spalling after 600° C but nothing of that sort was observed for fly ash samples (Sarker, Haque, and Ramgolam 2013). Alkali activated slags also offers remarkable potential as fire resistant material as observed by various researchers. High degree of stability even at as high temperature as 1000°C is shown in the literature (Temuujin et al. 2011). The presence of highly condensed gel product, low chemically bounded water and absence of CH were attributed to this superior performance (W.-C. Wang, Wang, and Lo 2014; Temuujin et al. 2011). Further studies by researchers (Zuda et al. 2007) showed that alkali activated slag has improved thermal properties such as thermal diffusivity and thermal conductivity due to refine pore structure. Research have shown that silica fume doesn't perform well as a fire resistant (Hertz et al. 2005). It has been observed that OPC with silica fume showed explosive spalling at a heating rate as low as 1° C/min and found that parameters such as increased moisture content, reduced permeability, and decreased tensile strength increased the rate of spalling (Hertz et al. 2005). However it was suggested (Morsy, Shebl, and Rashad 2008) that inclusion of metakaolin with SF can improve the resistance to fire. The best dosage of SF was concluded to be in the range of 10 to 15 % by volume of cement. But there is no standard procedure to study the high temperature effects testing on the alternate binder material. With a view to develop a novel sustainable carbon-negative

binder, an explicit study was carried out as explained in previous chapters to explore the possibility of carbonating waste iron powder to produce an acceptable binder. While previous chapters on mechanical behavior of iron-based novel binder confirmed acceptable mechanical behavior of iron-based binder for structural applications, the current chapter evaluates the résistance of this novel binder towards high temperature and provides valuable information durability characteristics of this novel iron-based binder at elevated temperatures. This chapter aims at substantiating the characteristics of the IC at high temperatures and explores the possibility of using this novel binder for high temperature applications.

9.2 Experimental Program

9.2.1 Materials, Mixtures and Specimen Preparation

A metallic iron powder generated as by-product of shotcreting facility with a median particle size of 19.03 µm, is used as chief raw material. They are elongated and angular in shape. Other materials such as Class F fly ash and metakaolin conforming to ASTM C 618, and limestone powder (median particle size of 0.7 µm) conforming to ASTM C 568 were also used for binder synthesis. For minimizing of water demand and obtaining necessary cohesiveness metakaolin was used. An organic reducing agent/chelating agent for metal cations (oxalic acid, in this case) was also used. Commercially available Type I/II OPC conforming to ASTM C 150 was used to prepare cement pastes to act as a as the baseline system to compare the properties of the novel iron-based binder systems. The mix proportion of the iron-based binder mixture used in this study consists of 60% iron

powder, 20% fly ash, 8% limestone, 10% metakaolin, and 2% organic acid by mass which was established as the best mixture by the authors in their previous works. This combination demonstrated the highest compressive strength and lowest porosity among a series of trial mixtures prepared as part of material design studies. The mixing procedure involves initial dry mixing of all the starting materials and then adding water to obtain a uniform cohesive mixture. A mass-based water-to-solids ratio (w/s)m of 0.24 was used to attain a cohesive mix, which also was arrived at based on several preliminary studies.

Prismatic specimens of size 127 mm (length) x 25.4 mm (depth) x 25.4 mm (width) were prepared in polypropylene molds and immediately placed inside clear plastic bags filled with 100% CO_2 in room temperature inside a fume hood. The samples were demolded after 1 day of carbonation in order to attain enough strength so as to open the molds without breaking the specimen. After demolding, the beams were placed again in a 100% CO_2 environment for another 5 days. The bags were refilled with CO_2 every 12 hours or so to maintain saturation level. After the respective curing durations of CO_2 exposure, the samples were placed in air at room temperature to allow the moisture to evaporate for 4 days. Companion OPC mixtures of the same size as mentioned above were prepared with a water-to-cement ratio (w/cm) of 0.40, which is common for moderate-strength concretes in many buildings and infrastructural applications. The OPC beams were demolded after 1 day and were kept in a moist chamber (>98% RH and 23±2 °C) for a total of 28 days. In order to investigate the high temperature effect on OPC and IC, besides ambient temperature the paste and mortar specimens were heated up to 300, 600 and 800°C in furnace with 3-5°C heating rate and kept at the target temperature for two

hours. After exposure to elevated temperatures the specimens were allowed to cool to the room temperature inside the furnace.

9.2.2 Determination of Flexural Strength using three-point bending test

The flexural strengths of both iron-based and OPC binders were determined using standard center-point loading as per ASTM C293/293M-10, on beams having a span of 101.6 mm. The three-point bend tests on prismatic beams were performed under mid-span deflection-controlled mode. For each mixture four replicate beams were tested.

9.2.3 Thermogravimetric analysis (TGA)

A Perkin Elmer STA 6000 simultaneous thermal analyzer was used for thermo-gravimetric analysis (TGA). The analyzer was programmed to increase the temperature from 30°C to 995°C at a rate of 15°C/minute in a N_2 environment. The samples for TGA were taken from the beam samples. Samples from both surface as well as core of the cylindrical specimens were analyzed in order to assess the influence of different elevated temperatures on iron carbonate binder.

9.2.4 Mercury Intrusion Porosimetry (MIP)

To evaluate the changes in pore structure, MIP was performed on small samples of oven dried novel iron-based binder samples using a porosimeter that can generate a maximum pressure of 414 MPa and evaluate a minimum pore diameter of 0.003 μm. The test was performed in two steps: the low pressure step removes the gases and fills the sample holder with mercury. The test is then carried out up to 345 KPa. The high pressure step reaches pressures of up to 414 MPa. The contact angle and surface tension values employed were 130° and 0.485 N/m respectively.

9.2.5 Fourier Transform Infrared Spectroscopy (FTIR)

FTIR spectra of the activated pastes were obtained using an ATI Mattson Genesis FTIR spectroscope with a single reflection attenuated total reflectance diamond crystal attachment. The spectra of the reaction products before and after each temperature were obtained in the wavenumber range of 4000 to 400 cm−1 at a resolution of 1 cm−1.

9.2.6 X-ray diffraction (XRD)

XRD was performed on samples to determine phase composition of novel iron-based binder at different temperatures. The XRD patterns of powdered samples were evaluated using High Resolution X-ray Diffractometer (PANALYTICAL X'PERT PRO) in the 2θ range of 10-90° with an increment of 0.05°.

9.2.7 Scanning Electron Microscopy and Electron Microprobe

Microstructural study of the iron-based systems before and after high temperature exposure was carried out using a Philips XL30 Field Emission Environmental scanning electron microscope (FESEM). Prismatic cube samples of size 10 mm x 10 mm x 10 mm was cut from the beam samples using a diamond saw and the small samples were mounted to the stub with epoxy resin for FESEM. A suitable combination of grinding and polishing is applied to achieve a level of flatness which eliminates the errors. The microstructural study was carried out on the sample near the surface of the beam sample. The elemental mapping was performed using JEOL JXA-8530F Hyperprobe (Electron Microprobe).

9.3 Results and Discussions

9.3.1 Flexural Strength and Pore-structure

Figure 9-1(a) presents the results of flexural strength of novel iron-based binder and OPC paste at different temperatures. It is observed that at room temperature, iron-based binder has much higher strength (approximately 85 %) as compared to OPC. But as the temperature increased to 300°C, a major loss in strength was observed for iron-based binder (around 84 % of its initial strength) whereas OPC gained strength (by around 34.87%) although at 300°C iron-based binder shows almost similar strength as compared to OPC. The strength gained in the OPC can be attributed to the autoclaving effect (Rashad et al 2014) which increased the rate of product formation. The pore structure of OPC also supports the diffusion of steam for autoclaving effect. On the other hand, the strength loss in iron-based binder at 300°C was attributed to the decomposition of carbonate binding complex (carbonate-oxalate-cancrinite) (Olysych et al. 2011; Das, Souliman, et al. 2014). This loss in strength is also reflected in the form of about 20% reduction in bulk density which is presented in Figure 9-1(b). At 600°C, there was a slight increase in the strength for iron-based binder whereas OPC lost its strength by 42 %. The loss in strength in OPC can be attributed to the decomposition of CH at around 500 °C and the subsequent rehydration of calcium oxide which leads to increase in volume by 44% (U. Schneider 1988). The degradation of the CSH gel product may also contribute to the strength loss. On the other hand, slight increase in strength in iron-based binder may be attributed to temperature-induced crystallization process which is evaluated later in this chapter. At 800°C, the residual strength of iron-based binder increased significantly by 68 percent when compared to residual strength at 600°C

whereas OPC lost almost all its mechanical strength. Strength loss for OPC can be attributed to the total decomposition of gel product (Andiç-Çakır, Çopuroğlu, and Ramyar 2015) whereas significant increase in strength in iron-based binder is likely to be caused by increase in crystallinity and formation of denser structure at 800°C which are evaluated later in this chapter. At 800°C, iron-based binder exhibits about 2.7 MPa which is about 5 times higher as compared to that of OPC.

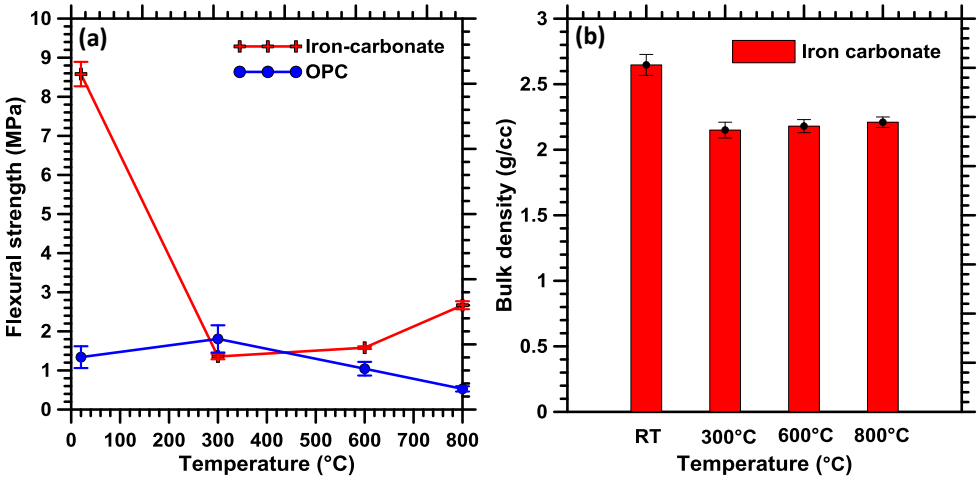

Figure 9-1: (a) flexural strength of novel iron-based binder and OPC paste; (b) bulk density of iron-based binder at different temperatures

Mercury intrusion porosimetry (MIP) is performed on the iron-based binder samples at different temperatures in order to assess effect of pore structure on strengths at elevated temperatures. Samples were collected approximately 5 mm under the surface of the prismatic beams used for flexural strength evaluation. Figure 9-2 shows the MIP intrusion curves and the differential plots at different temperatures. Results suggest that the total volume of mercury intruded increased significantly when the temperature was increased from 20 °C to 300 °C. The volume remained almost same when the temperature was increased from 300 °C to 600°C and the volume reduced by 20% as compared to that at 600°C when the temperature was increased from 600 °C to 800°C.

Figure 9-3 shows evolution of porosity, evaluated using MIP, as the temperature is increased 20 °C to 300 °C. Porosity remains almost invariant of temperatures at the range of 300 °C to 600°C and beyond 600°C the porosity starts decreasing. These results are in line with the flexural strengths observed in iron-based binder at different temperatures (Figure 9-1(a)).

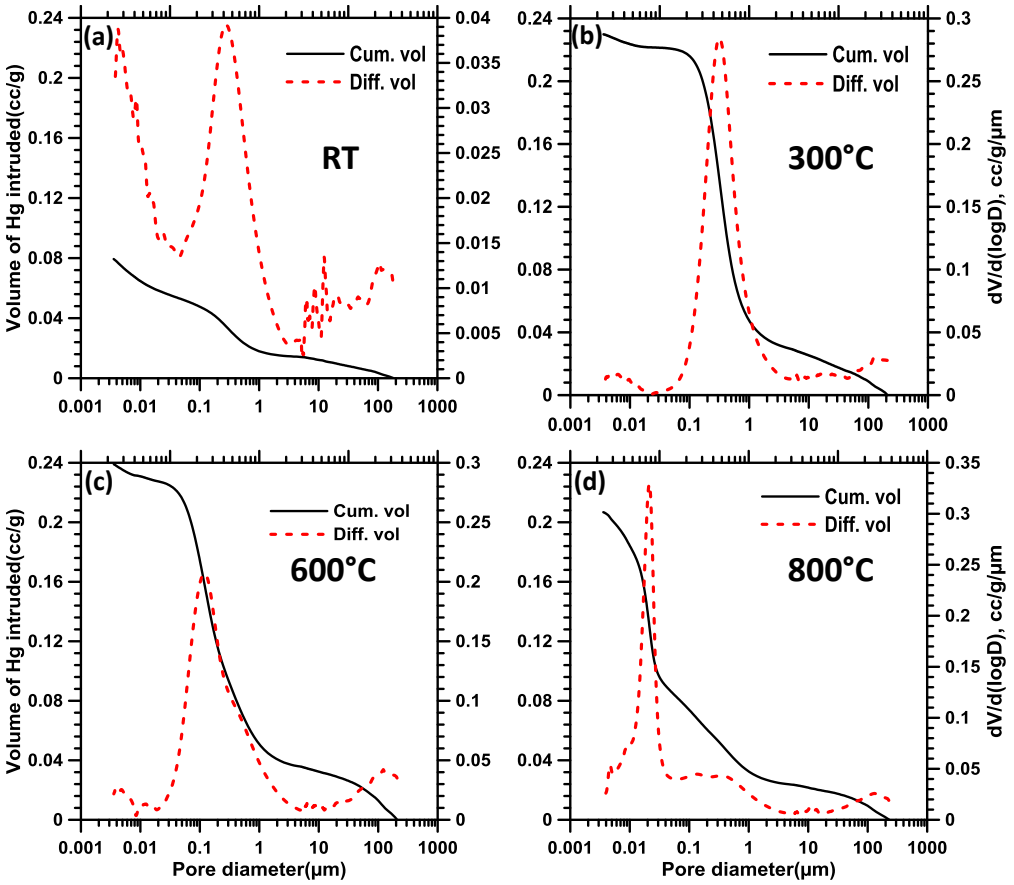

Figure 9-2: Pore-structure information evaluated using MIP at (a) room temperature; (b) 300°C; (c) 600°C; (d) 800°C

The differential intrusion plots are also shown in Figure 9-1 for different temperatures with a view to understand the effect of elevated temperatures on the pore-size that provides valuable qualitative comparison of densification as the temperature is increased. The quantified critical pore diameters at different temperatures are shown in Figure 9-3.

The critical pore diameter increases slightly as the temperature is increased from 20 °C to 300 °C. But, beyond 300 °C, critical pore diameter decreases significantly. At 600 °C, the critical pore diameter dropped from 0.28 micron to 0.12 micron and at 800 °C the diameter even further reduced to 0.02 micron. It gives an indication that the degree of crystallinity increases as the temperature is increased from 300 to 600°C. It increases even more at 800°C which is also responsible for significant increment in strength with increase in temperature at that range.

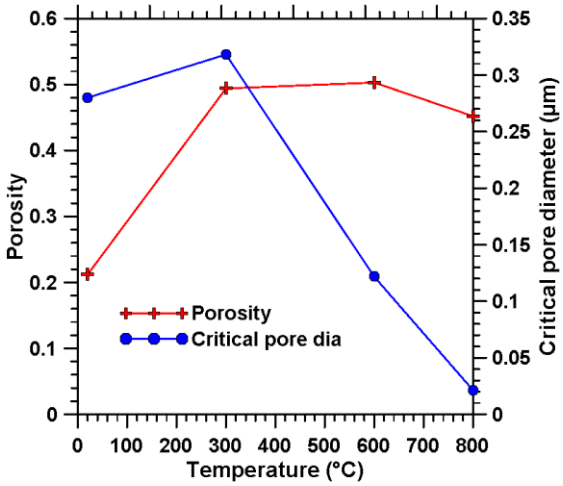

Figure 9-3: Variation of porosity and critical pore diameter with varying exposure-temperature

9.3.2 Extent of thermal decomposition using TGA

Thermogravimetric analysis is performed on iron-based binder samples at different temperatures to evaluate stability of different phases in iron-based novel binder at elevated temperatures. Thermal stability of the reaction product especially iron carbonate complex is critical towards its mechanical behavior at elevated temperatures which is evaluated here. Figure 9-4 shows TG and DTG plots for samples exposed to different temperatures. The TG curves suggest that the total weight remaining increases as the sample exposure-temperature is increased. The maximum amount of increase is observed

when the exposure-temperature is increased from room temperature to 300 °C. Total weight remaining increased from 80% for room temperature sample to about 96% for the sample exposed to 300°C implying a significant amount to thermal decomposition of iron carbonate complex reaction product. It is also reflected in the form of drastic increase in porosity (Figure 9-3) due to decomposition of iron carbonate oxalate reaction product as the exposure-temperature is increased from room temperature to 300 °C.

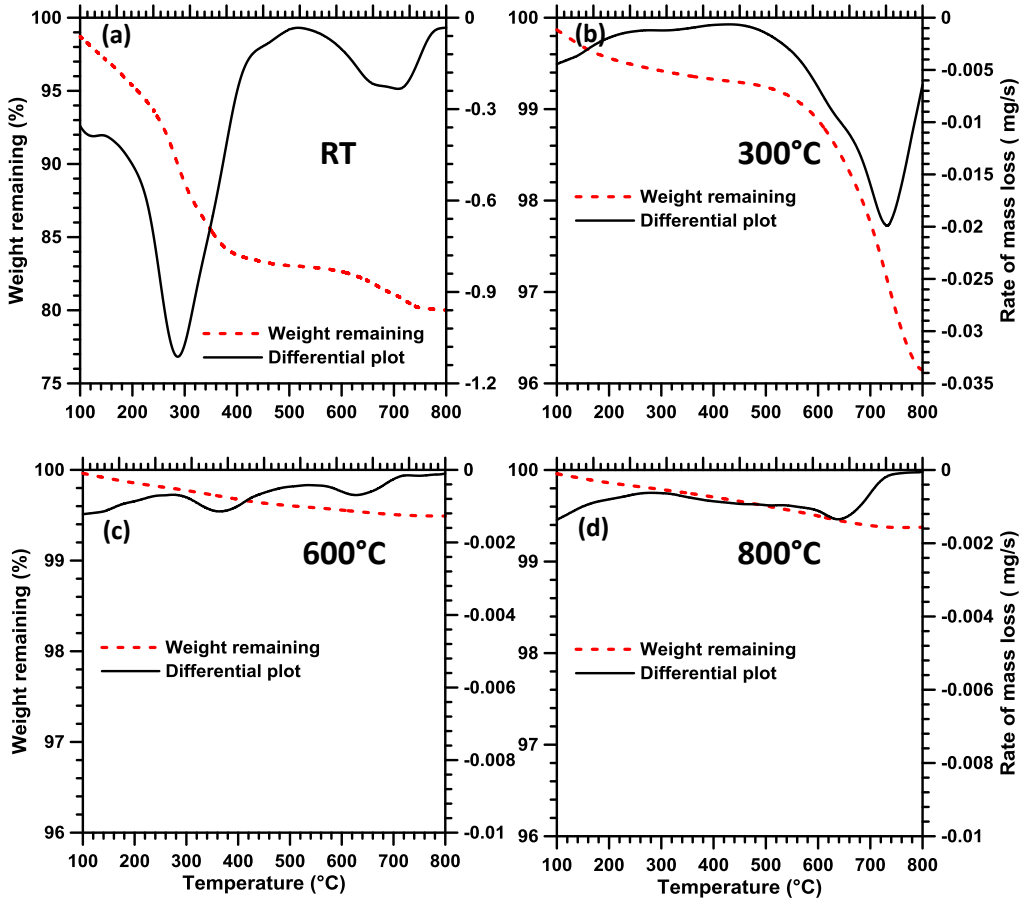

Figure 9-4: TG and DTG curves for iron-based binder samples exposed to (a) room temperature; (b) 300°C; (c) 600°C; (d) 800°C

At room temperature, three distinct peaks were observed. The peak around 110 °C represents the evaporable water, the one at 300 °C (Das, Souliman, et al. 2014; Olysych et al. 2011) represents thermal decomposition of carbonate-oxalate-cancrinite and the one

at around 750 °C is attributable to decomposition of calcium carbonate. All the peaks are strong and distinct at room temperature.

As the temperature was elevated to 300 °C, the peak at 110°C became nonexistent and the peak at 300°C lost its intensity significantly as compared to room temperature. This can be attributed to the fact that the water is evaporated and the iron carbonate complex is decomposed leaving the trace amount in the system. Table 9-1 shows that the weight loss in the temperature range 250-400°C decreased from 9% to 0.14% which represents the decomposition of iron carbonate complex. At 300 °C, the calcite peak is still present in the system as calcium carbonate is expected to be decomposed at higher temperatures. Table 9-1 shows that the binder retains calcium carbonate when the sample is heated from room temperature to 300 °C.

For the sample exposed to 600°C, the major change was observed for the peak at around 750 °C. The peak at around 750 °C, which corresponds to thermal decomposition of calcite, reduced its intensity significantly implying almost complete decomposition of calcite present in the system (faster decomposition of calcite due to presence of organic acid). Table 9-1 shows only trace amount of calcite (0.07%) remaining in the system. Figure 9-4(c) shows the iron carbonate peak but it is insignificant considering only trace amount (0.15%) of weight loss corresponding to that temperature range as shown in Table 9-1.

At 800 °C, the iron carbonate complex and calcium carbonate complex has totally decomposed although some trace amounts are left in the system as shown in Table 9-1. Hence, it is most likely that some crystalline iron oxides are formed after decarbonation

of iron carbonate which is responsible for increase in strength. This aspect is evaluated in detail using FTIR and XRD spectra as reposted in the forthcoming sections.

Table 9-1: Quantitative analysis using TGA for samples exposed to different temperatures

Percent weight loss (250 to 400 °C)				Percent limestone powder remaining (%)			
20°C	300°C	600°C	800°C	20°C	300°C	600°C	800
9.05	0.14	0.15	0.04	4.85	4.841	0.07	0.05

9.3.3 Evaluation of effect of elevated temperature using FTIR

Figure 9-5 shows the FTIR spectra of Iron-based binder subjected to different temperatures in order to evaluate evolution of reaction product as the temperature is increased. Overall, three distinct peaks are observed in the spectra that is needed to be evaluated here. The peak at around 1410-1425 cm^{-1} represent stretching of the carbonate (C-O) bond whereas the peak at 860-880 cm^{-1} represents out of plane bending of C-O bond (Smith 1998; Miller and Wilkins 1952). The peak observed at around 930-1060 cm-1 represents the asymmetric stretching of Si-O-Si bond present in fly ash (Smith 1998; Miller and Wilkins 1952; Rovnaník, Bayer, and Rovnaníková 2013).

At room temperature, peaks corresponding to stretching and out of plane bending of C-O bond (inorganic carbonate) are present indicating presence of iron carbonate and calcite in the system although they are not individually differentiable through this process. A broad peak corresponding to asymmetric stretching of Si-O-Si is also present. The broadness of the peak (higher width) signifies presence of structural disorder in the silicate network and thus, amorphous nature of silicates at room temperature (Dimas, Giannopoulou, and Panias 2009; Smith 1998).

When the temperature is increased to 300 °C, the intensity of carbonate peaks (1424 and 875 cm^{-1}) relative to silicate peak (1048 cm^{-1}) is reduced which can be attributed to complete thermal decomposition of iron carbonate reaction product as was confirmed by TGA results in the previous section. Hence, the carbonate peaks for the sample exposed to 300 °C represents presence of mainly calcium carbonate as was found in TGA results. The broad silicate peak corresponding to amorphous silica is still present at 300 °C.

At 600 °C, the carbonate (C-O) peaks disappear due to complete decarbonation as was found in TGA results in the previous section and the width of the silicate peak is reduced significantly as compared to that in lower temperatures. This reduction in width can be attributed to the increase in polymerization of silica species and decrease in variability of the Si species which is reflected in the form of slight increasing tendency of flexural strength as the exposure-temperature is increased from 300°C to 600°C.

The carbonate peak is absent for the sample at 800 °C as all the carbonates are decomposed well below that temperature as confirmed by TGA. The width of the peak for Si-O-Si is reduced further as the temperature is increased from 600 to 800°C implying conversion of more free amorphous silica into relatively more polymerized silica. Another important observation from the FTIR spectra is that the silicate peak becomes narrower and more symmetric as the exposure temperature is increased after decarbonation of iron carbonate (beyond 300°C). These results imply reduction in the amount of amorphous silica and formation of relatively more crystalline silica species resulting in increased flexural strength relative to the strength at 300°C. It should be noted that the crystalline phases generally show characteristic peaks at wavenumbers lower than 750 cm^{-1}. Hence any possible formation of crystalline product due to thermal

decomposition is not detectable using FTIR spectra with minimum wavenumber higher than 750 cm^{-1}. This aspect is evaluated further using XRD spectra for more insight on the evolution of reaction product and possible formation of crystalline products at higher temperatures as presented in the forthcoming section.

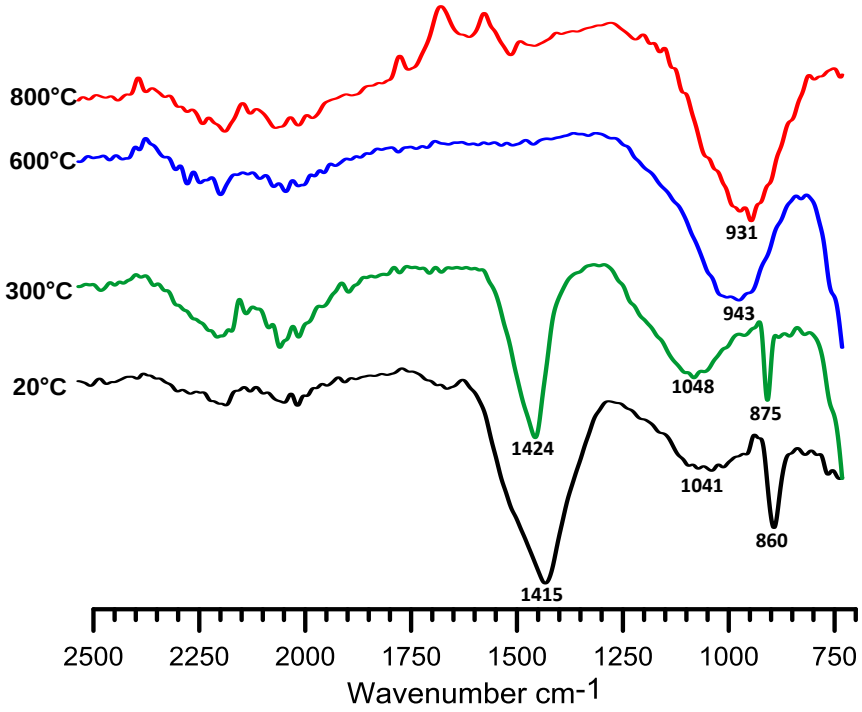

Figure 9-5: FTIR spectra for iron-based binder samples exposed to different temperatures

9.3.4 X-ray diffraction (XRD) analysis of materials after exposure to elevated temperature

XRD is done on the samples subjected to various temperatures in order to evaluate elemental compositions/ possible formation of new compounds at different temperatures that is responsible for the mechanical behavior shown in Figure 9-1.

At room temperature, siderite, which is naturally occurring iron carbonate mineral, is found predominantly as expected. In addition, peaks corresponding to calcite are also visible. One peak each of quartz and magnetite (Fe_3O_4) is also present. While waste iron

powder from shot blasting facility is expected to contain some oxidized iron particles (Fe_3O_4), fly ash contains trace amount of quartz which is captured here at room temperature sample.

When the temperature is increased from room temperature to 300°C, iron carbonate decomposes in presence of oxygen and forms magnetite (Fe_3O_4) (Koziol 1999).

$$6FeCO_3 + O_2 \rightarrow Fe_3O_4 + 3CO_2 \uparrow \quad [9\text{-}1]$$

Formed magnetite is further oxidized to γ-Fe_2O_3 (Lepp 1957)

$$4Fe_3O_4 + O_2 \rightarrow 6\gamma - Fe_2O_3 \quad [9\text{-}2]$$

The above oxidation reaction is thermodynamically favorable above 200°C (Lepp 1957). That's why mixture of both Fe_3O_4 and γ-Fe_2O_3 are present in the XRD spectra for the sample exposed to 300°C. Again, decomposition of iron carbonate results in drastic reduction in flexural strength. Besides, peak corresponding to calcite is also detected in the XRD spectra at 300°C which is in line with the TGA results presented in the previous section.

Starting at 375°C γ-Fe_2O_3 is oxidized further to α-Fe_2O_3, which is hematite. In addition, at temperatures above 575°C magnetite is also directly oxidized to form hematite (Lepp 1957).

$$4Fe_3O_4 + O_2 \rightarrow 6\alpha - Fe_2O_3 \quad [9\text{-}3]$$

The sample exposed to 600°C shows both magnetite and hematite in the XRD spectra. Both magnetite and hematite are crystalline in nature and hence it justifies strength-increment with increasing temperature. Sample exposed to 800°C also shows both

magnetite and hematite in the XRD spectra. But, the number of peaks corresponding to hematite is higher at 800°C as compared to that found at lower temperatures implying increase in crystallinity. Again, increase in number of peaks corresponding to quartz at 800°C implies polymerization of free silica at elevated temperature which supports the earlier hypothesis on polymerization of silica (reduction in full-width at half-maximum (FWHM) of silicate peak) at elevated temperatures identified by FTIR spectra (Figure 9-5). Another interesting finding is that the FWHM of the peaks corresponding to Fe_3O_4 and Fe_2O_3 reduces (as can be seen from Figure 9-6) as the temperature is increased from 300°C to 800°C implying significantly higher crystallinity at higher temperature which is reflected in the form of significant increase in flexural strength. The XRD spectra for sample exposed to 800°C matches well with that of α-Fe_2O_3 nanoparticles (hematite) (Dar and Shivashankar 2014).

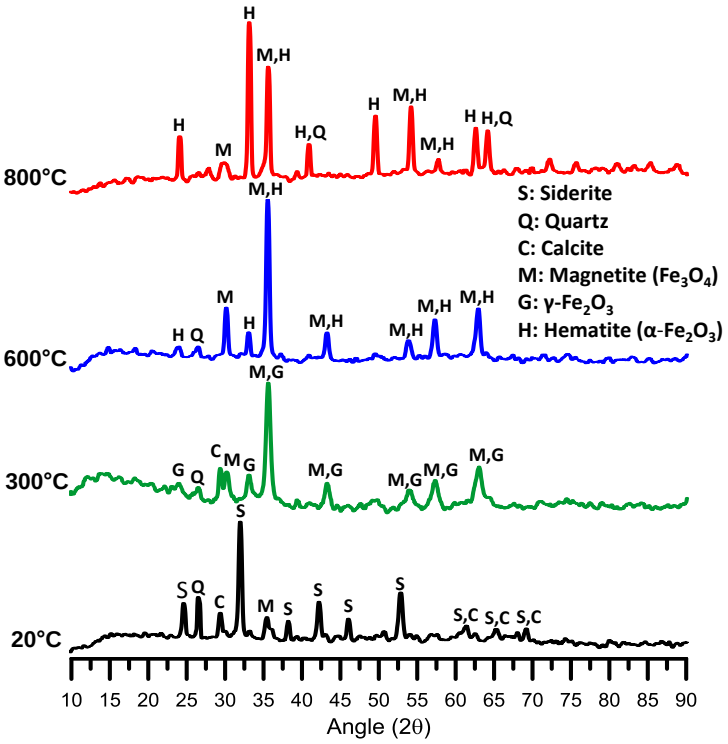

Figure 9-6: XRD spectra for iron-based binder samples exposed to different temperatures

9.3.5 Microstructural Evaluation

Figure 9-7(a) shows micrograph of sample at room temperature. The bright particles are the iron particles. It was confirmed in the previous chapter on pore- and micro-structural characterization through EDS that the reaction product (light gray phase around iron particles) contains iron, carbon and oxygen as the major component, followed by silica, aluminum, and calcium. The results from TGA, and XRD also confirms formation of iron carbonate as the major reaction product in the system as shown in the previous sections of this chapter. Denser reaction product formation around unreacted angular iron particle is distinctively visible in the micrograph. While the carbonate reaction product helps to bind all the materials together, unreacted iron is likely to facilitate microstructural reinforcement in the binder thereby exhibiting superior mechanical behavior. When the sample is exposed to 300° C, the denser light grey phases around unreacted iron particles, seen at room temperature, are converted to porous black phases as can be seen in Figure 9-7 (b) which is attributed to decomposition of iron carbonate as was confirmed through TGA and XRD results. Not significant distinct difference is visible between the samples at 300° C and 600° C except the fraction of black phases in the micrograph is reduced to some extent. At, 800° C the black phases around the iron particles vanished and the microstructure looks denser which is reflected in the form of increased flexural strength due to polymerization of silica and formation of crystalline phases such as hematite at elevated temperatures as confirmed by FTIR and XRD spectra.

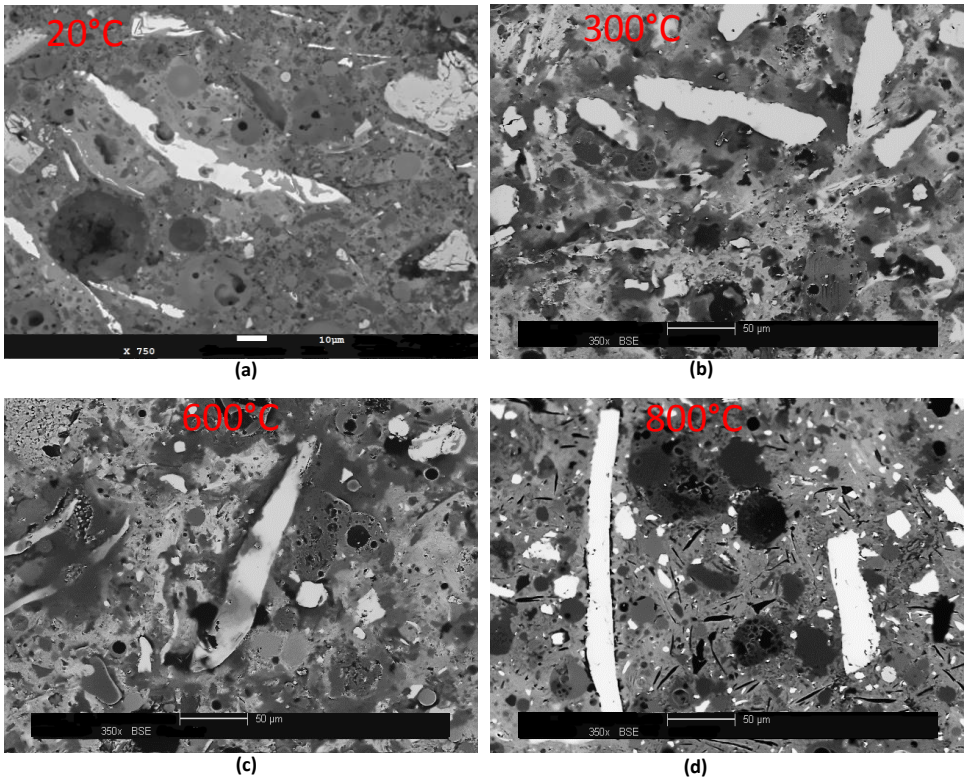

Figure 9-7: Evolution of microstructure with increasing exposure-temperature

Figure 9-8 shows elemental maps (using electron microprobe coupled with EDS) of samples exposed to various temperatures. The elemental maps of Iron confirms that the bright (white) phases in the microstructure are iron particles. Among all the elements, carbon is found to be most sensitive to elevated exposures which is expected, considering decarbonation of iron carbonate and calcium carbonate being major difference caused by exposure to elevated temperatures, established here using TGA, FTIR and XRD data. The elemental maps corresponding to 300° C shows black region around iron particles signifying thermal decomposition of iron carbonate formed around iron particles. But, all other areas, except on the iron particle and the area around iron particles, show presence of carbon from calcite. Thermal decomposition of calcite at 600° C and 800° C, which is established using TGA, FTIR and XRD, is also evident in the form of reduction of

fraction of carbon in the maps as the temperature is increased. Si maps show that Si is relatively dispersed at room temperature and 300° C. But, it forms pockets and dispersion is significantly reduced at 600° C and 800° C which supports that fact that amorphous silica is polymerized here to form these distinct agglomerations as was found using FTIR and XRD spectra. Distinct pockets of alumina is found in the maps corresponding to room temperature and 300° C. But, the distribution is slightly diffused at 600° C and 800° C. While the elemental maps for Ca show presence of Ca in distinct pockets at room temperature and 300° C, Ca is significantly diffused entirely in the microstructure, except the iron particles which is attributed to thermal decomposition of calcite at 600° C and 800° C established using TGA, FTIR and XRD.

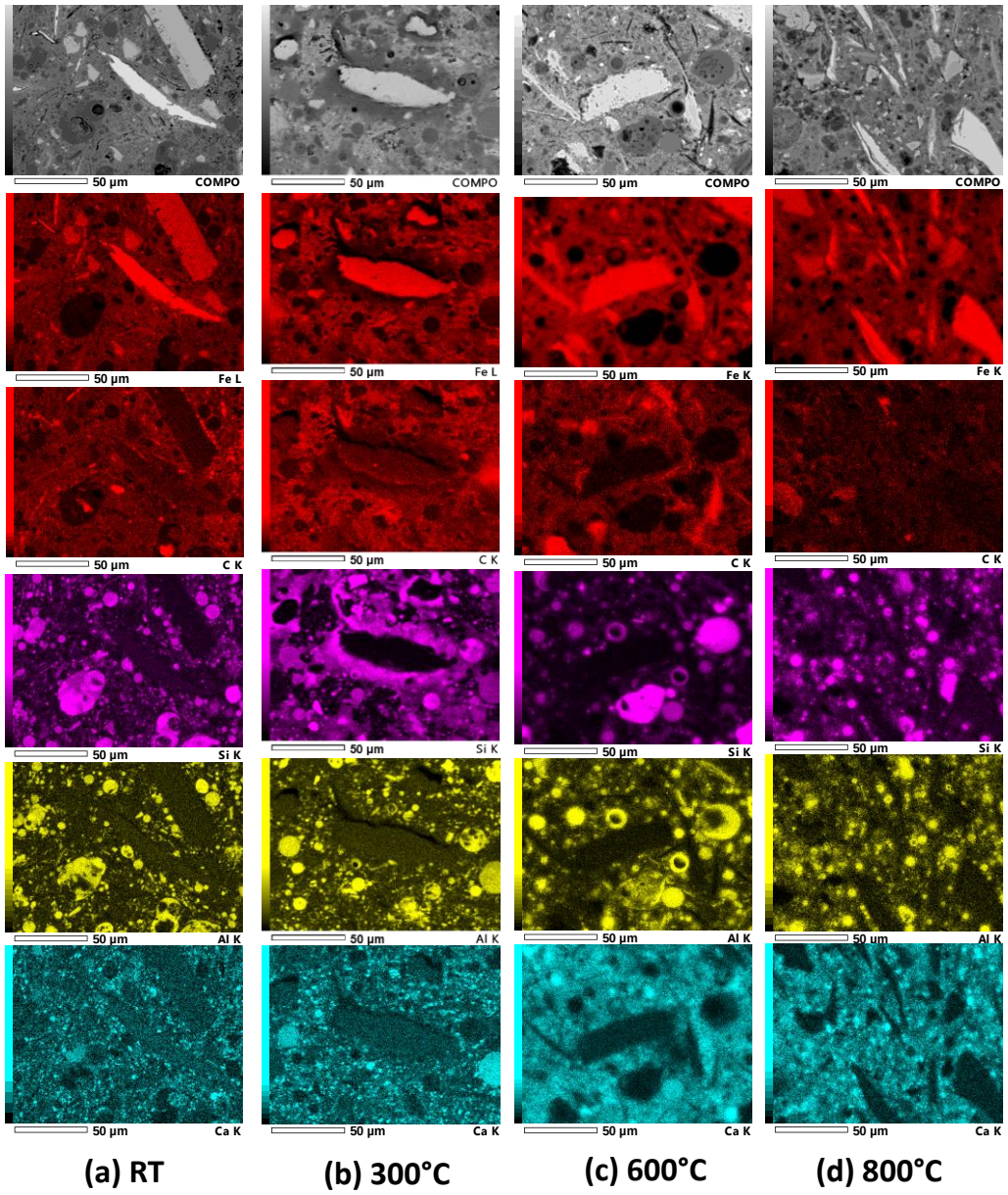

Figure 9-8: Elemental maps using electron microprobe at different temperatures

9.4 Conclusions

This chapter reports effect of various elevated temperatures on the mechanical behavior and microstructure of novel iron-based binder. While novel iron-based binder shows significantly higher flexural strength as compared to OPC paste at room temperature, iron-based binder loses its strength significantly at 300° C due to thermal decomposition of iron carbonate although it still shows similar strength as OPC. Complete loss of iron carbonates at 300° C, confirmed using TGA and XRD spectra, has been established to be the cause of strength-loss at 300° C. Porosity, measured using MIP, increased significantly at 300° C as compared to that at room temperature due to decomposition of iron carbonate. While flexural strengths of OPC paste and novel iron-based binder are almost similar at 300° C, OPC loses about 70% of its strength at 800° C. On the contrary, iron-based binder gains about 80% strength as compared to its strength at 300° C due to formation of crystalline products such as magnetite and hematite after decomposition of iron carbonate as confirmed with XRD spectra. Thus, at 800° C, novel iron-based binder exhibits a flexural strength which is 2 times and 5 times higher as compared to that of OPC paste at room temperature and 800° C respectively. Results of this comprehensive study establish effects of various elevated temperatures on strength and microstructure of novel iron-based binder.

Chapter 10 Effect of Metallic Particulate Reinforcement in OPC

10.1 Introduction

Large quantities of metallic iron powder are generated as bag-house dust waste during the electric arc furnace (EAF) manufacturing process of steel and from shot-blasting operations of structural steel sections, which are generally landfilled at large economic and environmental expenses (Das, Souliman, et al. 2014). Potential use of this waste material as a partial replacement of ordinary portland cement (OPC) in concretes can help develop a beneficial pathway for the utilization of this material, and at the same time reduce the consumption of OPC, thereby resulting in sustainable cementitious composites. Past studies have investigated the use of several metallic waste materials in concrete (Azeez et al. 2013; Y.-C. Kan, Pei, and Chang 2004; Maslehuddin et al. 2013; Rai et al. 2002). Improved mechanical and durability properties as compared to conventional concrete have been reported. The use of waste iron powder as a partial replacement of sand (~20% by volume) in concrete has been shown to increase compressive and flexural strengths (Ismail and AL-Hashmi 2008). Previous studies have also shown that the inclusion of iron aggregates in heavyweight concrete increases the fracture toughness (Y.-C. Kan, Pei, and Chang 2004; Y. C. Kan, Yang, and Pei 2012). A recent study by the authors has reported the beneficial effect of carbonation of metallic iron powder to form a binding material akin to OPC paste, which demonstrated increased fracture properties as compared to the OPC paste. This study intends to evaluate the potential application of waste iron powder in OPC mortars towards the development of sustainable cementitious composites. It is anticipated that the elongated iron particulates

will fundamentally alter the crack propagation mechanism in these composites, to deliver microstructure-designed tough and economical OPC-based composites.

In this chapter, the influence of iron particulates on fracture behavior of OPC mortars has been explored through compliance-based strain energy release rates (Das, Aguayo, et al. 2014; Mobasher 2011; Wecharatana and Shah 1983; Das, Hendrix, et al. 2014) and a concomitant evaluation of the fracture process zone (FPZ), which is a complex localized zone at the tip of the advancing crack, containing the main crack as well as various branches of secondary cracks and micro-cracks. FPZ in quasi brittle materials has been shown to provide valuable information on fracture behavior of such materials (Shah 1985; Kobayashi et al. 1985; Shah 1995a; Mobasher 2011). Several experimental techniques are available to quantify the geometric characteristics of FPZ including: high speed photography (Bhargava and Rehnström 1975), acoustic emission (Haidar et al. 2005; Carpinteri and Lacidogna 2003; Maji, Ouyang, and Shah 1990), scanning electron microscopy (SEM) (Mindess and Diamond 1980; Hadjab.S, Chabaat, and Thimus 2007; Nemati 1997; X. Hu and Wittmann 1990), laser-speckle interferometry (Jia and Shah 1994; Horii and Ichinomiya 1991), and digital image correlation (DIC) (Das, Aguayo, et al. 2014; Das, Hendrix, et al. 2014; Yates, Zanganeh, and Tai 2010; Nunes and Reis 2012a; Roux, Réthoré, and Hild 2009; Skarżyński, Syroka, and Tejchman 2011; Skarżyński, Kozicki, and Tejchman 2013; Skarżyński and Tejchman 2013; Das, Aguayo, et al. 2015). In this study, digital image correlation (DIC), a non-contact digital speckle-tracking method for determination of surface displacement and strains through image correlation (Das, Aguayo, et al. 2014; Das, Hendrix, et al. 2014; Yates, Zanganeh, and Tai 2010; Nunes and Reis 2012a; Roux, Réthoré, and Hild 2009; Skarżyński, Syroka, and

Tejchman 2011; Skarżyński, Kozicki, and Tejchman 2013; Skarżyński and Tejchman 2013; Das, Aguayo, et al. 2015), is used to obtain direct measurements of the localized zone to better understand crack propagation in iron particulate-reinforced mortars. The relationship between FPZ and tension-softening response has motivated the extraction of tensile parameters of the composite from flexural load-deflection through the use of an analytical tension model (Das, Aguayo, et al. 2015; Mobasher, Bakhshi, and Barsby 2014; Mobasher et al. 2014; C. Soranakom and Mobasher 2007; Chote Soranakom and Mobasher 2008). The experimentally determined strain energy release rates, visual surface strain fields and the geometric features of the FPZ, and the back-calculated tensile properties of the composites are related to provide a fundamental understanding of the influence of the presence and content of metallic particulate reinforcement on the strain localization and crack-propagation behavior of the composite mortars.

10.2 Experimental program

10.2.1 Materials and mixture proportions

Commercially available Type I/II ordinary portland cement (OPC) conforming to ASTM C 150 is the main material used in this study. The particulate reinforcement used in this study is a metallic waste iron powder having a median particle size of 19 μm, obtained from an industrial shot-blasting operation. The particle size distributions of OPC and iron powder are shown in Figure 10-1. The iron powder consists of 88% Fe and 10% Oxygen (due to some amount of atmospheric oxidation) along with trace quantities of Cu, Mn, and Ca. The mortar mixtures were prepared using silica sand that had an average particle size of 0.6 mm.

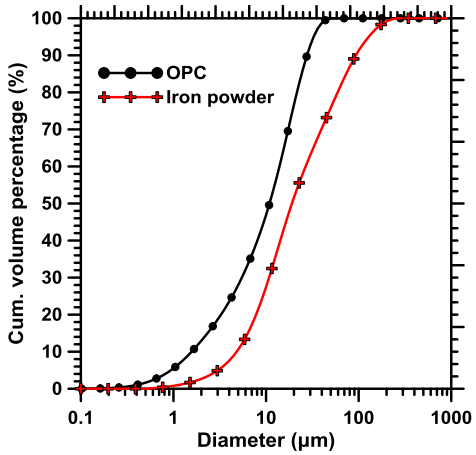

Figure 10-1 : Particle size distributions (PSD) of metallic iron powder and OPC. The iron powder used here is coarser than the OPC.

Four different mortar mixtures were proportioned with a water-to-cement ratio by mass $(w/c)_m$ of 0.50, and a constant aggregate (sand) volume of 50%. The four mortar mixtures contained 0, 10, 20, and 30% of metallic waste iron powder by volume respectively as a replacement of OPC. The mortar mixes were cast in 50 mm cubes for compressive strength test and 250 mm x 50 mm x 50 mm prismatic members for flexural strength. For fracture tests, 330 mm x 75 mm x 25 mm beams were casted. For each of these tests, four replicate specimens were prepared. The samples were demolded after one day and placed in moist environment (RH>98%) at a temperature of 23 ± 2^{o}C until the desired age of testing. Companion paste samples were also prepared and kept in sealed containers for pore and micro-structural evaluation.

10.2.2 Strength and pore structure evaluation

The compressive strengths were obtained in accordance with ASTM C 109 and flexural strength (in three-point loading) in accordance with ASTM C293/293M-10. The pore structure of the plain and particulate-reinforced paste samples was evaluated using mercury intrusion porosimetry (MIP). A porosimeter that can detect minimum pore

diameter of 0.003 μm was employed for this study. This test was performed in two steps: (i) evacuation of gasses and filling the sample holder with mercury in the low-pressure run that increases the pressure from ambient to 345 kPa, and (ii) intrusion of mercury into the sample at high pressure (maximum pressure of 414 MPa). The contact angle and surface tension used for the analysis were 130° and 0.485 N/m respectively. Even though the matrix type influences the contact angle, this aspect was not considered in this study. The pores in the porous media are assumed to be cylindrical in shape. The procedure of extraction of pore-structure features from MIP data is described in detail elsewhere (Das, Aguayo, et al. 2014; Das, Stone, et al. 2014e, -; Moon, Kim, and Choi 2006; Ghafari et al. 2014; Sánchez-Fajardo, Torres, and Moreno 2014; Carniglia 1986).

10.2.3 Scanning electron microscopy for microstructural evaluation

Microstructural evaluation of OPC-iron powder blended system was carried out using a Philips XL30 field emission environmental scanning electron microscope (FESEM). Small pieces from the core of the paste samples were cut using a diamond saw. A suitable combination of grinding and polishing was employed to achieve a level of flatness appropriate for microstructural evaluation. Prior to polishing, the sample was ultrasonically cleaned, rinsed with ethyl alcohol and dried to remove any debris from sectioning/handling. An epoxy encapsulation and vacuum impregnation procedure was then implemented, followed by overnight curing of the sample at room temperature. In order to planarize and remove deformations caused by sectioning, silicon carbide (SiC) abrasive discs were used. Successive polishing steps were carried out using smaller sized abrasives, and final polishing was done using 0.04 μm colloidal silica suspension. The polished sample was then imaged under FESEM in the backscattered mode.

10.2.4 Three point bending test and digital image correlation for evaluation of fracture behavior

Three-point bend tests were performed on notched beams of size 330 mm x 76 mm x 25 mm (span of 305 mm and notch depth of 19 mm) as shown in Figure 10-2. Four replicate beams were tested for each mixture. The beams were tested in a closed loop testing machine under crack mouth opening (CMOD) controlled mode. CMOD was measured continuously using a clip gauge. The beams were loaded in a force-controlled mode until a load of 100 N after which they were subjected to displacement (CMOD) controlled mode. The CMOD-controlled stage was terminated at a constant CMOD value of 0.038 mm for all samples and load-controlled stage was initiated for unloading. The beams were unloaded to 50 N at a constant rate of 556 N/mm before shifting to the CMOD-controlled stage again. Thus, subsequent loading (CMOD-controlled) and unloading (load-controlled) cycles were employed until a terminal CMOD of 0.18 mm was reached. The loading-unloading cycles in the load-CMOD response were required to determine compliance-based resistance (R) curves, which are presented in detail in a forthcoming section.

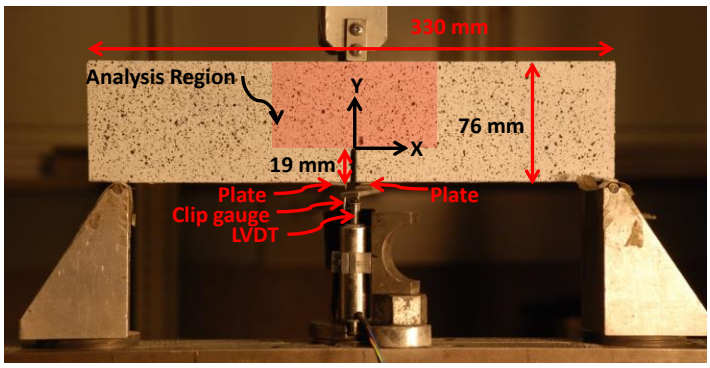

Figure 10-2: Experimental setup for closed loop CMOD-controlled three-point bending test

Digital image correlation (DIC) was performed on the notched beams undergoing loading and unloading for direct determination of fracture process zone (FPZ), which is expected to provide insights into the crack propagation behavior of particulate reinforced OPC systems. DIC is a non-contact speckle-tracking optical method for measurement of displacement field on the specimen surface. In this method, the correlation between the subsets of images from the deformed and undeformed state is determined in order to calculate the displacement fields. The fundamentals and application of DIC to the study of cementitious systems has been well-documented (Das, Aguayo, et al. 2014; Das, Hendrix, et al. 2014; Yates, Zanganeh, and Tai 2010; Nunes and Reis 2012a; Roux, Réthoré, and Hild 2009; Skarżyński, Syroka, and Tejchman 2011; Skarżyński, Kozicki, and Tejchman 2013; Skarżyński and Tejchman 2013; Das, Aguayo, et al. 2015). The beam surface was speckled with random black-and-white patterns to provide adequate contrast. A CCD camera was used to capture images every 5 seconds during the test using VIC-snap^{TM} software. After the test, the digital images were correlated to obtain strain and displacement fields using VIC-2D^{TM} software (Das, Aguayo, et al. 2014). The strain and displacement fields are used to extract important features such as crack-extension, length and width of FPZ as described later in this chapter.

10.3 Results and discussions

10.3.1 Microstructure of particulate-reinforced OPC binder

In order to investigate the distribution of iron particles in the OPC mortar matrix, microstructural analysis was carried out on polished samples after a hydration age of 28 days. Figure 10-3(a) and (b) show backscattered electron (BSE) images of the mortar microstructure with 30% iron powder by volume, at different magnifications. Figure 10-3

(a) shows the general view of microstructure where the bright (high density) iron particles and the matrix consisting of the reaction products (gray phase) and pores (black) are shown. The higher magnification image (Figure 10-3(b)) shows elongated iron particles which are likely to improve the fracture performance of OPC systems through mechanisms such as crack bridging and deflection, which are evaluated in greater detail later in this chapter. The matrix cracks observed at higher magnifications (Figure 10-3(b)) are generated while cutting/grinding of the samples for microscopy, and should necessarily be considered only as sample preparation artifacts.

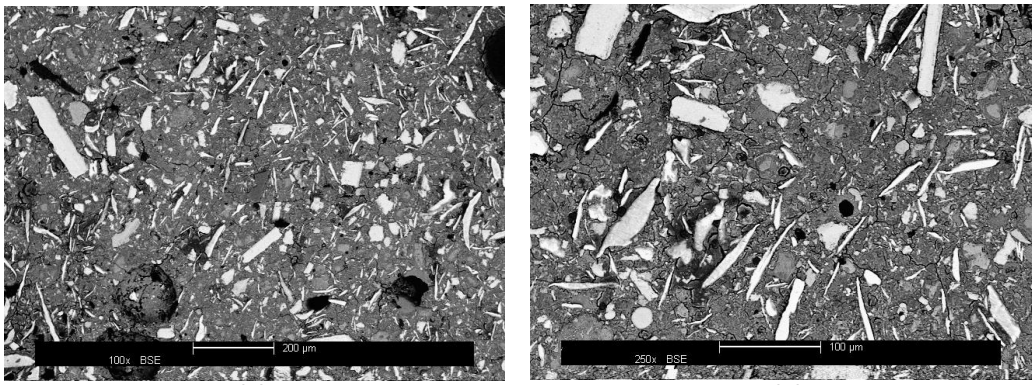

Figure 10-3: BSE image showing distribution of iron particles in a paste containing 30% by volume of iron particles: (a) at 100X (Scale bar indicates 200 µm), and (b) at 250X (Scale bar indicates 100 µm). The cracks observed in these pastes are a result of the cutting and sample preparation method for imaging.

10.3.2 Strength and pore-structure as a function of iron powder volume fraction

Figure 10-4(a) shows the total porosity and the average pore diameter of the plain and iron powder modified binder systems after 28 days of hydration. The porosity and average pore diameter are found not to be influenced significantly by the incorporation of iron powder in these systems, despite reduction in the OPC contents. In other words, the hydration of cement is not adversely affected by the presence of iron powder. It is well known that iron is passive in alkaline media, and thus, does not interfere with cement

hydration. It also needs to be noted here that the mortar mixtures were proportioned at a constant water-to-cement ratio, and thus, while the OPC content reduced through iron incorporation, the water content was also lowered. The average pore diameter and porosity for all four mixtures are within a relatively narrow range of 0.0151-to-0.0162 μm and 34-to-37% respectively. Figure 10-4(b) shows the compressive and flexural strengths of 28-day moist-cured plain OPC and iron powder incorporated mortars. All the mortars show similar compressive strengths irrespective of the level of OPC replacement by iron powder, which can be attributed to the similar pore structure features as shown in Figure 10-4(a). While compressive strengths remain roughly unaltered with iron powder inclusion, the flexural strength is observed to increase slightly with increase in iron powder volume fraction, which can likely be attributed to the mostly elongated iron particles (See Figure 10-3) serving as micro-reinforcement in the matrix. Strength and pore structure results shown in this section indicate that waste iron powder can be incorporated in cementitious systems without compromising any of the pertinent mechanical properties. The forthcoming sections specifically highlight the beneficial impacts of these particulate reinforcing materials on the crack propagation and energy release response of cementitious systems.

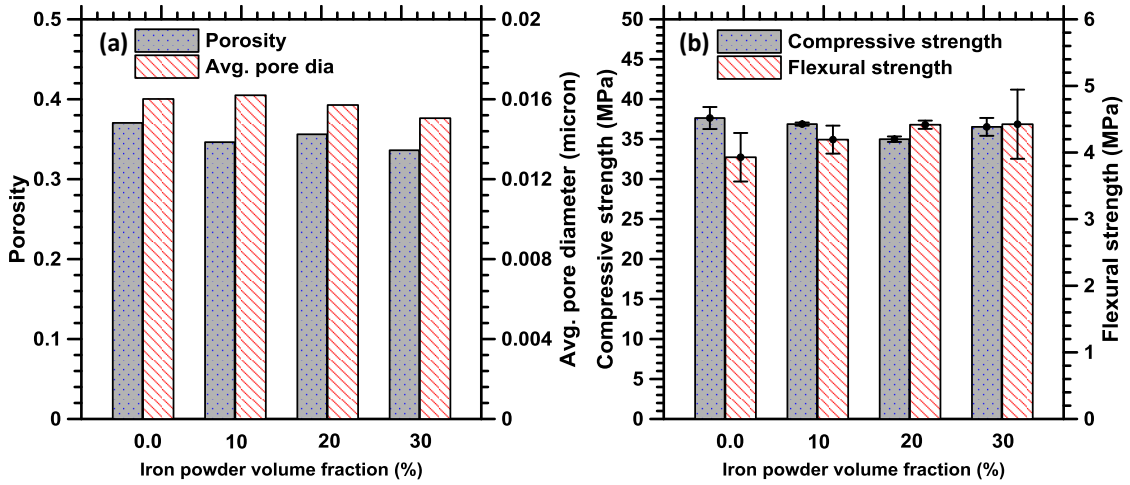

Figure 10-4: Relationship between iron powder volume fraction and: (a) porosity and average pore diameter, and (b) compressive and flexural strengths of the mortars after 28 days of hydration

10.3.3 Beneficial enhancement in the fracture response through particulate inclusions

In this section, the fracture behavior of metallic powder reinforced OPC mortar systems is evaluated using an effective crack approach (Shah 1995a; Mobasher 2011). The dominant crack-propagation mechanism in such particulate reinforced composite systems is also evaluated using surface strain mapping.

The representative cyclic load-CMOD responses of the plain and iron particulate incorporated OPC mortars are shown in Figure 10-5(a). Here, multiple loading-unloading cycles are employed in order to obtain unloading compliances at various stages in the post-peak regime which is used to obtain the resistance (R) curves. The peak flexural load increases with increase in iron powder volume fraction as expected, the reasons for which were elucidated earlier. The enhancement in peak load is in line with the iron powder content up to a replacement level of 20%, beyond which the enhancement is not very pronounced. The area under the load-CMOD curve, which is a measure of the material toughness, also increases with an increase in iron powder content. Figure 10-5(b) depicts the residual loads at a CMOD value of 0.16 mm. An increase in residual load with

increasing iron powder content is observed, signifying better post-peak response and crack-tolerance. Similar to the peak load, the enhancement in residual load is also not very prominent beyond an iron powder volume fraction of 20%. While the above results might indicate that replacing OPC by 20% of metallic iron powder (by volume) provides (near-) optimal results in terms of maximum and residual load capacities, this is strictly not correct when true fracture parameters are considered; an aspect which is elucidated in detail in the remainder of the chapter.

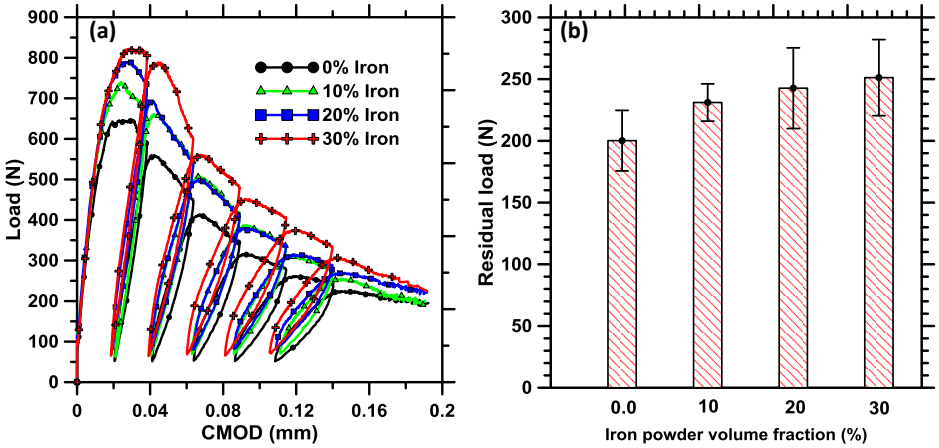

Figure 10-5: Representative: (a) Load-CMOD response; (b) residual load at CMOD 0.16 mm of blended mortars with different iron powder volume fraction

3.3.1 Strain energy release rates and the influence of metallic particulate reinforcement

This section presents the effect of metallic iron particulate reinforcement on fracture behavior of mortars in terms of strain energy release rates, and brings out the fundamental differences in crack propagation imparted by the inclusion of iron powder. The R-curves are obtained based on the assumption that stable crack propagation results in an increase in compliance. Contribution of both elastic and inelastic strain energies are considered in the development of the R-curves. The elastic components are calculated

from the unloading compliances whereas inelastic CMOD is employed to calculate the inelastic component of strain energy release rate. The total strain energy release rate (G_R) is given as (Das, Aguayo, et al. 2014; Mobasher 2011; Wecharatana and Shah 1983; Das, Hendrix, et al. 2014):

$$G_R = G_{elastic} + G_{inelastic} = \frac{P^2}{2t}\frac{\partial C}{\partial a} + \frac{P}{2t}\frac{\partial (CMOD_{inelastic})}{\partial a} \qquad [10\text{-}1]$$

Here C is the unloading compliance, t is the thickness of the specimen, P is the applied load, and a is the crack length. The unloading compliances and inelastic CMOD values are obtained from cyclic load-CMOD responses (Figure 10-5(a)). The unloading compliances are used to obtain crack extension (Δa) values corresponding to each loading-unloading cycle, as described in (Das, Aguayo, et al. 2014). The unloading compliances and inelastic CMOD values are then plotted as a function of crack-extension (Δa) and the relationships are differentiated in order to obtain the rate terms in Equation 10-1.

Figure 10-6(a) shows the R-curves for the plain OPC mortar and those incorporating different amounts of iron powder. All the R-curves comprise of two regions: one where the strain energy release rate increases with increase in crack extension, denoting the development of a fracture process zone at the tip of the propagating crack, and the other, an energy plateau where strain energy release rate remains relatively constant, signifying steady-state crack extension after near-complete development of the fracture process zone. The results suggest that the maximum strain energy release rate (or, in other words, a quantification of the fracture resistance) increases with increase in iron powder content. The crack bridging/deflection effects of the elongated iron particles, shown in the micrographs in Figure 10-3 , resists crack extension, contributing to this observation. The

crack deflection effect of elongated iron particles can also be observed from the smaller crack extension values corresponding to initiation of the energy plateau, as the iron powder content is increased. The steady-state crack propagation is reached at much lower crack extension when iron powder is incorporated in the OPC mortars since these particles help dissipate a significant amount of energy through increase in tortuosity of the microcracks in the process zone thereby resulting in reduction in crack-extension. Incorporation of 30% by volume of metallic iron powder in place of OPC yields approximately 34% increase in the strain energy release rate, signifying significantly improved fracture-response as compared to pure OPC mortars.

Figure 10-6(b) depicts the contribution of elastic and inelastic components of strain energy release rate separately in order to bring out the fundamental differences in crack-propagation imparted by iron particles and the influence of particulate volume fraction in the mortar. The elastic component corresponds to energy release rate due to incremental crack growth and it is a reflection of elastic property of the material (Mobasher 2011; Das, Aguayo, et al. 2014; Shah 1995a). On the other hand, inelastic component corresponds to permanent deformation due to crack opening. The trends in this figure suggest that the elastic component of strain energy release rate increases significantly as the iron powder volume fraction is increased whereas a reduction is noticed in the inelastic component. Increase in elastic component with increase in iron powder content can be attributed to microstructural strengthening of the mortar matrix through iron particulate reinforcement. For the plain OPC mortar, the inelastic component of strain energy release rate is dominant – i.e., the dominant mechanism of energy release is crack opening. Incorporation of 10% of iron powder by volume increases the elastic component

and decreases the inelastic component, but the inelastic component still is dominant. Further increase in iron powder content alters the trend, with the elastic component, i.e., energy release due to incremental crack growth, being dominant than the energy release through crack opening. At a 30% iron powder content, the elastic component is 50% larger than the inelastic component of strain energy release rate. The comparative analysis of the contributions of elastic and inelastic strain energy release rates shows that by incorporating 20% or more of iron powder by volume in the OPC mortar matrix, significant resistance to cracking is obtained. The microstructural strengthening facilitated by the iron particles also results in an increase in tensile properties of the system as is shown in the following section.

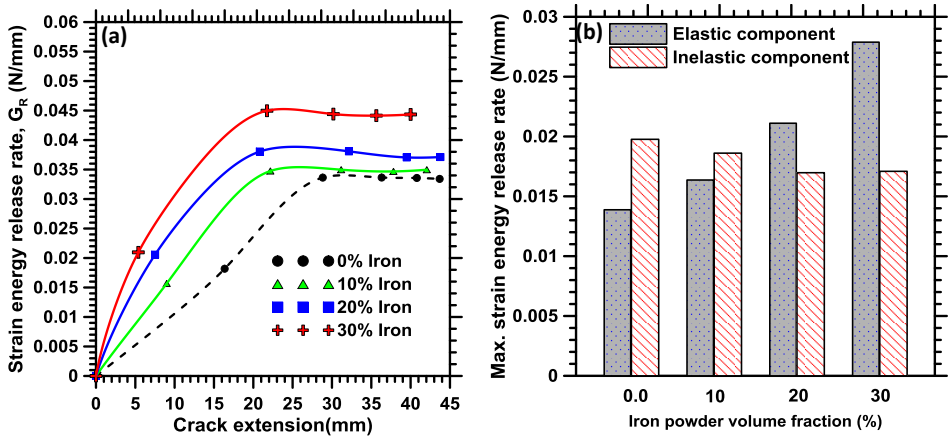

Figure 10-6: (a) Strain energy release rates, and (b) separated elastic and inelastic components of strain energy release rates, as a function of iron powder volume fraction.

10.3.4 Tensile properties of the composite mortars

It is generally more convenient to experimentally extract the flexural response of cementitious systems than their tensile response. However, the flexural behavior is not completely indicative of the material's response to cracking since the presence and growth of the crack in the pre-peak regime is ignored. Tensile constitutive relationships

provide a more accurate representation of the material behavior. In this section, tensile material properties (tensile strength, modulus, and ultimate strain) are extracted from flexural load-deflection data using closed-form moment-curvature equations for a strain softening material (Chote Soranakom and Mobasher 2008; Chote Soranakom and Mobasher 2007). The procedure adopted here is adequately described in detail in (Mobasher, Bakhshi, and Barsby 2014; Mobasher et al. 2014; C. Soranakom and Mobasher 2007; Chote Soranakom and Mobasher 2008). The tensile parameters also relate well to the characteristics of the process zone at the tip of the advancing crack as will be elucidated in detail later.

Figure 10-7(a) shows the bilinear tension model adopted in this study for the extraction of tensile stress-strain response of iron powder-based particulate composites. The material parameters involved in this model for strain softening materials are tensile stiffness E, first cracking tensile strain ε_{cr}, tensile strength $\sigma_{cr} = E\varepsilon_{cr}$ and post-cracking modulus $E_{cr} = \eta E$, with $-\infty < \eta < 0$, and ultimate tensile strain $\varepsilon_{tu} = \alpha\varepsilon_{cr}$. The compression model describes an initial linear response until the yield point (ε_{cy}, σ_{cy}) is reached. Beyond the yield point, the material maintains a constant stress $\sigma_{cy} = \omega\varepsilon_{cr}\gamma E$, where $\gamma E = E_c$, the compressive modulus, and $\omega\varepsilon_{cr} = \varepsilon_{cy}$. The tensile parameters are normalized with respect to either of the two intrinsic material parameters: E or ε_{cr}, to define a closed-form solution for the moment-curvature response and the load-deflection calculation. The normalized parameters are obtained based on a best-fit optimization procedure to the experimental load-deflection data. More details can be found in (Mobasher, Bakhshi, and Barsby 2014; Mobasher et al. 2014; C. Soranakom and Mobasher 2007; Chote Soranakom and Mobasher 2008) .

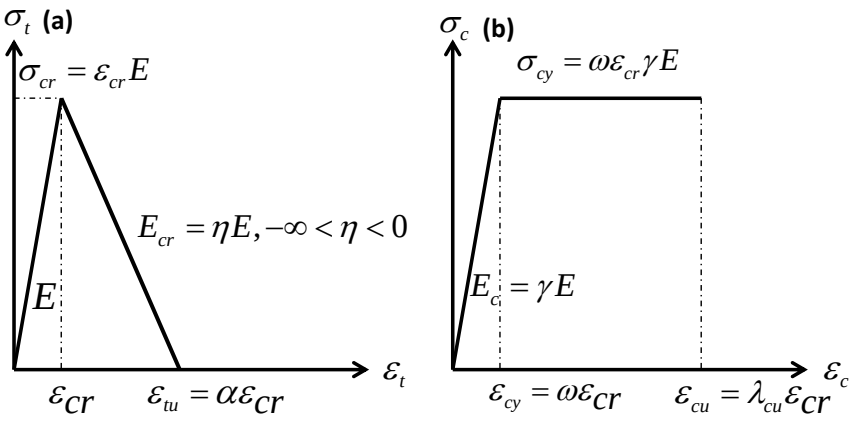

Figure 10-7: Simplified: (a) tension, and (b) compression models for strain-softening cementitious materials (Mobasher, Bakhshi, and Barsby 2014; Mobasher et al. 2014; C. Soranakom and Mobasher 2007; Chote Soranakom and Mobasher 2008)

Figure 10-8(a) shows the experimental flexural load-deflection data used to extract the tensile parameters. The corresponding tensile stress-strain responses obtained using the procedure detailed above are shown in Figure 10-8(b). Both tensile strength and ultimate tensile strain increases with an increase in iron powder volume fraction, the reasons for which were explained earlier. The increase in tensile strength is observed to be proportional to the content of iron powder in the mortars. An increase in tensile toughness, most notably the post-peak toughness, is also observed with increase in iron powder content.

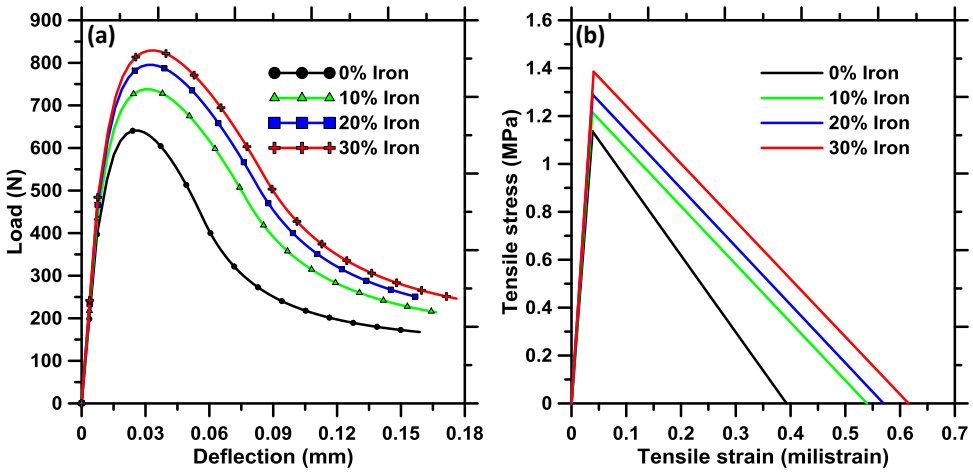

Figure 10-8: (a) Flexural load-deflection curves, and (b) extracted tensile stress-strain responses for plain and iron powder incorporated mortar mixtures.

Figure 10-9(a)-(c) quantifies the changes in tensile strength, ultimate tensile strain and tensile modulus as a function of the iron powder volume fraction for the mortars studied. All the tensile parameters, as would be expected, increase with increase in iron powder volume fraction. The elastic modulus of the composite increases because of the presence of metallic iron which has a higher E value. While the relationship between tensile strength and iron powder volume fraction is found to be linear, non-linear relationships exist between the iron powder content and the ultimate tensile strain or elastic modulus. Ultimate tensile strain goes up by more than 50% when 30% of iron powder by volume is incorporated into the mortars, but the corresponding increase in elastic modulus and tensile strengths are 15% and 25% respectively. Thus it can be stated that the impact of metallic particulate incorporation is in enhancing the tensile toughness of the composite rather than the strength or stiffness, even though the latter parameters are also enhanced, notwithstanding the substantial levels of OPC replacement.

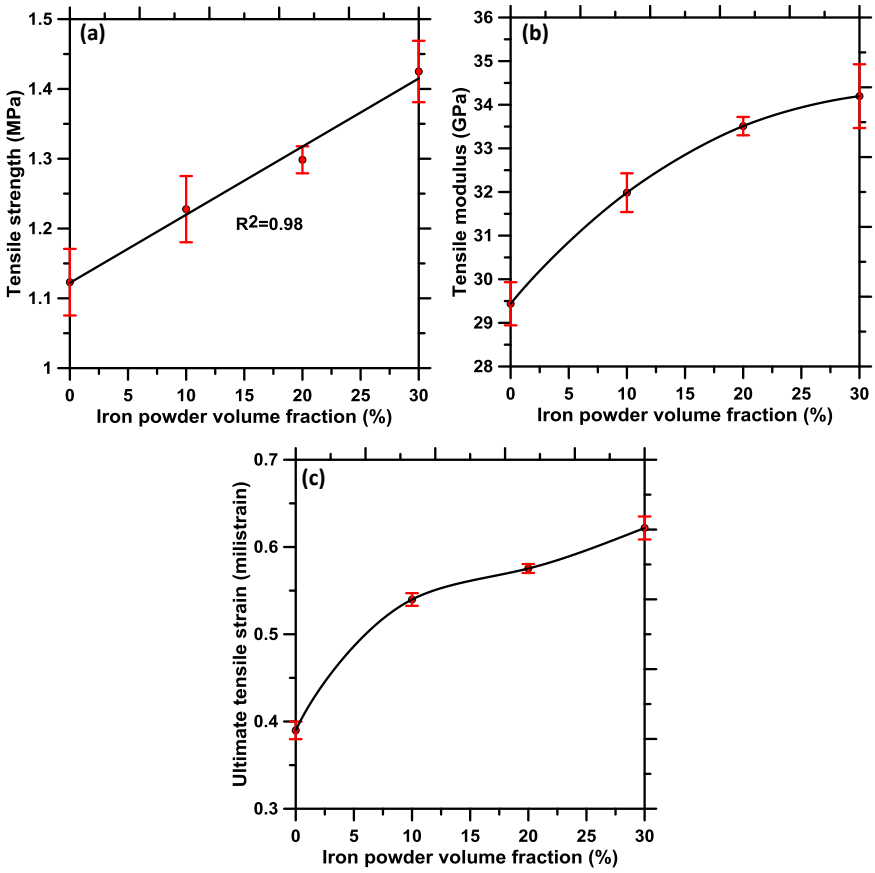

Figure 10-9: Relationships between iron powder volume fraction and: (a) tensile strength, (b) tensile modulus, and (c) ultimate tensile strain of the OPC-iron powder composite mortars

10.3.5 Strain localization in composite mortars

While the earlier section on strain energy release rates indirectly pointed to the fundamental differences in crack propagation mechanism imparted by the iron particles, this section focuses on the identification and direct measurement of fracture process zone (FPZ) at the tip of the advancing crack and its features using digital image correlation (DIC). Since the fracture energy and the tension softening response of cementitious systems are related to the characteristics of FPZ, proper quantification of the FPZ features – length, width, and area – helps better understand the influence of iron powder incorporation on crack extension (propagation) and strain localization.

10.3.5.1 Determination of crack-extension and geometric features of FPZ

Digital image correlation (DIC) is a non-contact optical method for the direct measurement of strain and displacement fields (Das, Aguayo, et al. 2014; Das, Hendrix, et al. 2014; Yates, Zanganeh, and Tai 2010; Nunes and Reis 2012a; Roux, Réthoré, and Hild 2009; Skarżyński, Syroka, and Tejchman 2011; Skarżyński, Kozicki, and Tejchman 2013; Skarżyński and Tejchman 2013; Das, Aguayo, et al. 2015). DIC has been shown to be an effective tool to understand the fracture behavior of cementitious materials (Das, Aguayo, et al. 2014; Das, Aguayo, et al. 2015; Nunes and Reis 2012a; Das, Hendrix, et al. 2014; Skarżyński, Kozicki, and Tejchman 2013). Several time-and-CMOD stamped images of the analysis region (Figure 10-2) are used to calculate the displacement fields. The horizontal (u) and vertical (v) displacement fields in the analysis region are computed by minimization of the correlation coefficient (C) using VIC-2D software™. Figure 10-10(a) shows a representative load-CMOD response and a typical horizontal displacement field (3D plot) for a composite mortar. The crack extension is measured as the extent of displacement jump at x=0 mm with a threshold displacement jump value of 0.005 mm to qualify the jump as contributing to crack extension. The process of quantification of crack extension has discussed in detail elsewhere (Das, Aguayo, et al. 2014). The X-component of the Lagrangian strain field (ε_{xx}), given in Equation 10-2 (Sutton, Orteu, and Schreier 2009; Hjelmstad 2005; Das, Aguayo, et al. 2015), corresponds to the crack opening direction.

$$\varepsilon_{xx} = \frac{\partial u}{\partial x} + \frac{1}{2}\left[\left(\frac{\partial u}{\partial x}\right)^2 + \left(\frac{\partial v}{\partial x}\right)^2\right] \qquad [10\text{-}2]$$

Hence ε_{xx} is used to quantify the inelastic region at the tip of the crack. Figure 10-10 (b) shows the strain (ε_{xx}) corresponding to 95% of the peak load in the post-peak regime for the mixture containing 30% iron powder and Figure 10-10(c) shows the strain profile along the line 'L' marked in Figure 10-10(b). Here 95% of the peak load is chosen since full width of FPZ (i.e., in the x-direction) is developed at that loading state (Shah 1995a; Das, Aguayo, et al. 2015; Skarżyński, Syroka, and Tejchman 2011) and it is considered to be the critical limit beyond which unstable crack propagation starts (Shah 1995a; Mobasher 2011; Das, Aguayo, et al. 2014). The surface strain profile is fitted using a normal distribution function (Equation 10-3). The standard deviation, σ, is the fitting parameter. Since 95% of the values of the normal distribution function falls within $\pm 2\sigma$ of the mean value, the width of FPZ at the considered distance from the notch can be taken as 4σ. A similar approach has been successfully adopted in a recent publication (Das, Aguayo, et al. 2015).

$$f(x,\sigma) = \frac{1}{\sigma\sqrt{2\pi}} e^{-\frac{1}{2}\left(\frac{x}{\sigma}\right)^2} \qquad [10\text{-}3]$$

It should be noted that the width of fracture process zone determined using DIC is greatly influenced by the image resolution (Skarżyński, Kozicki, and Tejchman 2013). Hence, the FPZ characteristics presented in this study are used only to compare the fracture response of mortars containing different volume fractions of metallic particulate reinforcement. Length of FPZ is also an important parameter that determines the cohesive stress distribution in the FPZ. Length of FPZ is determined directly from the strain fields based on the extent of strain localization in the direction of crack growth. In this study, the FPZ is considered to be terminated when the local strains are lower than 20% of the

maximum strain at the tip of the notch. As in the case of FPZ width, the FPZ length is also specimen size- and-geometry dependent.

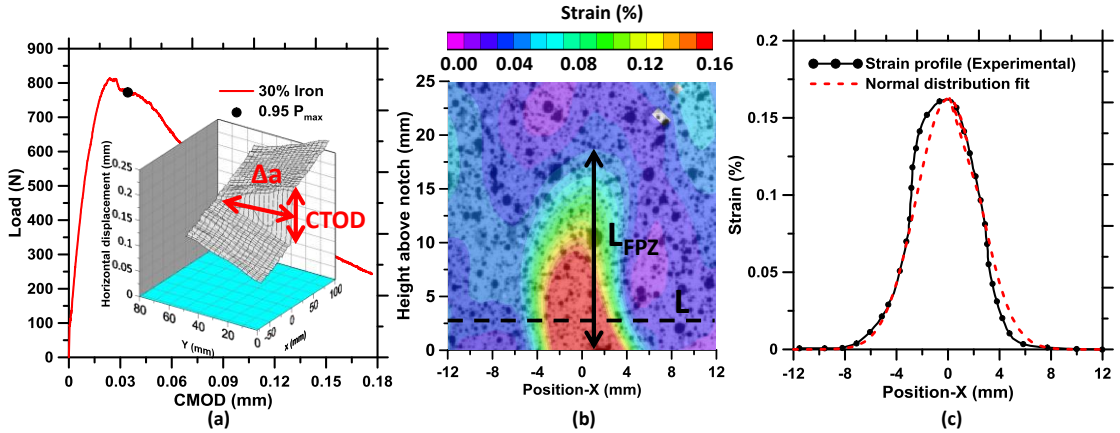

Figure 10-10: (a) Load-CMOD response with a representative horizontal displacement field shown as a 3D plot in the inset, (b) Lagrangian strain (ε_{xx}) field at 95% of the peak load in the post-peak regime, and (c) experimental strain profile 2.5 mm above notch and the fitted normal distribution curve to obtain width of FPZ for the 30% iron powder containing mortar.

10.3.5.2 Influence of iron powder incorporation on the FPZ in particulate composite

It has been shown earlier that the incorporation of iron powder results in increase in strain energy release rates and that the dominant mechanism shifts from one of inelastic permanent deformation to elastic incremental crack growth. The energy release rate during crack propagation in quasi-brittle materials is dependent on the characteristics of the FPZ at the tip of the advancing crack. Therefore this section deals with a quantification of the FPZ characteristics as a function of the metallic powder content in the mortar. Figure 10-11 shows the Lagrangian strain fields (a1-to-d1) and the corresponding displacement fields (a2-to-d2) for the plain and iron powder incorporated mortars. Qualitative observation of the strain fields show increasing FPZ lengths and relatively unchanged widths with increasing iron powder content. Crack extension, calculated through tracking the displacement jump with a threshold limit of 0.005 mm,

are also shown visually in Figure 10-11(a2-to-d2) using the horizontal displacement fields, calculated using DIC.

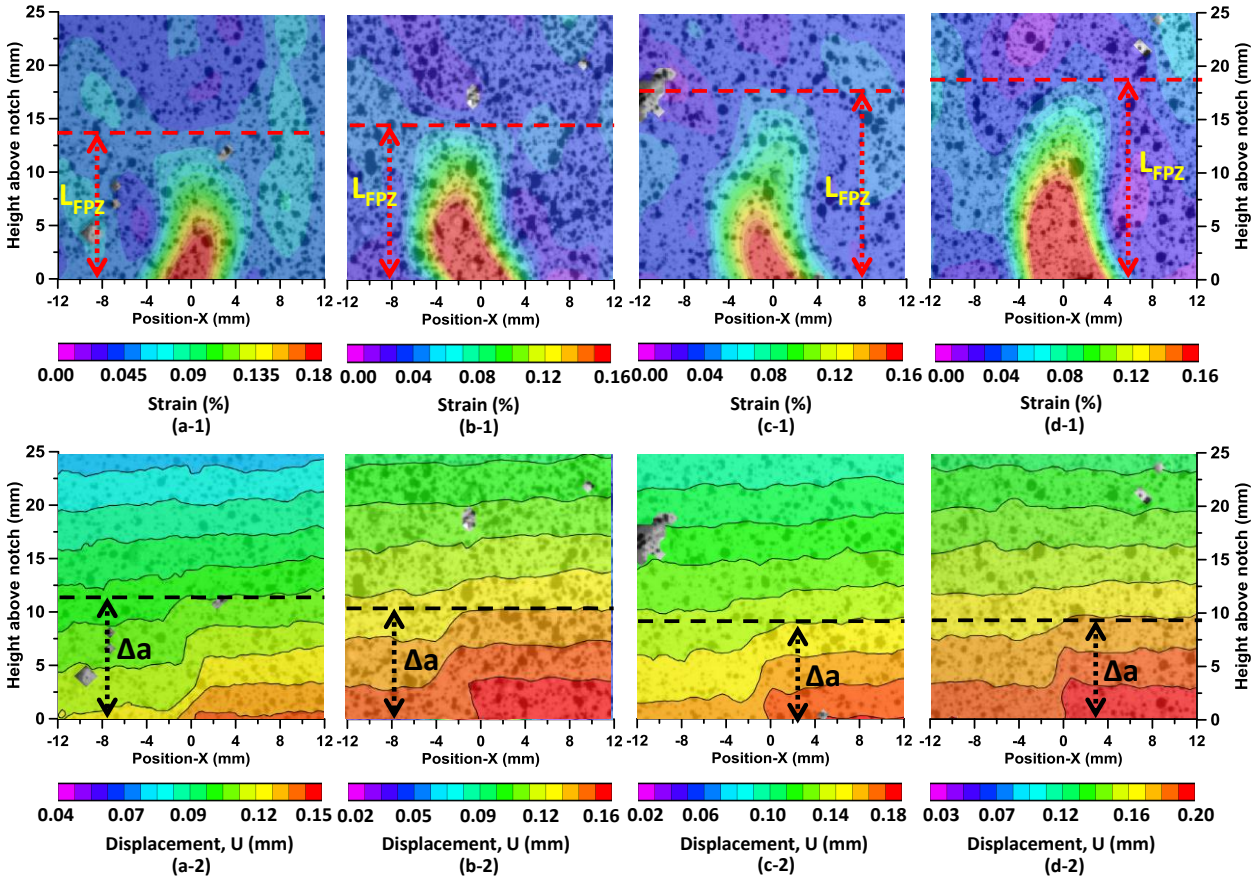

Figure 10-11: Lagrangian strain (ϵ_{xx}) fields (a1-to-d1) and displacement (x-direction) fields (a2-to-d2) corresponding to 95% of the peak load in the post-peak regime showing length and width of FPZ and the crack extension from the displacement jumps. The images labeled a, b, c, and d corresponds to 0%, 10%, 20%, and 30% of iron powder replacing OPC respectively, in the mortars.

Figure 10-12 (a) shows the quantified lengths and widths of FPZ corresponding to 95% of the peak load at the post peak regime, at a location 4 mm above the notch, as a function of volume fraction of iron powder. The length of FPZ increases with an increase in the iron powder content while the width remains relatively unaffected (Figure 10-11 a1-d1). The increasing FPZ length is an indication of energy dissipation through micro-

cracking, crack arresting and deflection in the direction of crack driving force, aided by the presence of metallic particulate reinforcement which impedes the extension of the main crack. This can be easily noticed from Figure 10-6(b) that clearly depicts an increase in the elastic component of strain energy release rate when the iron powder content is increased. The relatively unchanged width of FPZ can be linked to that fact that, while the total strain energy release rates increase considerably with iron powder content, the inelastic component, signifying crack opening undergoes only modest changes (Figure 10-6(b)). Thus, as a fraction of the energy release rate, the inelastic component is reduced with increasing metallic particulate content, but its magnitude is unaffected in the range of particulate volumes considered in this study. The quantitative descriptors of FPZ show that they are well-related to the trends in energy release rates.

Figure 10-12(b) shows the FPZ area and crack extension as a function of iron powder content in the mortar. FPZ widths are determined at every 1 mm height above the notch and the values are numerically integrated to obtain the total FPZ area at 95% of the peak load in the post-peak regime. The FPZ area increases significantly with increase in iron powder volume fraction, contributed primarily by increased FPZ lengths, as shown in Figure 10-12(a). The crack extension corresponding to 95% of the peak load decreases as the iron powder content is increased. This is because significant amount of strain energy is released through mechanisms that resist the extension of the main crack, which is manifested through an increase in the FPZ length. Beyond an iron powder content of 20%, the increase in FPZ area and the reduction in crack extension are not substantial even though the elastic component of the strain energy release rate was noted to further increase. The increase in elastic strain energy release rate can be attributed to the increase

in peak load with increasing iron powder content. Note that the elastic component of the strain energy release rate is proportional to the square of the load (Equation 10-1).

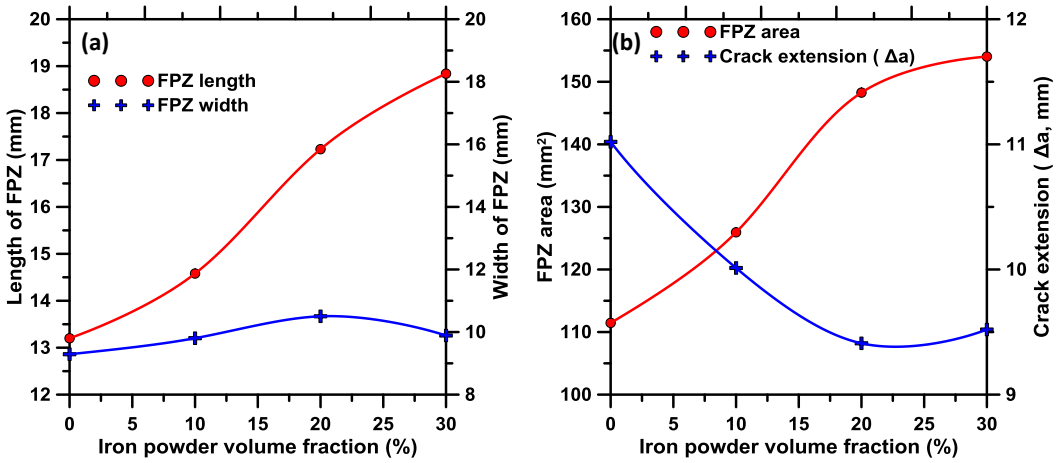

Figure 10-12: Relationship between volume fraction of iron powder and: (a) FPZ length and width, and (b) FPZ area and crack extension.

10.3.5.3 Correlating FPZ characteristics with tensile properties of the composites

It was mentioned earlier that the tensile response of quasi-brittle materials are related to the characteristics of the FPZ. The prevous section also showed that the FPZ characteristics (its length, in partiular) can be adequately related to the elastic strain energy release rate. Figure 10-13(a) quantifies these relationships as a function of iron powder content for the composite mortars investigated here. The elastic component of strain energy release rate and the tensile modulus increases linearly with increase in FPZ length at 95% of the peak load in the post-peak regime. The reasons for such observations have been explained in detail before. Figure 10-13(b) relates the FPZ area to total strain energy release rate and the area under the tension softening part of the predicted tensile stress-strain curves. Maximum strain energy release rate increases with increase in FPZ area as expected, again for the reasons explained earlier. FPZ has been reported in several

publications to be responsible for softening nature of tensile stress-strain curve in quasi-brittle materials (Das, Aguayo, et al. 2015; Mihashi and Nomura 1996; H. H. Chen and Su 2013). Hence, it is not surprising that the area under softening (post-peak) portion of the tensile stress-strain curve, a measure of post-peak tensile toughness, is well-correlated to FPZ area. The incorporation of metallic particulate inclusions increases the tensile strength and tensile modulus, but as discussed earlier, the largest impact is on the ultimate tensile strains, which results in the post-peak toughness being significantly impacted.

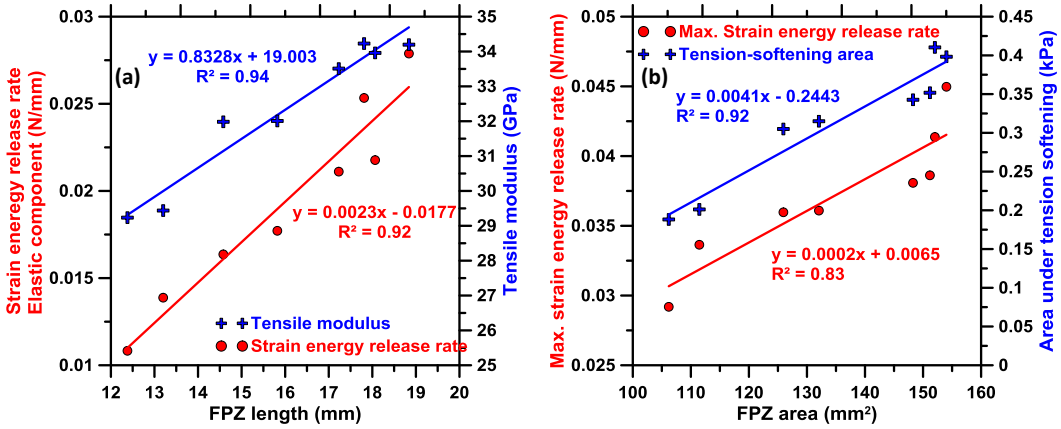

Figure 10-13: Relationships between: (a) FPZ length and the elastic component of strain energy release rate and tensile modulus, and (b) FPZ area and maximum strain energy release rate and area under softening portion of tensile stress-strain curve. The FPZ lengths and are correspond to 95% of the peak load in the post-peak region.

The study reported in this chapter has shown that metallic iron particulates can be used as an OPC replacement material without compromising the strength of the material, yet significantly improving its fracture response. While conventional fiber reinforcement is used in OPC systems to attain such beneficial fracture behavior, the use of metallic iron particulate reinforcement helps achieve similar results at significantly reduced OPC contents in the cementitious systems, thereby contributing the cause of sustainability also.

10.4 Conclusions

The influence of elongated metallic iron particulate (a waste material obtained from EAF-based steel production and shot-blasting of structural steel sections) reinforcement on the crack propagation response of cementitious mortars has been elucidated in this work. Mortars containing up to 30% of iron powder as a replacement of OPC by volume demonstrated comparable or better mechanical and pore-structure features as that of control mortars. R-curves, extracted from cyclic load-CMOD response, showed that the maximum strain energy release rate increased with iron powder content, thereby signifying better crack-tolerance. When the strain energy release rate was separated into its elastic and inelastic components, it was observed that the elastic component (attributed to incremental crack growth in the direction of crack propagation) increased with iron powder content while the inelastic component (attributed to permanent deformation due to crack opening) remained relatively unchanged. The dominant energy release rate controlling mechanism switched from inelastic to elastic between iron powder volume fractions (replacing OPC) of 10 and 20%.

Digital image correlation (DIC) was used to identify and measure the geometric features of the fracture process zone (FPZ) in the composite mortars. The FPZ widths (in the crack opening direction) remained relatively unchanged whereas the length (in the direction of crack extension) was found to increase with increase in iron powder content. The quantified FPZ features are in line with the elastic and inelastic components of strain energy release rates. Flexural load-deflection relationships were used to back-calculate important tensile parameters such as tensile strength, tensile modulus, and ultimate tensile strains of the composite mortars. All the tensile parameters increased with

increase in iron powder content; an increase of 50% in the ultimate tensile strain when 30% of OPC was replaced by iron powder being the most significant. Thus the major impact of metallic particulate incorporation is in enhancing the tensile toughness of the composite rather than the strength or stiffness, even though the latter parameters are also improved, notwithstanding the substantial levels of OPC replacement. The FPZ lengths and areas were well correlated to the area under softening (post-peak) portion of the tensile stress-strain curve, a measure of post-peak tensile toughness. This study has shown that the use of waste metallic iron particulate reinforcement as replacement for OPC results in comparable strengths and vastly improved crack propagation (fracture) response of these composites. The results demonstrated here are similar to those attained by the use of small volumes of fiber reinforcement, with the added advantage of OPC reduction, thus ensuring significant sustainability benefits also to these composites.

Chapter 11 Summary and Conclusions

Detailed experimental results and analysis on the synthesis and mechanical properties of a unique binder system that utilizes the carbonation of metallic iron powder for cementation properties is investigated. The key aspects of the study are:

- Waste iron powder in combination with commonly used concrete ingredients such as fly ash, limestone powder, and metakaolin as minor components can be carbonated to produce a binding material with acceptable properties for a wide range of construction applications. In addition, this route of binder formation is a method of CO_2 minimization both in terms of CO_2 trapping in the form of carbonate formation as well as provision of an alternate structural binder that helps reduce portland cement consumption.
- The compressive strength of the binder systems were significantly influenced by the fly ash content. While limestone in the chosen range did not influence the strength at lower fly ash contents, the synergistic effects were evident at higher fly ash contents. Metakaolin primarily influenced the processing of the binder by providing cohesion to the mixtures. CO_2 exposure duration and air curing duration were also found to be influential on the mechanical properties of the binder.
- The mixture proportions and carbonation duration for novel iron-based binder was established based on carbonation efficiency, studied using TGA, for optimal mechanical performance.
- Fundamental characterization of pore- and micro-structure of a novel iron-based complex binder system has been done. Increasing the carbonation duration from 1 to 4 days significantly reduced the total pore volume in the iron carbonate binder

as determined by MIP. This was in turn reflected in the compressive strength of the binders, while the critical pore size remained relatively unchanged.

- A comparison with the pore structure of 28-day cured OPC pastes showed that the overall pore volume was lower in iron carbonated binders; however, the critical pore sizes were larger.
- Secondary and backscattered imaging revealed many of the important features of the microstructure of this novel binder material. The influence of carbonation on the reaction product formation on iron particle surfaces was established. A dense, heterogeneous microstructure was obtained after carbonation. The reaction product analysis using TGA and XRD confirmed formation of iron carbonate.
- The flexural strength, fracture toughness (K_{IC}^{S}), and the critical crack tip opening displacement ($CTOD_c$) of the iron-based binders were significantly higher than those of the OPC matrices, for both the unreinforced and glass-fiber reinforced systems. The improved performance of the iron-based binder systems were attributed to the presence of the elastic, unreacted metallic particles that facilitate crack bridging and deflection.
- The iron-based binder systems showed significantly higher strain energy release rates than the OPC-based binder at all fiber loadings. It was found that the elastic component of the strain energy release rate was higher than the inelastic component for iron-based binders, attributable to the superior effects of the unreacted metallic particulate phase that provide crack growth resistance.
- The surface strain profiles, obtained from DIC, are utilized to locate and quantify the region of strain localization. The width and area of localized region above the

notch for iron-based binder was consistently higher than the OPC binder in both control and fiber-reinforced states. This was attributed to the major improvement in post-peak strain capacity of the iron-based binder, quantified through inverse analysis, thereby facilitating higher amount of inelastic deformation and thus better resistance to crack-propagation.

- The individual intrinsic phase elastic properties in the novel iron-based binder system was determined using statistical nanoindentation technique. Seven distinct phases were identified. The iron carbonate reaction product was further classified as low-density, medium-density and high-density iron carbonate. The individual elastic properties are also quantified.
- The individual phase elastic properties determined using nanoindentation along with the pore volume fraction from MIP and solid phase volume fractions from different methods were used in multi-step micromechanical mean-field homogenization models (Mori-Tanaka method) to determine a homogenized Young's modulus of the composite material. The homogenized Young's modulus, was found to be in good agreement with the experimental macro-scale Young's modulus.
- The effect of various elevated temperatures on the mechanical behavior and microstructure of novel iron-based binder is also elucidated. While novel iron-based binder showed significantly higher flexural strength as compared to OPC paste at room temperature, iron-based binder lost its strength significantly at 300° C due to thermal decomposition of iron carbonate although it still shows similar strength as OPC. Complete decomposition of iron carbonate at 300° C, confirmed

using TGA and XRD spectra, has been established to be the cause of strength-loss at 300° C for iron-based binder.

- While OPC paste lost about 70% of its strength at 800° C, iron-based binder gained about 80% strength as compared to its strength at 300° C due to formation of crystalline products such as magnetite and hematite after decomposition of iron carbonate as confirmed by XRD spectra. Thus, at 800° C, novel iron-based binder exhibits a flexural strength which is 2 times and 5 times higher as compared to that of OPC paste at room temperature and 800° C respectively.
- Fracture response of mortars containing up to 30% of iron powder as a replacement of OPC was evaluated inspired by the findings of the beneficial influence of elongated metallic iron on the crack propagation response of iron-based binder. R-curves showed that the maximum strain energy release rate increased with iron powder content, thereby signifying better crack-tolerance.
- The FPZ widths (in the crack opening direction) measured using DIC remained relatively unchanged whereas the length (in the direction of crack extension) was found to increase with increase in iron powder content. The quantified FPZ features are in line with the elastic and inelastic components of strain energy release rates.

REFERENCES

Aboudi, Jacob. 1991. “Mechanics of Composite Materials- A Unified Micromechanical approach((Book)).” *Amsterdam and New York, Elsevier(Studies in Applied Mechanics.* 29.

Allison, Crispin. 2012. “Flexible Liners for Corrosion Protection of Pipelines.” https://dspace.lib.cranfield.ac.uk/handle/1826/7388.

Altun, Fatih, Tefaruk Haktanir, and Kamura Ari. 2007. “Effects of Steel Fiber Addition on Mechanical Properties of Concrete and RC Beams.” *Construction and Building Materials*, Fracture, Acoustic Emission and NDE in Concrete (KIFA-4), 21 (3): 654–61. doi:10.1016/j.conbuildmat.2005.12.006.

Ambikadevi, V. R, and M Lalithambika. 2000. “Effect of Organic Acids on Ferric Iron Removal from Iron-Stained Kaolinite.” *Applied Clay Science* 16 (3–4): 133–45. doi:10.1016/S0169-1317(99)00038-1.

Andersson, Martin, Jinliang Yuan, and Bengt Sundén. 2010. “Review on Modeling Development for Multiscale Chemical Reactions Coupled Transport Phenomena in Solid Oxide Fuel Cells.” *Applied Energy* 87 (5): 1461–76.

Andiç-Çakır, Özge, Oğuzhan Çopuroğlu, and Kambiz Ramyar. 2015. “Effect of High Temperature on Mechanical and Microstructural Properties of Cement Mortar.” Accessed May 10. http://www.irbnet.de/daten/iconda/CIB13098.pdf.

Archie, Gustave E. 1942. “The Electrical Resistivity Log as an Aid in Determining Some Reservoir Characteristics.” *Trans. AIMe* 146 (1): 54–62.

Arino, Antonio M., and Barzin Mobasher. 1999. “Effect of Ground Copper Slag on Strength and Toughness of Cementitious Mixes.” *ACI Materials Journal* 96 (1). http://www.concrete.org/Publications/ACIMaterialsJournal/ACIJournalSearch.aspx?m=details&ID=430.

Ar, Irfan, and Gülşen Doğu. 2001. “Calcination Kinetics of High Purity Limestones.” *Chemical Engineering Journal* 83 (2): 131–37.

Ataka, Yuji, Shinsuke Kato, and Qingyu Zhu. 2005. “Evaluation of Effective Diffusion Coefficient in Various Building Material and Absorbents by Mercury Intrusion Porosimetry.” *Journal of Environmental Engineering(Transaction of AIJ),* no. 589: 15–21.

Atiş, Cengiz Duran. 2002. “Heat Evolution of High-Volume Fly Ash Concrete.” *Cement and Concrete Research* 32 (5): 751–56. doi:10.1016/S0008-8846(01)00755-4.

Atluri, Satya N. 2004. *The Meshless Method (MLPG) for Domain & BIE Discretizations*. Vol. 677. Tech Science Press Forsyth. http://www.techscience.com/books/mlpg_atluri.html.

Azeez, Ali Basheer, Kahtan S. Mohammed, Mohd Mustafa Al Bakri Abdullah, Kamarudin Hussin, Andrei Victor Sandu, and Rafiza Abdul Razak. 2013. "The Effect of Various Waste Materials' Contents on the Attenuation Level of Anti-Radiation Shielding Concrete." *Materials* 6 (10): 4836–46.

Bachu, Stefan, W. D. Gunter, and E. H. Perkins. 1994. "Aquifer Disposal of CO2: Hydrodynamic and Mineral Trapping." *Energy Conversion and Management* 35 (4): 269–79. doi:10.1016/0196-8904(94)90060-4.

Bakhshi, Mehdi, Christopher Barsby, and Barzin Mobasher. 2014. "Comparative Evaluation of Early Age Toughness Parameters in Fiber Reinforced Concrete." *Materials and Structures* 47 (5): 853–72. doi:10.1617/s11527-013-0098-1.

Banthia, N., F. Majdzadeh, J. Wu, and V. Bindiganavile. 2014. "Fiber Synergy in Hybrid Fiber Reinforced Concrete (HyFRC) in Flexure and Direct Shear." *Cement and Concrete Composites* 48 (April): 91–97. doi:10.1016/j.cemconcomp.2013.10.018.

Banthia, N., and J. Sheng. 1996. "Fracture Toughness of Micro-Fiber Reinforced Cement Composites." *Cement and Concrete Composites*, Toughness of FRC Composites, 18 (4): 251–69. doi:10.1016/0958-9465(95)00030-5.

Bazant, Zdenek P., and Milan Jirásek. 2002. "Nonlocal Integral Formulations of Plasticity and Damage: Survey of Progress." *Journal of Engineering Mechanics* 128 (11): 1119–49.

Becher, Paul F. 1991. "Microstructural Design of Toughened Ceramics." *Journal of the American Ceramic Society* 74 (2): 255–69. doi:10.1111/j.1151-2916.1991.tb06872.x.

Bencardino, Francesco, Lidia Rizzuti, Giuseppe Spadea, and Ramnath N. Swamy. 2008. "Stress-Strain Behavior of Steel Fiber-Reinforced Concrete in Compression." *Journal of Materials in Civil Engineering* 20 (3): 255–63.

Bénézeth, P., J. L. Dandurand, and J. C. Harrichoury. 2009. "Solubility Product of Siderite (FeCO 3) as a Function of Temperature (25–250 C)." *Chemical Geology* 265 (1): 3–12.

Berndt, M. L. 2009. "Properties of Sustainable Concrete Containing Fly Ash, Slag and Recycled Concrete Aggregate." *Construction and Building Materials* 23 (7): 2606–13. doi:10.1016/j.conbuildmat.2009.02.011.

Bhargava, Jitendra, and Åke Rehnström. 1975. "High-Speed Photography for Fracture Studies of Concrete." *Cement and Concrete Research* 5 (3): 239–47. doi:10.1016/0008-8846(75)90006-X.

Bhushan, Bharat. 2010. *Handbook of Micro/nano Tribology*. CRC press. https://books.google.com/books?hl=en&lr=&id=KO0IRB1zirQC&oi=fnd&pg=P

A3&dq=Handbook+of+micro/nanotribology&ots=lKvVSVontK&sig=AbE9gAHUReVAsjpaWLgus9EppMU.

Bonavetti, V., H. Donza, G. Menéndez, O. Cabrera, and E. F. Irassar. 2003. "Limestone Filler Cement in Low W/c Concrete: A Rational Use of Energy." *Cement and Concrete Research* 33 (6): 865–71. doi:10.1016/S0008-8846(02)01087-6.

Bruno, Jordi, Paul Wersin, and Werner Stumm. 1992. "On the Influence of Carbonate in Mineral Dissolution: II. The Solubility of FeCO 3 (s) at 25 C and 1 Atm Total Pressure." *Geochimica et Cosmochimica Acta* 56 (3): 1149–55.

Bulychev, S. I., V. P. Alekhin, M. H. Shorshorov, A. P. Ternovskii, and G. D. Shnyrev. 1975. "Determining Young's Modulus from the Indentor Penetration Diagram." *Ind. Lab.* 41 (9): 1409–12.

Byun, Daewon, and Kenneth L. Schere. 2006. "Review of the Governing Equations, Computational Algorithms, and Other Components of the Models-3 Community Multiscale Air Quality (CMAQ) Modeling System." *Applied Mechanics Reviews* 59 (2): 51–77.

Carniglia, S. C. 1986. "Construction of the Tortuosity Factor from Porosimetry." *Journal of Catalysis* 102 (2): 401–18. doi:10.1016/0021-9517(86)90176-4.

Carpinteri, Alberto, and Giuseppe Lacidogna. 2003. "Damage Diagnostic in Concrete and Masonry Structures by Acoustic Emission Technique." *Facta Universitatis-Series: Mechanics, Automatic Control and Robotics* 3 (13): 755–64.

Carroll, John J., and Alan E. Mather. 1992. "The System Carbon Dioxide-Water and the Krichevsky-Kasarnovsky Equation." *Journal of Solution Chemistry* 21 (7): 607–21.

Carroll, Susan A., and Kevin G. Knauss. 2005. "Dependence of Labradorite Dissolution Kinetics on CO 2 (aq), Al (aq), and Temperature." *Chemical Geology* 217 (3): 213–25.

Chan, Sammy Yin Nin, Gai-Fei Peng, and Mike Anson. 1999. "Fire Behavior of High-Performance Concrete Made with Silica Fume at Various Moisture Contents." *ACI Materials Journal* 96 (3). http://www.concrete.org/Publications/InternationalConcreteAbstractsPortal.aspx?m=details&i=640.

Chengsheng, Ouyang, Mobasher Barzin, and Shah Surendra P. 1990. "An R-Curve Approach for Fracture of Quasi-Brittle Materials." *Engineering Fracture Mechanics* 37 (4): 901–13. doi:10.1016/0013-7944(90)90087-W.

Chen, H. H., and R. K. L. Su. 2013. "Tension Softening Curves of Plain Concrete." *Construction and Building Materials* 44 (July): 440–51. doi:10.1016/j.conbuildmat.2013.03.040.

Chen, Jinlong, Xiaochuan Zhang, Nan Zhan, and Xiaoyan Hu. 2010. “Deformation Measurement across Crack Using Two-Step Extended Digital Image Correlation Method.” *Optics and Lasers in Engineering*, Micro and Nano Metrology in Experimental Mechanics, 48 (11): 1126–31. doi:10.1016/j.optlaseng.2009.12.017.

Chen, J. J., A. K. H. Kwan, and Y. Jiang. 2014. “Adding Limestone Fines as Cement Paste Replacement to Reduce Water Permeability and Sorptivity of Concrete.” *Construction and Building Materials* 56 (April): 87–93. doi:10.1016/j.conbuildmat.2014.01.066.

Chindaprasirt, Prinya, Chai Jaturapitakkul, and Theerawat Sinsiri. 2005. “Effect of Fly Ash Fineness on Compressive Strength and Pore Size of Blended Cement Paste.” *Cement and Concrete Composites* 27 (4): 425–28. doi:10.1016/j.cemconcomp.2004.07.003.

Chithiraputhiran, Sundararaman, and Narayanan Neithalath. 2013. “Isothermal Reaction Kinetics and Temperature Dependence of Alkali Activation of Slag, Fly Ash and Their Blends.” *Construction and Building Materials* 45 (August): 233–42. doi:10.1016/j.conbuildmat.2013.03.061.

Choi, Hojin, Tongchai Tonsuwannarat, and others. 2002. “Unique Roles of Hydrocarbons in Flow-Induced Sweet Corrosion of X-52 Carbon Steel in Wet Gas Condensate Producing Wells.” *CORROSION 2002*. https://www.onepetro.org/conference-paper/NACE-02559.

Clerk-Maxwell, J. 1875. “XXII.—On the Dynamical Evidence of the Molecular Constitution of Bodies.” *J. Chem. Soc.* 28: 493–508.

Constantinides, Georgios, and Franz-Josef Ulm. 2004. “The Effect of Two Types of C-S-H on the Elasticity of Cement-Based Materials: Results from Nanoindentation and Micromechanical Modeling.” *Cement and Concrete Research* 34 (1): 67–80. doi:10.1016/S0008-8846(03)00230-8.

———. 2007. “The Nanogranular Nature of C–S–H.” *Journal of the Mechanics and Physics of Solids* 55 (1): 64–90.

Constantinides, G., K. S. Ravi Chandran, F. -J. Ulm, and K. J. Van Vliet. 2006. “Grid Indentation Analysis of Composite Microstructure and Mechanics: Principles and Validation.” *Materials Science and Engineering: A* 430 (1–2): 189–202. doi:10.1016/j.msea.2006.05.125.

Constantinides, G., F.-J. Ulm, and K. Van Vliet. 2003. “On the Use of Nanoindentation for Cementitious Materials.” *Materials and Structures* 36 (3): 191–96.

Cook, Raymond A., and Kenneth C. Hover. 1999. “Mercury Porosimetry of Hardened Cement Pastes.” *Cement and Concrete Research* 29 (6): 933–43. doi:10.1016/S0008-8846(99)00083-6.

Crolet, J. L. 1985. “The Role of Acetate Ions in CO 2 Corrosion.” *J. L. Crolet and M. R. Bonis. Societe Nationale Elf Aquitaine(Production), 64018 Pau Cedex France. Corrosion, 83/160. NACE, Houston, TX.$ 3. 00 per Copy*.

Crolet, J. L., N. Thevenot, and S. Nesic. 1998. “Role of Conductive Corrosion Products in the Protectiveness of Corrosion Layers.” *Corrosion* 54 (3): 194–203.

Dar, M. Ibrahim, and S. A. Shivashankar. 2014. “Single Crystalline Magnetite, Maghemite, and Hematite Nanoparticles with Rich Coercivity.” *RSC Advances* 4 (8): 4105–13.

Da Silva, W. R. L., J. Němeček, and P. Štemberk. 2013. “Application of Multiscale Elastic Homogenization Based on Nanoindentation for High Performance Concrete.” *Advances in Engineering Software*, Special Issue dedicated to Professor Zden ek Bittnar on the occasion of his Seventieth Birthday: Part I, 62–63 (August): 109–18. doi:10.1016/j.advengsoft.2013.04.007.

Das, Sumanta, Matthew Aguayo, Vikram Dey, Robert Kachala, Barzin Mobasher, Gaurav Sant, and Narayanan Neithalath. 2014. “The Fracture Response of Blended Formulations Containing Limestone Powder: Evaluations Using Two-Parameter Fracture Model and Digital Image Correlation.” *Cement and Concrete Composites* 53 (October): 316–26. doi:10.1016/j.cemconcomp.2014.07.018.

Das, Sumanta, Matthew Aguayo, Gaurav Sant, Barzin Mobasher, and Narayanan Neithalath. 2015. “Fracture Process Zone and Tensile Behavior of Blended Binders Containing Limestone Powder.” *Cement and Concrete Research* 73 (July): 51–62. doi:10.1016/j.cemconres.2015.03.002.

Das, Sumanta, Alyson Hendrix, David Andrew Stone, Barzin Mobasher, and Narayanan Neithalath. 2014c. “Flexural Fracture Response of a Novel Iron Carbonate Matrix - Glass Fiber Composite and Its Comparison to Portland Cement-Based Composites.” *Construction and Building Materials* Under Review.

Das, Sumanta, Beshoy Souliman, David Andrew Stone, and Narayanan Neithalath. 2014. “Synthesis and Properties of A Novel Structural Binder Utilizing the Chemistry of Iron Carbonation.” *ACS Applied Materials & Interfaces*, May. doi:10.1021/am5011145.

Das, Sumanta, David Stone, Diana Convey, and Narayanan Neithalath. 2014. “Pore- and Micro-Structural Characterization of a Novel Structural Binder Based on Iron Carbonation.” *Materials Characterization* 98 (December): 168–79. doi:10.1016/j.matchar.2014.10.025.

Davydov, D., M. Jirásek, and L. Kopeckỳ. 2011. “Critical Aspects of Nano-Indentation Technique in Application to Hardened Cement Paste.” *Cement and Concrete Research* 41 (1): 20–29.

Dayalan, E., G. Vani, J. R. Shadley, and S. Shirazi. 1995. “Modeling CO 2 Corrosion of Carbon Steels in Pipe Flow.” *E. Dayalan, G. Vani, J. R. Shadley, S. A. Shirazi, and E. F. Rybicki, Paper*, no. 118.

Demirel, Bahar, and Oğuzhan Keleştemur. 2010. “Effect of Elevated Temperature on the Mechanical Properties of Concrete Produced with Finely Ground Pumice and Silica Fume.” *Fire Safety Journal* 45 (6–8): 385–91. doi:10.1016/j.firesaf.2010.08.002.

De Waard, C., U. Lotz, and D. E. Milliams. 1991. “Predictive Model for CO2 Corrosion Engineering in Wet Natural Gas Pipelines.” *Corrosion* 47 (12): 976–85. doi:10.5006/1.3585212.

Dias, W. P. S., G. A. Khoury, and P. J. E. Sullivan. 1990. “Mechanical Properties of Hardened Cement Paste Exposed to Temperatures up to 700 C (1292 F).” *ACI Materials Journal* 87 (2). http://www.concrete.org/Publications/InternationalConcreteAbstractsPortal.aspx?m=details&i=1981.

Do, Duong D. 1982. “On the Validity of the Shrinking Core Model in Noncatalytic Gas Solid Reaction.” *Chemical Engineering Science* 37 (10): 1477–81.

Drucker, Daniel Charles, and William Prager. 2013. “Soil Mechanics and Plastic Analysis or Limit Design.” *Quarterly of Applied Mathematics* 10. http://www.citeulike.org/group/13900/article/11885975.

Dugstad, Arne. 1992. “The Importance of FeCO 3 Supersaturation on the CO 2 Corrosion of Carbon Steels.” *A. Dugstad, Paper*, no. 14.

Dugstad, Arne, and others. 1998. “Mechanism of Protective Film Formation during CO2 Corrosion of Carbon Steel.” In *CORROSION 98*. NACE International. https://www.onepetro.org/LOGOUT?dest=https%3A%2F%2Fwww.onepetro.org%2Fconference-paper%2FNACE-98031.

Eckart, Carl. 1948. “The Thermodynamics of Irreversible Processes. IV. The Theory of Elasticity and Anelasticity.” *Physical Review* 73 (4): 373.

El-Lateef, HM Abd, Vagif Maharram Abbasov, Leylufer Imran Aliyeva, and Teyyub Allahverdi Ismayilov. 2012. “Corrosion Protection of Steel Pipelines against CO 2 Corrosion—a Review.” *Chem. J* 2 (2): 52–63.

Elssner, G., D. Korn, and M. Ruehle. 1994. “The Influence of Interface Impurities on Fracture Energy of UHV Diffusion Bonded Metal-Ceramic Bicrystals.” *Scripta Metallurgica et Materialia* 31 (8): 1037–42.

Eshelby, J. D. 1957. “The Determination of the Elastic Field of an Ellipsoidal Inclusion, and Related Problems.” *Proceedings of the Royal Society of London A:*

Mathematical, Physical and Engineering Sciences 241 (1226): 376–96. doi:10.1098/rspa.1957.0133.

Fairén, Alberto G., David Fernández-Remolar, James M. Dohm, Victor R. Baker, and Ricardo Amils. 2004. "Inhibition of Carbonate Synthesis in Acidic Oceans on Early Mars." *Nature* 431 (7007): 423–26. doi:10.1038/nature02911.

Feldman, R. F. 1984. "Pore Structure Damage in Blended Cements Caused by Mercury Intrusion." *Journal of the American Ceramic Society* 67 (1): 30–33. doi:10.1111/j.1151-2916.1984.tb19142.x.

Flaathen, Therese K., Sigurður R. Gislason, Eric H. Oelkers, and Árný E. Sveinbjörnsdóttir. 2009. "Chemical Evolution of the Mt. Hekla, Iceland, Groundwaters: A Natural Analogue for CO2 Sequestration in Basaltic Rocks." *Applied Geochemistry* 24 (3): 463–74. doi:10.1016/j.apgeochem.2008.12.031.

Flower, David J. M., and Jay G. Sanjayan. 2007. "Green House Gas Emissions due to Concrete Manufacture." *The International Journal of Life Cycle Assessment* 12 (5): 282–88. doi:10.1065/lca2007.05.327.

Formaggia, Luca, Fabio Nobile, Alfio Quarteroni, and Alessandro Veneziani. 1999. "Multiscale Modelling of the Circulatory System: A Preliminary Analysis." *Computing and Visualization in Science* 2 (2-3): 75–83.

Gal, Erez, Avshalom Ganz, Liran Hadad, and Roman Kryvoruk. 2008. "Development of a Concrete Unit Cell." *International Journal for Multiscale Computational Engineering* 6 (5). http://www.dl.begellhouse.com/journals/61fd1b191cf7e96f,5f614aef50b96bb2,4a8b6f6109900253.html.

Gal, Erez, and Roman Kryvoruk. 2011. "Fiber Reinforced Concrete Properties- a Multiscale Approach." *Computers & Concrete* 8 (5): 525–39.

Garsany, Yannick, Derek Pletcher, Bill M. Hedges, and others. 2002. "The Role of Acetate in CO2 Corrosion of Carbon Steel: Has the Chemistry Been Forgotten?" In *CORROSION 2002*. NACE International. https://www.onepetro.org/LOGOUT?dest=https%3A%2F%2Fwww.onepetro.org%2Fconference-paper%2FNACE-02273.

Gdoutos, Emmanuel E. 2006. *Fracture Mechanics: An Introduction*. Vol. 123. Springer. http://books.google.com/books?hl=en&lr=&id=w7swgZq4xRoC&oi=fnd&pg=PR9&dq=Fracture+Mechanics:+an+introduction&ots=N8k6xn9HLm&sig=-PvkiLLeZk4KXurKdFCqSmVA6Vg.

Gelderblom, Hanneke, Álvaro G. Marín, Hrudya Nair, Arie van Houselt, Leon Lefferts, Jacco H. Snoeijer, and Detlef Lohse. 2011. "How Water Droplets Evaporate on a Superhydrophobic Substrate." *Physical Review E* 83 (2): 026306. doi:10.1103/PhysRevE.83.026306.

Georgali, B., and P. E. Tsakiridis. 2005. “Microstructure of Fire-Damaged Concrete. A Case Study.” *Cement and Concrete Composites*, Cement and Concrete Research in Greece, 27 (2): 255–59. doi:10.1016/j.cemconcomp.2004.02.022.

Ghaboussi, J., J. H. Garrett Jr, and X. Wu. 1990. “Material Modeling with Neural Networks.” In *Proceedings of the International Conference on Numerical Methods in Engineering: Theory and Applications, Swansea, UK*, 701–17.

Ghaboussi, J., J. H. Garrett Jr, and Xiping Wu. 1991. “Knowledge-Based Modeling of Material Behavior with Neural Networks.” *Journal of Engineering Mechanics* 117 (1): 132–53.

Ghafari, Ehsan, Hugo Costa, Eduardo Júlio, António Portugal, and Luisa Durães. 2014. “The Effect of Nanosilica Addition on Flowability, Strength and Transport Properties of Ultra High Performance Concrete.” *Materials & Design* 59 (July): 1–9. doi:10.1016/j.matdes.2014.02.051.

Ghorbani, Rahim, Fabio Matta, and Michael A. Sutton. 2014. “Full-Field Displacement Measurement and Crack Mapping on Masonry Walls Using Digital Image Correlation.” In *Advancement of Optical Methods in Experimental Mechanics, Volume 3*, 187–96. Springer. http://link.springer.com/chapter/10.1007/978-3-319-00768-7_23.

Ghosh, Somnath, Kyunghoon Lee, and Prasanna Raghavan. 2001. “A Multi-Level Computational Model for Multi-Scale Damage Analysis in Composite and Porous Materials.” *International Journal of Solids and Structures* 38 (14): 2335–85.

Giammar, Daniel E., Robert G. Bruant, and Catherine A. Peters. 2005. “Forsterite Dissolution and Magnesite Precipitation at Conditions Relevant for Deep Saline Aquifer Storage and Sequestration of Carbon Dioxide.” *Chemical Geology* 217 (3): 257–76.

Giesche, Herbert. 2006. “Mercury Porosimetry: A General (Practical) Overview.” *Particle & Particle Systems Characterization* 23 (1): 9–19. doi:10.1002/ppsc.200601009.

Gislason, Sigurdur Reynir, Domenik Wolff-Boenisch, Andri Stefansson, Eric H. Oelkers, Einar Gunnlaugsson, Hólmfridur Sigurdardottir, Bergur Sigfusson, et al. 2010. “Mineral Sequestration of Carbon Dioxide in Basalt: A Pre-Injection Overview of the CarbFix Project.” *International Journal of Greenhouse Gas Control* 4 (3): 537–45. doi:10.1016/j.ijggc.2009.11.013.

Gitman, Inna Mikhailovna. 2006. “Representative Volumes and Multi-Scale Modelling of Quasi-Brittle Materials.” http://www.narcis.nl/publication/RecordID/oai:tudelft.nl:uuid:b9073796-fd46-433f-a405-1b226ce9583a.

Golubev, Sergey V., and Oleg S. Pokrovsky. 2006. “Experimental Study of the Effect of Organic Ligands on Diopside Dissolution Kinetics.” *Chemical Geology* 235 (3): 377–89.

Gopalaratnam, Vellore S., and Ravindra Gettu. 1995. “On the Characterization of Flexural Toughness in Fiber Reinforced Concretes.” *Cement and Concrete Composites* 17 (3): 239–54. doi:10.1016/0958-9465(95)99506-O.

Goto, Seishi, and Della M. Roy. 1981. “The Effect of W/c Ratio and Curing Temperature on the Permeability of Hardened Cement Paste.” *Cement and Concrete Research* 11 (4): 575–79. doi:10.1016/0008-8846(81)90087-9.

Graybeal, Benjamin A. 2007. “Compressive Behavior of Ultra-High-Performance Fiber-Reinforced Concrete.” *ACI Materials Journal* 104 (2). http://www.concrete.org/Publications/InternationalConcreteAbstractsPortal.aspx?m=details&i=18577.

Griffith, Alan A. 1921. “The Phenomena of Rupture and Flow in Solids.” *Philosophical Transactions of the Royal Society of London. Series A, Containing Papers of a Mathematical or Physical Character*, 163–98.

Hadjab.S, H., M. Chabaat, and J.-Fr Thimus. 2007. “Use of Scanning Electron Microscope and the Non-Local Isotropic Damage Model to Investigate Fracture Process Zone in Notched Concrete Beams.” *Experimental Mechanics* 47 (4): 473–84. doi:10.1007/s11340-006-9001-0.

Haidar, K., G. Pijaudier-Cabot, J. F. Dubé, and A. Loukili. 2005. “Correlation between the Internal Length, the Fracture Process Zone and Size Effect in Model Materials.” *Materials and Structures* 38 (2): 201–10. doi:10.1007/BF02479345.

Handoo, S. K., S. Agarwal, and S. K. Agarwal. 2002. “Physicochemical, Mineralogical, and Morphological Characteristics of Concrete Exposed to Elevated Temperatures.” *Cement and Concrete Research* 32 (7): 1009–18. doi:10.1016/S0008-8846(01)00736-0.

Han, J., B. N. Brown, and S. Nešic. 2010. “Investigation of the Galvanic Mechanism for Localized Carbon Dioxide Corrosion Propagation Using the Artificial Pit Technique.” *Corrosion* 66 (9): 095003–095003.

HAN, Weixin. 2009. “Glass Ceramic of High Hardness and Fracture Toughness Developed from Iron-Rich Wastes.” *Acta Metallurgica Sinica (English Letters)* 22 (3): 181–90. doi:10.1016/S1006-7191(08)60087-3.

Hedges, Bill, Lorraine McVeigh, and others. 1999. “The Role of Acetate in CO2 Corrosion: The Double Whammy.” *CORROSION 99*. https://www.onepetro.org/conference-paper/NACE-99021.

Herget, G., and K. Unrug. 1976. “In Situ Rock Strength from Triaxial Testing.” *International Journal of Rock Mechanics and Mining Sciences & Geomechanics Abstracts* 13 (11): 299–302. doi:10.1016/0148-9062(76)91828-3.

Hjelmstad, Keith D. 2005. *Fundamentals of Structural Mechanics*. Springer. http://link.springer.com/content/pdf/10.1007/b101129.pdf.

Hobbs, D. W. 1964. “The Tensile Strength of Rocks.” *International Journal of Rock Mechanics and Mining Sciences & Geomechanics Abstracts* 1 (3): 385–96. doi:10.1016/0148-9062(64)90005-1.

———. 1967. “Rock Tensile Strength and Its Relationship to a Number of Alternative Measures of Rock Strength.” *International Journal of Rock Mechanics and Mining Sciences & Geomechanics Abstracts* 4 (1): 115–27. doi:10.1016/0148-9062(67)90009-5.

Holloway, Sam. 1997. “An Overview of the Underground Disposal of Carbon Dioxide.” *Energy Conversion and Management*, Proceedings of the Third International Conference on Carbon Dioxide Removal, 38, Supplement: S193–98. doi:10.1016/S0196-8904(96)00268-3.

Horii, Hideyuki, and Toshimichi Ichinomiya. 1991. “Observation of Fracture Process Zone by Laser Speckle Technique and Governing Mechanism in Fracture of Concrete.” In *Current Trends in Concrete Fracture Research*, edited by Z. P. Bažant, 19–29. Springer Netherlands. http://link.springer.com/chapter/10.1007/978-94-011-3638-9_2.

Hori, Muneo, and Sia Nemat-Nasser. 1993. “Double-Inclusion Model and Overall Moduli of Multi-Phase Composites.” *Mechanics of Materials* 14 (3): 189–206. doi:10.1016/0167-6636(93)90066-Z.

Horstemeyer, M. F. 2010. “Multiscale Modeling: A Review.” In *Practical Aspects of Computational Chemistry*, 87–135. Springer. http://link.springer.com/chapter/10.1007/978-90-481-2687-3_4.

Horstemeyer, M. F., M. M. Matalanis, A. M. Sieber, and M. L. Botos. 2000. “Micromechanical Finite Element Calculations of Temperature and Void Configuration Effects on Void Growth and Coalescence.” *International Journal of Plasticity* 16 (7): 979–1015.

Horstemeyer, M. F., and S. Ramaswamy. 2000. “On Factors Affecting Localization and Void Growth in Ductile Metals: A Parametric Study.” *International Journal of Damage Mechanics* 9 (1): 5–28.

Howind, T., J. J. Hughes, W. Zhu, Francisca Puertas, Sara Goñi Elizalde, Maria Soledad Hernandez, Ana Guerrero Bustos, Marta Palacios, and Jorge S. Dolado. 2011. “Mapping of Mechanical Properties of Cement Paste Microstructures.” http://oa.upm.es/12563/.

Hu, Chuanlin, and Zongjin Li. 2014. “Micromechanical Investigation of Portland Cement Paste.” *Construction and Building Materials* 71 (November): 44–52. doi:10.1016/j.conbuildmat.2014.08.017.

Hughes, John J., and Pavel Trtik. 2004. “Micro-Mechanical Properties of Cement Paste Measured by Depth-Sensing Nanoindentation: A Preliminary Correlation of Physical Properties with Phase Type.” *Materials Characterization* 53 (2): 223–31.

Hu, G. K, and G. J Weng. 2000. “The Connections between the Double-Inclusion Model and the Ponte Castaneda–Willis, Mori–Tanaka, and Kuster–Toksoz Models.” *Mechanics of Materials* 32 (8): 495–503. doi:10.1016/S0167-6636(00)00015-6.

Hu, X., and F. Wittmann. 1990. “Experimental Method to Determine Extension of Fracture-Process Zone.” *Journal of Materials in Civil Engineering* 2 (1): 15–23. doi:10.1061/(ASCE)0899-1561(1990)2:1(15).

Ibrahimbegović, Adnan, and Damijan Markovič. 2003. “Strong Coupling Methods in Multi-Phase and Multi-Scale Modeling of Inelastic Behavior of Heterogeneous Structures.” *Computer Methods in Applied Mechanics and Engineering* 192 (28): 3089–3107.

Iii, R. B. Evans, G. M. Watson, and E. A. Mason. 1961. “Gaseous Diffusion in Porous Media at Uniform Pressure.” *The Journal of Chemical Physics* 35 (6): 2076–83. doi:10.1063/1.1732211.

Ikeda, A. 1985. “Prevention of CO 2 Corrosion of Line Pipe and Oil Country Tubular Goods.” *A. Ikeda, S. Mukai and M. Ueda, Central Research Laboratories, Sumitomo Metal Industries, Ltd., 1-3, Nishinagasu-Hondori, Amagasaki, Japan*.

“Influence of Aggregate Size and Gradation on Acoustic Absorption of Enhanced Porosity Concrete.” 2004. *ACI Materials Journal* 101 (1). http://www.concrete.org/Publications/InternationalConcreteAbstractsPortal.aspx?m=details&i=12991.

Irwin, G. R. 1958. “Analysis of Stresses and Strains near the End of a Crack Traversing a Plate, Discussion.” *J. Appl. Mech.*, 299–301.

Ismail, Zainab Z., and Enas A. AL-Hashmi. 2008. “Reuse of Waste Iron as a Partial Replacement of Sand in Concrete.” *Waste Management* 28 (11): 2048–53. doi:10.1016/j.wasman.2007.07.009.

Jenq, Yeoushang, and Surendra P. Shah. 1985. “Two Parameter Fracture Model for Concrete.” *Journal of Engineering Mechanics* 111 (10): 1227–41.

Jenq, Y. S., and S. P. Shah. 1985. “A Fracture Toughness Criterion for Concrete.” *Engineering Fracture Mechanics* 21 (5): 1055–69. doi:10.1016/0013-7944(85)90009-8.

Jia, Z., and S. P. Shah. 1994. “Two-Dimensional Electronic-Speckle-Pattern Interferometry and Concrete-Fracture Processes.” *Experimental Mechanics* 34 (3): 262–70. doi:10.1007/BF02319764.

Johnson, Maureen Lynn. 1991. “Ferrous Carbonate Precipitation Kinetics-A Temperature Ramped Approach.” *Rice University, Houston*. http://scholarship.rice.edu/handle/1911/16451.

Joosten, Michael W., Juri Kolts, Justin W. Hembree, Mohsen Achour, and others. 2002. “Organic Acid Corrosion in Oil and Gas Production.” *CORROSION 2002*. https://www.onepetro.org/conference-paper/NACE-02294.

Kanouté, P., D. P. Boso, J. L. Chaboche, and B. A. Schrefler. 2009. “Multiscale Methods for Composites: A Review.” *Archives of Computational Methods in Engineering* 16 (1): 31–75.

Kan, Yu-Cheng, Kuang-Chih Pei, and Chien-Lung Chang. 2004. “Strength and Fracture Toughness of Heavy Concrete with Various Iron Aggregate Inclusions.” *Nuclear Engineering and Design*, SMiRT 16. Selected and Updated Papers from the 16th International Conference on Structural Mechanics in Reactor Technology, Washington DC, 228 (1–3): 119–27. doi:10.1016/j.nucengdes.2003.06.008.

Kan, Yu Cheng, Hsuan Chih Yang, and Kuang Chih Pei. 2012. “Strength and Toughness of Steel Fiber Reinforced Heavy Concrete.” *Advanced Materials Research* 512: 2908–13.

Kast, W., and C. -R. Hohenthanner. 2000. “Mass Transfer within the Gas-Phase of Porous Media.” *International Journal of Heat and Mass Transfer* 43 (5): 807–23. doi:10.1016/S0017-9310(99)00158-1.

Katz, A. J., and A. H. Thompson. 1986. “Quantitative Prediction of Permeability in Porous Rock.” *Physical Review. B, Condensed Matter* 34 (11): 8179–81.

———. 1987. “Prediction of Rock Electrical Conductivity from Mercury Injection Measurements.” *Journal of Geophysical Research: Solid Earth* 92 (B1): 599–607. doi:10.1029/JB092iB01p00599.

Kemp, P. H. 1971. “Chemistry of Natural waters—III Carbonic Acid.” *Water Research* 5 (8): 611–19.

Kermani, Bijan, and Liane M. Smith. 1997. *A Working Party Report on CO2 Corrosion Control in Oil and Gas Production: Design Considerations*. Vol. 688. Maney Pub.

Kermani, M. B., and A. Morshed. 2003. “Carbon Dioxide Corrosion in Oil and Gas Production-A Compendium.” *Corrosion* 59 (8): 659–83.

Kermani, M. B., and L. M. Smith. 1997. “CO2 Corrosion Control in Oil and Gas Production. Design Considerations (EFC 23).” *European Federation of Corrosion Publications*, no. 23: 4–12.

Klein, Elisa, Marco De Lucia, Thomas Kempka, and Michael Kühn. 2013. “Evaluation of Long-Term Mineral Trapping at the Ketzin Pilot Site for CO2 Storage: An Integrative Approach Using Geochemical Modelling and Reservoir Simulation.” *International Journal of Greenhouse Gas Control* 19 (November): 720–30. doi:10.1016/j.ijggc.2013.05.014.

Kobayashi, A. S., N. M. Hawkins, D. B. Barker, and B. M. Liaw. 1985. “Fracture Process Zone of Concrete.” In *Application of Fracture Mechanics to Cementitious Composites*, edited by S. P. Shah, 25–50. NATO ASI Series 94. Springer Netherlands. http://link.springer.com/chapter/10.1007/978-94-009-5121-1_2.

Koteeswaran, Mythili. 2010. “CO2 and H2S Corrosion in Oil Pipelines.” http://brage.bibsys.no/xmlui/handle/11250/182434.

Kouznetsova, Varvara, Marc GD Geers, and WA Marcel Brekelmans. 2002. “Multi-Scale Constitutive Modelling of Heterogeneous Materials with a Gradient-Enhanced Computational Homogenization Scheme.” *International Journal for Numerical Methods in Engineering* 54 (8): 1235–60.

Kouznetsova, V., W. A. M. Brekelmans, and F. P. T. Baaijens. 2001. “An Approach to Micro-Macro Modeling of Heterogeneous Materials.” *Computational Mechanics* 27 (1): 37–48.

Koziol, Andrea M. 1999. “Experimental Determination of Siderite (Iron Carbonate) Stability Under Moderate Pressure-Temperature Conditions, and Application to Martian Carbonate Parageneses.” In *Lunar and Planetary Science Conference*, 30:1226. http://adsabs.harvard.edu/abs/1999LPI....30.1226K.

Krottenthaler, M., C. Schmid, J. Schaufler, K. Durst, and M. Göken. 2013. “A Simple Method for Residual Stress Measurements in Thin Films by Means of Focused Ion Beam Milling and Digital Image Correlation.” *Surface and Coatings Technology*, Proceedings of the 39th International Conference on Metallurgical Coatings and Thin Films (ICMCTF) ICMCTF 2012 Proceedings of the 39th International Conference on Metallurgical Coatings and Thin Films (ICMCTF), 215 (January): 247–52. doi:10.1016/j.surfcoat.2012.08.095.

Kumar, Aditya, Tandre Oey, Guillermo Puerta Falla, Ryan Henkensiefken, Narayanan Neithalath, and Gaurav Sant. 2013. “A Comparison of Intergrinding and Blending Limestone on Reaction and Strength Evolution in Cementitious Materials.” *Construction and Building Materials* 43 (June): 428–35. doi:10.1016/j.conbuildmat.2013.02.032.

Kumar, Rakesh, and B Bhattacharjee. 2003. “Study on Some Factors Affecting the Results in the Use of MIP Method in Concrete Research.” *Cement and Concrete Research* 33 (3): 417–24. doi:10.1016/S0008-8846(02)00974-2.

Kumar, R., A. Thangaraj, R. N. Bhat, and P. Ratnasamy. 1990. “Synthesis of Iron-Silicate Analogs of Zeolite Beta.” *Zeolites* 10 (2): 85–89. doi:10.1016/0144-2449(90)90023-K.

Kwan, Wai Hoe, Mahyuddin Ramli, and Chee Ban Cheah. 2014. “Flexural Strength and Impact Resistance Study of Fibre Reinforced Concrete in Simulated Aggressive Environment.” *Construction and Building Materials* 63 (July): 62–71. doi:10.1016/j.conbuildmat.2014.04.004.

Lackner, Klaus S. 2002. “Carbonate Chemistry for Sequestering Fossil Carbon.” *Annual Review of Energy and the Environment* 27 (1): 193–232. doi:10.1146/annurev.energy.27.122001.083433.

Lackner, Klaus S., Christopher H. Wendt, Darryl P. Butt, Edward L. Joyce, and David H. Sharp. 1995. “Carbon Dioxide Disposal in Carbonate Minerals.” *Energy* 20 (11): 1153–70.

LaManna, Jacob M., and Satish G. Kandlikar. 2011. “Determination of Effective Water Vapor Diffusion Coefficient in Pemfc Gas Diffusion Layers.” *International Journal of Hydrogen Energy* 36 (8): 5021–29. doi:10.1016/j.ijhydene.2011.01.036.

Lawrence, G. P. 1978. “Stability of Soil Pores During Mercury Intrusion Porosimetry.” *Journal of Soil Science* 29 (3): 299–304. doi:10.1111/j.1365-2389.1978.tb00777.x.

Lee, Jaesung, Yunping Xi, Kaspar Willam, and Younghan Jung. 2009. “A Multiscale Model for Modulus of Elasticity of Concrete at High Temperatures.” *Cement and Concrete Research* 39 (9): 754–62.

Lee, Sung Oh, Tam Tran, Byoung Hi Jung, Seong Jun Kim, and Myong Jun Kim. 2007. “Dissolution of Iron Oxide Using Oxalic Acid.” *Hydrometallurgy* 87 (3–4): 91–99. doi:10.1016/j.hydromet.2007.02.005.

Lepp, Henry. 1957. *Stages in the Oxidation of Magnetite*. Vol. 42. 9-10. MINERALOGICAL SOC AMER 1015 EIGHTEENTH ST, NW SUITE 601, WASHINGTON, DC 20036.

Lide, David R. 2003. *CRC Handbook of Chemistry and Physics, 84th Edition*. CRC Press.

Lin, Qing, and Joseph F. Labuz. 2013. “Fracture of Sandstone Characterized by Digital Image Correlation.” *International Journal of Rock Mechanics and Mining Sciences* 60 (June): 235–45. doi:10.1016/j.ijrmms.2012.12.043.

Linter, B. R., and G. T. Burstein. 1999. “Reactions of Pipeline Steels in Carbon Dioxide Solutions.” *Corrosion Science* 41 (1): 117–39.

Liu, Yong. 2008. *Modeling and Simulation of Methane Production from Hydrate Reserves*. ProQuest.

Li, Xiaodong, and Bharat Bhushan. 2002. “A Review of Nanoindentation Continuous Stiffness Measurement Technique and Its Applications.” *Materials Characterization* 48 (1): 11–36. doi:10.1016/S1044-5803(02)00192-4.

Lloyd, D. J. 1994. “Particle Reinforced Aluminium and Magnesium Matrix Composites.” *International Materials Reviews* 39 (1): 1–23.

Lotz, U., L. Van Bodegom, and C. Ouwehand. 1991. “The Effect of Type of Oil or Gas Condensate on Carbonic Acid Corrosion.” *Corrosion* 47 (8): 635–45.

Lower, Stephen K. 1999. “Carbonate Equilibria in Natural Waters.” *Simon Fraser University* 544. http://www.chem1.com/acad/pdf/c3carb.pdf.

Macklin, Paul, Steven McDougall, Alexander RA Anderson, Mark AJ Chaplain, Vittorio Cristini, and John Lowengrub. 2009. “Multiscale Modelling and Nonlinear Simulation of Vascular Tumour Growth.” *Journal of Mathematical Biology* 58 (4-5): 765–98.

Mai, Y. W., and M. I. Hakeem. 1984. “Slow Crack Growth in Cellulose Fibre Cements.” *Journal of Materials Science* 19 (2): 501–8. doi:10.1007/BF02403237.

Maji, A. K., C. Ouyang, and S. P. Shah. 1990. “Fracture Mechanisms of Quasi-Brittle Materials Based on Acoustic Emission.” *Journal of Materials Research* 5 (01): 206–17. doi:10.1557/JMR.1990.0206.

Markovic, Damijan, and Adnan Ibrahimbegovic. 2004. “On Micro–macro Interface Conditions for Micro Scale Based FEM for Inelastic Behavior of Heterogeneous Materials.” *Computer Methods in Applied Mechanics and Engineering* 193 (48): 5503–23.

Maroto-Valer, M. Mercedes, Zhong Tang, and Yinzhi Zhang. 2005. “CO 2 Capture by Activated and Impregnated Anthracites.” *Fuel Processing Technology* 86 (14): 1487–1502.

Maroto-Valer, M. M., D. J. Fauth, M. E. Kuchta, Y. Zhang, and J. M. Andresen. 2005. “Activation of Magnesium Rich Minerals as Carbonation Feedstock Materials for CO 2 Sequestration.” *Fuel Processing Technology* 86 (14): 1627–45.

Maslehuddin, M., A. A. Naqvi, M. Ibrahim, and Z. Kalakada. 2013. “Radiation Shielding Properties of Concrete with Electric Arc Furnace Slag Aggregates and Steel Shots.” *Annals of Nuclear Energy* 53 (March): 192–96. doi:10.1016/j.anucene.2012.09.006.

Matter, Jürg M., and Peter B. Kelemen. 2009. “Permanent Storage of Carbon Dioxide in Geological Reservoirs by Mineral Carbonation.” *Nature Geoscience* 2 (12): 837–41. doi:10.1038/ngeo683.

McClintock, Frank A. 1968. “A Criterion for Ductile Fracture by the Growth of Holes.” *Journal of Applied Mechanics* 35 (2): 363–71.

McGrail, B. Peter, H. Todd Schaef, Anita M. Ho, Yi-Ju Chien, James J. Dooley, and Casie L. Davidson. 2006. “Potential for Carbon Dioxide Sequestration in Flood Basalts.” *Journal of Geophysical Research: Solid Earth (1978–2012)* 111 (B12). http://onlinelibrary.wiley.com/doi/10.1029/2005JB004169/full.

Mehta, Povindar Kumar, and Paulo JM Monteiro. 2006. *Concrete: Microstructure, Properties, and Materials*. Vol. 3. McGraw-Hill New York.

Miehe, C., and A. Koch. 2002. “Computational Micro-to-Macro Transitions of Discretized Microstructures Undergoing Small Strains.” *Archive of Applied Mechanics* 72 (4-5): 300–317.

Mihashi, H., and N. Nomura. 1996. “Correlation between Characteristics of Fracture Process Zone and Tension-Softening Properties of Concrete.” *Nuclear Engineering and Design* 165 (3): 359–76. doi:10.1016/0029-5493(96)01205-8.

Mijno, Violaine, Lionel J. J. Catalan, François Martin, and Jean-Claude Bollinger. 2004. “Compositional Changes in Cement-Stabilized Waste during Leach Tests—comparison of SEM/EDX Data with Predictions from Geochemical Speciation Modeling.” *Journal of Colloid and Interface Science* 280 (2): 465–77. doi:10.1016/j.jcis.2004.08.025.

Miled, K., K. Sab, and R. Le Roy. 2011. “Effective Elastic Properties of Porous Materials: Homogenization Schemes vs Experimental Data.” *Mechanics Research Communications* 38 (2): 131–35. doi:10.1016/j.mechrescom.2011.01.009.

Miller, Foil A., and Charles H. Wilkins. 1952. “Infrared Spectra and Characteristic Frequencies of Inorganic Ions.” *Analytical Chemistry* 24 (8): 1253–94.

Mindess, Sidney, and Sidney Diamond. 1980. “A Preliminary SEM Study of Crack Propagation in Mortar.” *Cement and Concrete Research* 10 (4): 509–19. doi:10.1016/0008-8846(80)90095-2.

Mobasher, Barzin. 2011. *Mechanics of Fiber and Textile Reinforced Cement Composites*. CRC Press.

Mobasher, Barzin, Mehdi Bakhshi, and Christopher Barsby. 2014. “Backcalculation of Residual Tensile Strength of Regular and High Performance Fiber Reinforced Concrete from Flexural Tests.” *Construction and Building Materials* 70 (November): 243–53. doi:10.1016/j.conbuildmat.2014.07.037.

Mobasher, Barzin, Amir Bonakdar, and Mehdi Bakhshi. 2015. *Back-Calculation Procedure for Cyclic Flexural Fracture Tests in Fiber Reinforced Concrete*. ACI Technical Report SP-300—5.

Mobasher, Barzin, Vikram Dey, Zvi Cohen, and Alva Peled. 2014. "Correlation of Constitutive Response of Hybrid Textile Reinforced Concrete from Tensile and Flexural Tests." *Cement and Concrete Composites* 53 (October): 148–61. doi:10.1016/j.cemconcomp.2014.06.004.

Mondal, Paramita, Surendra P. Shah, and Laurence Marks. 2007. "A Reliable Technique to Determine the Local Mechanical Properties at the Nanoscale for Cementitious Materials." *Cement and Concrete Research* 37 (10): 1440–44.

Moody, Neville R., William W. Gerberich, Nancy Burnham, and Shefford P. Baker. 1998. *Fundamentals of Nanoindentation and Nanotribology*. Warrendale, PA (United States); Materials Research Society. http://www.osti.gov/scitech/biblio/6177899.

Moon, Han Young, Hong Sam Kim, and Doo Sun Choi. 2006. "Relationship between Average Pore Diameter and Chloride Diffusivity in Various Concretes." *Construction and Building Materials* 20 (9): 725–32. doi:10.1016/j.conbuildmat.2005.02.005.

Mori, T, and K Tanaka. 1973. "Average Stress in Matrix and Average Elastic Energy of Materials with Misfitting Inclusions." *Acta Metallurgica* 21 (5): 571–74. doi:10.1016/0001-6160(73)90064-3.

Morsy, M. M., S. S. Shebl, and A. M. Rashad. 2008. "Effect of Fire on Microstructure and Mechanical Properties of Blended Cement Pastes Containing Metakaolin and Silica Fume." *Asian Journal of Civil Engineering (Building and Housing)* 9 (2). http://www.sid.ir/EN/VEWSSID/J_pdf/103820080205.pdf.

Mukhopadhyay, A. K, S. K Datta, and D Chakraborty. 1999. "Fracture Toughness of Structural Ceramics." *Ceramics International* 25 (5): 447–54. doi:10.1016/S0272-8842(98)00056-X.

Mura, Toshio. 1987. *Micromechanics of Defects in Solids*. Vol. 3. Springer. http://books.google.com/books?hl=en&lr=&id=N_JmtkfsdZgC&oi=fnd&pg=PA1&dq=Micromechanics+of+defects+in+solids&ots=P0x_Fo2tee&sig=KFSjTSKPOecibj3KNBTF-A5NGWU.

Naganuma, Takeshi, Kise Yukimura, Norifumi Todaka, and Shuji Ajima. 2011. "Concept and Experimental Study for a New Enhanced Mineral Trapping System by Means of Microbially Mediated Processes." *Energy Procedia*, 10th International Conference on Greenhouse Gas Control Technologies, 4: 5079–84. doi:10.1016/j.egypro.2011.02.482.

Naus, Dan J. 2006. *The Effect of Elevated Temperature on Concrete Materials and Structures - a Literature Review*. ORNL/TM-2005/553. Oak Ridge National Laboratory (ORNL). http://www.osti.gov/scitech/biblio/974590.

Neithalath, Narayanan, Milani S. Sumanasooriya, and Omkar Deo. 2010. "Characterizing Pore Volume, Sizes, and Connectivity in Pervious Concretes for Permeability Prediction." *Materials Characterization* 61 (8): 802–13. doi:10.1016/j.matchar.2010.05.004.

Nelson, Michael G. 2004. *Carbon Dioxide Sequestration by Mechanochemical Carbonation of Mineral Silicates*. University of Utah (US). http://www.osti.gov/scitech/biblio/826304.

Nemati, Kamran M. 1997. "Fracture Analysis of Concrete Using Scanning Electron Microscopy." *Scanning* 19 (6): 426–30. doi:10.1002/sca.4950190605.

Nemat-Nasser, Sia, and Muneo Hori. 1999. *Micromechanics: Overall Properties of Heterogeneous Materials*. Vol. 2. Elsevier Amsterdam. http://tocs.ulb.tu-darmstadt.de/93002114.pdf.

Němeček, Jiří, Vít Šmilauer, and Lubomír Kopecký. 2011. "Nanoindentation Characteristics of Alkali-Activated Aluminosilicate Materials." *Cement and Concrete Composites* 33 (2): 163–70. doi:10.1016/j.cemconcomp.2010.10.005.

Němeček, J., V. Šmilauer, and L. Kopeckỳ. 2009. "Characterization of Alkali-Activated Fly-Ash by Nanoindentation." In *Nanotechnology in Construction 3*, 337–43. Springer. http://link.springer.com/chapter/10.1007/978-3-642-00980-8_45.

Nesic, S., J. Postlethwaite, and S. Olsen. 1996. "An Electrochemical Model for Prediction of Corrosion of Mild Steel in Aqueous Carbon Dioxide Solutions." *Corrosion* 52 (4): 280–94. doi:10.5006/1.3293640.

Nordsveen, M., S. Nešić, R. Nyborg, and A. Stangeland. 2003. "A Mechanistic Model for Carbon Dioxide Corrosion of Mild Steel in the Presence of Protective Iron Carbonate Films—Part 1: Theory and Verification." *Corrosion* 59 (5): 443–56. doi:10.5006/1.3277576.

Nunes, L. C. S., and J. M. L. Reis. 2012a. "Estimation of Crack-Tip-Opening Displacement and Crack Extension of Glass Fiber Reinforced Polymer Mortars Using Digital Image Correlation Method." *Materials & Design* 33 (January): 248–53. doi:10.1016/j.matdes.2011.07.051.

Nyborg, R., and A. Dugstad. 1997. "Effect of Chromium on Mesa Corrosion Attack of Carbon Steel." *R. Nyborg, A. Dugstad, and P-E. Drdegreesnen(Inst. for Energy Technology, Norway)*, 9–14.

Nyborg, Rolf. 2005. "Controlling Internal Corrosion in Oil and Gas Pipelines." *Business Briefing: Exploration & Production: The Oil & Gas Review* 2: 70–74.

Nyborg, Rolf, Egil Gulbrandsen, Trine Loeland, Kemal Nisancioglu, and others. 2000. "Effect of Steel Microstructure and Composition on Inhibition of CO2 Corrosion." *CORROSION 2000*. https://www.onepetro.org/conference-paper/NACE-00023.

Nyborg, Rolf, and others. 2002. "Overview of CO2 Corrosion Models for Wells and Pipelines." *CORROSION 2002*. https://www.onepetro.org/conference-paper/NACE-02233.

Oelkers, Eric H. 2001. "General Kinetic Description of Multioxide Silicate Mineral and Glass Dissolution." *Geochimica et Cosmochimica Acta* 65 (21): 3703–19.

Oelkers, Eric H., Sigurdur R. Gislason, and Juerg Matter. 2008. "Mineral Carbonation of CO2." *Elements* 4 (5): 333–37. doi:10.2113/gselements.4.5.333.

Ohmoto, Hiroshi, Yumiko Watanabe, and Kazumasa Kumazawa. 2004. "Evidence from Massive Siderite Beds for a CO2-Rich Atmosphere Before~ 1.8 Billion Years Ago." *Nature* 429 (6990): 395–99.

Oliver, W.c., and G.m. Pharr. 1992. "An Improved Technique for Determining Hardness and Elastic Modulus Using Load and Displacement Sensing Indentation Experiments." *Journal of Materials Research* 7 (06): 1564–83. doi:10.1557/JMR.1992.1564.

———. 2004. "Measurement of Hardness and Elastic Modulus by Instrumented Indentation: Advances in Understanding and Refinements to Methodology." *Journal of Materials Research* 19 (01): 3–20. doi:10.1557/jmr.2004.19.1.3.

Olysych, L. V., M. F. Vigasina, L. V. Melchakova, L. P. Ogorodova, I. V. Pekov, and N. V. Chukanov. 2011. "Thermal Evolution and Thermochemistry of the Cancrinite-Group Carbonate-Oxalate Mineral." *Geochemistry International* 49 (7): 731–37. doi:10.1134/S0016702911050089.

Onsager, Lars. 1931a. "Reciprocal Relations in Irreversible Processes. I." *Physical Review* 37 (4): 405.

———. 1931b. "Reciprocal Relations in Irreversible Processes. II." *Physical Review* 38 (12): 2265.

Orowan, E. 1948. "Brittle Fracture of Notched Specimens." *Rep. Progr. Phys* 12: 185–99.

Pelisser, F., E. L. Guerrino, M. Menger, M. D. Michel, and J. A. Labrincha. 2013. "Micromechanical Characterization of Metakaolin-Based Geopolymers." *Construction and Building Materials* 49: 547–53.

Peng, Sheng, Qinhong Hu, and Shoichiro Hamamoto. 2012. “Diffusivity of Rocks: Gas Diffusion Measurements and Correlation to Porosity and Pore Size Distribution.” *Water Resources Research* 48 (2): W02507. doi:10.1029/2011WR011098.

Phan, L. T., N. J. Carino, D. Duthinh, and E. Garboczi. 1997. “NIST International Workshop on Fire Performance of High Strength Concrete.” *NIST, Gaithersburg, MD, February*, 13–14.

Pharr, G. M. 1998. “Measurement of Mechanical Properties by Ultra-Low Load Indentation.” *Materials Science and Engineering: A* 253 (1–2): 151–59. doi:10.1016/S0921-5093(98)00724-2.

Pichler, Bernhard, Christian Hellmich, and Herbert A Mang. 2007. “A Combined Fracture-Micromechanics Model for Tensile Strain-Softening in Brittle Materials, Based on Propagation of Interacting Microcracks.” *International Journal for Numerical and Analytical Methods in Geomechanics* 31 (2): 111–32.

Plessis, J. Prieur Du, and Jacob H. Masliyah. 1988. “Mathematical Modelling of Flow through Consolidated Isotropic Porous Media.” *Transport in Porous Media* 3 (2): 145–61. doi:10.1007/BF00820342.

Popescu, C. D., M. Muntean, and J. H. Sharp. 2003. “Industrial Trial Production of Low Energy Belite Cement.” *Cement and Concrete Composites* 25 (7): 689–93. doi:10.1016/S0958-9465(02)00097-5.

Potirniche, G. P., M. F. Horstemeyer, G. J. Wagner, and P. M. Gullett. 2006. “A Molecular Dynamics Study of Void Growth and Coalescence in Single Crystal Nickel.” *International Journal of Plasticity* 22 (2): 257–78.

Qafoku, Odeta, Libor Kovarik, Ravi K. Kukkadapu, Eugene S. Ilton, Bruce W. Arey, Jiri Tucek, and Andrew R. Felmy. 2012. “Fayalite Dissolution and Siderite Formation in Water-Saturated Supercritical CO2.” *Chemical Geology* 332–333 (November): 124–35. doi:10.1016/j.chemgeo.2012.09.028.

Qian, Dong, Gregory J. Wagner, Wing Kam Liu, Min-Feng Yu, and Rodney S. Ruoff. 2002. “Mechanics of Carbon Nanotubes.” *Applied Mechanics Reviews* 55 (6): 495–533.

Rai, Amit, J. Prabakar, C. B. Raju, and R. K. Morchalle. 2002. “Metallurgical Slag as a Component in Blended Cement.” *Construction and Building Materials* 16 (8): 489–94.

Ravikumar, Deepak, Sulapha Peethamparan, and Narayanan Neithalath. 2010. “Structure and Strength of NaOH Activated Concretes Containing Fly Ash or GGBFS as the Sole Binder.” *Cement and Concrete Composites* 32 (6): 399–410. doi:10.1016/j.cemconcomp.2010.03.007.

Rehan, R., and M. Nehdi. 2005. “Carbon Dioxide Emissions and Climate Change: Policy Implications for the Cement Industry.” *Environmental Science & Policy* 8 (2): 105–14. doi:10.1016/j.envsci.2004.12.006.

Rehder, Benjamin, Kingsten Banh, and Narayanan Neithalath. 2014. “Fracture Behavior of Pervious Concretes: The Effects of Pore Structure and Fibers.” *Engineering Fracture Mechanics* 118 (March): 1–16. doi:10.1016/j.engfracmech.2014.01.015.

Reis, J. M. L. 2006. “Fracture and Flexural Characterization of Natural Fiber-Reinforced Polymer Concrete.” *Construction and Building Materials* 20 (9): 673–78. doi:10.1016/j.conbuildmat.2005.02.008.

Riedel, W., K. Thoma, S. Hiermaier, and E. Schmolinske. 1999. “Penetration of Reinforced Concrete by BETA-B-500 Numerical Analysis Using a New Macroscopic Concrete Model for Hydrocodes.” In *Proceedings of the 9th International Symposium on the Effects of Munitions with Structures*. http://hsrlab.gatech.edu/AUTODYN/papers/paper79.pdf.

Rivera-Grau, L. M., M. Casales, I. Regla, D. M. Ortega-Toledo, J. G. Gonzalez-Rodriguez, and L. Martinez Gomez. 2012. “CO2 Corrosion Inhibition by Imidazoline Derivatives Based on Coconut Oil.” *Int. J. Electrochem. Sci* 7: 13044–57.

Robertsausten, W. Chandler. 1887. “On Certain Mechanical Properties of Metals, Considered in Relation to the Periodic Law.” *Proceedings of the Royal Society of London* 43 (258-265): 425–28.

Roesler, Jeffrey, Glaucio H. Paulino, Kyoungsoo Park, and Cristian Gaedicke. 2007. “Concrete Fracture Prediction Using Bilinear Softening.” *Cement and Concrete Composites* 29 (4): 300–312. doi:10.1016/j.cemconcomp.2006.12.002.

Rossol, Michael N., John H. Shaw, Hrishikesh Bale, Robert O. Ritchie, David B. Marshall, and Frank W. Zok. 2013a. “Characterizing Weave Geometry in Textile Ceramic Composites Using Digital Image Correlation.” *Journal of the American Ceramic Society* 96 (8): 2362–65. doi:10.1111/jace.12468.

Roux, S., J. Réthoré, and F. Hild. 2009. “Digital Image Correlation and Fracture: An Advanced Technique for Estimating Stress Intensity Factors of 2D and 3D Cracks.” *Journal of Physics D: Applied Physics* 42 (21): 214004. doi:10.1088/0022-3727/42/21/214004.

Rovnaník, Pavel, Patrik Bayer, and Pavla Rovnaníková. 2013. “Characterization of Alkali Activated Slag Paste after Exposure to High Temperatures.” *Construction and Building Materials* 47: 1479–87.

Sakai, M., and R. C. Bradt. 1986. “Graphical Methods for Determining the Nonlinear Fracture Parameters of Silica and Graphite Refractory Composites.” In *Fracture*

Mechanics of Ceramics, 127–42. Springer. http://link.springer.com/chapter/10.1007/978-1-4615-7023-3_10.

Sanahuja, Julien, Luc Dormieux, and Gilles Chanvillard. 2007. "Modelling Elasticity of a Hydrating Cement Paste." *Cement and Concrete Research* 37 (10): 1427–39.

Sánchez-Fajardo, V. M., M. E. Torres, and A. J. Moreno. 2014. "Study of the Pore Structure of the Lightweight Concrete Block with Lapilli as an Aggregate to Predict the Liquid Permeability by Dielectric Spectroscopy." *Construction and Building Materials* 53 (February): 225–34. doi:10.1016/j.conbuildmat.2013.11.093.

Sanchez-Palencia, Enrique, and André Zaoui. 1987. "Homogenization Techniques for Composite Media." In *Homogenization Techniques for Composite Media*. Vol. 272. http://adsabs.harvard.edu/abs/1987LNP...272.....S.

Sarker, Prabir K., Rashedul Haque, and Karamchand V. Ramgolam. 2013. "Fracture Behaviour of Heat Cured Fly Ash Based Geopolymer Concrete." *Materials & Design* 44 (February): 580–86. doi:10.1016/j.matdes.2012.08.005.

Sarshar, R., and G. A. Khoury. 1993. "Material and Environmental Factors Influencing the Compressive Strength of Unsealed Cement Paste and Concrete at High Temperatures." *Magazine of Concrete Research* 45 (162): 51–61. doi:10.1680/macr.1993.45.162.51.

Schapery, R. A. 1975. "A Theory of Crack Initiation and Growth in Viscoelastic Media." *International Journal of Fracture* 11 (1): 141–59. doi:10.1007/BF00034721.

Scheidegger, Adrian E. 1963. "Physics of Flow through Porous Media." In *Physics of Flow through Porous Media*. University of Toronto. http://bases.bireme.br/cgi-bin/wxislind.exe/iah/online/?IsisScript=iah/iah.xis&src=google&base=REPIDISCA&lang=p&nextAction=lnk&exprSearch=167376&indexSearch=ID.

Schneider, M., M. Romer, M. Tschudin, and H. Bolio. 2011. "Sustainable Cement Production—present and Future." *Cement and Concrete Research*, Special Issue: 13th International Congress on the Chemistry of Cement, 41 (7): 642–50. doi:10.1016/j.cemconres.2011.03.019.

Schneider, Ulrich. 1988. "Concrete at High Temperatures — A General Review." *Fire Safety Journal* 13 (1): 55–68. doi:10.1016/0379-7112(88)90033-1.

Scrivener, Karen L. 2004. "Backscattered Electron Imaging of Cementitious Microstructures: Understanding and Quantification." *Cement and Concrete Composites*, Scanning electron microscopy of cements and concretes, 26 (8): 935–45. doi:10.1016/j.cemconcomp.2004.02.029.

Seifritz, W. 1990. "CO2 Disposal by Means of Silicates." *Nature* 345: 486.

Shah, Surendra P. 1985. *Application of Fracture Mechanics to Cementitious Composites*. Springer Science & Business Media.

———. 1995a. *Fracture Mechanics of Concrete: Applications of Fracture Mechanics to Concrete, Rock and Other Quasi-Brittle Materials*. John Wiley & Sons. http://books.google.com/books?hl=en&lr=&id=v63v9KnKVHYC&oi=fnd&pg=PR15&dq=Fracture+mechanics+of+concrete:+applications+of+fracture+mechanics+to+concrete,+rock,+and+other+quasi-brittle+materials&ots=NizUs39Ekn&sig=9V0hHGG1k0LO0P5-8exlSRy9GUo.

Shannon, DW. 1976. "Role of chemical components in geothermal brines on corrosion of metals." In *Journal of the electrochemical society*, 123:c247–c247. electrochemical soc inc 10 south main street, Pennington, NJ 08534.

Singer, Philip C., and Werner Stumm. 1970. "The Solubility of Ferrous Iron in Carbonate-Bearing Waters." *Journal (American Water Works Association)*, 198–202.

Sivakumar, A., and Manu Santhanam. 2007. "Mechanical Properties of High Strength Concrete Reinforced with Metallic and Non-Metallic Fibres." *Cement and Concrete Composites* 29 (8): 603–8. doi:10.1016/j.cemconcomp.2007.03.006.

Skarżyński, Ł, J. Kozicki, and J. Tejchman. 2013. "Application of DIC Technique to Concrete—Study on Objectivity of Measured Surface Displacements." *Experimental Mechanics* 53 (9): 1545–59. doi:10.1007/s11340-013-9781-y.

Skarżyński, Ł., E. Syroka, and J. Tejchman. 2011. "Measurements and Calculations of the Width of the Fracture Process Zones on the Surface of Notched Concrete Beams." *Strain* 47 (June): e319–32. doi:10.1111/j.1475-1305.2008.00605.x.

Skarżyński, Ł., and J. Tejchman. 2013. "Experimental Investigations of Fracture Process Using DIC in Plain and Reinforced Concrete Beams under Bending." *Strain* 49 (6): 521–43. doi:10.1111/str.12064.

Smit, R. J. M., W. A. M. Brekelmans, and H. E. H. Meijer. 1998. "Prediction of the Mechanical Behavior of Nonlinear Heterogeneous Systems by Multi-Level Finite Element Modeling." *Computer Methods in Applied Mechanics and Engineering* 155 (1): 181–92.

Sneddon, Ian N. 1965. "The Relation between Load and Penetration in the Axisymmetric Boussinesq Problem for a Punch of Arbitrary Profile." *International Journal of Engineering Science* 3 (1): 47–57.

Soranakom, Chote, and Barzin Mobasher. 2007. "Closed-Form Moment-Curvature Expressions for Homogenized Fiber-Reinforced Concrete." *ACI Materials Journal* 104 (4). http://www.concrete.org/Publications/InternationalConcreteAbstractsPortal.aspx?m=details&i=18824.

———. 2008. “Correlation of Tensile and Flexural Responses of Strain Softening and Strain Hardening Cement Composites.” *Cement and Concrete Composites* 30 (6): 465–77. doi:10.1016/j.cemconcomp.2008.01.007.

Soranakom, C., and B. Mobasher. 2007. “Closed-Form Solutions for Flexural Response of Fiber-Reinforced Concrete Beams.” *Journal of Engineering Mechanics* 133 (8): 933–41. doi:10.1061/(ASCE)0733-9399(2007)133:8(933).

Sorelli, Luca, Georgios Constantinides, Franz-Josef Ulm, and François Toutlemonde. 2008. “The Nano-Mechanical Signature of Ultra High Performance Concrete by Statistical Nanoindentation Techniques.” *Cement and Concrete Research* 38 (12): 1447–56. doi:10.1016/j.cemconres.2008.09.002.

Stanley, Kolodzie. 1980. “Analysis of pore throat size and use of the waxman-smits equation to determine ooip in spindle field, Colorado.” In . Society of Petroleum Engineers. doi:10.2118/9382-MS.

Sumanasooriya, Milani S., and Narayanan Neithalath. 2011. “Pore Structure Features of Pervious Concretes Proportioned for Desired Porosities and Their Performance Prediction.” *Cement and Concrete Composites* 33 (8): 778–87. doi:10.1016/j.cemconcomp.2011.06.002.

Sun, J. B., G. A. Zhang, W. Liu, and M. X. Lu. 2012. “The Formation Mechanism of Corrosion Scale and Electrochemical Characteristic of Low Alloy Steel in Carbon Dioxide-Saturated Solution.” *Corrosion Science* 57 (April): 131–38. doi:10.1016/j.corsci.2011.12.025.

Sun, Wei. 2006. “Kinetics of Iron Carbonate and Iron Sulfide Scale Formation in CO2/H2S Corrosion.” Ohio University. https://etd.ohiolink.edu/!etd.send_file?accession=ohiou1163783193&disposition=attachment.

Sutton, Michael A., Jean-José Orteu, and Hubert W. Schreier. 2009. “Image Correlation for Shape, Motion and Deformation Measurements.” *Springer, New York, Doi* 10: 978–0.

Suzuki, Takayuki, and Mototsugu Sakai. 1994. “A Model for Crack-Face Bridging.” *International Journal of Fracture* 65 (4): 329–44. doi:10.1007/BF00012372.

Swanson, B.F. 1981. “A Simple Correlation Between Permeabilities and Mercury Capillary Pressures.” *Journal of Petroleum Technology* 33 (12). doi:10.2118/8234-PA.

Tabor, David. 1951. *The Hardness of Metals*. Vol. 10. ClarendonP.

Tanaka, Kyoji, and Kiyofumi Kurumisawa. 2002. “Development of Technique for Observing Pores in Hardened Cement Paste.” *Cement and Concrete Research* 32 (9): 1435–41. doi:10.1016/S0008-8846(02)00806-2.

Tassew, S. T., and A. S. Lubell. 2014. “Mechanical Properties of Glass Fiber Reinforced Ceramic Concrete.” *Construction and Building Materials* 51 (January): 215–24. doi:10.1016/j.conbuildmat.2013.10.046.

Taxiarchou, M., D. Panias, I. Douni, I. Paspaliaris, and A. Kontopoulos. 1997. “Removal of Iron from Silica Sand by Leaching with Oxalic Acid.” *Hydrometallurgy* 46 (1–2): 215–27. doi:10.1016/S0304-386X(97)00015-7.

Temuujin, Jadambaa, William Rickard, Melissa Lee, and Arie van Riessen. 2011. “Preparation and Thermal Properties of Fire Resistant Metakaolin-Based Geopolymer-Type Coatings.” *Journal of Non-Crystalline Solids* 357 (5): 1399–1404. doi:10.1016/j.jnoncrysol.2010.09.063.

Thaulow, Niels, Ulla Hjorth Jakobsen, and Boyd Clark. 1996. “Composition of Alkali Silica Gel and Ettringite in Concrete Railroad Ties: SEM-EDX and X-Ray Diffraction Analyses.” *Cement and Concrete Research* 26 (2): 309–18. doi:10.1016/0008-8846(95)00219-7.

Thomas, Job, and Ananth Ramaswamy. 2007. “Mechanical Properties of Steel Fiber-Reinforced Concrete.” *Journal of Materials in Civil Engineering* 19 (5): 385–92.

Tominaga, Yasutaka, Shuichi Arikawa, Satoru Yoneyama, Yasuhisa Fujimoto, and Yohei Omoto. 2014. “Observation of Thermal Strain on Electronic Packages Using Digital Image Correlation.” In *Advancement of Optical Methods in Experimental Mechanics, Volume 3*, 151–57. Springer. http://link.springer.com/chapter/10.1007/978-3-319-00768-7_18.

Tomson, M. B., M. L. Johnson, and others. 1991. “How Ferrous Carbonate Kinetics Impacts Oilfield Corrosion.” In *SPE International Symposium on Oilfield Chemistry*. Society of Petroleum Engineers.

Toro, Sebastian, Pablo J. Sánchez, Alfredo Edmundo Huespe, Sebastian Miguel Giusti, Pedro J. Blanco, and R. A. Feijóo. 2014. “A Two-Scale Failure Model for Heterogeneous Materials: Numerical Implementation Based on the Finite Element Method.” *International Journal for Numerical Methods in Engineering* 97 (5): 313–51.

Trtik, Pavel, Beat Münch, and Pietro Lura. 2009. “A Critical Examination of Statistical Nanoindentation on Model Materials and Hardened Cement Pastes Based on Virtual Experiments.” *Cement and Concrete Composites* 31 (10): 705–14. doi:10.1016/j.cemconcomp.2009.07.001.

Trusty, P. A., and J. A. Yeomans. 1997. “The Toughening of Alumina with Iron: Effects of Iron Distribution on Fracture Toughness.” *Journal of the European Ceramic Society* 17 (4): 495–504. doi:10.1016/S0955-2219(96)00099-4.

Unger, Jörg F., and Stefan Eckardt. 2011. “Multiscale Modeling of Concrete.” *Archives of Computational Methods in Engineering* 18 (3): 341–93.

Vance, Kirk. 2014. *Early Age Characterization and Microstructural Features of Sustainable Binder Systems for Concrete*. http://adsabs.harvard.edu/abs/2014PhDT.....13V.

Vance, Kirk, Matthew Aguayo, Tandre Oey, Gaurav Sant, and Narayanan Neithalath. 2013. "Hydration and Strength Development in Ternary Portland Cement Blends Containing Limestone and Fly Ash or Metakaolin." *Cement and Concrete Composites* 39 (May): 93–103. doi:10.1016/j.cemconcomp.2013.03.028.

Vance, Kirk, Aashay Arora, Gaurav Sant, and Narayanan Neithalath. 2015. "Rheological Evaluations of Interground and Blended Cement–limestone Suspensions." *Construction and Building Materials* 79 (March): 65–72. doi:10.1016/j.conbuildmat.2014.12.054.

Van Houtte, Paul, Anand Krishna Kanjarla, Albert Van Bael, Marc Seefeldt, and Laurent Delannay. 2006. "Multiscale Modelling of the Plastic Anisotropy and Deformation Texture of Polycrystalline Materials." *European Journal of Mechanics-A/Solids* 25 (4): 634–48.

Videm, Ketil, Jon Kvarekval, Teresa E. Perez, Guillermo Fitzsimons, and others. 1996. "Surface Effects on the Electrochemistry of Iron and Carbon Steel Electrodes in Aqueous CO2 Solutions." *CORROSION 96*. https://www.onepetro.org/conference-paper/NACE-96001.

Wang, Shuangzhen, Larry Baxter, and Fernando Fonseca. 2008. "Biomass Fly Ash in Concrete: SEM, EDX and ESEM Analysis." *Fuel* 87 (3): 372–79. doi:10.1016/j.fuel.2007.05.024.

Wang, Wei-Chien, Her-Yung Wang, and Ming-Hung Lo. 2014. "The Engineering Properties of Alkali-Activated Slag Pastes Exposed to High Temperatures." *Construction and Building Materials* 68 (October): 409–15. doi:10.1016/j.conbuildmat.2014.06.016.

Wang, Z. M., A. K. H. Kwan, and H. C. Chan. 1999. "Mesoscopic Study of Concrete I: Generation of Random Aggregate Structure and Finite Element Mesh." *Computers & Structures* 70 (5): 533–44.

Webb, Paul A. 2001. "An Introduction to the Physical Characterization of Materials by Mercury Intrusion Porosimetry with Emphasis on Reduction and Presentation of Experimental Data." *Micromeritics Instrument Corp, Norcross, Georgia*. http://www.intranet.micromeritics.com/Repository/Files/mercury_paper.pdf.

Wecharatana, M., and S. P. Shah. 1983. "A Model for Predicting Fracture Resistance of Fiber Reinforced Concrete." *Cement and Concrete Research* 13 (6): 819–29. doi:10.1016/0008-8846(83)90083-2.

Winslow, Douglas N. 1984. "Advances in Experimental Techniques for Mercury Intrusion Porosimetry." In *Surface and Colloid Science*, edited by Egon Matijević

and Robert J. Good, 259–82. Springer US. http://link.springer.com/chapter/10.1007/978-1-4615-7972-4_6.

Worrell, Ernst, Lynn Price, Nathan Martin, Chris Hendriks, and Leticia Ozawa Meida. 2001. "Carbon Dioxide Emissions from the Global Cement Industry." *Annual Review of Energy and the Environment* 26 (1): 303–29. doi:10.1146/annurev.energy.26.1.303.

Wriggers, P., and S. O. Moftah. 2006. "Mesoscale Models for Concrete: Homogenisation and Damage Behaviour." *Finite Elements in Analysis and Design* 42 (7): 623–36.

Wu, S. L., Z. D. Cui, F. He, Z. Q. Bai, S. L. Zhu, and X. J. Yang. 2004. "Characterization of the Surface Film Formed from Carbon Dioxide Corrosion on N80 Steel." *Materials Letters* 58 (6): 1076–81. doi:10.1016/j.matlet.2003.08.020.

Xu, Hua, and Jannie S. J. Van Deventer. 2002. "Microstructural Characterisation of Geopolymers Synthesised from Kaolinite/stilbite Mixtures Using XRD, MAS-NMR, SEM/EDX, TEM/EDX, and HREM." *Cement and Concrete Research* 32 (11): 1705–16. doi:10.1016/S0008-8846(02)00859-1.

Xu, Tianfu, John A Apps, and Karsten Pruess. 2004. "Numerical Simulation of CO2 Disposal by Mineral Trapping in Deep Aquifers." *Applied Geochemistry* 19 (6): 917–36. doi:10.1016/j.apgeochem.2003.11.003.

Xu, Tianfu, John A. Apps, and Karsten Pruess. 2005. "Mineral Sequestration of Carbon Dioxide in a Sandstone–shale System." *Chemical Geology*, Geochemical Aspects of CO2 sequestering Geochemical Aspects of CO2 sequestering, 217 (3–4): 295–318. doi:10.1016/j.chemgeo.2004.12.015.

Xu, Tianfu, John A. Apps, Karsten Pruess, and Hajime Yamamoto. 2007. "Numerical Modeling of Injection and Mineral Trapping of CO2 with H2S and SO2 in a Sandstone Formation." *Chemical Geology* 242 (3–4): 319–46. doi:10.1016/j.chemgeo.2007.03.022.

Yang, C. C. 1997. "APPROXIMATE ELASTIC MODULI OF LIGHTWEIGHT AGGREGATE." *Cement and Concrete Research* 27 (7): 1021–30. doi:10.1016/S0008-8846(97)00099-9.

Yang, C. C., and R. Huang. 1996. "Double Inclusion Model for Approximate Elastic Moduli of Concrete Material." *Cement and Concrete Research* 26 (1): 83–91. doi:10.1016/0008-8846(95)00196-4.

Yang, Hongqun, Zhenghe Xu, Maohong Fan, Rajender Gupta, Rachid B Slimane, Alan E Bland, and Ian Wright. 2008. "Progress in Carbon Dioxide Separation and Capture: A Review." *Journal of Environmental Sciences* 20 (1): 14–27. doi:10.1016/S1001-0742(08)60002-9.

Yates, J. R., M. Zanganeh, and Y. H. Tai. 2010. “Quantifying Crack Tip Displacement Fields with DIC.” *Engineering Fracture Mechanics*, International Conference on Crack Paths 2009, 77 (11): 2063–76. doi:10.1016/j.engfracmech.2010.03.025.

Yuan, Yuan, Jianyong Huang, Xiaoling Peng, Chunyang Xiong, Jing Fang, and Fan Yuan. 2014. “Accurate Displacement Measurement via a Self-Adaptive Digital Image Correlation Method Based on a Weighted ZNSSD Criterion.” *Optics and Lasers in Engineering* 52 (January): 75–85. doi:10.1016/j.optlaseng.2013.07.016.

Zhang, J. L., X. Liu, Y. Yuan, and H. A. Mang. 2014. “A Multiscale Model for Predicting the Elasticity Modulus and the Strength of Ultra-High Performance Fiber Reinforced Concrete.” *Computational Modelling of Concrete Structures*, 159.

Zhang, Mingzhong, Guang Ye, and Klaas van Breugel. 2013. “Microstructure-Based Modeling of Permeability of Cementitious Materials Using Multiple-Relaxation-Time Lattice Boltzmann Method.” *Computational Materials Science* 68 (February): 142–51. doi:10.1016/j.commatsci.2012.09.033.

Zhang, Peng, Chen-hui Liu, Qing-fu Li, and Tian-hang Zhang. 2013. “Effect of Polypropylene Fiber on Fracture Properties of Cement Treated Crushed Rock.” *Composites Part B: Engineering* 55 (December): 48–54. doi:10.1016/j.compositesb.2013.06.005.

Zhu, Wenzhong, John J. Hughes, Nenad Bicanic, and Chris J. Pearce. 2007. “Nanoindentation Mapping of Mechanical Properties of Cement Paste and Natural Rocks.” *Materials Characterization* 58 (11): 1189–98.

Zienkiewicz, Olek C., and Robert L. Taylor. 2005. *The Finite Element Method for Solid and Structural Mechanics*. Butterworth-heinemann. http://books.google.com/books?hl=en&lr=&id=VvpU3zssDOwC&oi=fnd&pg=PP1&dq=multiscale+modelling+solid+mechanics&ots=f2V6fTENZ3&sig=zbOfc8Ua6qOnP_27VBxWWmN7OII.

Zohdi, Tarek I., and Peter Wriggers. 2008. *An Introduction to Computational Micromechanics*. Vol. 20. Springer. http://books.google.com/books?hl=en&lr=&id=QBED3Dkj6bwC&oi=fnd&pg=PA1&dq=introduction+to+computational+micromechanics&ots=z0mRKCH9yO&sig=9B1Wc7NkUG_KlIdWBbGhhmXtTis.

Zohdi, T., M. Feucht, D. Gross, and P. Wriggers. 1998. “A Description of Macroscopic Damage through Microstructural Relaxation.” *International Journal for Numerical Methods in Engineering* 43 (3): 493–506.

Zohdi, T. I., and P. Wriggers. 2001. “Computational Micro-Macro Material Testing.” *Archives of Computational Methods in Engineering* 8 (2): 131–228.

Zuda, Lucie, Pavel Rovnaník, Patrik Bayer, and Robert Černỳ. 2007. “Thermal Properties of Alkali-Activated Slag Subjected to High Temperatures.” *Journal of Building Physics* 30 (4): 337–50.